UNIVERSITÀ
DI PAVIA

PhD IN BIOMEDICAL SCIENCES

DEPARTMENT OF MOLECULAR MEDICINE
UNIT OF HUMAN PHYSIOLOGY
PhD Director: Chiar.mo Prof. Egidio D'Angelo

Interaction of Cerium Oxide Nanoparticles with biological systems

Tutors:

Prof. Laforenza Umberto

Dott. Sommi Patrizia

PhD dissertation of

Stefania Coniglio

XXXIV Cycle
Academic Year 2020-2021

Index

Abstract

Engineered nanoparticles (NPs) are commercially produced materials having at least one dimension less than 100 nm. NPs have gained considerable interest for their potential application in many areas, due to their distinctive physicochemical and electrical properties.

Among all the possible applications, antioxidant properties are particularly interesting. Oxidative stress is a condition in which free radical concentration (*i.e.*, reactive oxygen species (ROS) and reactive nitrogen species (RNS), originating from metabolic reactions) exceeds the antioxidant capacity of the cells. Oxidative stress and generation of free radicals are associated, among other pathologies/diseases, with neurodegenerative conditions, such as Alzheimer's and Parkinson's diseases.

Cerium oxide nanoparticles (**CNPs**) are under active investigation as promising agents in the therapy of several diseases involving free radicals or oxidative stress. CNPs have been proven to be effective free radical scavengers with almost no toxicity. They seem to exert a neuroprotective effect on neuronal cells and be effective in the treatment of cerebral ischemia or hypoxia caused by stroke as well as reduce inflammation, prevent radiation-induced damage and exert a selective anticancer activity.

This project aimed to understand how CNPs, as super-small nanoparticles specifically interact with biological systems. In particular, the first part of the project aimed to understand the CNP-cell interaction by investigating cell adhesion and internalization.

For this purpose, negatively charged CNPs with a core size of 6 nm and an overall hydrodynamic diameter of 14.8 nm, functionalized with Polyacrylic acid (PAA), were used.

The HeLa cells line was initially used to evaluate the CNP-cell adhesion. SEM and TEM analysis showed that no CNPs were observed on the cell membrane (planar membrane), but a very specific and exclusive interaction was present with the cell microvilli. CNPs seemed to adhere in such a way as to form a continuous and uniform layer covering the entire microvillus length. The interaction with the microvilli membrane was so specific that the CNPs adhesion stopped right at the base of the microvillus in the proximity of the planar membrane. Such adhesion, named **microvillus mediated adhesion** (**MMA**) was not dependent on the nanoparticles core chemical composition, since it has been observed using both ceria and magnetite NPs with a dimension of < 40 nm. On the contrary, it was shown to depend on the surface charge of the NPs, as no MMA was observed when using CNPs with a neutral or positive functionalization. Moreover, such adhesion was not cell-specific, as it was observed, in addition to HeLa cells, in three different cell lines. MMA was shown to depend on the presence of lipid rafts, more abundant and different in composition than the planar membrane, since the CNPs adhesion was altered by depleting cholesterol and altering the synthesis of sphingolipids. On the contrary, the adhesion was not blocked when the microvillus skeleton was altered by reducing the polymerization of actin. Different from the common mechanisms of NPs adhesion and internalization described so far, MMA depends specifically on the membrane composition of microvilli (specifically lipid rafts), but not on the microvillus integrity. The strict dependence of the CNPs adhesion on microvilli was also shown by the direct relationship between MMA and microvilli density during the cell cycle.

The internalization process that followed MMA showed to be influenced by the adhesion process. CNPs were found to accumulate inside endolysosomes still adherent to what has been identified as microvilli. The involvement of microvilli in the internalization processes suggests that MMA differs from the commonly described uptake mechanisms and might represent an interesting alternative approach for selective NP delivery.

The second part of this research focused on the possible use of a model animal, like **Drosophila melanogaster**, in assessing the antioxidant effects of CNPs *in vivo*. The first goal was to find the right conditions to investigate whether CNPs could diffuse to different fly tissues/organs and to subsequently monitor the Ce oxidation state and evaluate the antioxidant effect based on their distribution.

The results showed that flies could be fed with CNPs without showing signs of toxicity and that the ingested NPs could be followed along the entire intestine. It was shown that the CNPs interacted with the enterocytes luminal membrane and were internalized. As proof of their internalization, in addition to immunofluorescence, a high level of free radicals induced in the enterocytes was strongly reduced by the presence of the CNPs, thus proving that the NPs were able to be internalized and exercise their scavenging activity. Moreover, the presence of CNPs in other areas of the fly body, like the ovaries, suggested they could also diffuse from the intestine. These preliminary results suggested that, although with many limitations, the *in vivo* CNPs–cell interaction study using Drosophila offered a higher level of complexity compared to the cell culture, by mimicking the NPs diffusion in the human body.

This preliminary study was focused on understanding the distribution of Ce as well as Ce^{3+}/Ce^{4+} equilibrium inside different organs of the fly body, to be performed at the European Synchrotron Radiation Facility (**ESRF**) in Grenoble (France). This analysis will represent a further step toward the experimental assessment of the chemical mechanisms responsible for the CeO_2 activity in several degenerative diseases in which oxidative stress and free radicals production play a crucial role.

The Drosophila fly model was also exploited for the study of a new kind of nanoparticles, specifically, **Fe_3O_4 NPs covered with a boron carbide core** (**B-IONPs**). This was part of a bigger project which consider the use of nanoparticles of boron carbide as an alternative and more efficient delivery system of ^{10}Boron (^{10}B) for **Boron neutron capture therapy** (**BNCT**). Preliminary studies of the distribution of B-IONPs in Drosophila were performed, in order to prove the advantage of the use of NPs over the existing compounds, like borated aminoacids. The results showed that the B-IONPs were efficiently absorbed by the flies to distribute in the different organs. Moreover, it was possible to quantify the biodistribution of ^{10}B in the guts, heads, and ovaries after the ingestion of p-Boronophenylalanine (***BPA***), a boron delivery agent. These results confirmed the use of Drosophila as an alternative to the more complex and expensive animal models for BNCT. This would be the first step toward a more complex protocol, where tumor-bearing Drosophila fly would be treated with BNCT, and the post-irradiation effects followed *in vivo*.

1. Introduction

1.1 Nanoparticles

1.1.1 Generalities

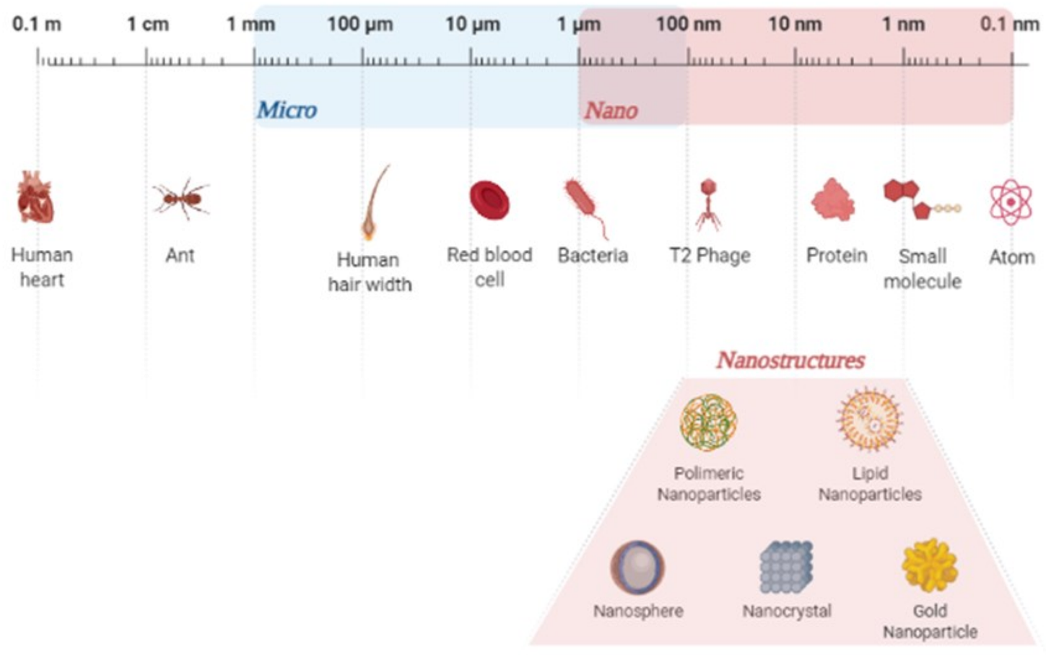

Figure 1. Nanoscale integration of Nanoparticles and Biomolecules. *Nanoparticles are defined as particles with a diameter ranging from 1 to 100 nm.*

In the literature, NPs have been defined in a variety of ways; however, a single internationally accepted definition for Nanomaterials (NMs) does not exist. A nanometer (nm) is an International System of Units (Système international d'unités, SI) unit that represents 10^{-9} meters in length (**Figure 1**). According to *ASTM E2456-06 (2020) Standard Terminology Relating to Nanotechnology,* a Nanoparticle is defined as "a particle with lengths in two or three dimensions greater than 1 nm and smaller than 100 nm and which may or may not exhibit a size-related intensive property".

NPs are also defined as zero-dimensional nanomaterials distinguishing them from one- and two-dimensional nanomaterials that have either one or two dimensions larger than nanoscale respectively. They are differentiated from their bulk counterparts in terms of size, chemical reactivity, mobility, energy absorption, etc. [Murthy S.K., et al., 2007] This characteristic enables them to possess some unique properties compared to the bulk counterparts they are synthesized from, like excellent reactivities, high surface areas, exceptional mobilities, superb mechanical, chemical, and electrical properties. This one-of-a-kind phenomenon has prompted a new industrial revolution by enabling the synthesis and manufacture of desired-size particles with novel properties and applications [Murthy S.K., et al., 2007].

Nanoparticles (**NPs**) are now commonly used in a variety of fields, including analytical chemistry and environmental science, as well as pharmacy, agriculture, medicine, and the pharmaceutical industry. This is owing to the special properties of NPs as well as the innovation they bring to such applications.

Since Nobel Laureate Richard P. Feynman proposed nanotechnology in his now-famous 1959 lecture "There's Plenty of Room at the Bottom", several ground-breaking advances in physics, chemistry, and biology have shown Feynman's ideas of controlling matter at an exceedingly small scale, the level of molecules and atoms, i.e., the nanoscale [Sanchez F., et al., 2010]. However, Nanotechnology originated as a discipline just in the 1980s, and since then, there has been a growth in scientific publications and interest in the field, with research intensifying in the 2000s (**Figure 2**) as a result of increased technological, political, and market exposure, which has resulted in both controversy and development. Similarly, the commercialization of products focused on nanoscale technology advances started to emerge.

It is difficult to know how many items on the market today include nanomaterials: their unique properties have sparked a lot of interest. As a result of this growth, several experts estimate that the research and commercialization of nanomaterials will continue to increase exponentially over the next few years.

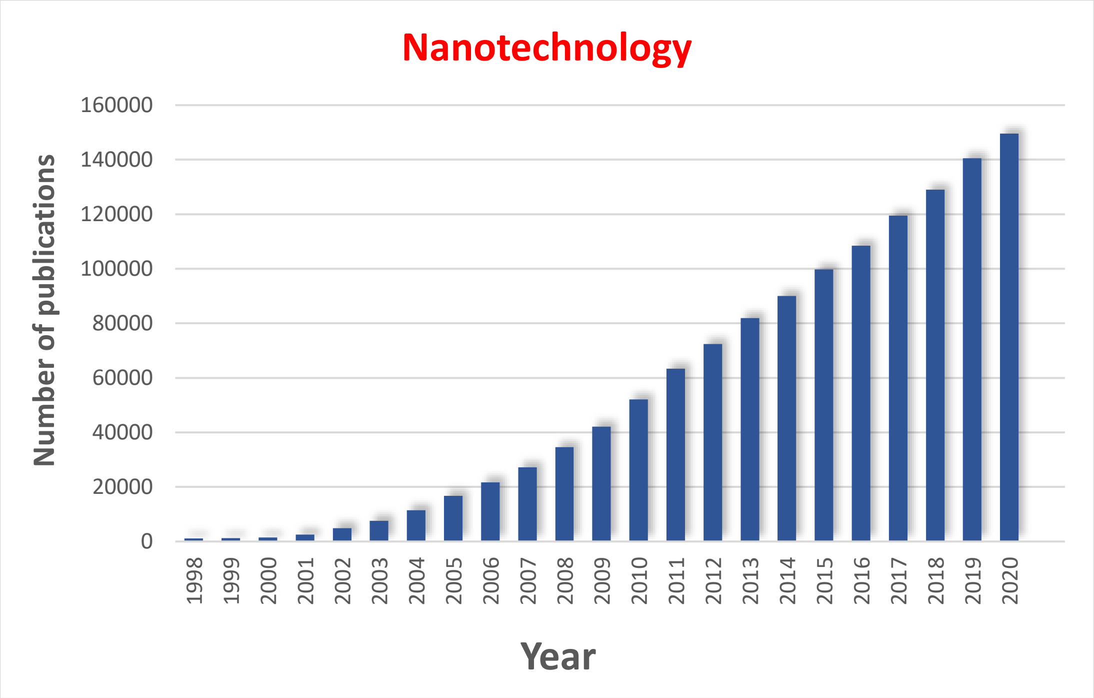

Figure 2. Number of publications per year in the Scopus database containing the keyword "Nanotechnology".

1.1.2 Characterization of NPs

As opposed to the bulk materials from which they are synthesized, NPs have several distinct characteristics. Very high surface areas, outstanding reactivities, extraordinary mobilities, and excellent mechanical, biological, and electrical properties are only a few of these characteristics. On the other hand, the properties of certain nanoparticles are extremely dependent on their size and chemical composition [Sajid M., et al, 2020].

While it is common to think of nanoparticles as simple molecules, they are actually complex mixtures. Even in the easiest situations, the relationships between at least two distinct elements of the substance must be considered. Every nanoparticle has an extremely high surface area to volume ratio, which is one of the reasons for some of its peculiar properties. However, because of the high surface area, the surface of any given nanoparticle is an essential component of the substance.

In certain cases, the precise structure of the nanoparticle's surface is intimately connected to its final application. A nanoparticle designed to interact with biological systems, for example, will have appropriate functional groups attached to its surface, such as short-chain peptides. In fact, in many cases, surface functionalization is essential to the production of nanoparticles with the desired properties. This is mostly related to the fact that many nanoparticles lose their unique properties after aggregating and precipitating. As a result, considerable effort is spent in preparing nanoparticles that can be monodispersed in the desired medium. Typically, this entails preparing NPs with a coating that aids in particle dispersion. These coatings may take the form of surfactants, which form transient Van-der-Waals interactions with the surface and exist in equilibrium with the free surfactant molecule in some cases. In other situations, molecules or ions are attached to the particle's surface, stabilizing the particle suspension because of the repulsion forces.

A nanoparticle may thus be divided into two or three layers:

1. ***surface***, that is often functionalized,
2. ***shell,*** material that is applied intentionally,
3. ***core*** material. Since this is essentially the center of the nanoparticle, is often used to refer to the nanoparticle itself [Christian P., et al., 2008].

Another important factor to consider when discussing nanoparticles for biomedical applications is the ***protein corona***, which can be described as the set of proteins that are absorbed on the nanoparticle’s surface once they circulate in a biological environment.

The surface

Metal ions, small molecules, surfactants, and polymers can all be used to functionalize the surface of a nanoparticle. Preparing NPs with a charged surface is a quick and easy way to produce NPs that disperse in aqueous media. However, certain materials lack suitable surfaces for the stabilization of localized charges. It is normal in all these situations to use a small molecule that will bind to the surface of the particle through a covalent-like bond and often include charge-carrying groups.

A surfactant, such as sodium dodecyl sulfate (SDS), may also be used to create a stable dispersion of nanoparticles [Qiu S., et al., 1999]. In this case, the nanoparticle forms in the center of a micella, and the hydrophobic interactions between the surfactant tail and the particle surface drive the surfactant binding to the particle's surface. It is important to note that these structures are distinct from those in which a molecule is covalently attached to the nanoparticle's surface and the surfactant is in contact with free surfactant molecules in the media [Shaw D.J., 1992]. As the mechanism is filtered, this equilibrium shifts such that the free surfactant concentration remains constant at the essential micelle concentration. As a consequence of this change in equilibrium, extreme dilution results in colloid volatility and precipitation.

A final type of surface-active molecule includes those based on monofunctional long-chain molecules such as amines, phosphines, carboxylates, and thiols. These molecules covalently link to unique locations on the nanoparticle's surface and have long chains that stretch into the dispersion medium, providing stability. Typically, these are added to the particle's surface during preparation and can be adjusted later. It is not uncommon for such materials to be prepared for dispersion in hydrophobic solvents and then modified with PEG to impart water dispersibility.

The shell

The word "*shell*" refers to a second layer that is structurally distinct from the core material. The quantum dots with a nucleus of one element, such as cadmium selenide, and a *shell* of another material, such as zinc sulfide, are fine examples of both elements.

Additionally, polymer nanoparticles such as polystyrene-polyaniline may be used as an illustrative example. [Luo X., et al., 2007] Although these materials may be deliberately prepared, this would not exclude them from occurring naturally. For instance, it is well established that after preparation, iron nanoparticles rapidly shape layers of iron oxide on their surface. Since these layers do not actually infiltrate the whole molecule, the nanoparticle may have a central *shell* structure rather than being pure iron [Sun Y., et al., 2007].

The Core

The *core* is the essential very center of the NPs. When discussing the *core* of NPs, it is important to consider mainly three aspects.

The first one is that there is a widespread trend in the physical sciences to refer to the *core* as to the nanoparticle itself. It should be recognized that the properties of concern to the physics and chemistry groups are typically governed by the *core*'s properties. This is not to say that the *core* structure alone can dictate a nanoparticle's destiny and environmental conduct. There are situations where the precise structure of the whole nanoparticle is essential for reliably evaluating its overall properties. [Wuister S.F., et al., 2004]

A second critical factor to remember when discussing the heart of a nanoparticle is the enormous diversity that can exist. This is particularly true when it comes to inorganic nanoparticles. It is well established that the majority of inorganic materials occur in several phases and that the process of the material has a significant impact on its physical properties. Although nanoparticles may be prepared in a single step, it is not uncommon for two phases to coexist [Rempel J.Y., et al., 2006]. Additionally, even precise representations of nanoparticles will result in incorrect conclusions. It is well established that numerous crystal defects and other twinning and packaging phenomena can result in extremely complex core compositions in nanoparticles. Although it is impossible to analyze all samples for toxicology research to these standards, it is critical to have some potential differences in mind in case any unexpected findings are discovered later.

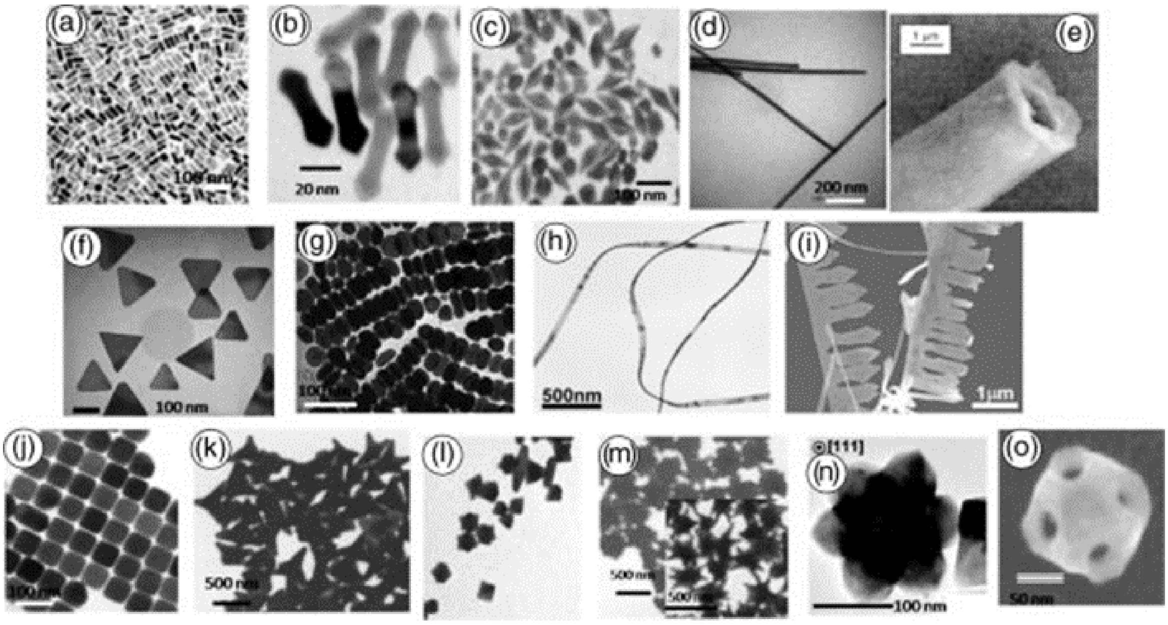

Figure 3. Nanoparticles morphologies. *A few examples of TEM and SEM images of 1D, 2D, and 3D noble metal nanoparticles (NMNPs) of complex morphologies synthesized by colloid chemical synthetic approach: (a) nanorods; (b) nanoshuttles; (c) nanobipyramids; (d) nanowires; (e) a nanotubule; (f) triangular nanoplates; (g) nanodiscs; (h) nanoribbons; (i) nanobelts; (j) nanocubes; (k) nanotetrapods; (l) and (m) star-shaped nanoparticles; (n) a nanohexapod; and (o) a nanocage. Reproduced from: Sau T.K., et al., 2010.*

Finally, and perhaps most importantly, the morphology of nanoparticles should be considered. While several nanoparticles currently in use are nominally isotropic, several other morphologies are possible. In **Figure 3** some of the most common examples of morphologies of metal nanoparticles are reported. Perhaps the most prevalent is a straightforward rod or cable (**Figure 3, a**), such as a carbon nanotube (CNT). However, for a variety of components, tetrapods (**Figure 3, k**), pyramids (**Figure 3, c**), nanocubes (**Figure 3, o**), and star-shaped (**Figure 3, m**) have been prepared. Mostly, modulation of these shapes is linked to the process of the system's elements, but it may also be related to variations in the materials' structure. Although very few of these materials have found practical uses to date, there is a strong likelihood that they will, and therefore the precise morphology of the nanomaterial will become a far more complicated problem.

1.1.4 Protein Corona

In recent years, NPs have been widely investigated for biological applications, owing to their many superior properties. However, a significant restriction of NPs application is their uncertain destiny *in vivo* as a consequence of the development of "**protein corona**" (**PC**). Upon entering a biological environment, the surface of the NP is quickly coated with a layer of biomolecules, primarily proteins. The presence of this PC around the NP poses major limits for the use of nanomaterials inside the biological systems, in terms of biodistribution and toxicity. On the nanoscale, the influence of the formation of PC on NPs can heavily influence their properties, due to the high surface to volume of nanomaterials. For this reason, studying in detail the interaction of NPs with biological fluids is of vital importance for the development of new NPs-based medical devices [Pinals R.L., et al., 2020].

Common biological fluids are generally aqueous solutions with high concentrations of ions and biomolecules (often hundreds of mM), which might interact with nanomaterial surfaces. Blood and serum are highly complex, including over hundreds of distinct protein species at concentrations more than 80 mg/mL, which is a completely different environment from the organic solvents or gaseous phases in which nanomaterials are commonly generated.

Biofluids contain a diverse range of biomolecules, particularly proteins, which may be seen as a "cloud" around the NP. According to how strong the interaction of this "cloud" around the nanoparticle is, it is possible to distinguish between "**soft**" and "**hard**" protein corona (**Figure 4**) [Ke P.C., et al., 2017]. Some will reversibly adsorb to the NP surface, forming a monolayer (**hard corona**). The "hard" corona is considered as an equilibrium state long enough to confer a new biological identity to the NM. Adsorption may be accompanied by (partial) unfolding, exposing hydrophobic moieties that can adsorb additional proteins as a second layer (**soft corona**). This means that protein interaction will change the physicochemical characteristics of the produced NPs, affecting biological processes such as cellular uptake, proliferation, and cytotoxicity, as well as the targeting and delivery capacities of the nanostructures [Zanganeh S., et al., 2016].

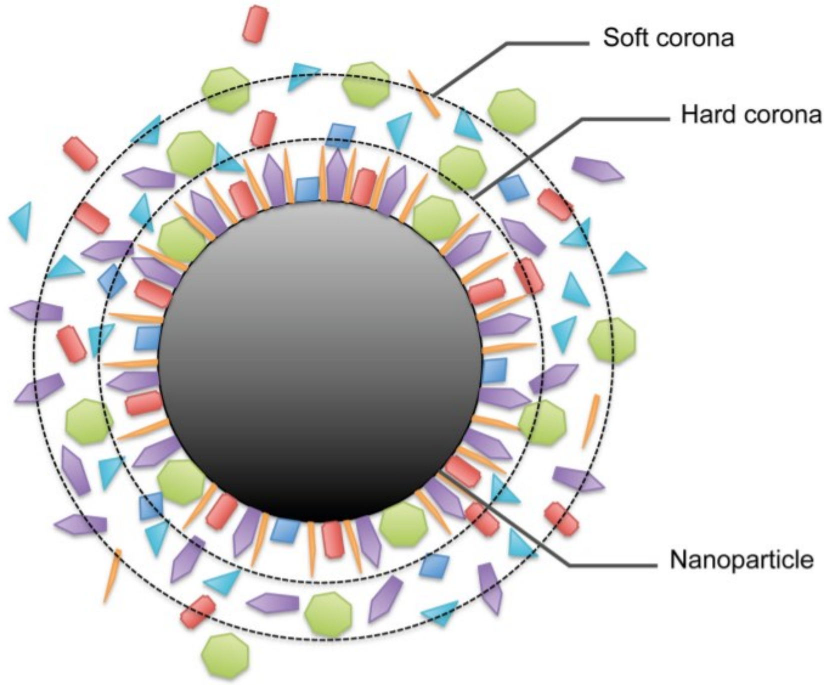

Figure 4*. *Schematic representation of protein corona. *A hard and soft layer of proteins covers the surface of the nanoparticle. The proteins in the hard corona are more tightly associated with the particle surface, making them less dynamic than the proteins in the soft corona. Reproduced from Wolfarm J., et al., 2014*

To date, a direct relationship between the structure of the NPs and the resulting PC has not yet been fully understood, even if some studies showed that the features that play a major role in these interactions are the size, the charge, and the surface functionalization of the NP [Treuel L., et al., 2015]. It is important to highlight that the majority of studies have been focused on the characterization of the "hard" PC, as it is stable enough to be isolated and analyzed. Soft corona, on the contrary, is composed of proteins with lower affinity, implicating that the composition can change over time. For this reason, during the characterization and study of the soft corona on NPs, the proteins can be easily detached, thus making the study of soft corona a challenge.

To summarize, PC creation is not a static event. Until they achieve a stable state, proteins will continually adsorb and desorb from the NP surface. Up to this point, it has been shown that highly abundant proteins can be gradually replaced by less abundant proteins with a greater affinity for the NP surface. So far, the main techniques available for the study of the protein corona are **Fluorescence Correlation Spectroscopy** (**FCS**) or **Dynamic Light Scattering** (**DLS**) [Hadjidemetriou M., et al., 2016].

1.2 Cytoplasmatic membrane and Endocytosis pathways

1.2.1 Cytoplasmatic membrane

The plasma membranes are crucial for the life of the cells. They enclose the cells, define the boundaries, maintain essential differences between the cytosol and the extracellular matrix.

For example, ion gradients across membranes, established by activities of specialized membrane proteins, can be used to synthesize ATP, to drive the transmembrane movement of selected solutes or, in very specialized cells like nerve or muscle, to produce and transmit electrical signals, or more, to enclose receptors that can act as sensors for external signals.

Despite having a lot of different functions, all biological membranes have a common general structure. Each membrane is composed of a very thin film of lipid and protein molecules, held together mainly by non-covalent interactions. They are dynamic and fluid structures, in which the lipids are arranged as a continuous double layer (**lipid bilayer**) about 5 nm thick

(**Figure 5**). The lipid bilayer provides the basic fluid structure and serves as a relatively impermeable barrier to the passage of most water-soluble molecules.

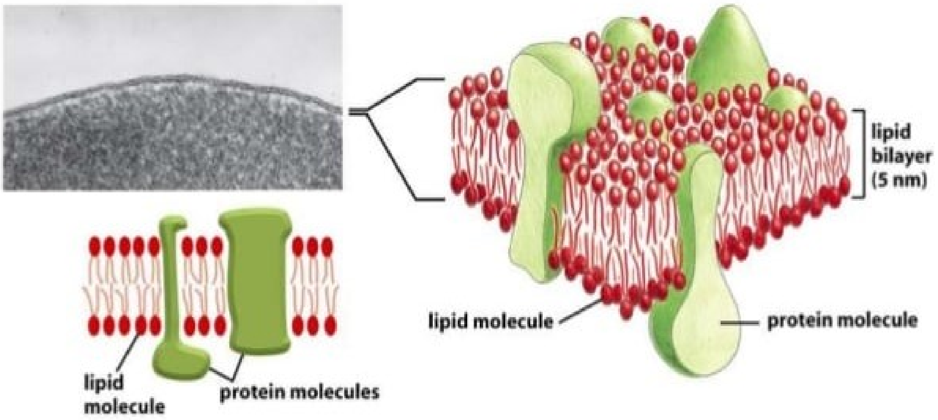

Figure 5. Structure of the cytoplasmatic membrane. *Electron micrograph of a plasma membrane seen in cross-sections and schematic drawings of the cell membrane generic structure, showing the general disposition of its lipid and protein constituents. Adapted from Alberts B., Molecular biology of the cells, 2017.*

Most of the functions of the membrane are mediated by **transmembrane proteins**, for example, catalyzing membrane-associated reactions (like ATP synthesis) or mediating the transports of solutes across the membrane. Other transmembrane proteins serve as structural links with the cytoskeleton, while others serve as a receptor to detect chemical signals in the cell's environment. It is estimated that about 30% of all the proteins encoded in an animal cell's genome are membrane proteins.

The first studies aimed at understanding the structure of the plasma membrane were based on physicochemical observations on red blood cells. If placed in hypotonic solutions, they undergo lysis, leaving an empty bag, called "shadow", the analysis of which revealed that they were constituted mainly from phospholipids. The first plasmatic membrane model predicted that it was formed by a monomolecular film of phospholipids arranged in a palisade, with the hydrophilic heads facing the water and the tails water repellent towards the air. At the same time, other scholars, examining the chemical composition of red blood cells, showed that, in aqueous solution, the area occupied by the phospholipids extracted from the erythrocyte shadows was double that to the erythrocyte area itself. This suggests that the membrane is not formed by a monolayer, but by a double layer of phospholipids, which hydrophobic tails, attracted by hydrophobic forces, arrange themselves frontally, while the hydrophilic heads are oriented towards the aqueous environment external and internal to the cell.

Every membrane type has its own characteristic globular and non-filamentous proteins, which, thanks to the fact that the interactions between lipids and those between proteins and lipids are non-covalent, can move laterally in the plane of the membrane.

The lipid bilayer is not homogeneous, not only between different cells but even between the two phospholipid layers: the plasma membrane shows a marked asymmetry, with a different composition of lipid and proteins, which reflects the different functions of the two monolayers.

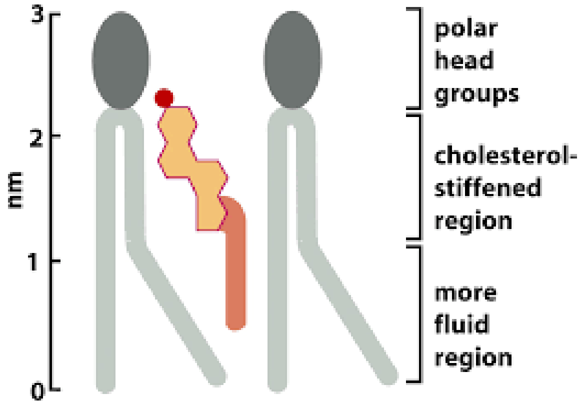

***Figure 6*. Cholesterol disposition in the lipid bilayer.** *Schematic representation of a cholesterol molecule interacting with two phospholipid molecules in one monolayer. Adapted from Alberts B., Molecular biology of the cells, 2017.*

Essentially the plasma membranes are made of lipids, proteins, and carbohydrates. Membrane lipids generically are not a homogeneous family, but they tend to vary by nature and quantity, from membrane to membrane. In the plasmalemma of the prokaryotic cells, lipids are almost exclusively represented by phospholipids and glycolipids; in eukaryotic cells, on the other hand, there are phospholipids, glycolipids, sphingolipids, and cholesterol (**Figure 6**). Usually, in the internal portion of the membrane, it is possible to find mainly phospholipids. The main membrane phospholipids are phosphatidylserine, phosphatidylethanolamine, especially in the inner layer. On the other hand, in the outer layer phosphatidylcholine and sphingomyelin are more common.

Membrane carbohydrates are usually present in the form of oligosaccharides glycoproteins and glycolipids, only in the outer leaflet, in contact with the extracellular environment. They constitute the so-called **glycocalyx,** which performs as a receptor, mediating cell recognition, and they have a protective function since they protect the plasma membrane from mechanical and chemical insults. Also, they help the cells to maintain hydration thanks to the presence of electrical charges of sialic acid, which can retain water molecules.

At physiological temperatures, the cell membrane is in the liquid-crystalline lamellar state, in which the hydrocarbon chains of lipids are in the fluid state, so they manifest considerable freedom of movement. For this reason, both lipids and proteins can move within their own monolayer freely.

In biological membranes, this stiffness is resolved by a higher concentration of **cholesterol**, which allows the membrane to have a semi-fluid structure by preventing the crystallization of the aliphatic chains of phospholipids. The main factors that determine the fluidity of the cell membrane are, in addition to the temperature, the length of the fatty acids, the degree of unsaturation of the fatty acids of the tails of phospholipids, the characteristics of the polar heads, and the concentration of cholesterol in the membrane. When a lipid bilayer reaches a specific low temperature, defined as **transition temperature**, it can lose its fluidity. The chains of the phospholipid are arranged more strictly and their chains become longer because they are more saturated. For these reasons, it is defined as a crystallin structure that commonly, for biological membranes, is reached at a temperature below 10°C. Thus, the presence of cholesterol in the membranes regulates the fluidity and amplifies the range of transition temperature.

Several types of movements have been described in the plasmatic membrane. These movements can be **intramolecular** or **intermolecular**. Intermolecular movement takes place mainly in horizontal ("**lateral diffusion**"), but rarely the movement of lipids occurs from one face of the membrane to the other ("**flip-flop diffusion**") helped by the presence of proteins called *Flippase*. The Flip-Flop diffusion contributes to a continuous re-arrangement of the composition of phospholipids in the inner and the outer part of the bilayer [Alberts B., Molecular biology of the cells, 2017].

1.2.2 Lipid rafts

Lipids and proteins are not re-arranged casually across the plasmatic membrane, but they can often form different domains or micro-domains that have different functions. For example, most cells, like epithelial cells, can have one **apical domain**, and one **basal domain**: they both have a completely different composition of lipids and proteins.

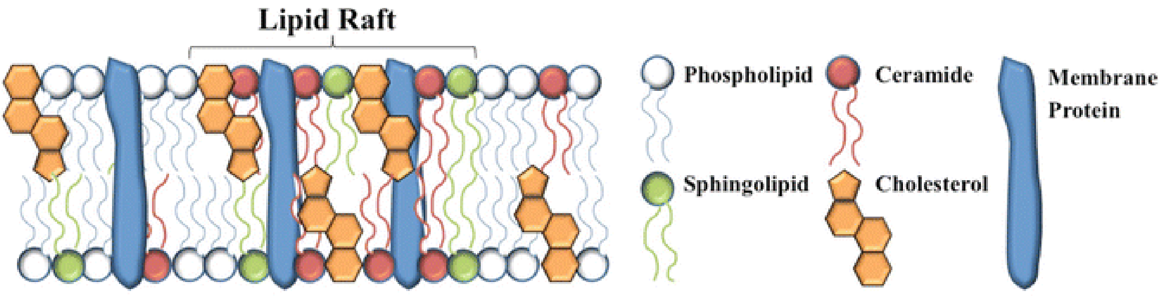

***Figure** 7. **Schematic representation of lipid rafts and cholesterol**, typical constituents of the membranes of microvilli In the lipid rafts is possible to observe the higher concentration of cholesterol, some specific protein, and some type of phospholipid, like sphingolipid and ceramide. Adapted from: Parsons G.K.S., et al., 2012.*

One type of these micro-domains is the so-called **lipid rafts**. Lipid rafts are specific regions of the membranes that have a higher concentration of glycosphingolipids (usually present in the outer part), like sphingomyelin, and cholesterol (**Figure 7**). For this reason, they are more rigid than the rest of the membrane, possess a more crystalline structure, and are detergent-resistant (most commonly Triton X-100). Probably because of this operational definition, lipid rafts have acquired a confusing array of acronyms over the years, including DIGs (detergent-insoluble glycosphingolipids), DICs (detergent-insoluble complexes), DRMs (detergent-resistant membranes), to name a few.

Usually, lipid rafts are extremely dynamic structures, because they can change their composition fast and they can move laterally across the membrane. They have been researched for a long, and they seem to participate in a lot of different functions, from cell-cell communication to internalization. It is no exaggeration to state that the lipid raft concept has revolutionized the way we view complex events occurring at cellular membranes.

Lipid rafts tend to accumulate in specific portions of the cell membrane forming **membrane ruffles.** Sometimes, these membrane ruffles can be more structured and serve a specific role in specialized cells, like in the case of **microvilli** (for example in the brush border in the intestine or in the kidney). In other situations, membrane ruffles can be used by cells to "test" the environment or internalize particles.

Microvilli (singular: microvillus) are microscopic cellular membrane protrusions that increase the surface area for diffusion and minimize any increase in volume and are involved in a wide variety of functions, including absorption, secretion, cellular adhesion, and mechano-transduction. They are thin structures that can vary between 0.1 μm and several micrometers in length, and 70–150 nm in diameter. [Hye-Ran K., et al., 2019] Each microvillus has hundreds of actin filaments running parallel to the long axis on the inside.

The membrane lipids constituting rafts of kidney proximal tubule cell microvilli are mainly cholesterol and sphingomyelin, which together make up about 65% of the lipid in detergent-resistant membranes, whereas glycolipids represent less than 10% [Parking E.T., et al., 2001]. In contrast, brush border membranes isolated as microvillar vesicles from small intestinal enterocytes are particularly rich in glycolipids [Christiansen K., et al., 1981].

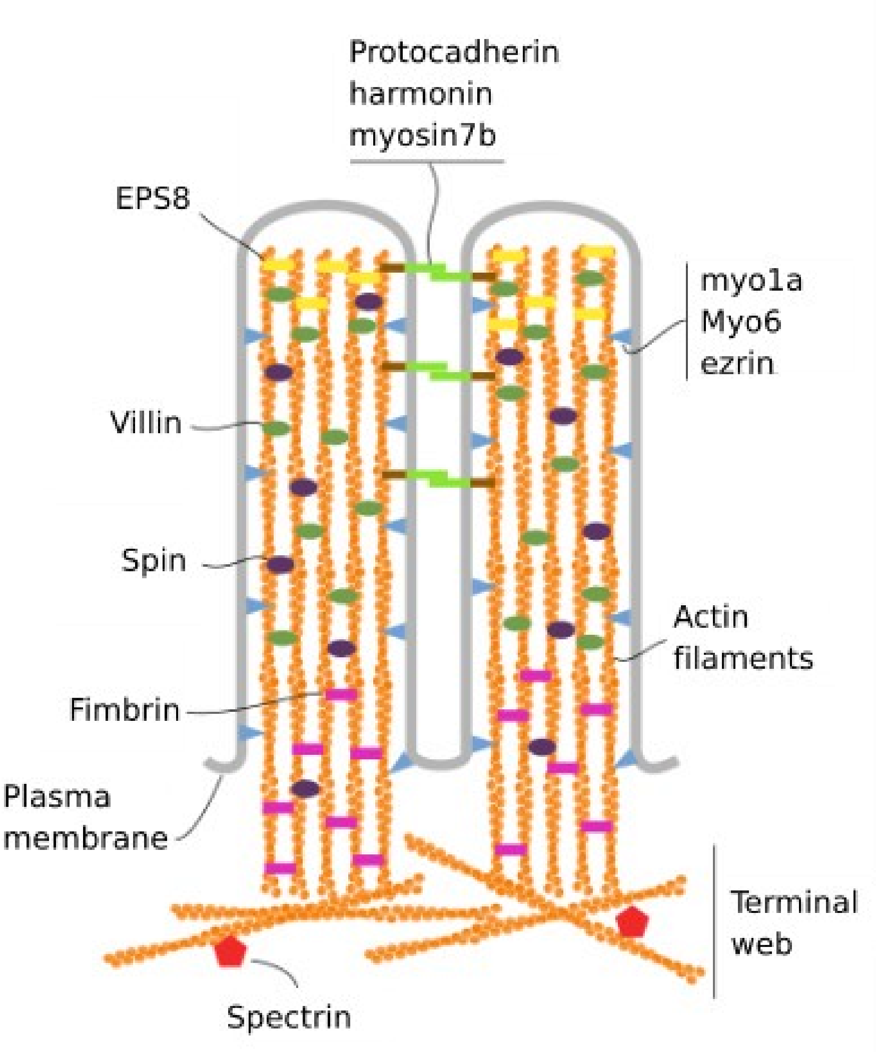

Figure 8*. **Molecular organization of microvilli**. See text from the description. Adapted from Crawley S.W., et al., 2014.*

Even though microvilli have predominantly identical exterior shapes, they can be extremely different according to the cell type and their function. In general, microvilli on intestinal epithelial cells maintain a constant length and are specialized for cell-surface enlargement, facilitating nutrient absorption. In contrast, lymphocyte microvilli - or even in some cancer cells - have characteristics similar to those of filopodia, which grow and shrink intermittently, via the alternate assembly and disassembly of their actin filaments [Hye-Ran K., et al., 2019].

On the interior part, the microvilli’s skeleton consists of 6 main proteins: actin, fimbrin, villin, myosin (Myo1A), calmodulin, and spectrin (non-erythrocytic) (**Figure 8**). The bundle of 30-40 actin filaments is parallel to the long axis, with their minus ends toward the tip of the microvillus. Fimbrin and villin link together the actin filaments, whereas Myo1A, Calmodulin, and pERM make the connections between the bundle and the membrane.

The plus end of actin filaments extends into the cytoplasm and forms a web with a hexagonal pattern, known as **terminal web**, that spreads through the cell periphery, connecting it to the cytoskeleton.

Microvilli are very dynamic structures: for example, it is estimated that every 20 minutes the skeleton of each microvillus is completely renewed; moreover, they disappear in cells entering mitosis [Tyska M.J., et al., 2002].

Microvilli can be found in a variety of cell types, but they're most common in epithelial cells, including gut enterocytes, kidney convoluted duct epithelium, or the epididymis. Microvilli are also seen in specialized sensory cells, placental cells, or movement cells. However, it was recently discovered that microvilli can be found in a variety of other cell types, like lymphocytes or cancer cells.

1.2.3 Membrane transports

The cellular membrane has selective permeability, which means that it allows the passage only of some specific substances. Some molecules can spread freely across the membrane, like small molecules, non-polar (O2 and CO2), and, more slowly, small uncharged polar molecules, such as urea and water; while molecules with large diameters or polar charges cannot freely enter the cell. Compounds that are not soluble in the cellular membrane must be transported into the cell by specific proteins, incorporated in the plasmalemma. The membrane proteins that mediate the transport are:

- transporter proteins,
- transporters that undergo conformational modifications by presenting one or more substrate-specific binding sites,
- channel proteins (especially ion channels) that bind the solute with less specificity.

Is possible to divide membrane transport into different categories: **passive transport** (or diffusion), **active transport,** and **secondary active transport**.

Passive transport

We define passive transport as when a solute can cross the membrane without the use of energy. In this case, the movement of the solutes is driven mostly by the different concentrations between the two sides of the membrane (**concentration gradient**).

It is possible to distinguish two categories of passive transport:

- simple diffusion, in which the solutes can cross freely the membrane;
- facilitated diffusion, in which the solutes are not soluble in the plasma membrane, so they can cross through the help of specific protein channels or carriers.

Carrier proteins mediate both passive and active transport of carbohydrates, amino acids, and nucleosides. Once the solute is bound in the compartment with higher concentration, the proteins undergo a conformational change that allows the transfer of the solute into the low concentration compartment.

In the case of channels, proteins interact with solute to carry much more weakly. They form water pores in the plasma membrane that, when open, allow the rapid diffusion of ions or small water-soluble molecules of suitable molecular weight and electric charge.

Active transport

In **active transport** proteins transport solutes against the electrochemical gradient, using the energy obtained from the hydrolysis of **ATP** (enzymatic activity). Each type of carrier protein has one or more specific binding sites for the solute. When the protein binds to a specific solute, it undergoes conformational changes (which require the use of ATP), which allow it to carry inside – or outside of the cell the solute.

In secondary active transport, the energy required to transport a solute against its concentration gradient is not provided directly by ATP, but by the existence of an electrochemical gradient of Na + (or H +) produced by **ionic pumps**. In secondary active transport, therefore, there is the coupled transport of two different species of solutes: Na^+ or H^+. In the *symport*, the transport of the two solutes occurs in the same direction, while in the *antiport* it takes place in the opposite direction [Alberts B., Molecular biology of the cells, 2017].

1.2.4 Endocytotic pathways, an overview

The mechanisms that regulate endocytosis are still under active investigation and a lot of questions need to be answered. The reason is that, to elucidate in detail these mechanisms, is particularly difficult for many reasons, like:

- lack in the literature of generally accepted markers/inhibitors for different pathways.
- technical limitations (mostly imaging resolutions or cell homeostasis perturbation);
- Cross-talking of different pathways and their intrinsic complexity.

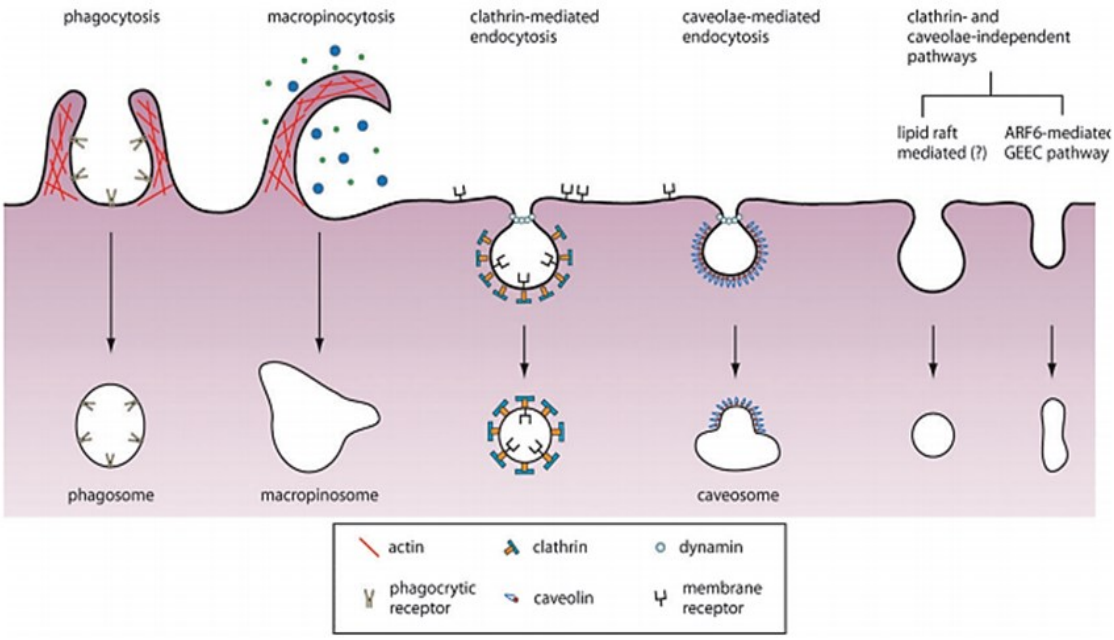

Figure 9*. *Most common classification of endocytic pathways in a typical eukaryotic cell. *Depending on the type of cell, or the material to be internalized, is possible to distinguish between Phagocytosis, Macropinocytosis, Clathrin-mediated endocytosis, Caveolae--mediated endocytosis, and Clathrin/Caveolae-independent endocytosis (like lipid raft mediated or ARF6 mediated). Reproduced from Chou L.Y.T., et al., 2011.*

In general, is possible to categorize endocytotic pathways into two macro-categories:

1. **Phagocytosis** (*i.e.*, cell eating), initially discovered in macrophages and only specific to some cell types, involves the acquisition of voluminous particulate material, entire cells, or microorganisms.
2. **Pinocytosis** (*i.e.,* cell drinking), is present in almost every eukaryotic cell and concerns the acquisition of fluid material or small solutes.

Depending on the protein and/or lipid involved, it is possible to divide pinocytosis into four subcategories, summarized in **Figure 9**: **Macrocytosis, Caveolae dependent**, **Clathrin-dependent**, **Clathrin, and Caveolae independent**.

All these processes are characterized by four essential steps:

1. a specific binding event at the cell surface;
2. plasma membrane budding and pinching off;

3. anchoring the resultant trafficking vesicle;
4. trafficking the vesicle to a specific intracellular organelle.

Another important distinction is between General Endocytosis and **Receptor-mediated endocytosis**. The former one leads to the non-specific intake of extracellular fluids (therefore all the molecules dissolved in them can enter the cell); rather than the receptor-mediated endocytosis leads to the recruitment of specific extracellular molecules (ligands) after they have bound to their receptors on the outer side of the plasma membrane.

Two different types of receptors are subject to endocytosis: the "**maintenance receptors**" are responsible for the intake of materials that will be used by the cell, such as the receptors for transferrin and for LDL (low-density lipoprotein), which mediate transport in the cells of iron and cholesterol, respectively; following the transport in the cell of the material bound to the receptors, the receptor return to the cell surface for a further intake cycle. The "**signal receptors**", on the other hand, are responsible for the binding of extracellular ligands that induce changes in the activity of the cell, for example, hormones or growth factors bind to the receptors present on the cell surface and trigger a physiological response inside the cell. Endocytosis is followed by the destruction of this type of receptor, a process called "*negative regulation of receptors*", which has the effect of reducing the sensitivity of the cell to further stimulation by the signal molecule.

1.2.5 Phagocytosis

Phagocytosis, the process by which white blood cells eliminate foreign invaders, is essential for the innate immune/inflammatory response. In mammals, there are mostly two classes of white blood cells that act as professional phagocytes, Macrophages, and Neutrophils, whose main purpose is to ingest invading microorganisms to protect us against infections. Macrophages also use this process to collect garbage, engulfing senescent or apoptotic cells and cell debris. Phagocytosis is also required for nonaxenic *D. discoideum* to survive and feed in the wild. The amebae and mammalian macrophages, neutrophils, and dendritic cells have contributed significantly to our understanding of phagocytosis.

Phagocytosis can be divided into several stages (**Figure 10**):

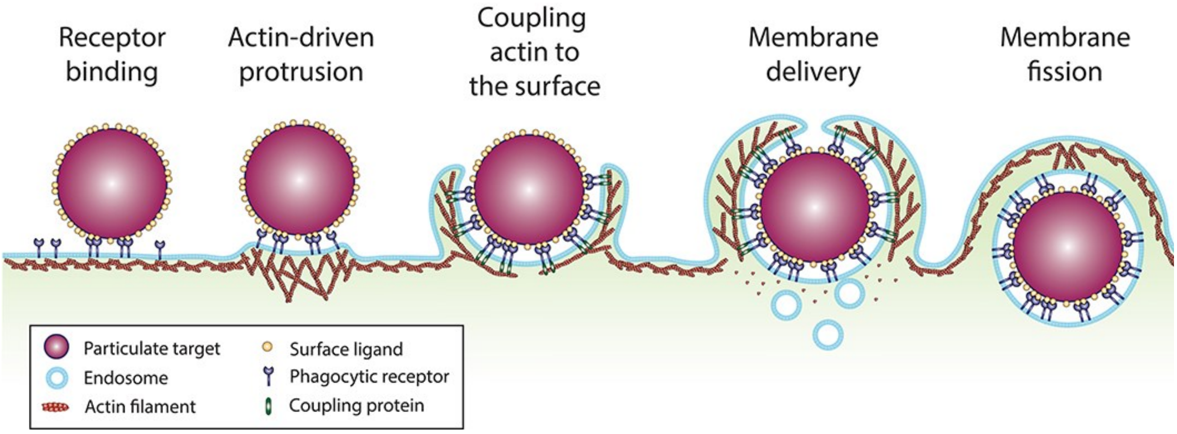

Figure 10. Sequence of events involved in particle uptake by Phagocytosis. *To be phagocytized, a particle must be first recognized by a specific receptor (dark blue) present along the plasma membrane of the cell. These receptors, once activated, stimulate the polymerization of actin, thus forming membrane protrusions that extend along the particle surface. In the end, the protrusions reach a meeting point (so the particle is fully surrounded), membrane fission enables the separation of the phagosome from the plasma membrane. Reproduced from Jaumouillé V., et al., 2020.*

1. substrate attachment to the cell surface via a transmembrane receptor or possibly via cell-surface adhesion proteins,
2. activation of a signaling cascade that results in spatiotemporal modulation of F-actin polymerization,
3. actin-dependent pseudopod extension to facilitate particle engulfment and internalization,
4. subsequent removal of the actin coat from the internalized phagosome and fusion and fission to form the mature phagolysosome.

One of the main differences between vesicles in pinocytosis and phagocytosis is that the diameter of phagosomes depends on the size of the ingested particle – sometimes being as large as the entire cell itself - rather than vesicles in pinocytosis are usually small and uniform. Once inside the cell, the material must be digested: the phagolysosome is formed when the phagosome and the lysosome fuse, releasing lysosomal enzymes and activating other lytic compounds to digest the phagocytosed particle.

Is possible to define phagocytosis as a triggered process, which means that not all the particles that get close to the cell can be phagocytized, but they must be recognized by specific receptors. In mammalian cells, already several types of receptors have been studied, the most known of them is the Fc receptor (FcR). In particular, FcR bind to immunoglobulins on the Fc domain, like with IgG. This binding causes a conformational change in the receptor that initiates a signaling cascade that causes the polymerization of actin, which drives the progression of the membrane over the particle. This kind of response stimulates a further activation of more receptors, since, with the progression of the membrane over the particle, more receptors in the membrane can bind to the particle.

Rho-family GTPases are responsible for the polymerization of actin, thus of the movement of the pseudopods. When Rho-GTPase is activated, switches on PI kinases, which stimulate an accumulation of PI(4,5)P_2 on the membrane. This passage is very important because when the Actin starts to polymerize, PI(4,5)P_2 is converted to PI(3,4,5)P_2, a passage necessary for the closing of the phagocytic cup [Alberts B., Molecular biology of the Cell, 2008].

Phagocytosis seems to be a very expensive process; it necessitates a significant contribution from the plasma membrane and frequently includes other organelles. Recently was confirmed that subcellular compartments such as endosomes, lysosomes, and the endoplasmic reticulum are all involved in the phagocytosis process [Canton I., et al., 2012].

Different studies report NPs internalization through phagocytosis. In these cases, phagocytes express non-opsonic receptors that can interact with the surface of several NPs. Efficient internalization of NPs through phagocytosis can be achieved through the modulation of the density of receptors, the concentration of NPs, and their surface. In particular, modulating the surface of the NPs is of vital importance for an adequate response. For example, Silica NPs (SiO_2) of 50 and 100 nm can trigger inflammation in THP-1 macrophage-like cells, rather than >100 nm did not. Moreover, the protein adsorbed on the surface of the NPs can stimulate cell reactivity like an inflammatory response [Sousa de Almedia M., et al., 2021]. In general, the NP interacts with the cell first with specific interaction with a receptor (through different kinds of forces, like Van der Waals interaction, ionic attraction, Hydrophobic/hydrophilic interaction, or a specific interaction of a protein absorbed on the surface). This initial interaction can lead to a signaling cascade that results in the polymerization of actin filaments and subsequent internalization of the nanoparticle. The resulting phagosome at the end can fuse with lysosomes for the digestion of the material internalized [Sousa de Almedia M., et al., 2021].

1.2.6 Clathrin-mediated endocytosis

Clathrin-mediated endocytosis (**CME**) represents one of the most important routes of internalization of cells responsible for nutrient uptake, efficient receptor signaling, or in neurons for synaptic vesicles recycling. CME, for these reasons, is by far the most studied endocytotic mechanism.

CME begins with the sorting of transmembrane receptors that, upon binding to their ligands, cause the development of 'coated pits' on the plasma membrane's cytosolic side. These pits are formed by the assembly of numerous cytosolic proteins, mostly Clathrin. Clathrin possesses a three-legged structure, called a triskelion. This structure is formed by the construction of three Clathrin heavy chains, each connected to a Clathrin light chain.

To assemble, the Clathrin triskelions require the help of other proteins, called **adaptor proteins** (**APs**), whose role is mainly to coordinate the Clathrin nucleation at the site of internalization in the membrane. This results in the development of a curved polygonal web of Clathrin triskelions, which eventually results in the deformation of the attached membrane. This deformation of the membrane is initiated by some membrane modeling proteins, that serve as a deforming template and that recruit the core-sorting adaptor AP-2. All these proteins work together in a highly coordinated way, ending with the formation of a **Clathrin-coated vesicle** (**CVV**). At this point, the newly formed vesicle is detached from the membrane thanks to the presence of the GTPase dynamin, which creates a ring shape at the vesicle neck [Traub L.M., 2009].

Once released, the vesicles lose their clathrin covering, migrate within the cell, and the contents of the vesicles are transferred to a dynamic network of tubules and vesicles collectively referred to as endosomes. The fluid within an endosome's lumen is acidified by the operation of an H + -ATPase proton pump located on the vesicle membrane; an acid pH typically permits the ligand to dissociate from its receptor. Endosomes are further classified into early endosomes, which are positioned in the cell's periphery regions near the site of neo synthesis, and late endosomes, which are located in the cell's interior, closest to the nucleus. Early endosomes gradually grow into late endosomes when the pH decreases and the internal shape and structure change. There is a development of buds on the luminal side of the vesicles, which invaginate inward to generate a succession of smaller vesicles that are concentrated within the late endosome (*i.e.,* formation of the multivesicular body).

Numerous studies examined the absorption of NPs in various cell types through CME. Internalization of 40 nm polystyrene (PS) nanoparticles was investigated in a variety of cell types, including cervical epithelial (HeLa), lung epithelial (A549), brain astrocytoma, and macrophage (J774A.1), demonstrating the participation of CME in all cells in association with other processes. Additionally, many other NPs have been demonstrated to be taken up by cells through CME, including silica-coated core-shell superparamagnetic iron oxide

(SPION-SiO2) with fluorescein isothiocyanate (FITC), AuNPs83, and poly (ethylene glycol)-D,L-polylactide (PEG-PLA) NPs. Most NPs ingested through CME end up in the acidic environment of lysosomes [Sousa de Almedia M., et al., 2021].

1.2.3 Caveolae – mediated endocytosis

The term "caveola" refers to flask-shaped invaginations with a diameter of 50–100 nm that may be observed in the plasma membrane of some mammalian cells. These structures are numerous in smooth muscle, endothelia, and adipocytes, accounting for about one-third of the plasma membrane's surface area [Kiss A.L., et al., 2009]. Caveolae production requires two critical components: **caveolin-1**, or **caveolin-3** (in striated muscle cells), and **cavin 1**. Additionally, other components such as **caveolin-2**, **cavins 2, 3**, and **4**, and other auxiliary proteins (e.g., Eps-15 homology domain 2 (EHD2), PACSIN2, and dynamin 2) are required for the creation, stability, and scission of caveolae. This route has been implicated in the transport of a variety of cargoes, including Shiga and Cholera bacterial toxins, non-enveloped virus polyomavirus and simian virus, albumin, folic acid, and plasma membrane components such as glycosylphosphatidylinositol (GPI)-anchored proteins [Cheng J.P.X., et al., 2016].

Internalization of NPs through caveolae-dependent endocytosis is a frequent mechanism. In fact, different kinds of nanoparticles have been proven to be internalized through this pathway, like an NPS conjugated with paclitaxel to human albumin (Nab-paclitaxel/ Abraxanes), or lipid nanoparticles coated with poly (styrene sulfonate), absorbed through caveolae in HeLa and human endothelial cells (HUVEC). Additionally, caveolae serve a critical role in transcytosis across endothelial cells, allowing for the transfer of solutes between the blood and peripheral tissues (e.g., heart and lungs). In lung endothelial cells

(BLMVEC)., albumin-coated polymeric NPs with diameters of 20, 40, and 100 nm demonstrated an effective transcytosis mechanism [Sousa de Almedia M., et al., 2021].

The material that is endocytosed through the caveolae is initially localized in **caveosomes**, vesicles with a neutral pH (unlike the early endosomes that are formed as a result of clathrin-mediated endocytosis, which have an acid pH). The caveosomes move along the microtubules to the endoplasmic reticulum (ER). From the ER, the endocytosed material can be released into the cytosol and subsequently can enter the nucleus through the nuclear pores. According to this model, nanomaterials captured in this way can avoid the fate of degradation in the lysosomes and reach a specific target organelle (such as the ER or the nucleus), an essential aspect in the context of drug delivery [Kou L., et al., 2013].

1.2.4. Macropinocytosis

Macropinocytosis, like phagocytosis, is an actin-dependent process that results in the engulfment of fluids and micron-sized particles (Macro-pinocytosis = drinking of macro components). This is a **non-selective** process in which plasma membrane ruffles absorb vast quantities of an external fluid, including particles and dissolved chemicals, forming macropinosomes, that generally have a diameter ranging from 0.2 to 5 mm.

Macropinocytosis enables the internalization of bigger macromolecules by cells without phagocytic activity, which is not feasible through other endocytotic processes such as clathrin- or caveolae-mediated endocytosis. Macropinocytosis may be constitutive or inducible, depending on the cell type.

When stimulated by growth factors (*e.g.,* epidermal and platelet-derived growth factors) or other chemicals, actin-rich extensions of the plasma membrane, referred to as **ruffles**, may retreat into the cell membrane or curve into circular ruffles that undergo membrane fission to create macropinosomes (**Figure 11**), large organelles of > 200 nm. This process may include a large number of molecules necessary for actin polymerization, cytoskeleton organization, macropinosome development, and closure, depending on the activation signal. Numerous small GTPases belonging to the Ras superfamily, kinases (p21-activated kinase 1 and protein kinase C), and lipids are included in this category (phosphoinositides and diacylglycerol) [Swanson J. A., et al., 2019].

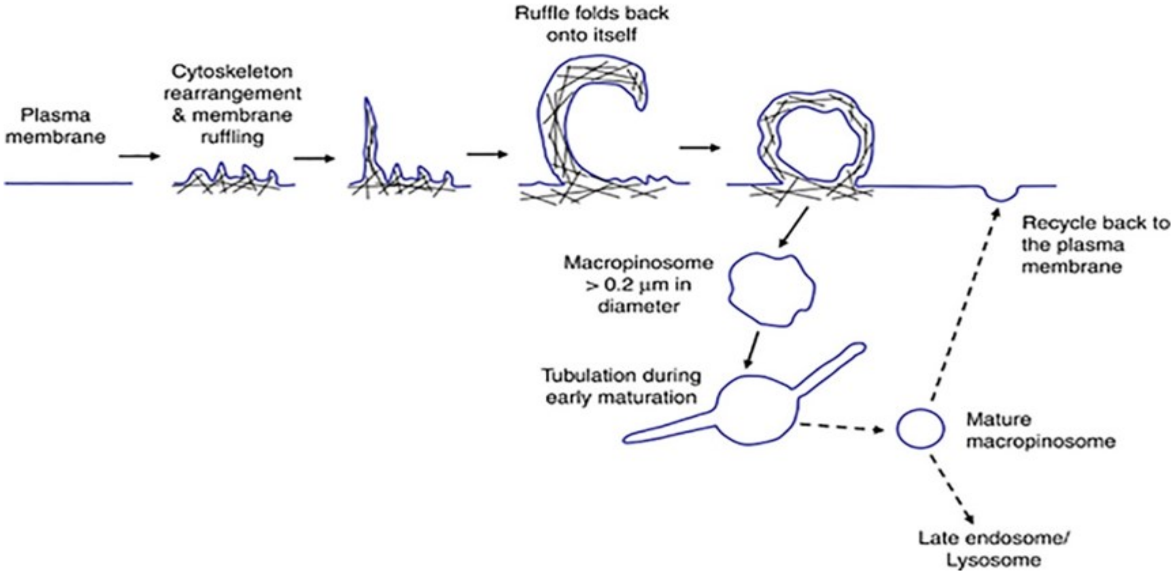

***Figure 11*. *Phases of Micropinocytosis*.** *Actin cytoskeleton rearrangement at the plasma membrane leads to the formation of membrane ruffles. Ruffles then fold back onto themselves, fuse at the base of the plasma membrane, trapping solute and soluble substances and forming macropinosomes. The content of the macropinosomes is either degraded at the late endosome/lysosome or recycled back to the plasma membrane. Reproduced from Lim J.P., et al., 2011.*

Depending on the cell type and activation pathway, the ruffles can be in different forms. Generally, it is possible to observe: planar folds (lamellipodia-like), circular cup-shaped extensions (circular ruffles), or, in some cases, large plasma membrane extrusions (blebs) (**Figure 12**).

Nanoparticles internalized through macropinocytosis are usually internalized non-specifically, which means that they are not recognized by specific receptors. However, more research is needed regarding the internalization of NPs through this specific route; it is possible, in fact, that some specific functionalization on the surface of the nanoparticles can trigger macropinocytosis.

Moreover, the difficulty in studying this mechanism is also due to the lack of specific and commonly recognized inhibitors for this endocytotic route. Generally, is possible to utilize some inhibitors of actin dynamics, like latrunculin A, cytochalasins B/D and jasplakinolide, or inhibitors of Na^+/H^+ ATPase (present on the ruffles), like amiloride or ethylisopropyl amiloride (EIPA) [Mercer J., et al., 2009].

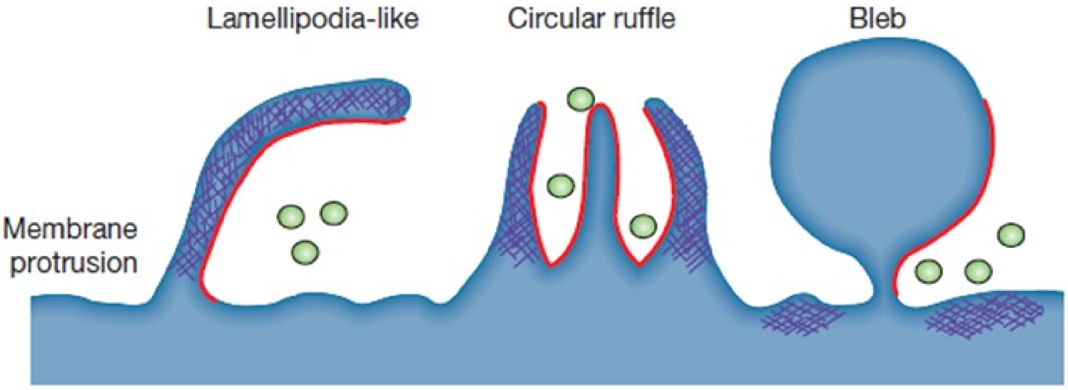

***Figure 12**. Schematic representation of different membrane protrusions.* *Ruffles in micropinocytosis are membrane protrusions that can be found in different shapes: lamellipodia-like, circular, or blebs. Reproduced from Mercer J., et al., 2009.*

1.2.9 Clathrin/Caveolae-independent endocytosis

Apart from endocytosis mediated by Clathrin and Caveolae, which requires coated vesicles, NPs and other cargos such as cellular fluids, growth hormones, and toxins may be absorbed through Clathrin/Caveolae-independent endocytosis. Typically, these processes are cholesterol-dependent and require a specific lipid composition. Despite extensive research on these mechanisms, their contribution to endocytotic uptake in mammalian cells remains unknown.

The Clathrin/Caveolae-independent endocytosis process can be classified into the following categories:

- Clathrin-independent carriers/GPI-AP enriched early endosomal compartment (CLIC–GEEC),
- RhoA-dependent,
- Arf6-associated,
- flotillin-assisted,
- fast endophilin-mediated endocytosis (FEME).

CLIC-GEEC pathway is dynamin-independent and ultimately leads to the formation of tubular/ring-like invagination, measuring around 200-600 nm in length and 40-80 nm in width. This process needs two small GTPases, cholesterol and actin.

RhoA-dependent endocytosis needs, contrary to CLIC-GEEC, the presence of dynamin. This pathway was studied mostly for the internalization of the Interleukin-2 receptor and Clostridium botulinum C2 toxin. **Arf6** was instead associated with the internalization of the major histocompatibility complex class I, β1-integrin, and E-cadherin. In particular, it seems that the main role of Arf6 is not in the endocytosis, but in recycling.

Flotillin (in particular, Flotillin 1 and 2) are proteins associated with membrane microdomains specifically important for induction of invaginations. This type of internalization can be dynamin-dependent (like for the internalization of epidermal growth factor) or dynamin-independent (like in the case of CTxB).

Fast-endophilin-mediated endocytosis (**FEME**) was described lately and is a non-constitutive mechanism initiated by the activation of certain receptors such as the b1 adrenergic receptor, the epidermal growth factor receptor, and the interleukin-2 receptor. This pathway occurs only when pre-enriched endophilin (endophilin-Ptdlns(4,5)P2-lamellipodin) is already present at the plasma membrane and accessible to bind to the activated receptor. FEME is defined by the rapid development, often within seconds, of tubulo-vesicular structures measuring 1 mm in diameter at the cell membrane [Sousa de Almedia M., et al., 2021].

Various NPs have been demonstrated to be taken up through clathrin/caveolae-independent endocytosis. For example, SPIONs and silica-coated iron oxide nanoparticles, with a negative surface charge and a diameter of 17–30 nm, were found to be internalized into HeLa cells through the CDC42 (CLIC–GEEC pathway) and caveolae [Bohmer N., et al., 2015]. Similarly, Arf6-associated endocytosis, caveolae-dependent endocytosis, and macropinocytosis were all linked with the absorption of polydopamine-coated mesoporous silica nanoparticles [Ding L., et al., 2017].

The extent to which all processes are involved in NPs internalization is unknown. Three plausible explanations exist:

1. problems in differentiating Clathrin/Caveolae-independent endocytosis from other processes;
2. Clathrin/caveolae-independent endocytosis is not the only entry mechanism involved in the internalization of NPs;
3. lack of specific information regarding the processes.

1.4 Physicochemical Properties of Nanoparticles affecting endocytosis

Due to their small size, nanoparticles must be very efficient and precise at reaching their biological targets. However, despite their "small" size, NPs cannot always diffuse across the **cell membrane (CM)** due to their polar nature. Because the CM is mostly permeable to small, non-polar molecules, NPs enter cells via endocytotic routes.

With the advancement of nanotechnology and the capacity to control the design of nanoparticles, it is critical to understand the function of endocytosis in nanoparticle internalization. This is critical for deciphering the nanoparticles' destiny once internalized, their toxicological profile, and their influence on the biological activity once inside the cells. Optimizing NPs' cellular uptake, targeting, and intracellular trafficking requires manipulating their physicochemical characteristics, such as size, shape, and surface properties. NPs can be classified into two types based on their constitutive bonds:

1. those formed via strong interactions, such as ionic, metallic, and covalent bonds (for example, quantum dots, gold nanoparticles, and carbon nanotubes);
2. those formed via weak interactions, such as hydrogen bonds, hydrophobic effect, coulombic forces, and their combination (e.g. micelles and vesicles).

Both "hard" and "soft" nanoparticles have a high inherent surface area, and as a result, interfacial forces dominate most of their interactions with the environment. But is important to underlying an important distinction between them. If hard nanoparticles have a well-defined solid-liquid interface with well-defined interfacial forces, soft nanoparticles, on the other hand, have a fluid–liquid interface with more dynamic interfacial deformations. For this reason, it is important to know what kind of nanoparticle we are dealing with to comprehend the nanoparticle/biological interactions and, more significantly, to understand how the nanoparticle interface exchanges materials with the environment.

For example, although soft nanoparticles are more delicate, they have surface energies comparable to those of biological systems. As a result, they assimilate more easily. On the other hand, hard nanoparticles have a significantly greater surface tension, to the point where they may cause unfavorable surface catalytic processes.

In general, the factors to consider for NPs endocytosis are: **size**, **shape**, **surface charge**, and **elasticity** (**Figure 13**). The reason is that these properties can influence the nanoparticle stability and, most importantly, their interactions with the biological environment (such as internalization and intracellular trafficking).

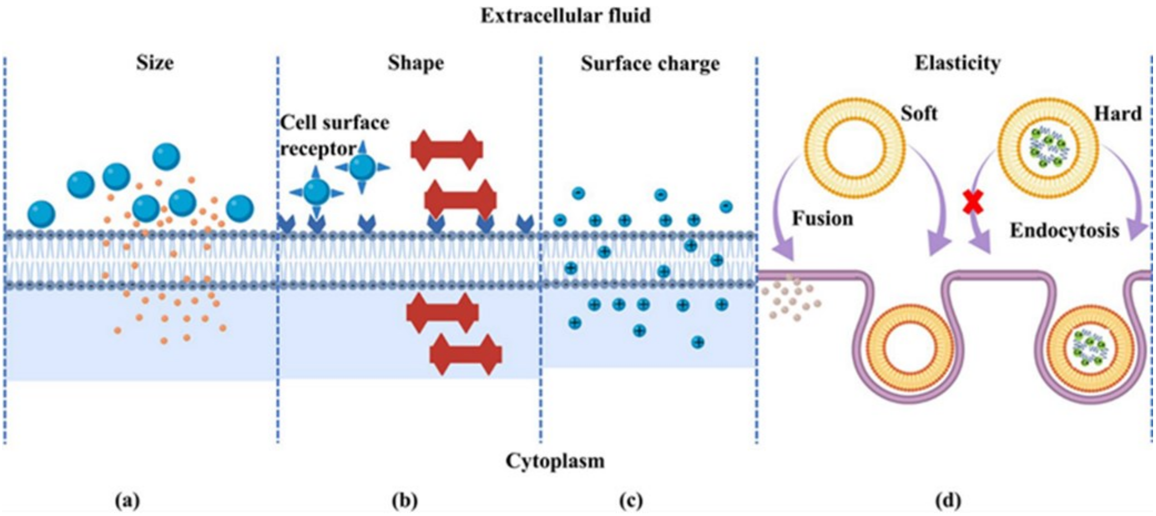

Figure 13. Cell uptake is affected by the physical parameters of nanoparticles: *size(a), shape (b), surface charge (c), and elasticity (d). Reproduced from Kiio T.M., et al., 2021.*

Size

The size of the nanoparticles is perhaps the most important parameter for endocytosis. In general, large particles (>500 nm) are internalized through phagocytosis or macropinocytosis, but several other uptake mechanisms can be involved in the uptake of particles of smaller size. However, it seems that, for phagocytosis and macropinocytosis, size is not the most relevant factor. The reason is that, as for phagocytosis, the endocytosis starts after the recognition from a specific receptor, rather than macropinocytosis is a type of endocytosis not specific but can engulf simultaneously particles of different sizes. Moreover, several studies show the internalization through phagocytosis of nanometer-sized particles, like a virus, AuNPs, Silver NPs, or quantum dots. Other studies, on the contrary, demonstrated that changes in the size of these particles didn’t influence the uptake through phagocytosis [Canton I., et al., 2012].

In contrast, Caveolae-based vesicles and Clathrin-based vesicles are usually of smaller size (around 60 nm for Caveolae-based and 120 nm for Clathrin-based). However, some studies demonstrated that particles ranging from 10 nm to 300 nm were endocytosed by mammalian cells through Clathrin-mediated endocytosis [Pelkmans L., et al., 2002], and a study showed Caveolae-mediated endocytosis for the uptake of particles of 100 nm in diameter [Wang Z., et al., 2009]. There is therefore great flexibility in the different entry mechanisms of the nanoparticles, and it is important to underline that most of the mechanisms operate simultaneously, making it difficult to identify a single-entry path.

Another important factor to consider in this context is the level of **aggregation** of the nanoparticles, because NPs aggregated, or as individual particles, can interact with cells in completely different ways. That’s because the aggregation level can contribute to an overall increase of the particle's size, affecting in this way the uptake and the intracellular distribution.

As a result of general physical interactions, nanoparticles may cause distortion and even total invagination of the membrane. Studies showed that when phospholipid membranes wrap around particles, the attractive contact between the nanoparticle's curved surface and the cell membrane causes the required deformation to engulf the nanoparticle. This process is influenced by both the adhesion forces between the membrane and the nanoparticles and the stiffness of the membrane. Together, these two factors define a crucial radius for nanoparticles to accomplish complete wrapping and internalization. Computer simulations utilizing dissipative particle dynamics corroborated these results, demonstrating further that complete wrapping does not always result in fission. Only when the membrane contains a heterogeneous area (*e.g.*, a lipid raft), the wrapped particle separate from the larger membrane. All models agree on one thing: particles need to have a minimum radius of 20-30 nm to be efficient in cellular absorption. This critical size is affected by several factors: the greater the bonding energy between the membrane and the nanoparticle, the smaller the minimum radius required. Furthermore, the size and the maximum number of captured nanoparticles also depend on the density of the possible ligands expressed on the surface of the nanoparticle [Canton I., et al., 2012].

All of this indicates that size alone is not sufficient to predict the type of endocytosis, but several other factors can be involved and play an important role.

Shape

When it comes to cellular interactions, the shape of the nanoparticle is just as significant as its size. For example, some recent *in vitro* research, employing gold particles, showed that the number of ingested particles decreased as the form of the nanoparticle changed from rod to cubic, spherical, and prism [Carnovale C., et al., 2019].

Often, the impact of shape is investigated by altering the aspect ratio of nanoparticles. Most of this research demonstrated that when the aspect ratio is lower, the uptake is greater. This may be explained by the increased energy needed to wrap a lipid membrane around a high aspect ratio nanoparticle. However, contradictory findings have been reported regarding this aspect, with cross-linked poly (ethylene glycol) hydrogels or mesoporous silica particles with a greater aspect ratio being absorbed more quickly and completely than those with a low aspect ratio [Francia V., et al., 2020].

Several studies have examined the impact of nanoparticle shape on both the effectiveness of uptake and the endocytotic processes involved in uptake, but the results are often discordant. Cylindric cationic poly (ethylene glycol) hydrogels with various aspect ratios, were both endocytosed by HeLa cells through a combination of Clathrin and caveolae endocytosis (based on cholesterol and tyrosine kinase dependence) [Gratton S.E.A., et al., 2008]. However, another research found that cholesterol did not affect the entrance of cylindric, worm-like, and spherical silica particles into A549 and RAW264.7 cells. The uptake of spherical silica particles was largely reliant on Clathrin, while the internalization of worm-like and cylindric silica was primarily dependent on microtubules [Herd H., et al., 2013]. The reasons for these discrepancies are not clear, but some factors are important and should be considered:

- First, the different types of cells used in those studies might contribute to generating these differences;
- Another reason is the fact that altering the form of the nanomaterial also alters its size. This implies that when comparing the uptake of variously shaped items, either the volume, maximum diameter, or a combination of the parameters should be maintained constant;
- Third, things that are not spherical may interact with the cell membrane in a variety of ways. Thus, the contact area between the nano-sized item and the cell surface varies depending on the orientation while engaging with the cell membrane. This may help to explain why the absorption of non-spherical nanomaterials seems to require several routes [Francia V., et al., 2020].

Charge

Another readily adjustable parameter is the surface charge, which has a significant effect on how NPs behave in biological environments.

Positively charged nanoparticles seem to be more effectively absorbed than neutral or negatively charged ones. [Gratton S.E.A., et al., 2008] However, more studies are demonstrating the opposite. Additionally, it has been observed that uptake rises with increasing charge density (either positive or negative) [Xiao K., et al., 2011]. Concerning the mechanism of internalization, some studies indicated that positively charged nanomaterials are primarily internalized via Clathrin-mediated endocytosis, with a small proportion of particles internalized via macropinocytosis, whereas negatively charged NPs are more likely to internalize via a cholesterol-dependent mechanism. Contrary to expectations, Clathrin-mediated endocytosis did not seem to be a significant route for either positively or negatively charged nanomaterials, while cholesterol-mediated absorption appeared to be similarly essential for both. [Francia V., et al., 2020]

There is a factor that is important to consider. Many research examining the impact of charge or other nanomaterial characteristics on cellular interactions were conducted in the absence of proteins derived from biological fluids (such as serum). This adds another layer of complexity since the charge of NPs tends to neutralize upon corona formation in a biological environment. Thus, NPs with varying charges in water may end up with a comparable charge, near to neutrality, when exposed to a biological medium. As a result, it is critical to ascertain if any of the previously reported charge-related effects vanish once the nanomaterials are applied to a biological environment [Francia V., et al., 2020].

Effect of NPs elasticity

Numerous studies have been conducted to investigate if the elasticity of nanoparticles is a significant physicochemical factor of their pharmacokinetics and biodistribution. Elasticity is a term that refers to a material's ability to flex under stress (e.g., shear, uniaxial, or bulk stresses). Numerous studies indicate that the flexibility of NPs affects how they interact with immune cells and organs.

To test the elasticity of NPs, it is possible to use several different techniques, such as mechanical tester, rheometer, extrusion, synchrotron X-ray diffraction, scanning tunneling microscopy, or atomic force microscopy (AFM). Among all of these, AFM is the most used for this purpose [Kiio T.M., et al., 2021].

Simulations showed a higher energy barrier for the internalization of soft and easily deformable nanoparticles than for rigid particles [Shen, Z., et al., 2019]. However, interactions between nanoparticles and cells cannot be explained simply in terms of the energy barrier needed to bend the lipid membrane. Other biological variables may also be implicated, which may account for the contradictory findings regarding the impact of elasticity on the uptake.

In general, the elasticity modulus of NPs is a critical characteristic that influences their pharmacokinetic behavior. It has been shown that the optimization of this property has an effect on the interactions of NPs with different cells, the circulation half-life, tumor targeting, and accumulation efficiency. Despite a lack of conclusive evidence on the uptake efficiency of soft NPs in endothelial cells, soft NPs were found to be effectively absorbed by cancer cells. Notably, the majority of *in vivo* and *in vitro* studies have shown that soft NPs are less likely to be absorbed by immune cells and have a longer circulation time than hard NPs. Nonetheless, several *in vitro* experiments reached contrary results [Kiio T.M., et al., 2021].

1.5 Intracellular fate of Nanoparticles

Following uptake, intracellular trafficking of NPs is critical because it dictates their eventual location inside cellular compartments, their cytotoxicity, and their therapeutic effectiveness. After the cells have internalized the NPs through one of the many different uptakes, they will be transferred in some membrane-bound intracellular vesicles known as **early endosomes**. Early endosomes, late endosomes, and recycling endosomes are the three categories of endosomes that develop at the plasma membrane.

The role of early endosomes is to transfer the cargo to the desired destination. Following some steps of maturation and differentiation, they can transform into the multivesicular late endosome, which will later integrate into the lysosomes, forming multilamellar **endolysosomal vesicles**. Inside these vesicles, there are hydrolytic enzymes that can digest and degrade the NPs inside **(Figure 14)** [Venkatachalam K., et al., 2015].

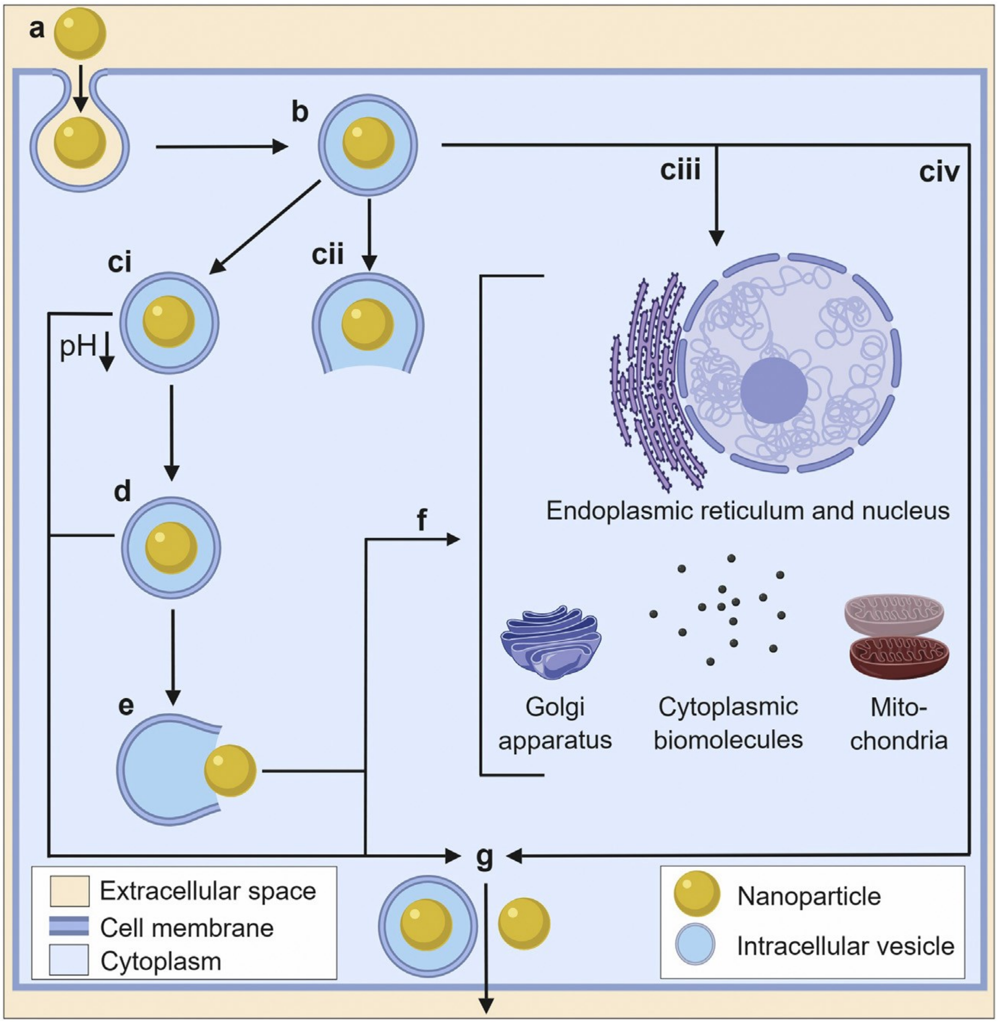

***Figure 14**. **Overview of main nanoparticle intracellular trafficking pathways and mechanisms**. (a) Cellular entry of nanoparticles often occurs through an endocytotic pathway. (b) After internalization, nanoparticles are typically trafficked to a sorting/early endosome which can undertake several intracellular transformations. (ci) The sorting/early endosome forms a late endosome as the pH decreases that then fuses with other components to become a lysosome (d) from which nanoparticles can either escape (e) for subsequent intracellular targeting (f) or in which nanoparticles can get degraded and/or exocytosed (g). An alternative to lysosome formation can either be (cii) endosomal escape and subsequent intracellular targeting (f), or (ciii) a recycling process through a recycling endosome located near the perinuclear region, or even (civ/g) rapid recycling directly to the plasma membrane. Reproduced from Donahue N.D., et al., 2019*

This is the general pathway, but there are some exceptions. Some NPs, for example, can escape this pathway and be released in the cytoplasm, bypassing the hydrolytic degradation. [Martens T.F., et al., 2014]

Another major barrier during endosomal processing is **exocytosis**. Exocytosis of NPs can occur in two different ways:

- by the trafficking of nanoparticles from the early endosome to the recycling endosome, that later fuses to the plasma membrane,
- or from the multivesicular body/late endosomes and lysosomes, where either intact nanoparticles, or just some component, can be ejected out of the cell.

An alternative route is **Autophagy**. During autophagy, the internalized NP is surrounded by **autophagosome** and delivered into the lysosome, together with other aggregated proteins or organelles that need to be recycled to maintain homeostasis. This path is activated usually during the absence of nutrients, in which the lysosomes tend to be localized in the perinuclear space, while the autophagy processes are activated [Anding A.L., et al., 2017].

It is well known that, since most of the nanoparticles end up digested into the lysosomes, this can constitute an ulterior barrier for the delivery and potential therapeutic effect of nanoparticles. However, it is important to underline that, as such, the optimal function of the lysosome is critical for the survival of the cell. For this reason, if the normal function of the lysosomes is altered, for example for the purpose of achieving higher cytosolic delivery of nanoparticles, this alteration may be harmful to the cell. This dysregulation of the normal cellular function may also induce or disrupt autophagy and thus the therapeutic or diagnostic potential of nanoparticles.

1.6 Toxicity of Nanoparticles

In recent years, the improvements obtained in the synthesis and surface modification of nanomaterials have allowed a wide range of applications for nanoparticles, from biomedical to biotechnological fields. However, while the commercialization of nanoparticles is expanding rapidly, their impact on health and the environment is so far poorly understood. As regards biomedicine, alongside the study of the internalization of NPs in cell models, scientists are making a global effort to clarify a possible cytotoxic effect of the different nanoparticles before their possible commercialization. For this reason, toxicological data relating to the **biocompatibility** of nanoparticles are of vital importance and more studies are necessary to identify the risk associated with exposure to nanomaterials.

In general, several variables can influence the cytotoxic effect of nanoparticles, the most influential of which is their **physicochemical properties**. For example, the core of nanoparticles can influence the toxicity: nanoparticles composed of known toxic metals such as cadmium [Kirchner C., et al., 2004] and silver [Wise J.P., et al., 2009] are generally more toxic than those made of inert materials such as gold [Bar-Ilan O., et al., 2009]. As for the size of the core, smaller particles with a core of the same material are generally more toxic than larger ones [Guo et al., 2008]. The reason is that smaller particles are thought to interact more with biological systems, because of a better cellular uptake, and a faster decomposition (due to a higher area-to-volume ratio than that of larger particles). Another factor that needs to be considered is the **surface ligands** of the nanoparticles, which can influence both their biodistribution and cytotoxicity [Hoshino et al., 2004].

This range of variables can lead to difficult structure-activity relationships. Various biological models have been proposed for toxicological evaluation, including both *in vitro* and *in vivo* methodologies. *In vitro* studies on cell cultures have shown that some nanoparticles can induce oxidative stress, interaction with DNA, stimulation of inflammatory protein secretion, ultimately leading to a reduction in vitality and apoptosis. It is evident that nanometric particles with large surface areas can activate transmembrane receptors and trigger various signal transduction pathways after interaction with the plasma membrane. Nanoparticles can therefore interfere with normal cell functions through interaction with intracellular macromolecules after internalization. [Lai D.Y., 2012]

The potential interactions between nanoparticles and cellular systems that can induce different cellular responses and cytotoxicity appear to be:

1. interaction with the plasma membrane that can cause instability associated with ion transport, signal transduction, and cell death;
2. interaction with mitochondria which can alter metabolism or interfere with antioxidant defenses and ROS production;
3. binding to DNA by damaging it, interfering with cell division and protein synthesis;
4. the interaction with the cytoskeleton that can stop vesicular traffic and cause mechanical instability and cell death;
5. an interaction with proteins, lipids, and other biomolecules that can lead to different types of 'corona' effects and biological effects [Lai D.Y., 2012].

However, the toxicological data relating to the biocompatibility of nanoparticles necessary to identify the risk associated with the exposure of nanoparticles are still inconsistent, due to a lack of standardization of the studies by the various authors (different NPs, different experimental conditions, and biological systems, *in vivo* or *in vitro)*. Therefore, identifying the chemical-physical characteristics of the nanoparticles necessary for their use in the biomedical field, and developing a sensitive and predictive nanotoxicity test for these nanomaterials is essential before their use in biomedicine.

1.7 Categories of Nanoparticles

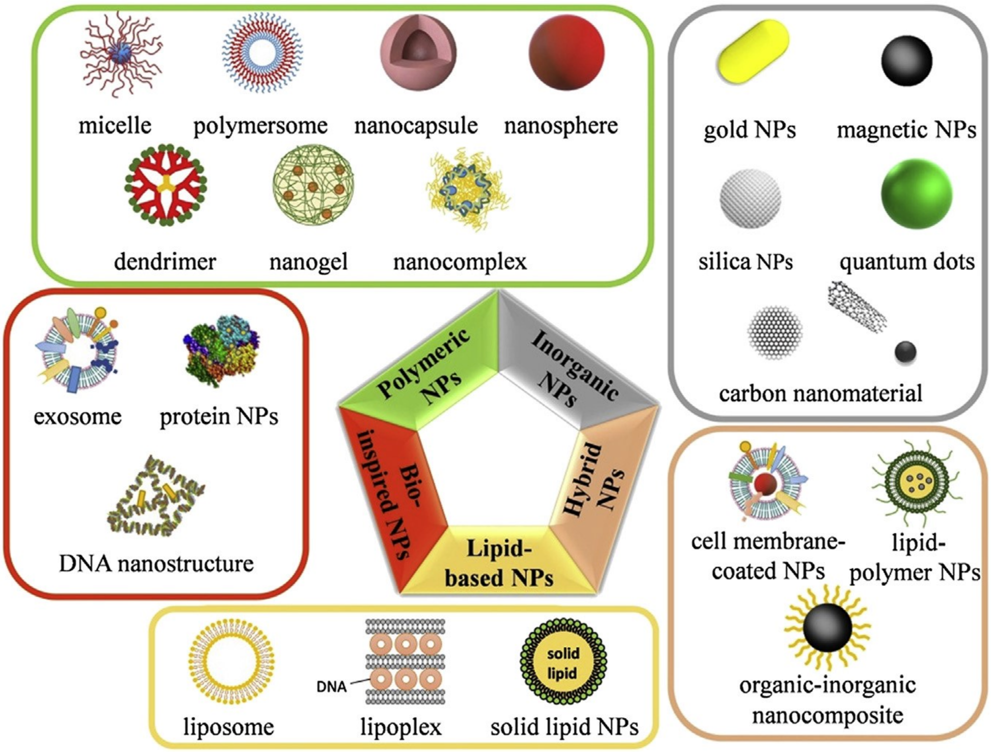

Figure 15. Categories of Nanoparticles based on the material*: polymeric NPs (green square), Inorganic NPs (grey square), Hybrid NPs (brown square), Lipid-based NPs (yellow NPs), Bio-inspired NPs (red square). Reproduced from: Lichen Y., et al., 2020.*

It is possible to classify NPs based on their properties (such as shape, size, activity) or based on the material they are composed of. Depending on the material, it is possible to distinguish five major categories: (**Figure 15**) [Lichen Y., et al., 2020].

1. ***Polymeric NPs***

- *Polymeric micelles (PMs)*, composed of a core/shell configuration and range in size from 20–200 nm.
- *Polymeric Nanospheres*, matrix-type, colloidal particles composed of hydrophobic polymers stabilized on the nanosphere surfaces by surfactants. Diameters range between 100 and 200 nm.

- *Nanocapsule*, nanovesicular structures composed of an inner liquid center encased in a polymeric membrane.
- *Polymersome*, derived from block or graft amphiphilic copolymers. They exhibit comparable properties to liposomes but are more stable.
- *Nanogels*, three-dimensional polymer networks on a nanoscale that have a strong potential for retaining water without dissolving in the aqueous media.
- *Dendrimers*, unimolecular NPs characterized by a well-defined, homogeneous, and monodisperse architecture composed of three distinct domains.
- *Nanocomplex*es, functional supramolecular nanocomposites produced when polymers and biomacromolecular drug cargoes, such as protein and nucleic acids, self-assemble through specific intra- and intermolecular interactions

2. ***Lipid-based NPs***

- *Liposomes*, a subclass of nano- or micrometer-sized phospholipid vesicles consisting of one or more lipid bilayers encasing the inner aqueous cores.
- *Solid-lipid NPs (SLNs)*, also referred to as lipospheres, are composed of a lipid matrix that remains solid at room and body temperatures and is covered with a monolayer of phospholipid. Vary in size from 50–1000 nm.

3. ***Bio-inspired NPs***

- *Exosomes* naturally produced carriers of genetic and proteomic material and are thought to be a major mode of cell-cell contact.
- *Protein NPs*, simple to synthesize and scale-up, their surface is amenable to modification due to the abundance of functional groups (i.e., carboxylic and amino groups) on the NP surface.

4. ***Hybrid NPs***
    - *Cell-membrane coated nanoparticles* have a synthetic nanoparticle core encased in a film of the natural cell membrane, which inherently mimics the characteristics of the source cells.
    - *Lipid-polymer nanoparticles*, core-shell NPs composed of three components: a polymer core, an inner lipid layer encasing the polymer core, and an outer lipid–PEG layer.
5. ***Inorganic NPs***
    - Composed of inorganic materials as the main constituent, examples are Cerium Oxide NPs, Magnetic (Iron-based), and Boron Oxide NPs.

1.8 Cerium Oxide NPs (CNPs)

Although cerium itself has almost no biological meaning in mammalian physiology, soluble Ce^{3+} salts (nitrate, acetate, chloride, etc.) have been used for medicinal purposes by humans for centuries owing to their antiemetic, bacteriostatic, immunomodulating, bactericidal, and antitumor function.

Not only is the insoluble oxide form of Ce (cerium oxide, CeO_2, Ceria) found naturally, but it is also processed in bulk and engineered as NP.

CNPs have consistently demonstrated antioxidant, enzyme-mimetic activity, and the ability to selectively scavenge a number of reactive oxygen and nitrogen species (**ROS** and **RNS**) in cell and animal models.

ROS are generated as waste products of aerobic metabolism and are often associated with oxidative stress (increased intracellular ROS levels leading to the development of a variety of diseases). ROS, on the other hand, are also signaling molecules in biochemical processes. Antioxidants are compounds that scavenge ROS or inhibit their development.

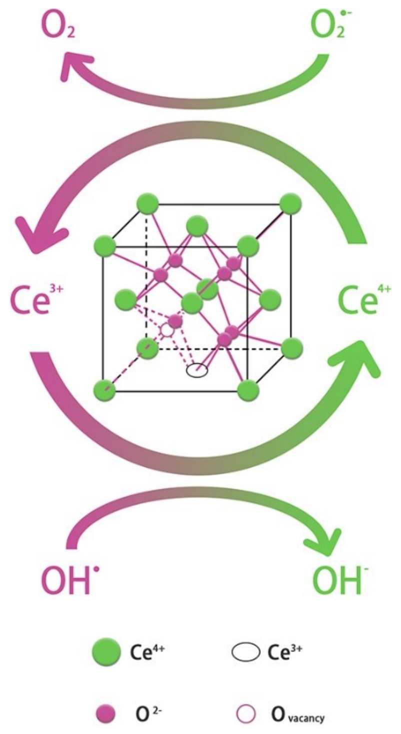

Figure 16. CNPs scavenging activity *of H2O2 and O2°- take place on the surface of the particle via a self-regenerating mechanism. Reproduced from Hongru Li, et al., 2020.*

Both the enzyme-mimicking and ROS/RNS scavenging capacities of CNPs are strongly dependent on the intrinsic physicochemical properties of nanoscale materials, the unique ability of CNPs to accumulate and release oxygen [Deshpande, S et al., 2012], and the relative thermodynamic performance of redox cycling between Ce^{3+} and Ce^{4+} ions on the surface of CNPs (**Figure 16**) [Korsvik C., et al., 2007]. As the absolute diameter of CNP decreases (*e.g.*, from 20 to 2 nm), a quantifiable depletion of oxygen atoms occurs, and the number of Ce^{3+} sites on the NP surface increases [Reed K., et al, 2014]. Therefore, when oxygen atoms are removed from the CNP surface, the oxidation state of Ce decreases (Ce^{4+} to Ce^{3+}), and the number of oxygen vacancies (defect sites) increases on the CNP surface. The ratio of Ce^{3+}/Ce^{4+} sites on the surface is inversely proportional to the CNPs' antioxidant/enzyme-mimetic activity.

Ce ions on the surface of CNPs will move between two valence states (Ce^{4+} and Ce^{3+}) in an aqueous solution. The CNPs' overall structural stability is best represented by the formula **CeO_{2-x}**, which highlights the existence of oxygen vacancies under these conditions. Additionally, to preserve electronic charge stability, each oxygen vacancy must be followed by the reduction of two surface Ce^{4+} ions [Reed K., et al, 2014].

Moreover, our group recently proved that the Ce^{4+}/Ce^{3+} ratio on the surface is strongly dependent on the intracellular localization of the nanoparticle [Ferraro D., et al., 2017]. In particular, by using HeLa cells as a model, we found that even if lysosomes are the main areas for CNP accumulation, additional CNPs can be found in other cell regions (in smaller amounts). Surprisingly, coupling on individual cells synchrotron micro-X-ray fluorescence (μXRF) with micro-XANES (μXANES) it was found that the oxidation state of cerium is dependent on CNPs intracellular localization. The regions with the highest CNP concentrations were characterized by Ce atoms in the Ce^{4+} oxidation state, while higher Ce^{3+} content was observed in regions surrounding these areas, suggesting that the different chemical environments strongly influence the oxidation state and, as a consequence, the ability to neutralize ROS.

It is essential to note that CNP-based prevention methods have the unique benefit of being self-regenerating antioxidants. For this reason, CNPs have been considered as possible antioxidant agents for treating disorders and diseases mediated by oxidative stress.

1.8.1 SOD and Catalase mimetic activity of CNP

In the cellular environment, ROS are produced normally as a result of physiological metabolism. The most common ROS normally produced by the cells are:

- Superoxide radical anion $O_2^{\bullet -}$
- Hydrogen peroxide (H_2O_2)
- Hydroxyl radical $^{\bullet}OH$

Numerous serious diseases are caused by oxidative stress, which is characterized by a cellular imbalance between endogenous antioxidant defenses (free radical scavenging by small-molecule antioxidants and/or redox enzymes) and ROS (e.g., superoxide radical anion ($O_2^{\bullet -}$); hydrogen peroxide (H_2O_2); hydroxyl radical ($^{\bullet}OH$)) generation within the cells. Through the lowering of ROS levels, CNPs have been proven to be protective *in vitro* (cells) and *in vivo* (animal) studies.

$O_2^{\bullet -}$ works as a signaling molecule in the cellular environment and is created during normal cellular metabolism. However, background $O_2^{\bullet -}$levels can rapidly increase as a result of the activation of **NADPH oxidases** during inflammatory responses and/or disruption of the mitochondrial electron transport chain, interfering with ATP synthesis. Normally, excess $O_2^{\bullet -}$ is managed and lowered by the action of **superoxide dismutase** (**SOD**) enzymes found extracellularly, as well as in the cytoplasm and mitochondria [Mccord, J.M. et al., 1969]. SOD enzymes eliminate $O_2^{\bullet -}$ by a two-step catalytic dismutation mechanism that converts $O_2^{\bullet -}$ to H_2O_2 and O_2:

(1) $O_2^{\bullet -} + 2H^+ + (Cu^+)\text{-SOD} \rightarrow H_2O_2 + (Cu^{2+})\text{-SOD}$

(2) $O_2^{\bullet -} + (Cu2+)\text{-SOD} \rightarrow O_2 + (Cu^+)\text{-SOD}$

(3) $2\ O_2^{\bullet -} + 2H^+ \rightarrow H_2O_2 + O_2$ (overall)

The SOD enzyme catalyzes the removal or addition of electrons from $O_2^{\bullet -}$. For instance, in step (1), the reduced (Cu^+)-SOD catalyzes the removal of an electron from $O_2^{\bullet -}$, resulting in the formation of H_2O_2. While in step (2), the oxidized (Cu^{2+})-SOD (produced in step 1) catalyzes the addition of an electron to another molecule of $O_2^{\bullet -}$ to produce O_2. Reduced (Cu^+)-SOD is regenerated, allowing the cycle to restart. In total, two $O_2^{\bullet -}$ molecules are dismutated for each H_2O_2 molecule created. Similarly, the catalytic process by which CNPs are thought to scavenge $O_2^{\bullet -}$ is as follows [Reed K., et al., 2014] (**Figure 17**):

(4) $O_2^{\bullet -} + Ce^{3+} + 2H^+ \rightarrow H_2O_2 + Ce^{4+}$ (Ce^{3+} is oxidized)

(5) $O_2^{\bullet -} + Ce^{4+} \rightarrow O_2 + Ce^{3+}$ (Ce^{4+} is reduced)

Catalase, glutathione peroxidases, and peroxiredoxins all operate to decrease the amount of H_2O_2 in cells, but **catalase (CAT)** is perhaps the most efficient antioxidant enzyme at disproportionately converting H_2O_2 to O_2 and H_2O [Karakoti, A., et al., 2010]. Detailed studies by other investigators have indeed found that CNPs with low Ce^{3+}/Ce^{4+} surface ratios function as efficient antioxidant CAT-mimetics with the following mechanism of action hypothesized:

$$(6)\ H_2O_2 + 2Ce^{4+} + 2OH^- \rightarrow 2H_2O + O_2 + 2Ce^{3+}$$

CNPs' ability to remove toxic quantities of $O_2^{\bullet -}$ and H_2O_2 from cellular surroundings while regenerating reduced Ce^{3+} ions on the NP surface, makes them good SOD and CAT mimics (**Figure 17**). The precise biochemical pathways by which CNPs work as antioxidant enzyme mimics inside the cellular environment, however, remain unclear. Furthermore, the biological significance of oxygen vacancies in CNPs remains unknown. The lack of consistency in the types of NPs used in various *in vitro* and *in vivo* studies, their generally poor physicochemical characterization, and the strong influence of different synthesis procedures on CNP lattice structure and surface reactivity are all significant issues impeding our intrinsic understanding of CNP antioxidant enzyme-mimetic activity.

So far, the SOD- and CAT-mimetic activities of CNPs have been studied mostly in aqueous environments. Is important to notice that, in this case, several intrinsic and extrinsic parameters can influence the catalytic efficiency of the mimetic, for example, the presence of H_2O_2 in solution, presence of phosphate ions ($(PO_4)^{3-}$) in solution, or the pH of the solution. When CNPs are exposed to H_2O_2, most of the NP’s SOD-mimetic activity is lost. However, after all, H_2O_2 is eliminated, the SOD-mimetic activity returns, although regeneration might take up to 14 days.

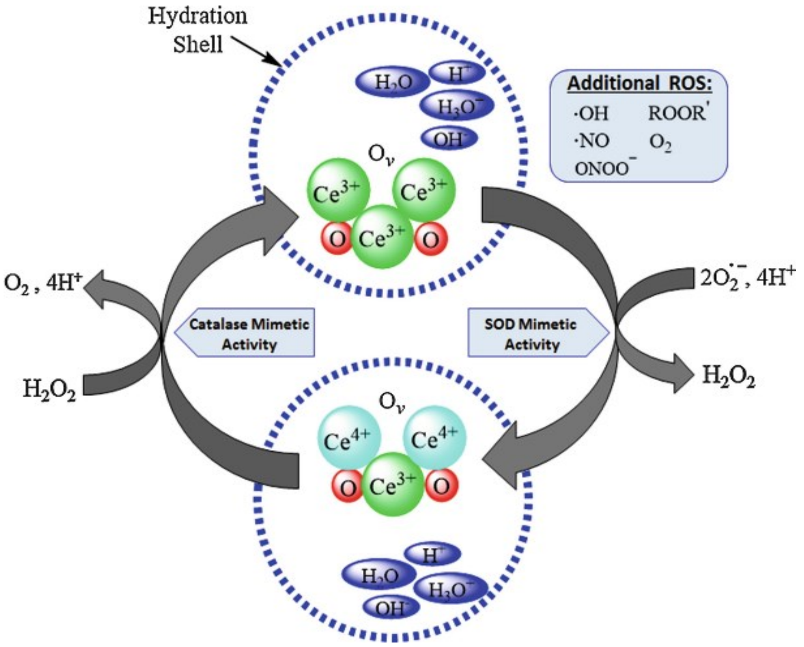

Figure 17. CNPs Catalase and SOD- mimetic Activity *depends on the equilibrium between Ce3+ and Ce4+. Reproduced from Rzigalinski B.A., et al., 2017.*

Numerous studies have demonstrated that when $(PO_4)^{3-}$ anions interact with CNPs, the observed SOD-mimetic activity is diminished while the observed CAT-mimetic activity is increased. Why does this happen? seems that the binding of $(PO_4)^{3-}$ anions to Ce^{3+} sites result in the formation of a $CePO_4$-like complex that inhibits Ce^{3+}/Ce^{4+} redox cycling and effectively stabilizes the CNP in the Ce^{3+} state [Xue, Y., et al., 2012], while the ability of CNPs to interconvert between the Ce^{3+} and Ce^{4+} states is critical for maintaining catalytic SOD-mimetic activity. The effect of $(PO_4)^{3-}$ anions on CNP SOD-mimetic action is critical since cells and tissues are expected to contain significant quantities of phosphate, which might have a significant effect on the biological activity of the CNPs.

About the effect of the pH of the solution on the CNP antioxidant activity, there are some controversies, since some articles show no correlation, while others show a strong effect of the pH on the CNPs' CAT-mimetic activity. The reason, probably, is due to the discrepancy in the synthesis and functionalization of the nanoparticles, as well as the propensity of the CNP Ce^{3+}/Ce^{4+} ratio on the surface to change over time in the aqueous oxygenated environments.

1.8.2 Other mimetic activities

CNPs are now considered good ROS scavengers, not just for their CAT- and SOD-mimetic activity, but also because there can scavenge both ROS such as •OH, or RNS (such as •NO or O2NO-). In particular, in 2009, Asati et al. [Asati A., et al., 2009], was the first to report **oxidase activity** of nanoceria, dependent on the pH and the size of the particles. They found that CNPs could oxidize a variety of substrates in the absence of any other oxidizing agent, including 3,3’,5,5’-tetramethylbenzidine (TMB), 2,2-azinobis(3-ethyl benzothiazoline-6-sulfonic acid) (ABTS), or dopamine (DOPA).

Peroxidase – mimetic activity was demonstrated by Tian Z. and colleagues [Tian Z., et al., 2015]. They suggested the following mechanism:

$$(7)\ Ce^{3+} + H_2O_2 + H^+ \rightarrow Ce^{3+} + OH^{\bullet} + H_2O$$

This reaction is dependent on the number of Ce^{3+} available on the surface of the particles (thus, indirectly on the size).

In addition, CNPs recently showed strong **phosphatase mimetic activity**. It was found [Kuchma M.H., et al., 2010] that Nanoceria can cleave the phosphate ester bond of p-nitrophenyl phosphate (pNPP), adenosine triphosphate (ATP), *o*-phospho-L-tyrosine but not that of DNA. Moreover, this activity is inhibited by tungstate and molybdate, but they are not able to block the catalase activity.

As for **Nitrosative stress** (i.e., excessive production of RNS, such as •NO or O_2NO^-), CNPs proved to be effective, again, depending on the Ce^{3+}/Ce^{4+} surface ratio. They have been shown to be good decomposers of •NO or O_2NO^- breakdown products (such as $CO_3^{\bullet-}$); all these products are very toxic for the cells, having high damaging potential for lipids, proteins, or DNA.

In addition, CNPs had also shown other mimetic effects other than CAT- and SOD-, both *in vivo* and *in vitro,* such as **peroxidase-like**, **oxidase-like**, or **ATPase-like** mimetic activity. Surprisingly, in all these situations, the Ce^{3+}/Ce^{4+} ratio was always determinant. The enzyme–mimetic activities of CNPs described so far are summarised in **Figure 18**.

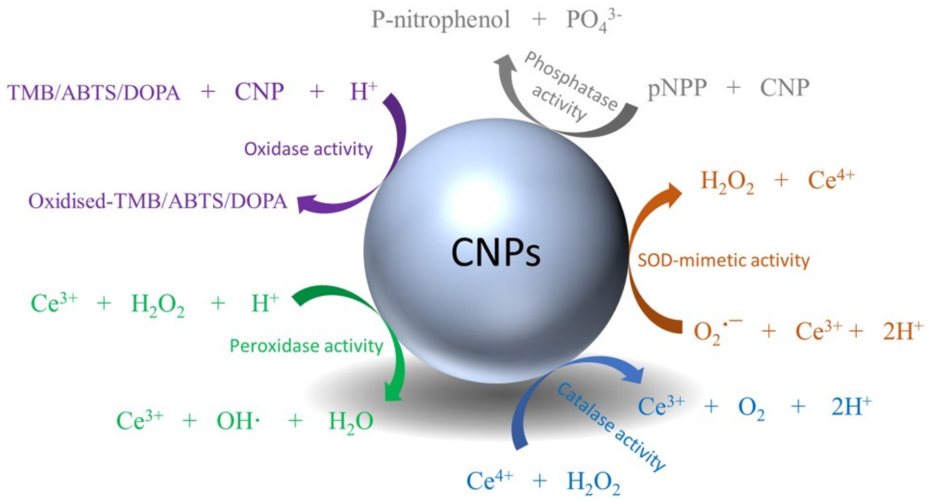

***Figure 18. Different mimetic activities of CNPs reported in the literature**: Oxidase activity, Phosphatase activity, SOD-mimetic activity, Catalase activity, and Peroxidase activity. Reproduced from Saifi M.A., et al., 2021.*

1.8.3 Biomedical application of nanoceria

Nanoceria has established itself as an important metal oxide nanoparticle due to its broad range of applications in a variety of areas, especially biomedicine. One of the reasons is that the nanoparticle form of cerium oxide is a more powerful antioxidant as compared to its bulk counterpart. In **Figure 19** there is a summary of some of the possible Biomedical applications of Nanoceria.

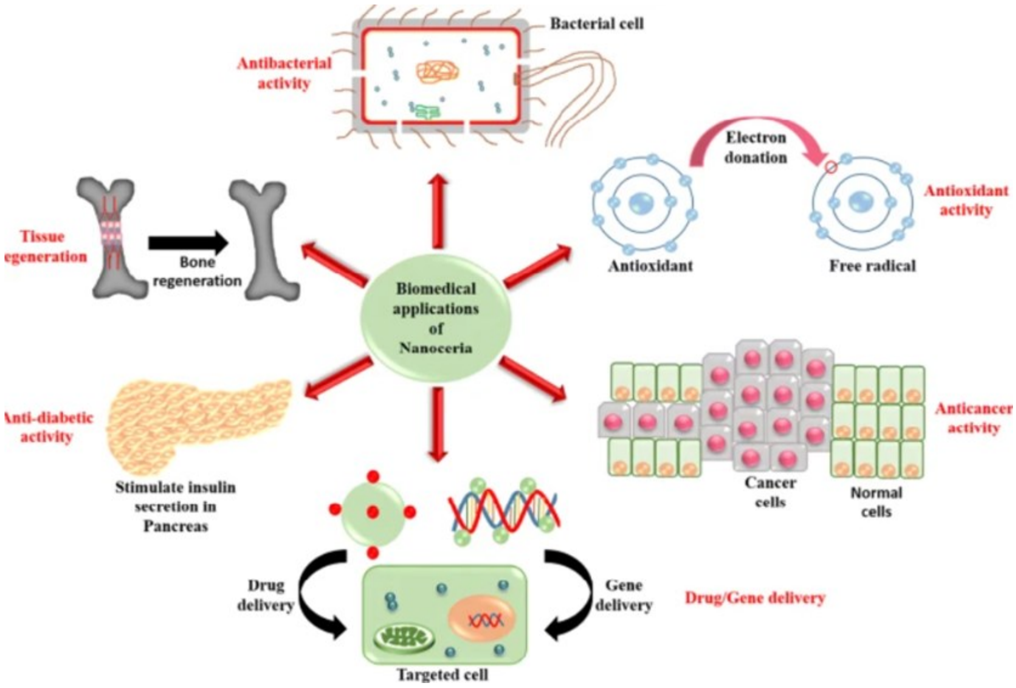

***Figure 19*. *Biomedical applications of nanoceria*.** *CNPs can cover a broad range of activities, from antibacterial to anticancer. Reproduced from Thakur N., et al., 2019*

Cancer therapy

Depending on the pH, CNPs have been shown to enhance or reduce the amount of ROS. For this reason, in cancer cells (that possess a more acidic pH), the amount of ROS (already high) tends to grow even more in the presence of CNPs, causing cytotoxic effects. On the contrary, normal cells, tend to reduce the amount of ROS, so they act as antioxidants, protecting the cells. This is a unique ability that makes CNPs great candidates for anticancer therapy: CNPs can act both as pro- and antioxidant, being able to selectively kill cancer cells, and protect the normal cells at the same time.

Moreover, by adding different ligands on the surface of the nanoparticles, it is possible to enhance the selective capabilities in cancer. For example, by adding Folic acid, Hijaz et al., [Hijaz M., et al., 2016] were able to selectively and efficiently target ovarian cancer cells and cause apoptosis.

However, the use of CNPs in cancer therapy is not limited to ROS scavenging, but there are also some indirect effects, such as suppression of metastasis, angiogenesis, or cell invasiveness. For example, Xiao et al. reported anti-metastatic and anti-migration effects of CNPs in gastric cancer through enhancing the expression levels of DEAH box helicase 15 (DHX15) [Xiao Y.F. et al., 2016], rather than Lord et al. discovered that heparin functionalized CNPs could be better antiangiogenic potential than either heparin or CNPs alone [Lord M.S, et al., 2013]. Interestingly, there is a wide variety of articles suggesting that these effects can be reversed or canceled, depending on the size and functionalization of the nanoparticles. Is possible to conclude that these two factors are fundamental to take into account for possible use in clinical research.

Diabetes, pancreatic beta-cell preservation

Apart from cancer, CNPs have been utilized to treat a variety of diseases associated with oxidative stress due to their exceptional antioxidant and anti-inflammatory capabilities. The loss of pancreatic - cells, which are extremely susceptible to free radical damage, is a critical step in the pathophysiology of diabetes. Apart from cytosolic and plasma membrane oxidoreductases, the mitochondrial respiratory chain is a key source of reactive oxygen species in pancreatic cells. For this reason, a lot of researchers tried to study the possible beneficial effects of nanoceria against diabetes. The results are surprising. CNPs have been shown effective:

- to protect pancreatic cell death by decreasing the ROS production and promoting insulin secretion;
- attenuate the secretion of pro-inflammatory cytokines (TNF-α or IL-6);
- decrease the expression of the transcription factor NF-kB;
- increase the expression of Nrf2, thus activating the antioxidant defense mechanism.

Antibacterial activity

The antibacterial activity of CNPs has been proven to be effective both against Gram-negative and Gram-positive bacteria. In general, is possible to summarize the antibacterial effect in two different mechanisms [Thakur N., et al., 2019]:

1. Direct contact mechanism nanoceria get directly absorbed and damage the outer cell wall by the generation of intracellular ROS;
2. Indirect contact mechanism nanoceria interacts with the environment (intercellular space), generating products (ROS) that damage the bacterial cells.

Usually, the indirect contact happens with polysaccharide encapsulated bacteria, since in this case, CNPs are not able to enter directly. Nanoceria's antibacterial activities are highly dependent on several critical variables, including its size, concentration, pH, surface coating, and surface chemistry.

Tissue regeneration

The capacity of nanoceria to repair tissue is a result of its ROS scavenging properties and angiogenic potentials. Additionally, nanoceria can promote stem cell differentiation, a process that aids in tissue regeneration [Das S., et al., 2014].

Neuroprotection

The majority of neurodegenerative disorders, including Alzheimer's, Parkinson's, Huntington's, Multiple Sclerosis, ischemia, traumatic brain injury, and aging itself, are linked with an abnormally high level of oxidative stress in the brain. However, the use of antioxidants to enhance the outcome of neurodegenerative disorders has had relatively little success so far. Our present pharmacological arsenal of antioxidants consists of molecules that scavenge and eliminate a single free radical. Thus, the repeated dosage is necessary, which is insufficient to deal with the number of radicals produced. Given CNPs' excellent potential as a regenerative antioxidant, it seemed natural to advance to their use in neurodegenerative illness.

Both Alzheimer's disease (AD) and Parkinson's disease (PD), in particular, are linked with elevated levels of oxidative stress. AD is defined by the initial death of cortical cholinergic neurons, whereas PD is defined by the early death of dopaminergic nigrostriatal neurons. There have been no *in vivo* trials with CNPs in AD animal models yet, although numerous *in vitro* studies indicate good potential.

Other applications

CNPs have been tested for a huge variety of different applications, especially involving oxidative stress. Some examples are cardiovascular diseases, wound healing, kidney disorders, or drug/gene delivery.

One of the most interesting of these applications is the improvement in wound healing by enhancing cytoprotective activities on different cells such as fibroblasts and keratinocytes. For example, Pezzini and colleagues [Pezzini I., et al., 2017] recently demonstrated that CNPs preserved mitochondrial functions and improved the energy balance in basal as well as pro-oxidant conditions in primary cultured skin fibroblasts. Further, CNPs also have proven to decrease inflammation post healing, accelerating the migration of the cells and increasing angiogenesis.

1.8.4 Biodistribution and toxicity of Nanoceria

Generally, CNPs have shown a trend of accumulation in organs like the liver, spleen, followed by lungs and kidneys, with some minimal brain distribution. An interesting analysis of CNPs biodistribution was performed on mice by Hirst S.M. and colleagues [Hirst S.M, et al., 2013], confronting different types of administrations: intraperitoneal (IP), oral, or intravenous (IV), for 5 weeks. They found a good deposition of CNPs in different organs after IP and IV, rather than no significant accumulation after oral administration.

However, unrestricted use of nanomaterials for a broad range of applications raises health and environmental issues because of their substantially longer persistence in the body, and CNPs are no exception. Despite the availability of *in vitro* and *in vivo* data indicating adverse effects of CNPs, there is a discrepancy about CNPs' putative toxicity potential. The toxicity of nanoceria is dependent on a number of variables, including particle size, production technique, cell type, dose/concentration, duration of exposure, and route of exposure.

CNPs, in fact, can cause:

- Apoptosis, through mitochondria-dependent pathway and autophagy in human blood monocytes at a relatively low dose (1-10 µg/ml) [Hussain S., et al, 2013]
- Inhibition of the differentiation of neuronal stem cells [Gliga A.R., et al 2017]
- Alteration of hepatic functions, activation of Kupffer cells, hepatocellular apoptosis, and granulomatous lesions in the livers of rats at 30 days after single IV exposure [Tsent M.T., et al., 2012]
- Induction of fibrosis in the lungs of rats, by changing the expression osteopontin and TGF-β, after intratracheal administration [Ma J.Y. et al., 2012]

These are just a few examples of the toxicity studies conducted so far about CNPs. However, different modification processes have been tried to improve their safety profile.

Many different factors need to be taken into account when considering the CNPs toxicity, such as the **synthesis method** or the number of **impurities** present in the preparation. However, the potential beneficial effects of these nanoparticles are so wide, and the applications so different, that further studies about their biological effect, biodistribution, and toxicity are needed before considering their clinical use.

2. Objectives

During this thesis work, the interaction of CNPs with biological systems was studied. These nanoparticles have particular antioxidant properties, which make them suitable for potential use in the therapeutic field, specifically in the treatment of pathologies such as neurodegenerative diseases, normally characterized by high levels of free radicals. The mechanism underlying their antioxidant capacities has so far been hypothesized, but not yet validated by means of a study of the behavior that these nanoparticles assume when placed in a biological environment. Understanding the CNPs behavior once inside cells, however, is crucial for optimizing their future use *in vivo*, as it is equally important to understand the uptake and internalization phases.

No commercial nanoparticles were used, whose characteristics are often difficult to know, but the nanoparticles were synthesized in-house by the group of Prof. U. Anselmi Tamburini of the Chemistry Department of the University of Pavia. Furthermore, the nanoparticles have been coated with capping agents which, binding to the surface of the NPs prevents the formation of aggregates due to electrostatic repulsion. Based on previous experiences it was decided to work with CNPs that had a diameter of less than 10 nm and had a negative charge, being functionalized with **polyacrylic acid** (**PAA**).

The work presented will be divided into two separate sections: analysis of the interaction of CNPs with biological systems *in vitro*, by using a cellular model, and analysis of the interaction of CNPs *in vivo*, by using an animal model.

3. Nanoparticles – cell interaction

3.1 Scientific background

The cellular internalization of NPs has been extensively investigated in the last two decades to exploit the potential benefits of NPs or to counteract their harmful effects on biological systems. The literature on NP–cell interaction varies widely due to significant differences in protocols, cell lines, and NP characteristics. However, it is largely recognized that the physicochemical properties of NPs play an essential role in making them more or less reactive toward the biological environment. Thus, size, stiffness, surface charge, functionalization, and composition, as well as the formation of a protein corona, play a pivotal role in this regard [Asati a., et al., 2010] [Canton I., et al., 2012]. Surface chemistry is especially relevant, and both surface coating and charge appear to be fundamental in determining if and how NP–cell interaction occurs. NPs are usually coated with polymeric macromolecules, such as polyethylene glycol (PEG), PAA, or dextran to avoid aggregation and precipitation in biological environments [Asati a., et al., 2010]. These surface modifications have a profound influence on the interaction of NPs with cells and have been shown to have a pivotal influence on NP uptake and intracellular localization, as well as toxicity after internalization. However, other factors play a crucial role in the NPs-cell internalization, like the surface charge of the NPs, their dimensions, or the type of cell [Asati a., et al., 2010].

In general, the process of NPs internalization relies on the endocytic machinery of the cell. The standard routes followed by cells to internalize exogenous material are pinocytosis, phagocytosis, and receptor-mediated endocytosis. Pinocytosis is involved in the internalization of fluids or solutes, which includes many unrelated endocytic mechanisms, like clathrin-mediated, caveolar, nonclathrin/noncaveolar (clathrin-independent), lipid-raft-mediated, and micropinocytosis [Mercer J., et al., 2009]. Usually, NP uptake follows these well-known mechanisms and no NP-specific mechanisms have been identified to date.

3.2 Materials and Methods

3.2.1 Nanoparticles synthesis

The main limit for the use of inorganic NP suspensions in a biological environment is their intrinsic instability, which leads to the development of agglomeration and precipitation. To overcome this problem, it was necessary to use a stabilizing polymer, which by producing a capping on the NPs it increases their stability over time. Polymers are often used in NPs synthesis to control nucleation and growth processes. They also prevent agglomeration through a steric hindrance mechanism or electrostatically, thus improving biocompatibility. In this case, it was used PAA which creates an overall negative charge on the surface of the NPs.

All the syntheses were carried out using sterilized glassware in order to avoid bacterial contamination. The CNPs were produced by direct precipitation from an aqueous solution and stabilized in presence of PAA, as described previously [Ferraro D., et al., 2017]. The precursor chosen for the synthesis is a Cerium (III) salt, Cerium nitrate hexahydrate $Ce(NO_3)_3 \cdot 6H_2O$ (Sigma Aldrich, purity ≥ 99.0%; 22350). 1,085 g of this salt were weighed and subsequently dissolved in 43.65 mL of distilled water, filtered (sterile minisart, 0.20µm). An aqueous suspension of PAA was then made by diluting 600 mg of commercial PAA suspension (*Polysciences, Inc.*, 63% w/w; 06513) with 31 mL distilled water. PAA was then transferred with multiple washes into a 50 mL tube. It was necessary to shake vigorously to develop as much foam as possible before continuing with another transfer (leaving the foam behind). Of the 31 mL of the diluted PAA solution, only 20 mL were added to the $Ce(NO_3)_3 \cdot 6H_2O$ solution, all under constant stirring and in a thermostated bath.

Concentrated NH_4OH solution (Sigma Aldrich, 28.0-30.0% di NH_3; 221228) was added dropwise to obtain pH ~12 and the solution was kept under constant stirring. Immediately after the addition of NH_4OH the solution is pale pink/red and milky. The suspension becomes a transparent brown solution after 4 hours and yellow and clear after 1 day. The solution is left under constant stirring for additional 24 hours in order to allow the complete evaporation of nitrogenous species that could affect the viability of the cells.

The final CNPs suspension had a CeO_2 content of ~6 mg/mL, as determined by inductively coupled plasma-optical emission spectrometry (**ICP-OES**) analysis. To remove excess PAA, the suspension was centrifuged at 13,000 *g* for 30 min and the pellet recovered in the original volume of deionized water.

To determine the role of the nanoparticles core chemical composition or the nanoparticles size on the interaction and internalization in the cells, different kind of nanoparticles were synthetized and characterized in our laboratory:

- nanoparticles of Iron Oxide (**IONPs**), that posses a core of Iron instead of Cerium and that vary in size;
- nanoparticles of Iron Oxide surrounded by a Boron Carbide core (**B-IONPs**), of larger size;
- nanoparticle of positive surface charge, obtained substituting PAA with polyethyleneimine (PEI) (**PCNPs**)
- nanoparticles with different functionalization, substituting PAA with dextran (**DCNPs**);
- and nanoparticles without functionalization, excluding altogether PAA from CNPs synthesis (**CNP w/o PAA**);

The IONPs were produced by direct precipitation of Fe_3O_4 from aqueous solution in the presence of PAA, as previously described [Santra, S. et al., 2009]. Iron salts solution was prepared by dissolving 0.18 g $FeCl_2 \cdot 4H_2O$ and 0.37 g $FeCl_3 \cdot 6H_2O$ in 2 ml 0.5 N HCl. This was added to 15 ml distilled H_2O and 2 ml of NH_4OH (30% NH_3) was added. The resulting dark suspension of IONPs was stirred for 30 s before adding 5 ml PAA solution (9.4% w/v) and stirred for an additional hour. The final suspension of PAA-IONPs was centrifuged at 1000 *g* for 30 min to remove the largest aggregates. The supernatant was centrifuged at 25 000 *g* for 30 min to remove the free PAA and other unreacted reagents. The pellet was washed twice and, eventually, recovered in deionized water. To obtain IONPs with different levels of aggregation, IONPs were sequentially centrifuged at 5000 and 10 000 *g* for 30 min. Each fraction was recovered in deionized water and characterized by DLS.

The B-IONPs were obtained by modifying the procedure used for IONPs and precipitating Fe_3O_4 in the presence of B_4CNPs. Commercial B_4C nanopowder (*SkySpring Nanomaterials Inc.,* Houston, TX, USA) was subjected to a ball milling treatment using a planetary mill (Fritsch pulverisette 7 premium line) with tungsten carbide jar and balls, to reduce agglomeration. The obtained nanopowder was recovered in deionized water. This suspension of B_4C (3 mg/ml) was added to the stirring iron salts solution prepared as above, before NH_4OH and PAA incorporation. After 1 hour, the resulting suspension was centrifuged at 300 *g* for 30 minutes to remove the largest aggregates and the supernatant was centrifuged at 15 000 *g* for 30 minutes to remove unreacted reagents. The pellet was washed twice and, eventually, recovered in deionized water.

The DCNPs were produced similarly to CNPs except for the substitution of PAA with 10 ml of dextran solution (16.21% w/v; dextran from *Streptococcus mutans,* average mol wt 9000 – 11000; *Sigma Aldrich*, St. Louis, MO, USA).

PCNPs were synthesized by direct precipitation from aqueous solution and functionalized with polyethyleneimine (PEI), as reported by Turin-Moleavin *et al.* Briefly, 2.50 ml 0.1 M solution of $Ce\ (NO_3)_3 \cdot 6H_2O$ was added dropwise under magnetic stirring to a mixture of 1.25 ml 0.1 M solution of PEI (800 Da-branched) with 7.50 ml NH_4OH (28–30%). The mixture was left under continuous magnetic stirring for 24 h. After completion of the reaction, the suspension was centrifuged at 17 000 *g* for 10 min and washed with deionized water. The supernatant was centrifuged at 25 500 *g* for 15 min and the pellet was washed three times with distilled H_2O.

For the preparation of fluorescent CNPs or fluorescent IONPs, DiI fluorescent dye (Sigma–Aldrich, St. Louis, MO, USA) was dissolved in dimethylsulfoxide (1.2 mg/mL) and then added under stirring to the 6 mg/mL CNPs or IONPs suspension (1:20 v/v), as described previously [Asati, A. et al., 2010]. The CNPs suspension was centrifuged at 17,000 · *g* for 20 min to remove free DiI in solution, and the pellet recovered in deionized water. Thanks to this approach it was possible to introduce a fluorescent molecule inside the ceria particles coated with PAA, without compromising the solubility of the nanoparticles themselves in aqueous solution and without reducing the number of functional groups available on their surface. This allowed following the nanoparticle-cell interaction using fluorometric techniques. DiI possesses a maximum emission wavelength of 585 nm, which means that it will be visualized in confocal microscopy with the color red.

3.1 Characterization of Nanoparticles

CNP, IONP, B-IONP characterization included **XRD**, **DLS**, **Z potential**, **SEM,** and **TEM** analysis.

The CeO_2 content was determined by **ICP-OES** analysis (ICP-OES Optima 3300 D; Perkin Elmer, Santa Clara, CA, USA).

X-Ray Powder Diffraction (XRD)

Description

The principle of operation of X-ray diffraction is based on **Bragg's law**. From this law it is possible to derive the angles obtained by coherent and incoherent scattering by the crystal: when X-rays are incident on an atom, they cause the movement of the electron cloud. The movement of these charges causes a re-emission of waves with the same frequency, slightly blurred due to various effects. This effect is known as *Rayleigh scattering* (or *elastic scattering*).

The re-emitted waves can interfere with each other constructively or destructively, the overlapping waves can add up to produce stronger peaks or subtract each other, thus generating a diffraction pattern on a detector. The wave interference pattern is the basis of X diffraction and can be explained through Bragg's law:

$$2d\ sin\theta = n\lambda$$

where λ is the wavelength of the incident X-rays, in the order of diffraction, the distance between the two adjacent crystalline planes, and θ is the angle that the beam forms with the crystalline plane. For a crystalline solid, the waves are scattered from lattice planes separated by a distance d.

When the diffracted waves interfere constructively, they remain in phase as long as the difference between the path lengths of the two waves is equal to an integer multiple of the wavelength. The path difference between two waves that undergo interference is given by $\boldsymbol{2dsin\theta}$, where $\boldsymbol{\theta}$ is the scattering angle (**Figure 20**).

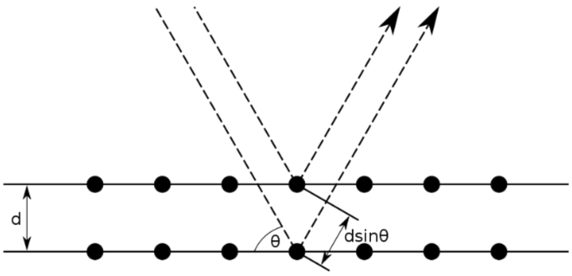

***Figure 20**. Representation of the model on which Bragg's law is based.*

A diffraction pattern is obtained by measuring the intensity of the scattered waves as a function of the dispersion angle. The peaks of greatest intensity that are obtained in the diffraction pattern are in those scattering angles that satisfy the Bragg condition.

Method

XRD analysis was performed on films obtained by evaporating 150 µL CNP, IONP, B-IONP suspensions on glass microscope slides. The XRD patterns were acquired using a Bruker D8 Advance diffractometer (Bruker Corp., Billerica, MA, USA) with a Cu anticathode (λ-Cu-K_α = 1.541838 Å) operated at 40 kV and 40 mA. Diffractograms were acquired in θ–θ mode, with a step of 0.03° 2 θ and an acquisition time of 20 s per step.

Dynamic Light Scattering (DLS) and Z potential

Description

The hydrodynamic diameter and Z potential of the NPs were evaluated with a Nano ZS90 DLS apparatus (Malvern Instruments, Malvern, UK). For DLS, three measurements were performed on diluted solutions (~1 mg/mL) for each sample, providing average sizes, distribution widths, polydispersion index, and associated standard deviations (SDs).

The DLS setup consists of a monochromatic light source, usually a laser, which is emitted through a polarizer towards the sample. The scattered light then passes through a second polarizer where it is collected by a photomultiplier (**Figure 21**).

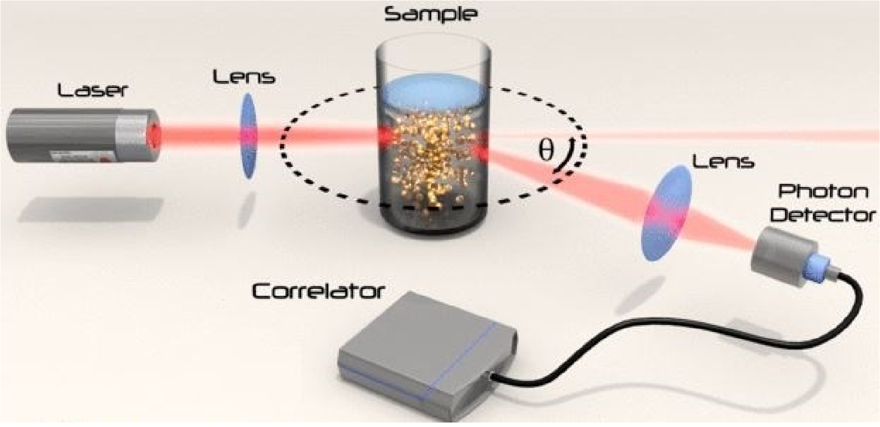

Figure 21. Schematic representation of a typical DLS setup.

In our case, 3 measurements were performed, each consisting of 13-14 runs, on dilute solutions (~ 1 mg / mL) for each sample, providing average sizes, distribution widths, polydispersion index, and associated deviations.

With the Dynamic Light Scattering technique, the diffusion of a laser beam by the surface of the NPs is measured through the use of two parameters (Absorption Index and Refractive Index) that make the reading selective. Furthermore, through DLS it is possible to examine dispersed or agglomerated NPs quickly and easily. The analysis applies to particles up to a diameter of ~ 1 nm without being destructive. The main advantage of this technique is to obtain the hydrodynamic radius/volume of the NPs in question, *i.e.,* both the capping agent and the interaction of the NPs with the solution in which they are dispersed are considered. This is very useful if the NPs of interest are used in biological environments, since it is possible to predict their behavior even in solvents other than the synthetic one, such as a culture medium.

However, the DLS technique has limitations as it can only be applied to well-dispersed systems that do not give rise to sedimentation phenomena.

The potential Z instead is the overall charge that a particle acquires in a specific medium. This charge is responsible for the electrostatic stabilization of the particles. The potential is determined with the same instrumental setup as the DLS, but in this case, the sample holder consists of a cuvette containing two electrodes, to which an electric field is applied. The particles will tend to move towards the electrode with an opposite charge compared to that present on their surface, causing a variation in the frequency of the light scattered by the sample. As in DLS analysis, the variations in the signal depend on the speed with which the particles move in the medium which, in turn, is related to their surface charge.

Method

The determination of the hydrodynamic diameter and the Z potential of the NPs was carried out starting from suspensions of the various products at a concentration of ~ 1 mg/ml, in order to obtain interference-free measurements. For the DLS characterization, each sample was allowed to equilibrate for 30 s at a temperature of 25 ° C and, subsequently, subjected to three measurements each consisting of 10 readings lasting 10 s. The determination of the Z potential was carried out on the same suspensions used for the previous analysis; for each sample, three measurements were made, each consisting of 12-14 readings. For both analyses, the instrument was programmed defining ceria as reference material (refractive index 2.100, absorption 1.000) and water as solvent (viscosity of 0.8872 cP, refractive index 1.330, and dielectric constant 78.5, at a temperature of 25 ° C).

Transmission electron microscopy (TEM)

Description

Transmission electron microscopy (TEM) is a microscopy technique in which an image is formed by passing an electron beam through a specimen. A suspension on a grid or an ultrathin section less than 100 nm thick is the most common specimen. The interaction of the electrons with the sample as the beam passes through the specimen creates a picture. The picture is then enlarged and focussed onto an imaging device, such as a fluorescent screen, a layer of photographic film, or a sensor linked to a charge-coupled device, such as a scintillator.

Transmission electron microscopes can image at a far better resolution than light microscopes thanks to the use of waves (*i.e.,* the electron quantum ones) with much smaller wavelength. This enables the instrument to capture fine detail, even as small as a single column of atoms, which is thousands of times smaller than a resolvable object seen in a light microscope.

Method

For TEM, a drop of NP suspension was placed on an ultrathin, carbon-membrane, 400-mesh copper grid and left to dry for 5 min. TEM imaging was performed using an FEI Titan 80-300 Cube transmission electron microscope (Hillsboro, OR, USA), operating at an accelerating voltage of 300 kV, equipped with an S-Twin objective lens, an FEI X-FEG Schottky electron source, a 2k · 2k US1000 Gatan CCD Camera, and an EDS Si(Li) EDAX detector.

ICP-OES analysis

The ICP-OES analysis was used to quantify the CeO_2 obtained in the synthesis of PAA-CNP and to determine the concentration of Ce ions released by the nanoparticles at various pHs. In order to carry out the analysis, it was necessary to carry out acid digestion in a bomb. The procedure involved placing 200 µl of suspension inside the bomb, *i.e.,* a hydrothermal reactor consisting of a Teflon container closed in a steel jacket, to which 200 µl of dH2O and 400 µl of ultrapure nitric acid were added. (Sigma Aldrich, very pure pa, concentration ≥ 65%, 30709-M). The digestion process was carried out in an oven at a temperature of 150 °C for 3 hours. In the end, the bomb was opened under the hood as the reaction leads to the formation of NOx species, which are notoriously harmful. The solution remaining inside the Teflon container was perfectly clear, indicating that digestion was successful.

In the case of PAA-CNP solubility studies, the supernatant obtained by ultracentrifugation did not need to be subjected to further treatments and could be analyzed as it is. For all the samples analyzed, 5.00 ml of the solution were transferred into a test tube and 100 µl ultrapure 65% HNO_3 were added in order to prevent the material from anchoring to the walls of the container.

3.2.3 Cells and treatments

Cell cultures

HeLa cervical cancer cells, human mesothelioma cells (MSTO and REN), human epidermoid carcinoma cells (A431), and monkey kidney-derived fibroblasts (COS-7), were maintained in DMEM with 10% FBS and 2 mM L-glutamine (Lonza, Basel, Switzerland) at 37°C in a humidified atmosphere of 5% CO_2 in the air. The cells can grow both in adhesion and in suspension, therefore the detachment of the confluent cells was performed with

Trypsin-EDTA (1x). Trypsin is an enzyme proteolytic, which digests the glycoprotein material present on the cell membrane, responsible for adhesion, without destroying or killing the cells.

When treated with NPs, cells were seeded at 3.0×10^5 in 9-cm^2 Petri dishes. When 50% confluency was reached, cells were washed and incubated with a fresh medium containing NPs for the time specified, at a concentration of 200 µg/mL, or as otherwise indicated.

For pulse-chase experiments, HeLa cells were incubated with CNPs for the indicated time (pulse) and, after removal of CNPs and extensive washing, cells were maintained in culture for an additional 2 h (chase). At the end of the chase period, cells were processed for further analysis.

For treatment at low temperature, Hela cells were preconditioned for 30 min at 4°C. After this period the CNPs were added to the cold culture medium and cells were incubated at 4°C for indicated times.

Viability test (MTT)

Description

The MTT test is a cell-based colorimetric assay to assess whether the molecule being tested has effects on cell viability. The **tetrazolium salt MTT** (3- (4,5-dimethylthiazol-2-yl) -2,5-diphenyl tetrazolium bromide), yellow, is transformed by the metabolically active cells to form formazan, purple, which quantity can be measured by using a **spectrophotometer**. Cells that have undergone cell death do not have the ability to convert the tetrazolium salt to formazan, so the formation of the purple color is an indicator of viable cells.

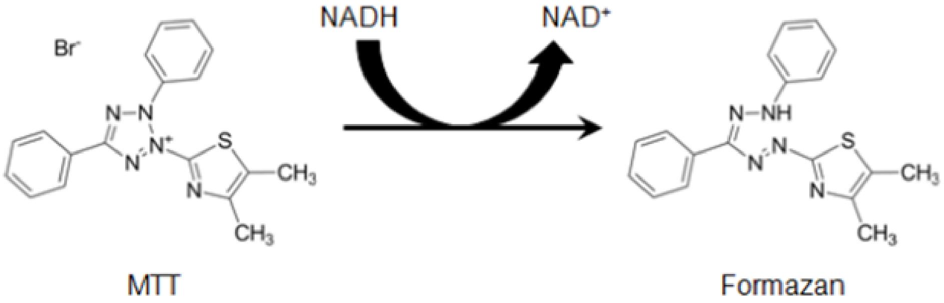

Figure 22. Reduction of MTT to Formazan. Reproduced from Riss T.L., 2016

The exact cellular mechanism related to the reduction of MTT to formazan involves a reaction with NADH, or similar reducing molecules, capable of transferring electrons to MTT (**Figure 22**). Formazan then accumulates inside the cell in the form of an insoluble precipitate, which must be solubilized to subsequently quantify the absorbance. The methods used for this purpose are several and can include the use of DMSO, acidified isopropanol, DMF, SDS, and/or combinations of detergents and organic solvents. The amount of signal generated depends on various parameters, including starting MTT concentration, duration of incubation, number of viable cells, and their metabolic activity. All these parameters should be considered when optimizing the test conditions in order to generate a sufficient amount of product to analyze.

The conversion of MTT to formazan by cultured cells is time-dependent. A longer incubation time will result in an accumulation of purple color in the cells and an increase in sensitivity; however, the incubation time is limited due to the cytotoxic nature of the reagents used for detection, which use energy extracted from the cell (using reducing equivalents such as NADH) to generate a signal. For log-phase growing cell populations, the amount of formazan produced is generally proportional to the number of viable metabolically active cells. Culture conditions that alter cell metabolism affect the rate of reduction of MTT to formazan. For example, as adhesion cells in the culture approach confluence and growth are inhibited due to contact, metabolism may slow down and the amount of reduced MTT will be less. Other adverse culture conditions, such as altered pH or depletion of essential nutrients such as glucose, can lead to a change in the ability of cells to reduce MTT [Riss T. L., 2016].

Method

To perform the viability assay, HeLa cells were seeded on a 96-well plate. $2x10^5$ cells were seeded in each well. The following day, treatments were carried out with the NPs at different concentrations. Cells that were used as negative control were treated with fresh medium; cells treated with an SDS solution at a concentration equal to 5 mg/ml were used as a positive control. The plate was placed in an incubator at 37 ° C for 15 minutes, 1 hour, or 24 hours.

The supernatant was removed from all cells and two washes were carried out with PBS (Phosphate Buffered Saline, without Ca2 + and Mg2 +), then 100 µl of fresh medium containing with 10 µl of MTT 5 mg/ml solution, previously prepared in PBS, was added to each well. The plate was incubated for two hours at 37°C. Finally, the supernatant was removed from each well, washed in PBS and 100 µl DMSO was added to each well to dissolve any formazan crystals that may have formed.

Finally, the samples were read with a microplate reader (Bio-Rad Model 680 microplate reader) using the wavelength of 540 nm. DMSO alone was used as a blank. Each sample was analyzed in triplicate and the mean value was then obtained from the measurements. Results are expressed as the average of three independent experiments. Cell viability was calculated as the ratio expressed as a percentage between the signal of the treated samples and the controls, both subtracted from the blank.

Alteration of membrane composition and endocytotic inhibition

Description

To alter the microvilli/membrane composition, different kinds of inhibitors were tested, like Myriocin and MβCD, both known to alter the lipid rafts and cholesterol compositions. **Myriocin**, also known as antibiotic ISP-1 and thermozymocidin, is a non-proteinogenic amino acid derived from certain thermophilic fungi. Myriocin is a very potent inhibitor of serine palmitoyltransferase, the first step in sphingosine biosynthesis [Miyake Y., et al., 1995]. Due to this property, it is used in biochemical research as a tool for depleting cells of sphingolipids.

Cyclodextrins (**CDs**) are cyclic oligosaccharides consisting of α-(1–4)-linked D-glycopyranose Units. Numerous studies have shown that exposing cells to βCDs results in the removal of cellular **cholesterol**. The degree of cholesterol depletion is a function of the βCD derivative used, its concentration, incubation time, temperature, and type of cells. MβCD was shown to be the most efficient as an acceptor of cellular cholesterol.

Other tested inhibitors included: Cytochalasin D (CytD), Wortmannin (Wort), Hypertonic sucrose (0.5 M), Nystatin (Nys), and Amiloride.

Method

For sphingolipid and cholesterol content alteration, myriocin and MβCD were used as previously described [Poole, K. et al., 2004]. To extract cholesterol, HeLa cells were incubated with freshly prepared 10 mM MβCD (Sigma–Aldrich), in a serum-free medium for 30 min. To inhibit sphingolipid synthesis, cells were grown with 10 µM Myriocin (Sigma–Aldrich) for 48 h. For modification of both cholesterol and glycosphingolipid, cells were treated with myriocin first, and then the myriocin-containing medium was substituted with a serum-free medium containing 10 mM MβCD, for 30 minutes.

To alter the microvilli cytoskeleton, CytD (Sigma-Aldrich #C8273) was used. Briefly, Cells were pre-treated for 1 hour with a fresh medium supplemented with CytD at a final concentration of 5 μM.

For all treatments, at the end of incubation, MβCD-, myriocin- or CytD- containing medium was removed and complete medium added with or without CNP.

For the inhibition of endocytosis, CytD (5 μM), Amiloride (100 μM), hypertonic sucrose (0,5 M) and Wortmannin (2 mM) were dissolved in DMEM + 10% FBS; Nystatin (25 μM) and MβCD (10 μM) were dissolved in DMEM w/o 10% FBS.

Briefly, cells were pre-incubated with the relative drug (CytD, Amiloride, Nyst, MβCD, Wort, or hypertonic sucrose) for 30 minutes at 37°C before incubation with the CNPs (200 μg/ml) for 15 minutes in the presence of the drug. After extensive washing, cells were incubated with a fresh medium containing the same drug, for a chase period of 1 hour. After this time, cells were treated with Trypsin for 2 minutes, centrifugated, and resuspended in Formaldehyde 4% for fixation for 15 minutes. Cells were then processed for flow cytometry.

Immunofluorescence and Confocal microscopy

Description

Immunofluorescence (**IF**) is an immunocytochemical technique that, by exploiting the recognition between antigen and antibody, allows recognition of specific components, generally proteins, within a cell. The technique can be performed following the direct method or indirect method: the direct method involves the use of an antibody conjugated directly to a fluorescent dye; the indirect method is based on the recognition of the antigen by an unlabelled primary antibody, which is in turn recognized by a secondary antibody, labeled with the fluorophore. The fluorescence signal can be viewed using a fluorescence microscope.

Confocal microscopy is a technique that has many more advantages compared to classical optical microscopy, such as obtaining a more precise picture of the three-dimensional architecture of the sample, revealing important information on the third dimension with higher resolution. In fact, it can provide information on the object of interest without interference, given by the structures outside the focal plane, which are removed, thus producing images rich in detail. In conventional optical microscopy, the entire sample is simultaneously exposed to the excitation light, and therefore the emission that is recorded comes from both the focal plane and from above and below it, thus obtaining a less sharp and obscured image. Basically, conventional microscopes create images with a depth of field of 2-3 µm but are theoretically capable of resolving two structures that are 0.2 µm apart. Confocal microscopy can solve these limitations by illuminating a single point of the sample at a time with a targeted beam. In particular, the fluorescent light emitted both by the planes in the focus, and outside, is collected by a lens, but only the light emitted by the focal plane can be concentrated and pass through a diaphragm, or **pinhole**, to be then detected by the photomultiplier tube (**PMT**, *i.e.,* the detector). Instead, the light coming from above and below the top cannot pass through the pinhole opening, being automatically excluded from the image. In this way, confocal microscopy can increase the resolution by a factor of 1.4 compared to conventional wide-field microscopy.

Method

For the IF experiments, cells were grown on 18 · 18 mm glass coverslips and incubated with fluorescent CNPs, as previously described [Ferraro D., et al., 2017]. Cells were first washed with PBS, then fixed in 4% formaldehyde for 15 min. After permeabilization with 0.2% saponin for 10 min, samples were incubated for 1 hour with rabbit anti-pERM primary antibody (1:200; Cell Signalling Technology, Leiden, The Netherlands), Phalloidin – FITC conjugated (1:500, Sigma Aldrich, Burlington, MA, United States), anti-Flotillin H-104 (1:50, Santa Cruz Biotechnology, Dallas, TX, United States), Choleric Toxin-660R (1:100, Biutium, San Francisco Bay Area), Lysosome-specific mouse-monoclonal anti-Lamp1 primary antibody (1:200, BD Biosciences, San Jose, CA, USA).

After the incubation time, cells were washed three times with PBS and then incubated for 1 hour with fluorescent secondary antibody Alexa488-labeled anti-rabbit (1:400; Jackson Immunoresearch, West Grove, PA, USA), Alexa488-labeled anti-mouse (1:400; Jackson Immunoresearch, West Grove, PA, USA) or Alexa647-labeled anti-rabbit (1:300, Abcam, ab96898). Nuclei were counterstained with Hoechst 33342 (Sigma–Aldrich). Samples were analyzed with a TCS SP8 confocal laser scanning microscope equipped with an HC PL APO CS2 40·/1.30 oil-immersion objective (Leica Microsystems, Heidelberg, Germany). Images were processed using ImageJ software and related plugins (National Institutes of Health, Bethesda, MD, USA).

Flow cytometry

Description

The flow cytometer is an instrument that allows a quick and automatic analysis of cell populations in suspension, measuring their physical and/or biochemical characteristics (volume, graininess, fluorescence); it allows to quantify and store several parameters at the same time for each cell in the population. The flow cytometer consists of four elements:

1. a fluidic system for transporting the sample into the analysis cell;
2. an excitation system that can consist of one or more light sources;
3. an electronic optical system that collects and processes signals;
4. a computer that, through specific programs, allows the control of the instrument and the analysis of the data by an operator through a graphic representation.

When the cells pass through the laser, a diffraction signal and a refraction/reflection signal are generated. The diffraction signal is picked up by the sensor which collects light in the front scatter channel (also called forward scatter) and provides information on the cellular volume. The refraction/reflection signal is picked up by the sensor that collects the light of the lateral scatter (also called side scatter, at 90 °) and provides information about the graininess inside the cells. For both signals, the intensity of the scatter is proportional to the size and shape of the cells analyzed.

Method

For the experiments, HeLa cells, or REN cells, were seeded in a 25-cm^2 culture flask at $6.0 \cdot 10^4$ cells/cm^2. After 24 h cells were treated with or without CNPs and then detached using trypsin–EDTA and recovered in sterile tubes. After fixation for 15 min in 10% formalin in PBS without Ca and Mg and permeabilization in 0.2% saponin, they were processed for antibody staining and flow cytometry.

For the experiments, it was used a D FACS Lyric (Becton Dickinson) Flow Cytometer was equipped with violet (405 nm, 50 mW), blue (488 nm, 50 mW) and red (642 nm, 50 mW) lasers (Invitrogen, Carlsbad, CA, USA). For each sample, at least 3.0×10^5 events were acquired at a flow rate of 200 µL/mL. Emission from the CNPs was stimulated with the blue laser and the fluorescence was detected using the band pass filter (574/26 nm). For pERM, stained with Alexa647-labeled anti-rabbit secondary antibody (Abcam, Cambridge, UK), we used red laser excitation and the bandpass filter (642/30 nm) for detection.

To measure the total DNA content FxCycle™ Violet staining (Thermo Fisher, USA), was used. It was excited with the 405 nm laser and the signal was detected in the violet channel (bandpass filter of 440/50 nm).

Transmission Electron Microscopy (TEM)

Method

For the analysis, HeLa cells were grown on 35-mm Petri dishes and directly fixed on the substrate by 2% glutaraldehyde (Sigma G5882) in 0.1 M cacodylate buffer (pH 7.3) for 20 min, at room temperature. The fixative was removed, and cells were extensively washed with 0.1 M cacodylate buffer. Cells were exposed to 1% aqueous OsO_4 for 20 min at room temperature for secondary fixation and washed in pure distilled water. Cell monolayers were exposed to 1% uranyl acetate aqueous solution, for 20 min at room temperature, washed with pure distilled water, and dehydrated through a graded series of ethanol (25, 50, 70, 90, 95, and 100%; 5 min each). Infiltration was carried out by placing cell monolayers in Durcupan ACM resin with ethanol as solvent, and then progressively increasing the resin concentration, that is, 25% resin + 75% ethanol, 50% resin + 50% ethanol, and 75% resin + 25% ethanol, for 90 min each, and 100% resin, overnight at room temperature. Monolayers were finally embedded with fresh pure resin, and after 2 h at room temperature moved to 60°C for 48 h. Ultrathin sections (70 nm) were cut with a Leica EM UC7 ultramicrotome (Wetzlar, Germany), placed on 300-mesh copper grids, stained with lead citrate, and washed with pure distilled water. Samples were imaged by an FEI Tecnai Spirit electron microscope, operating at an accelerating voltage of 120 kV, equipped with a Bio-Twin objective lens, a thermionic LaB_6 electron source, a 4k × 4k FEI Eagle CCD Camera, and an EDS Si(Li) EDAX detector.

Scanning Electron Microscopy (SEM)

Description

The Scanning Electron Microscope (SEM) is a morphological characterization technique that allows observation of massive samples with high resolution and considerably higher magnifications than ordinary optical microscopy. The instrument is based on the analysis of the sample using a beam of primary electrons, which can be generated by two main types of sources: traditional electron guns, which exploit the thermionic effect to collect electrons from a heated W filament or a crystal of LaB_6, or field emitters. The instrument used is a TESCAN Mira 3 microscope, which uses a field emission source and operates in a range of potentials between 5 and 25 kV. This type of emitter uses, as cathode, a single crystal of W shaped with a very thin tip. A very high electric field is applied to the material to extract electrons by tunnelling. The cathode is then followed by two anodes which have the purpose of accelerating the particles and preliminarily reducing the size of the beam.

This is followed by a series of six electromagnetic lenses, arranged along the SEM focusing column, which have the purpose of reducing the size of the electron brush and correcting aberrations, mainly astigmatism. A lens system is also used to deflect the electron beam to allow it to be scanned on the sample surface.

The interaction of the electron beam with the atoms making up the sample leads to the generation of different types of signals, of which the most exploited in the SEM analysis are the **secondary** (**SE**) and **backscattered** (**BSE**) electrons. *Secondary electrons* are generated by the collision between the primary electrons and those of the outermost layers of the atoms on the surface of the sample. This signal is therefore made up of low-energy electrons. The SEs are exploited to obtain high-resolution topographic information, as the number of these electrons generated also depends on the morphology of the surface of the solid. The result is an image that shows the surface of the sample as if it were illuminated by light; this allows to have a three-dimensional view of the surface characteristics. The *backscattered electrons* are instead the same electrons of the primary beam that are reflected by the sample as their trajectory is deflected by interaction with the electronic clouds of the atoms of the sample.

Being a signal obtained by elastic scattering, BSEs have higher energy than SEs, but guarantee a lower resolution as they are produced in smaller quantities and from more internal regions of the sample. The analysis of this signal allows to obtain information on the topography of the samples, but, above all, on their chemical composition as the quantity of BSE is directly proportional to the atomic number Z. Consequently, the images obtained in this way are characterized by a contrast linked to the atomic number of the constituent atoms. Specifically, the brightest regions are made up of heavy atoms, since they have a greater number of electrons and larger dimensions, they are more likely to be hit by the primary electrons and cause them to re-emerge from the surface.

Each of the signals generated by the primary beam is analyzed by a different detector. For the SEs, the Everhart-Thornley detector, belonging to the scintillator-photomultiplier type, is used. For BSE, on the other hand, a solid-state detector is used, consisting of a Li-doped Si crystal.

SEM allows us to examine only the surface of the samples. In the case of biological samples, they are prepared in such a way as to preserve the three-dimensional architecture of the vital cell unaltered despite it being completely dehydrated, as required to observe the sample in a vacuum. In general, the samples are fixed, passed through an alcoholic scale with increasing concentration, and, in this way, dehydrated with a process called critical-point drying. Once dehydrated, the sample is coated with 10 angstroms of graphite, which makes it electronically conductive.

Method

Two different fixation procedures have been used for SEM analysis. For ethanol fixation, the adherent cells were extensively washed with PBS and fixed with cold 70% ethanol at 20°C for at least 2 h. For observation, ethanol was removed, and the cells dried in the air before being processed for SEM. To preserve the 3D architecture, cells were dehydrated with hexamethyldisilane (HMDS; Sigma–Aldrich). Adherent cells were extensively washed with PBS and then with 0.05 M cacodylate buffer, pH 7.3. Fixation was performed for 2 h in 2.5% glutaraldehyde (Sigma G5882) in the cacodylate buffer at room temperature. Cells were dehydrated by increasing the concentration of ethanol (from 70 to 100%) for 15 min each. Drying was performed with HMDS, in substitution of the critical point method. After two 15-min incubations in 100% ethanol, ethanol was substituted with a 1:2 solution of HMDS: 100% ethanol and replaced with a 2:1 solution of HMDS: 100% ethanol, and finally 100% HMDS. The duration of these incubations was 20 min. Almost all the HMDS was removed, and only a thin layer of silane was left covering the bottom of the Petri dish that was kept open for 18–24 h to allow complete evaporation of HMDS. All steps including the use of glutaraldehyde or HMDS were performed in a fume hood.

All samples were carbon-coated and observed with a field-emission gun, high-resolution scanning electron microscope (Mira3 XMU; Tescan, Kohoutovice, Czech Republic) equipped with an EDAX EDS microprobe and SE and BSE detectors. The SE signal provided imaging of the cell surface morphology (morphological contrast). The BSE signal, being sensitive to local mean atomic numbers, was able to image the NPs (compositional contrast). The microscope operated at different voltages, depending on the information needed. To visualize the NPs present only on the cell surface, an accelerating voltage of 8–10 kV was used, while 15 kV was used to also visualize NPs inside the cells.

3.2.4 Statistical analysis

Parameters related to the cell cycle profile from the FxCycle Violet measurements were extracted by means of subjugating the cell population (after selecting the singlets) using the FlowJo™ version 10.0.7 software (Becton Dickinson, Ashland, OR, USA). The cell population was divided into three phases, G1, S, and G2+M, and the mean ± SD of the signal related to the DNA content was extracted with the software. As for the intensity of the signal associated with the CNPs, this was distributed asymmetrically. For this reason, to obtain an indicator of centrality, the distributions were fitted using a Landau function, using the data analysis framework ROOT [Bruna R., et al.]. For each curve, the fit provided the most probable value, along with the error of the fit. Values for the treated samples were normalized to those of the control samples.

Confocal and SEM images were processed and analyzed with LAS X and ImageJ/Fiji software. Colocalization analyses were performed using JaCoP, a plugin of ImageJ/Fiji software. Each cell was analyzed separately, for a better approximation of the colocalization. The pERM-CNPs colocalization is expressed using two different coefficients, widely used in the literature: **Pearson's correlation coefficient** (PCC) and **Mander's overlap coefficients** (MOC) [Adler J., et al., 2010]. The PCC is a well-known correlation measure that dates back to the late 1800s. It ranges from +1 (perfect correlation) to 1 (perfect but negative correlation), with 0 representing the lack of a link. It is only recently that it has been used for the detection of fluorophores' colocalization. The MOC can be defined as values ranging from 0 to 1, expressing the fraction of intensity in a channel that is located in pixels where there is above zero (or threshold) intensity in the other color channel [ImageJ]. The MOC is considered to be easier to interpret than the PCC since it only reports positive values. The two coefficients are almost identical and differ only in the use of the absolute intensity, by the MOC, or the deviation from the mean, by the PCC, a small but significant change [Adler J., et al., 2010]. For this reason, for a different and most complete interpretation of the colocalization, it was chosen to use both parameters. Statistical analysis was carried out with GraphPad Prims 7.

3.3 Results

3.3.1 Synthesis and characterization of CNPs

The synthesis of CeO2 nanoparticles was carried out using PAA as a surface-functionalized, in order to make the particles stable in an aqueous solution and avoid agglomeration/aggregation phenomena. The results obtained from the DLS analysis of the size and Z potential are shown in **Table 1**.

N° readings	**D_h (nm)**	**Z Potential (mV)**
1	14.37	-41.7
2	14.93	-40.6
3	15.03	-44.3
Average	**14.8 (±0.4) nm**	**-42 ± (2)**

***Table 1**. DLS and Z potential results for the sample PAA-CNPs*

The data showed that PAA-CNPs have a size close to 15 nm (14.8 on average) and are monodisperse. It was also confirmed that the value of the Z potential was negative, as expected from the presence of the PAA with carboxyl groups deprotonated.

The diffraction pattern of CNPs is shown in **Figure 23**.

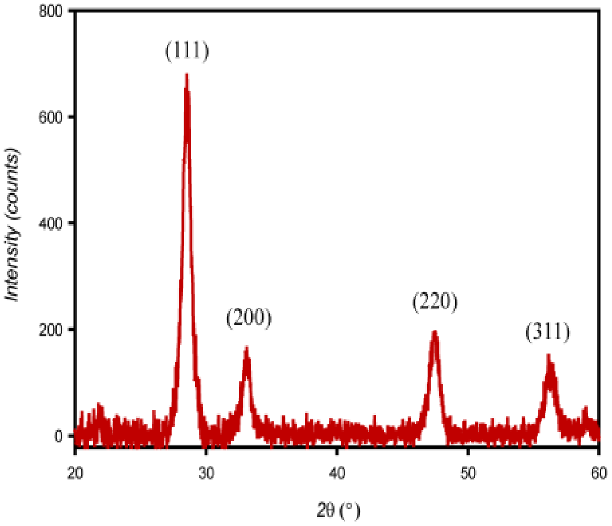

Figure 23. Diffraction pattern of CNPs

The pattern shows the presence of a single-phase attributable to ceria and there are no signs due to nitrogen salts, indicating that these have been eliminated from the sample. Furthermore, the peaks appear considerably widened due to the nanometric dimensions of the crystallites. By applying the Scherrer equation, it is obtained an average diameter of 6.0 (± 0.8) nm.

The dimensions of the particles observed with the DLS technique and with X-ray diffraction, respectively equal to 14.8 (± 0.4) nm and 6.0 (± 0.8) nm, are significantly different from each other. This is due to the fact that the DLS technique detects not only the nanoparticle but also its hydrodynamic surroundings, which also includes the capping polymer and the solvation sphere of the particle.

SEM and TEM Analysis

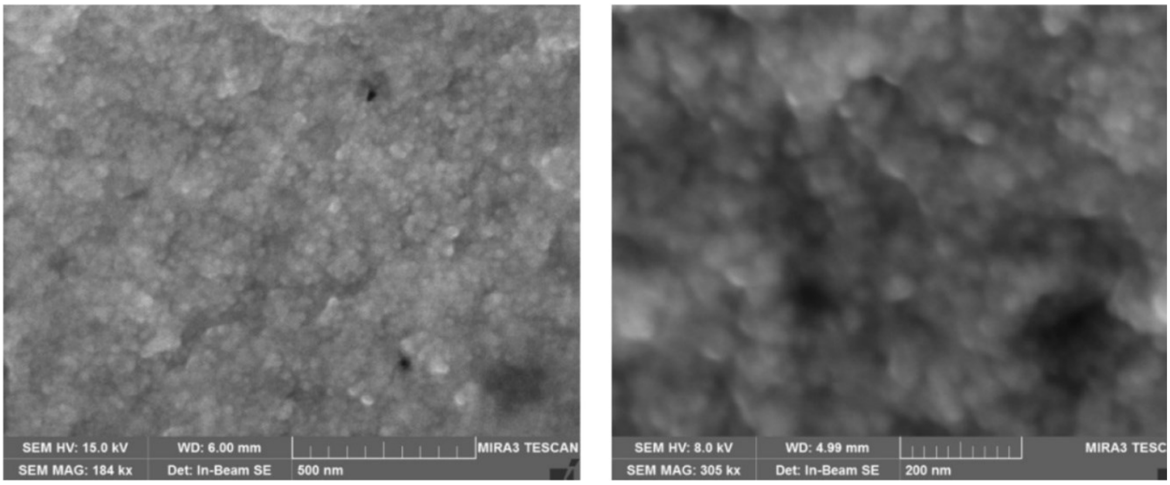

Figure 24. SEM images of CNPs

To determine the morphological and dimensional characteristics of the PAA-CNP, 50 µl of the suspension diluted 1:1000 in dH2O were deposited on a stub covered with conductive double-sided adhesive tape. The sample was observed at SEM. Representative images are shown in **Figure 24.**

Due to the small size, even the high resolution does not allow to completely resolve single NPs. However, it can be observed that they are spherical and homogeneous in size. The image analysis provides an average diameter of 20 (± 3) nm; this value is greater but close enough, to that obtained with the DLS. The observed difference is probably linked to the preparation of the sample, which required the dehydration of the drop placed on the stub, or to the fact that within the spheres observed there are more than one NP enclosed in the same shell formed by the polymer.

A far better resolution was obtained through TEM. As it’s possible to observe from **Figure 25**, TEM together with filtered bidimensional fast Fourier transform (2D-FFT) of several single particles, demonstrated that the CNPs were monocrystalline and confirmed

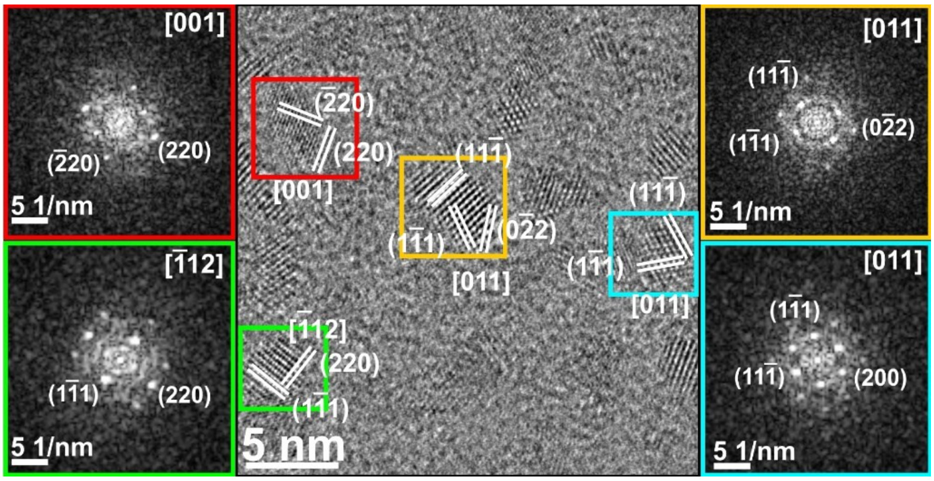

Figure 25. **HR-TEM images of representative CNPs**. *The central image shows four single CNPs that are indicated by the red, yellow, azure, and green boxes. Only the main lattice planes are indicated here. The crystallographic structure is confirmed by the 2D-FFT diffractograms showing the full structural characterization (left and right with corresponding colors).*

.

the fluoritic CeO_2 crystal structure. TEM images showed neither evidence of internal defects nor of significant agglomeration and estimated the mean particle size to be 2.9 ± 0.9 nm (80%, 2−4 nm; 20%, 4−6 nm).

Quantification of CNPs

The ICP-OES analysis was carried out to determine the actual amount of CeO2 NPs present within the CNPs suspensions obtained with the syntheses described above. Starting from the quantities used for the synthesis, it is possible to establish the theoretical concentration of the NPs:

$$mol\ Ce(NO_3)_3 \bullet 6H_2O = \frac{g\ (weight\ of\ product)}{PM} = \frac{1.0899\ g}{434.23\,\frac{g}{mol}} = 2.5100 \cdot 10^{-3}\ mol$$

$$mol\ Ce(NO_3)_3 = mol\ Ce^{n+} = mol\ CeO_2$$

$$\left(\frac{g}{L}\right)[CeO_2] = \frac{moli\ CeO_2}{V_{Tot}} \cdot PM_{CeO_2} = \frac{2.5100\ \cdot 10^{-3}\ mol}{0.06865\ L} \cdot 172.115\frac{g}{mol} = 6.2888\frac{g}{L}$$

The concentration of the ions Ce^{n+} was obtained through ICP_MS. Considering that during the preparation, the sample was diluted 10 times, the concentration obtained was (**Table 2**):

[CeO₂] theoretical (g/l)	[CeO₂] experimental (g/l)	Yield (%)
6-2888	6.5104	103.52 %

***Table 2.** The concentration of Ce^{n+} as obtained through ICP-MS and comparison with the theoretical concentration*

According to this result, the synthesis for PAA-CNP produced a concentration of CNPs of 6,5 mg/ml, with a quantitative yield.

3.3.2 Toxicity of CNPs

The toxicity limits of CNPs concerning the HeLa cell line were determined using the MTT cytotoxicity/ cytostatic test, based on mitochondrial functionality. As it's possible to observe in **Figure 26, A**, after 24 hours of treatment there is no evident sign of toxicity, with just the highest concentration of CNPs, equal to 500 µg / mL, showing toxicity of 13%. In particular, for lower concentrations (100 or 200 µg / mL) the viability of the cells partially increased (104,4% for 100 µg/ml and 103,4 for 200 µg/mL). This result is in accordance with literature data [Ribeiro F.M., at al., 2020], [Hosseini A., et al., 2013], [Zholobak N.M, et al., 2011] and it can be explained with the fact that CNPs can alter the cellular metabolism by reducing the ROS levels, thus creating better conditions for the cell.

Although the highest concentration (500 µg / mL) didn't show high toxicity, it was chosen the intermediate concentrations of 200 µg / mL and for this concentration, the viability was tested at different incubation times (**Figure 26, B**). Even in these cases, the nanoparticles didn't show signs of toxicity, with levels of viability superiors of 95% for all the incubation times tested. For this reason, 200 µg / mL was the concentration used for all the subsequent analyses

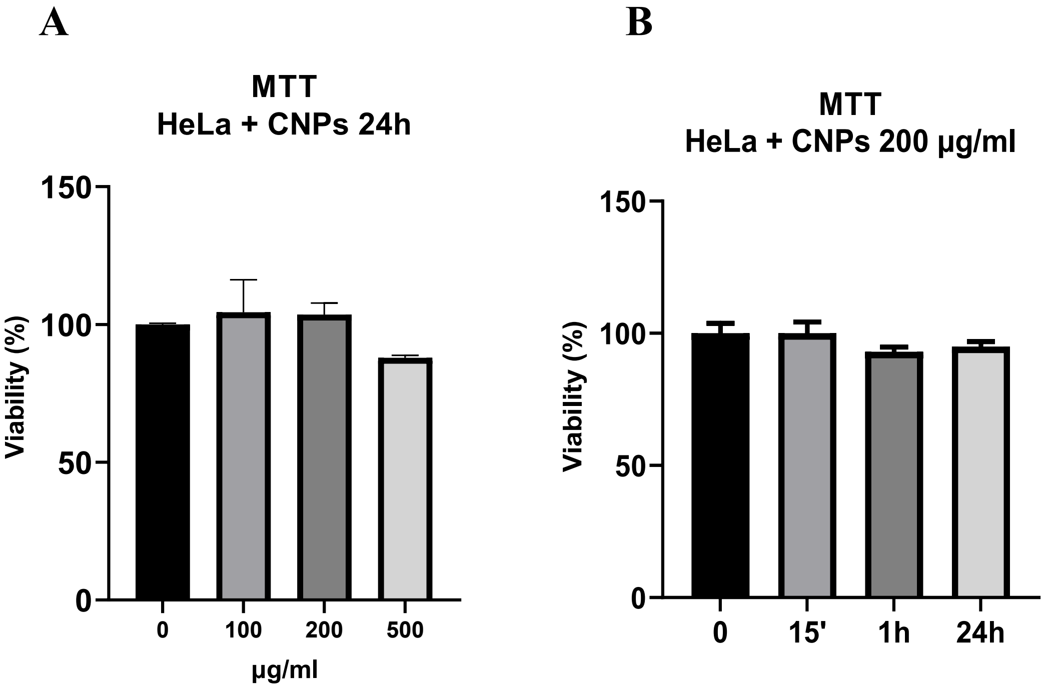

Figure 26. Effect of CNPs on the viability of HeLa cells. *Effect of different concentrations of CNPs (100, 200, or 500 µg/ml) after 24 h of incubation (A). Effect of different incubation times of CNPs 200 µg/ml on the viability of HeLa cells (B). Average from three independent experiments ± SD, versus the respective CTRL column.*

3.3.3 CNPs interaction with HeLa cells

To study the interaction of the nanoparticles with human cells, it was first evaluated the adhesion and intracellular distribution in HeLa cells. In particular, three different techniques of analysis were used: TEM, SEM, and Confocal microscopy.

TEM analysis

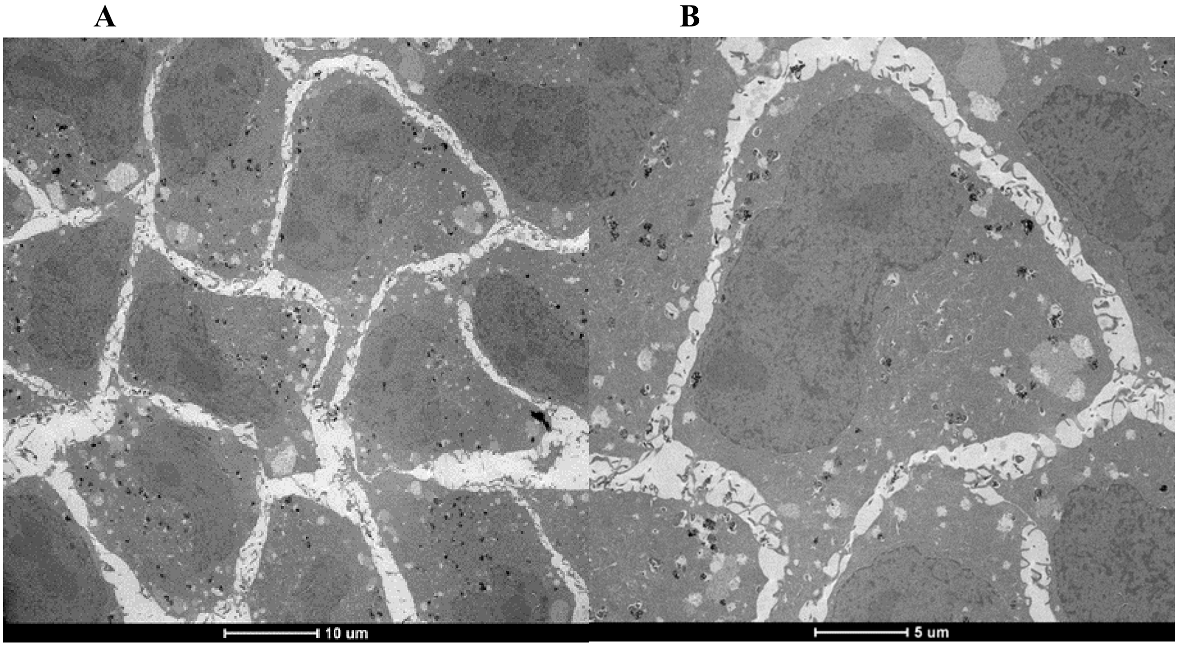

Figure 27. *Accumulation of CNPs electron-dense aggregates mostly present inside the endosomal–lysosomal vesicles of HeLa cells after 24h of incubation, observed by TEM. (B) enlargement of A.*

The representative images in **Figure 27** show the accumulation of CNPs of HeLa cells after 24 hours of incubation.

It is possible to observe that the CNPs are mostly accumulated in two regions: on the cell surface and inside endolysosomal structures. These results confirm previous observations from our group [Ferraro D., et al., 2017]. In particular, in that study, it was possible to

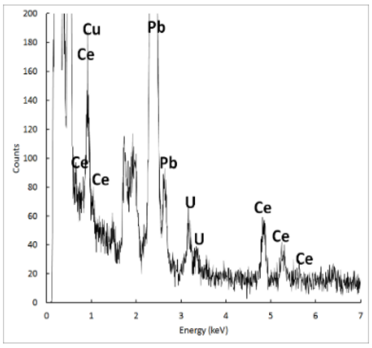

***Figure 28. Representative TEM-EDS analysis** of the CNPs aggregates inside HeLa cells after 24-hour incubation.*

identify the vesicles in which nanoparticles are accumulated after 24 hours of incubation as Lamp1 positive (lysosomal associated membrane protein 1).

The presence of CNPs in association with cells was confirmed by EDS analysis*,* in which the signals of Ce derived from the nanoparticles are evident (**Figure 28**). In the EDS spectrum, the signal of Pb and U were likely to derived from Lead Citrate and Uranyl Acetate, (*i.e.,* the staining agents).

SEM analysis

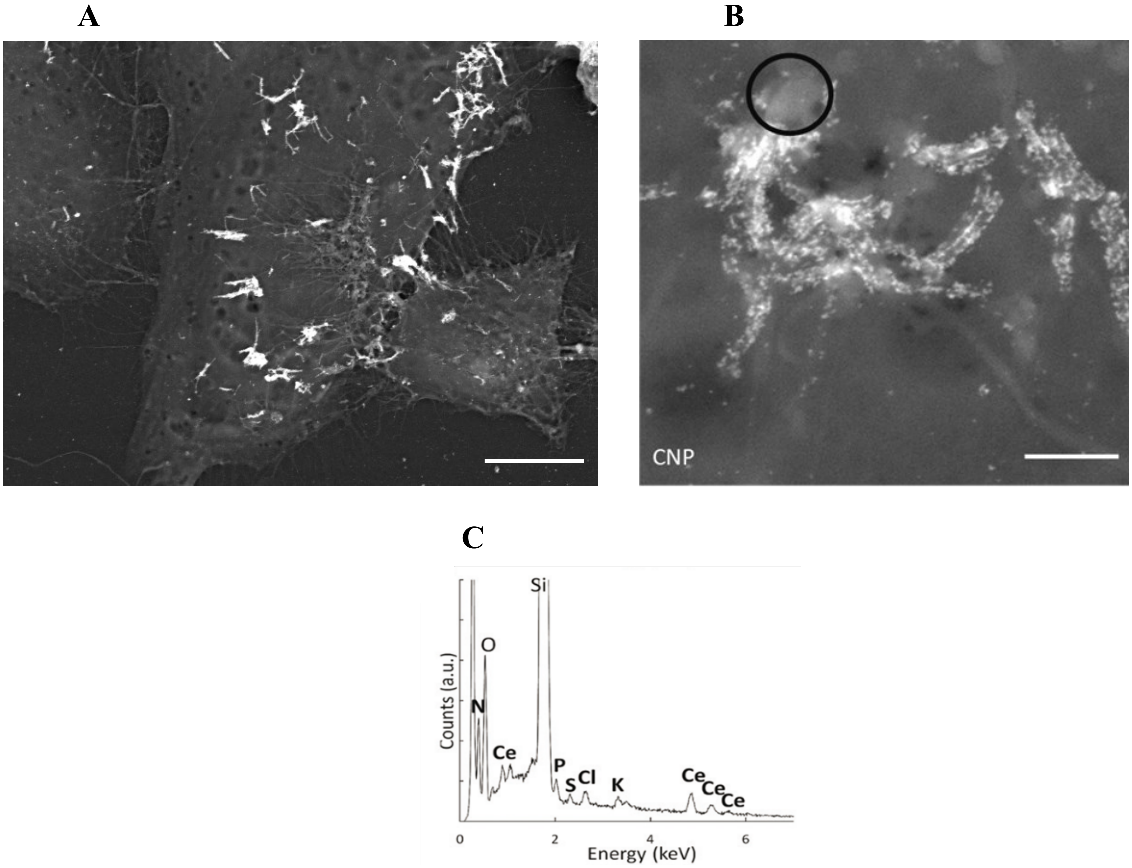

***Figure 29**. **(A-B) SEM-BSE analysis of HeLa cells incubated with CNPs for 24 h.** Due to the compositional contrast provided by the SEM-BSE imaging, CNPs were revealed as bright spots on a darker background, making the CNP-decorated cell protrusions visible (a single cell is shown in (A) and (B)). The use of an SEM accelerating voltage (8−10 kV) allowed visualization of only NPs on or just underneath the cell surface. However, only the superficial CNPs could be imaged at the maximum resolution; CNPs present in structures underneath the cell membrane looked blurred, as in the circled area in (B). Bar equal to 10 µm in (A) and 1 µm in (B). (C) Representative SEM-EDS analysis of the CNPs present on the cells. Signals other than Ce are due to the cell components or the glass support.*

A more complete characterization of CNPs distribution on the cell surface was achieved using SEM. This approach avoided ultrathin sectioning of the entire cell, as required by TEM, to obtain whole-cell images of CNPs distribution. Alcohol-fixed samples were imaged by SEM, using both secondary electron (SE) and backscattered electron (BSE) detectors (**Figure 29, A-B**). The BSE imaging provided effective visualization of CNPs distribution, due to the significant difference in mean atomic number between the NPs and cellular structures. In particular, is possible to observe the nanoparticles as a brighter spot on a darker background, which, in this case, represent the planar membrane of the cell. However, with the accelerating voltage (8-10 kV) is also possible to spot the NPs just underneath the cell surface, which appears as a blurred area, like in the black circle in **Figure 29, B**. Exactly like in the case of TEM analysis, SEM-EDS analysis confirmed that the brighter spots visible in the pictures are Ce atoms (**Figure 29, C**). The spectrum also highlighted the presence of other inorganic components, such as Cl, P, K, O, N, derived from the biological component of the sample. On the contrary, the presence of Si derives from the support on which the cells were adherent.

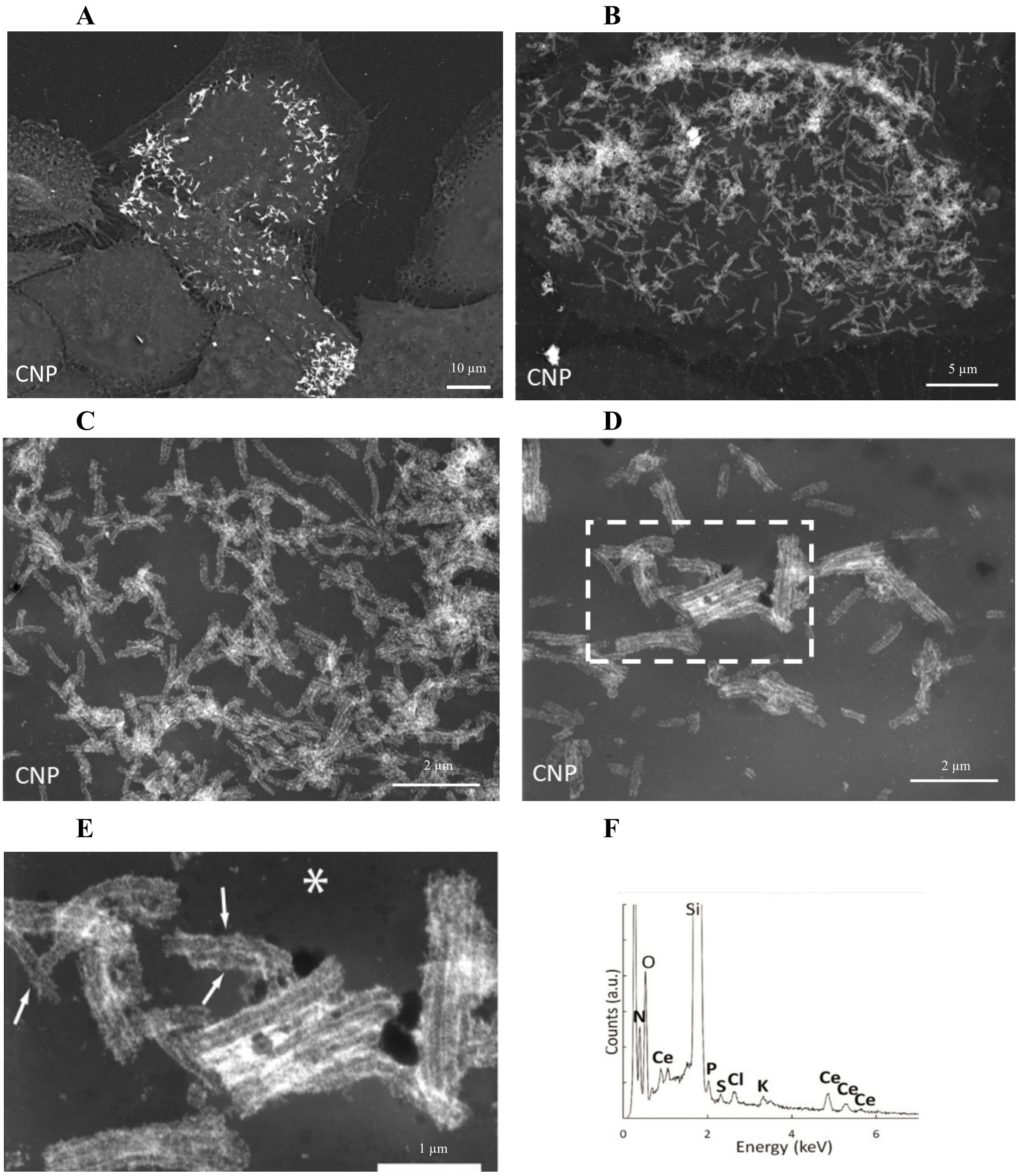

Figure 30. *(**A-E**) SEM-BSE analysis of HeLa cells incubated with CNPs for 24 h in different enlargements. Due to the compositional contrast provided by the SEM-BSE imaging, CNPs were revealed as bright spots on a darker background, making the CNP-decorated cell protrusions visible (a single cell is shown in (B), (C) and (D)). (A) visible in a small enlargement that, while some cells are heavily decorated with particles, in others, CNPs seem to be completely absent. Specificity of CNPs toward the microvilli was better appreciated at higher magnification, (D, E) where CNPs outlining the microvilli contours (arrows) became visible, while the rest of the membrane remained dark (*). (E) Enlargement of the area outlined in (D). (F) Representative SEM-EDS analysis of the CNPs present on the cells. Signals other than Ce are due to the cell components and are fixative.*

To further characterize the adhesion and internalization of CNPs on HeLa cells, further SEM images were obtained for a short incubation time, of about 5-15 minutes (**Figure 30**).

This analysis confirmed that no CNPs were present on the planar membrane of the whole cells, as CNPs were exclusively attached to structures that resembled cell protrusions (**Figure 30, B-E**). The shape, dimensions, and localization of these CNP-decorated protrusions resembled those of cell microvilli. Another interesting consideration is that the CNPs do not interact with all the cells in the same way. As it is possible to observe in **Figure 30, A**, there could be cells with their protrusions entirely covered with NPs, while others next to them show no NPs on their surface.

When these CNPs-covered protrusions were measured, the results showed that they have an average length of 1,067 ± 0,3 µm and an average diameter of 71 ± 1 nm (**Figure 31, A-B**). These values are in accordance with the length and diameter of microvilli reported in the literature [Fisher H.W., et al., 1967] [Lundgren E., et al., 1976].

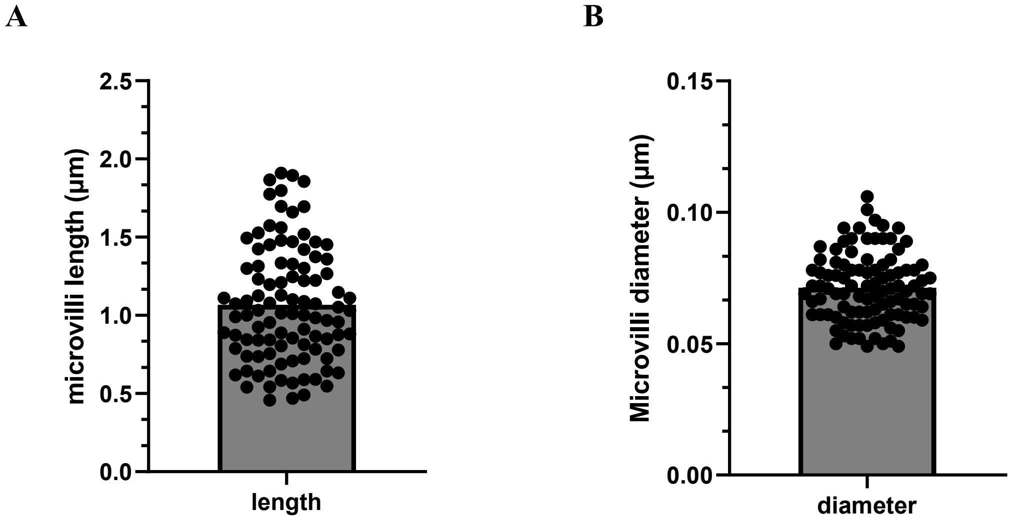

***Figure 31**. (A), microvilli length calculated from SEM pictures (as in **Figure 30**). (B) microvilli diameter, calculated from SEM images (as in **Figure 30**). At least four different pictures were analyzed, a total of 100 microvilli were considered. The diameter of each microvillus was calculated excluding the borders (≈ 10 nm for each side) as the signal is derived from the CNPs attached. Microvilli's length and diameter were calculated using ImageJ software.*

The same CNPs – covered structures were also evident when analyzed by SEM following a type of fixation that better preserve the 3-D morphology of the cell membrane. This type of analysis helped, even more, to confirm that the CNPs (indicated by the brighter areas in the picture) indeed adhered to the microvilli present on the thicker part of the cell body. The analysis of these types of samples also showed that compare to microvilli the cell processes contacting the substrate were not decorated with the CNPs (**Figure 32, A**).

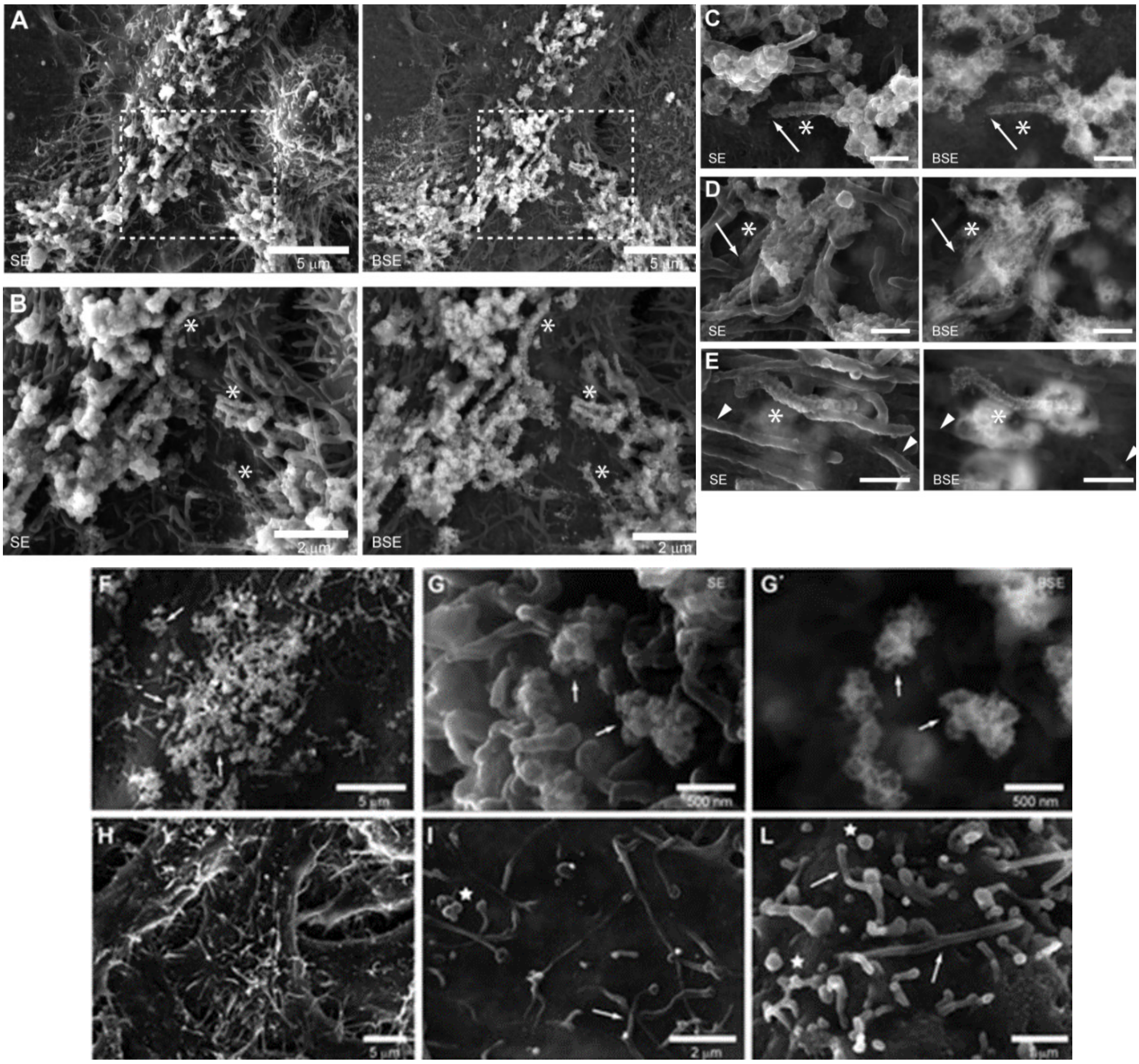

Figure 32. *(A−E) SEM-SE and BSE images of CNPs distribution in cells with preserved 3D morphology. The areas decorated by microvilli appeared brighter on both SE and BSE images. SE images showed the overall morphology better, while BSE showed only the areas where the CNPs were present. (A) Cells treated with CNPs for 24 h. CNP-decorated microvilli are mostly concentrated on top of the cell. (B) Enlargement of the area outlined in (A). Microvilli were heavily decorated with CNPs (asterisk) but almost no CNPs were visible on the underlying planar membrane. (C, D) Examples of microvilli are covered by CNPs along their entire length (asterisk). The complete absence of CNPs at the base of the decorated microvillus (arrows) showed high specificity for the microvillar membrane. Bar = 500 nm. (E) Detail of a microvillus decorated with CNPs (asterisk) next to nondecorated microvilli (arrowheads). Bar = 500 nm. For each couple of images reported: left, SE image; right, BSE image. (F−L) CNPs interacted with spherical membrane extrusions (buds), which together with microvilli, were not induced by CNPs. (F) HeLa cells were incubated with CNPs for 24 h. CNPs decorated the small bud-like structures (arrow) with high specificity, as for microvilli. (G, G') A region rich in bud-like structures (arrow) covered with CNPs. CNPs interacted poorly with the surrounding planar membrane. (H, I) Control HeLa cells showed evident protrusions. Microvilli (arrow) and small bud-like structures (star) were less (I) or more (L) densely distributed. (G, H−L) SE image. (F, G') BSE image.*

Higher magnifications showed the specificity of the adhesion as CNPs covered the entire length of the microvilli (**Figure 32, B–E, asterisk**) while leaving the rest of the cell membrane completely devoid of particles. A clear line of demarcation is, in fact, visible at the base of the microvilli where CNPs abruptly stopped adhering (**Figure 32, C, arrows**).

With this type of sample, it was possible to observe that CNPs also adhere to some spherical protrusions (**Figure 32, C, F, G**). These "buds" are however present also in the case of control cells (**Figure 32, H−L**), to suggest they were not artifacts induced by the NPs presence. The literature confirms that they indeed represent a different stage of full-grown microvilli, either developing microvilli budding from the membrane or the result of shrinking microvilli [Gorelik, J., et al., 2003]. Moreover, the measurement of the buds performed on these samples showed that their diameter was identical to that of microvilli, suggesting that they could be buds of undeveloped or growing microvilli. In general, the specificity of CNPs toward these structures was high (**Figure 32, G-G').**

Confocal microscopy

The results obtained so far suggested a strong dependence of CNPs adhesion to microvilli of HeLa cells as the first step for cellular internalization. To better understand this specific interaction, cells were incubated with fluorescent CNPs and analyzed by confocal microscopy. For this purpose, it was chosen the ezrin/radixin/moesin protein complex (**ERM**) as a specific marker for microvilli, so as to investigate how the CNPs adhesion correlates with the microvilli marker. In the specific, it had been chosen the antibody directed against the phosphorylated form of the complex (**pERM**).

As described by A. Hanono et al., [Hanono A., et al., 2006], the ERM protein complex is specific to microvilli, having the function of acting as a bridge between the plasma membrane and the actin of the microvillus itself. The ERM complex can exist in two forms, one inactive and one active. The inactive form is non-phosphorylated and it is found in a folded conformation, while the active (and phosphorylated) form has an open conformation in which the complex binds actin and the plasma membrane.

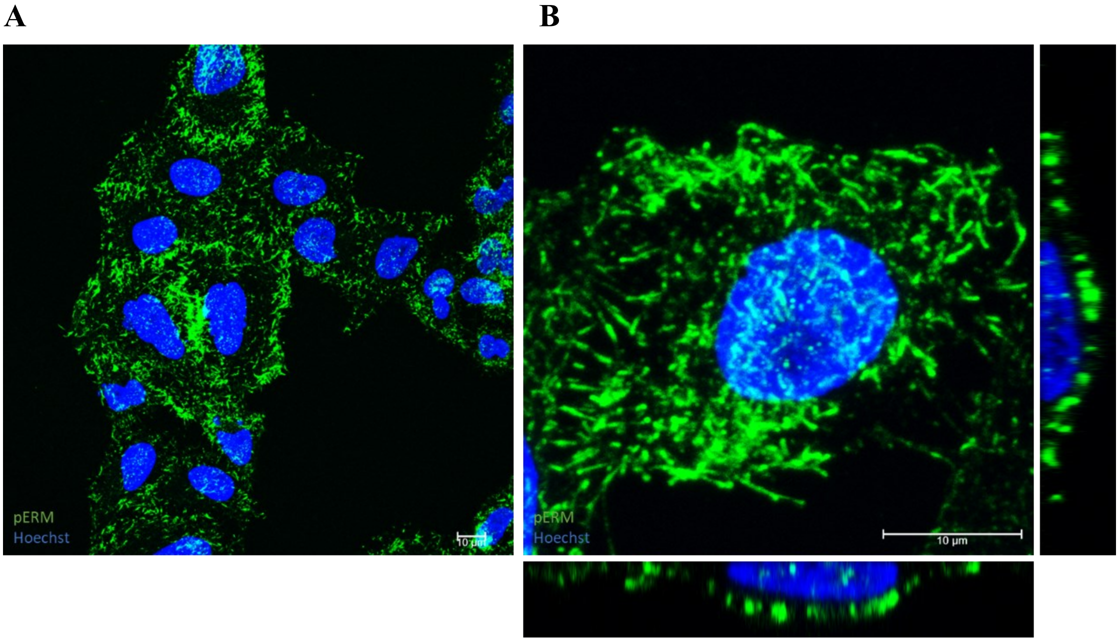

Figure 33. *(A, B) IF staining with pERM antibody (green) showed the presence of microvilli on the surface of HeLa cells. (B) Enlargement of a single cell and its relative cross-sections, showing the distribution of microvilli on the surface of the cell. Blue, nuclei, Green, pERM. Both pictures are maximum projections of 20 confocal planes. Each plane measures 0,35 µm.*

.

First, control HeLa cells were examined to verify the specificity of the antibody for the microvillar structures. As can be seen in **Figure 33, A**, pERM is clearly localized on microvilli distributed on the cell surface. This showed some variability in the density of the microvilli within different cells. It is possible, in fact, to notice how groups of cells are very intensely colored while others show less evident positivity.

To visualize the CNPs by confocal microscopy, NPs were made fluorescent thanks to the presence of the fluorophore DiI inserted in the outer layer of PAA formed during the synthesis (**FCNPs**). From the analysis of the mutual distribution of pERM and FCNPs, it was considered only the cell surface (**Figure 34**). In **Figures 34 G-I**, it is possible to notice how the FCNPS signal in a very similar to the distribution of the pERM signal, which appears "spaghetti-like". This observation confirms 1) that the antibody directed against the pERM phosphorylated complex that was chosen is a specific marker of microvilli, 2) that FCNPs distribute on microvilli and 3) that the CNPS-microvilli interaction, originally observed in SEM, is also clearly visible by immunofluorescence.

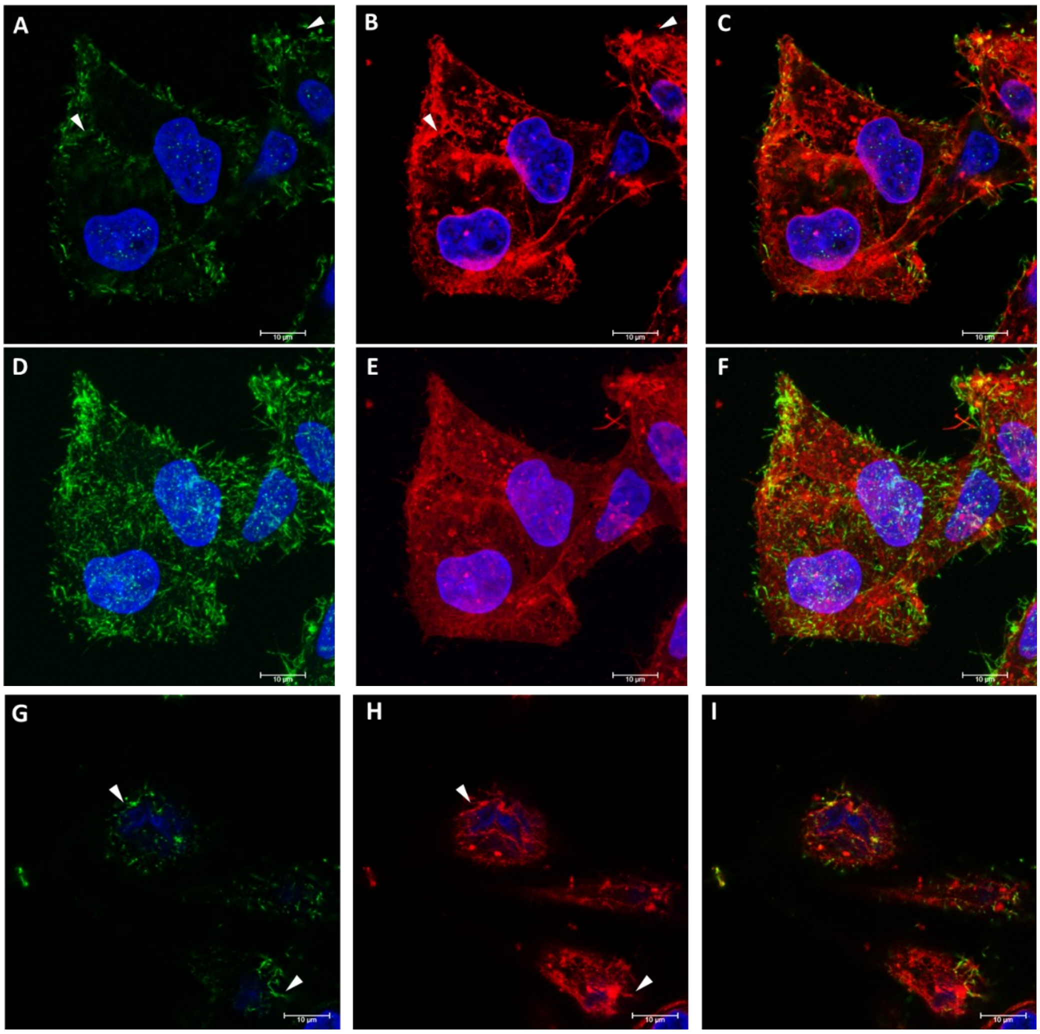

Figure 34. *FCNPs and pERM reciprocal distribution is shown by IF. (**A, D, G**) distribution of pERM (green), a component of microvilli membranes, on HeLa cells. (**B, E, H**) FCNPs (red) were present on the cell surface in a spaghetti-like distribution, or inside vesicles. (**C, F, I**) Merge images in which areas of colocalization FCNP-pERM are visible in yellow (some are indicated by arrowheads). Pictures A-C and G-H are single confocal planes; pictures D-E are maximum projections of 20 confocal planes. Each plane measures 0,35 µm.*

3.3.4 CNPs-Microvilli interaction

CNPs-pERM colocalization

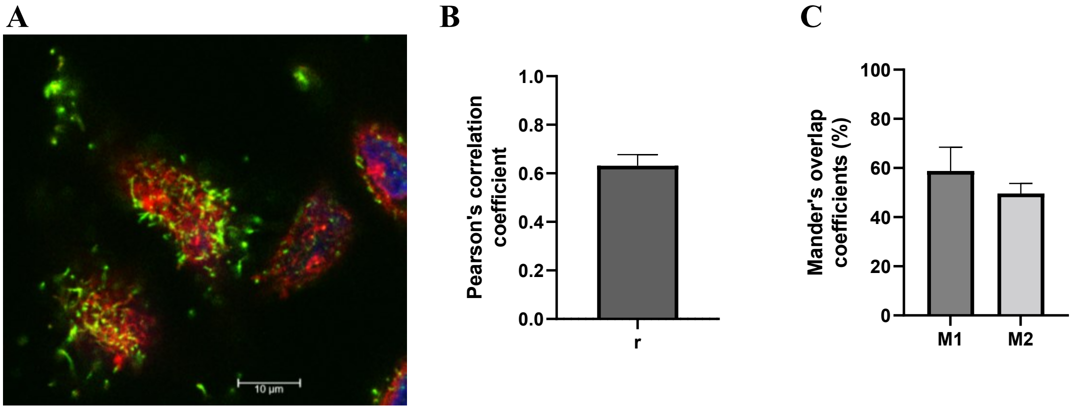

Figure 35. Co-localization analysis of FCNPs and pERM. (A) *Representative confocal image of HeLa cells incubated with FCNPs for 15 minutes. The image is a single confocal plane, specifically the upper part of the cell body, where just microvilli (indicated by pERM, green) and adherent FCNPs (red) were present. (B) PCC from pERM-FCNPs colocalization. (C) MOC (%) indicating the percentage of pERM colocalizing with FCNPs (M_1) and the percentage of FCNPs colocalizing with pERM (M_2). Data were analyzed using ImageJ software. Colocalization was calculated through the JACoP plugin. For the analysis at least 3 different images were considered. Just upper stacks were analyzed. Data are expressed as average ± SD.*

To better prove that there is a relationship between the pERM and FCNPs signals, the level of colocalization was analyzed. To do so, some factors had to be considered:

1. HeLa cells were incubated with FCNPs for short incubation times (of maximum 15 minutes) to avoid the signal derived from the internalized NPs.
2. For the calculation of the colocalization, only the uppermost portion of the cells was considered, since richer in microvilli.

Results are shown in **Figure 35**. **Figure 35, A** shows a representative image of HeLa cells incubated with FCNPs considered for the colocalization analysis. In this case, the results indicate a positive correlation between the two fluorophores, with a **Pearson's correlation coefficient** (**PCC**) equal to 0,631 ± 0,04. This level of colocalization was confirmed by **Mander's overlap coefficients** (**MOC**), with almost 60% (59% ± 9) of pERM colocalizing with CNPs (M_1) and, on the contrary, 50% (49,6% ± 4) of CNPs correlating with pERM (M_2).

Effect of different CNPs incubation times and concentrations

To better characterize the interaction seen so far, different analyses were performed in order to see if the adhesion of PAA-CNPs was influenced by: **incubation time**, **concentration**, **incubation medium,** or **temperature**.

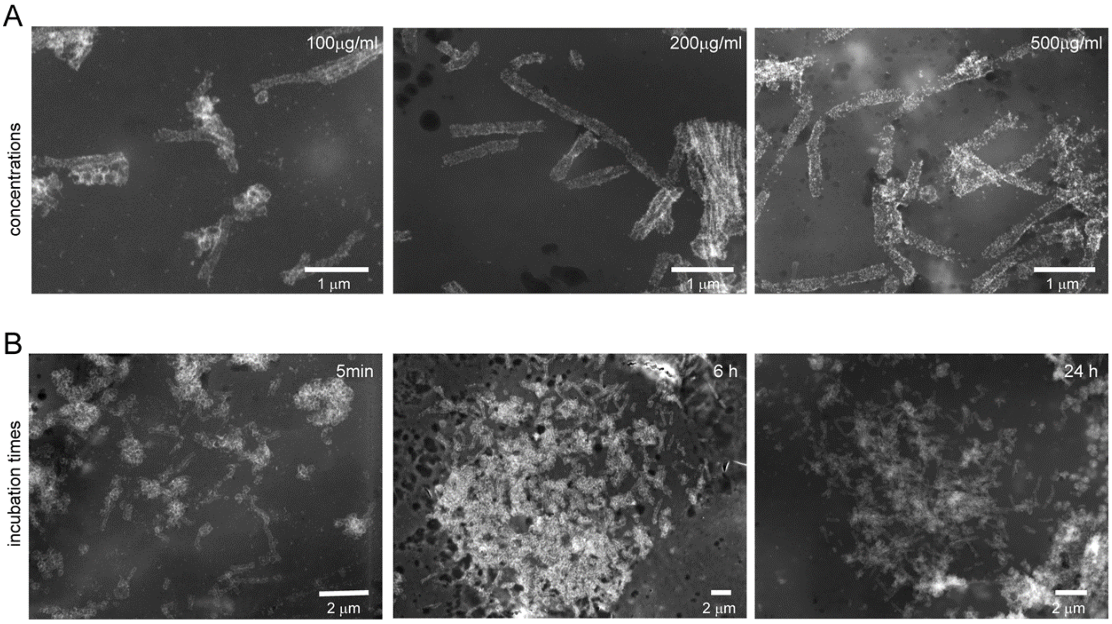

Figure 36. *CNPs adhesion for different concentrations (A) and incubation times (B). Regardless of the concentration used (100, 200, and 500 mg/mL) and the length of incubation (5 min, 6 h, and 24 h), CNPs showed specific adhesion on microvilli. SEM BSE images.*

As for the incubation time and the concentration, HR-SEM analysis showed that adhesion is a process that occurs very fast. Similarly to 24 hours of incubation, already after five minutes of incubation, it is possible to observe microvilli decorated with CNPs (**Figure 36-B**). Additionally, the interaction was not dependent on the concentration of the nanoparticles, since, ranging from 100 to 500 µg/ml, the adhesion does not seem to change (**Figure 36-A**).

Role of protein corona and the effect of incubation medium

Proteins present in the cell medium could interact with nanoparticles, forming a soft and hard protein corona [Ke P.C., et al., 2017], that can alter the main chemical characteristics of the nanoparticles, influencing the interaction with the cells. To understand whether the adhesion of the CNPs was mediated by the formation of protein corona on the nanoparticles, a simpler medium than the standard DMEM plus FBS was chosen, Hanks' balanced salt solution (HBSS). HBSS can be considered as a control to test the chemical interactions of the nanoparticles in absence of a potential protein corona formation. It was first measured the DLS and Z-potential values for just the CNPs dispersed in HBSS compared to DMEM plus FBS.

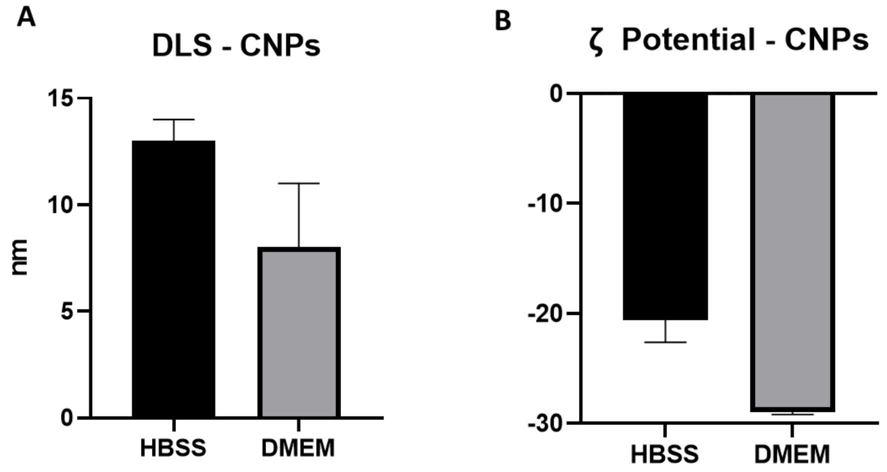

Figure 37. *(A) DLS analysis of CNPs in HBSS (medium without FBS) and DMEM (common cellular medium supplemented with FBS). (B) Z potential analysis of CNPs in HBSS or DMEM.*

The change in culture medium produced only a slight modification in the hydrodynamic dimension of the CNP (DLS: 8 ± 3 nm in DMEM; 13 ± 1 nm in HBSS. ζ potential: −20.6 ± 2 in DMM; −29 ± 0.2 in HBSS (**Figure 37**). This indicates that the medium in which the nanoparticles are dissolved does not influence the chemical properties of the nanoparticles and, therefore, the interaction with the cells.

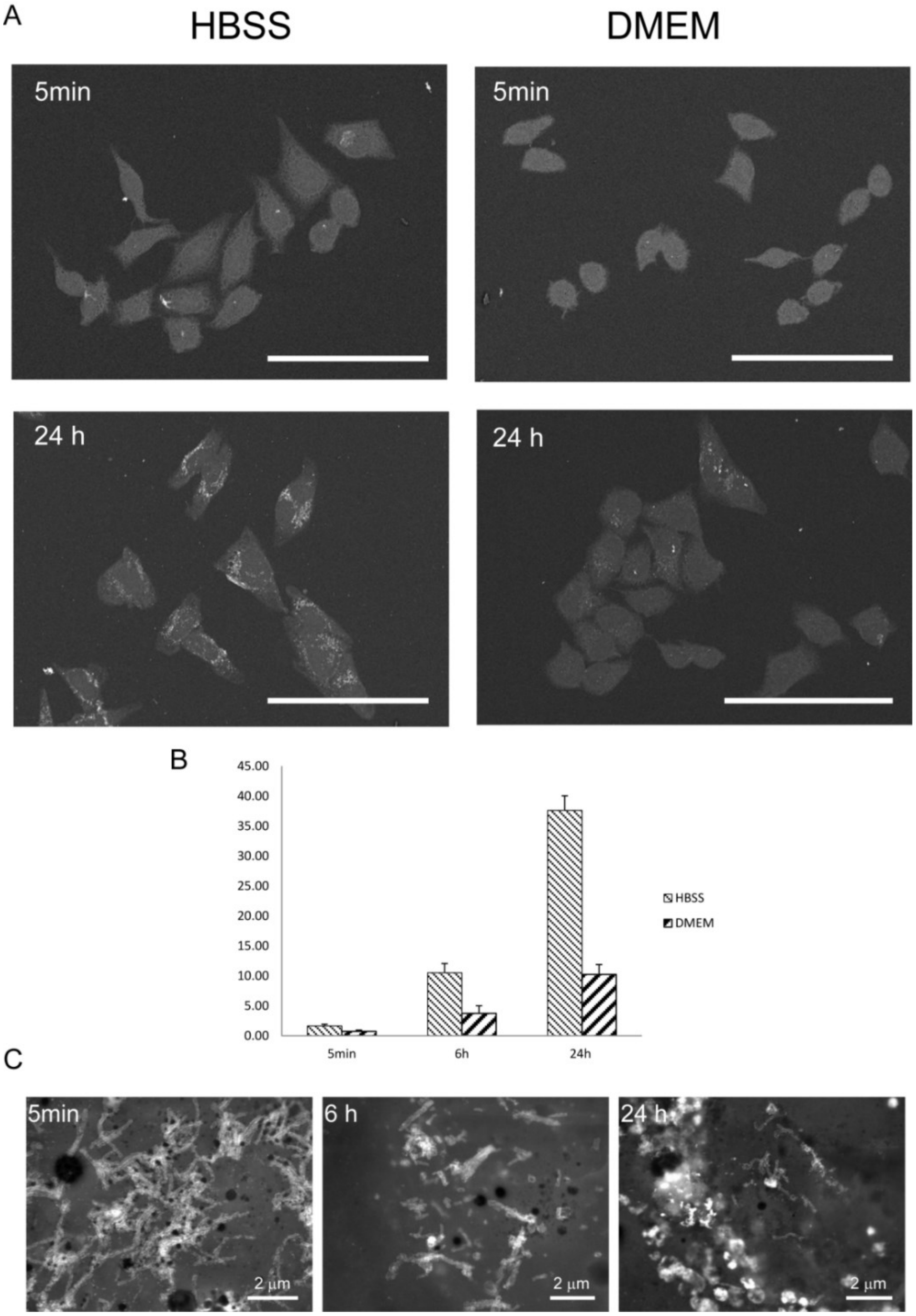

Figure 38. *CNPs adhesion was not mediated by proteins/components present in the culture medium. (A) Incubation of CNPs in the HBSS medium did not reduce cell adhesion compared to DMEM with FBS. SEM-BSE images. Bar = 50 µm. Images were acquired using an accelerating voltage of 15 kV with a BSE detector. Under these conditions, both the CNPs on the cell surface (brighter signal) and those already internalized (lower signal) could be observed. (B) After 5 minutes, 6 hours, and 24 hours, more CNPs interacted with cells when in HBSS than in DMEM. CNPs quantification was obtained thresholding the images in order to include both signals. (C) CNPs distribution, when incubated with HBSS for different times. The interaction was similar to that observed with DMEM. The image showing CNPs distribution after 5 minutes of incubation does not represent the average level of adhesion, but it was chosen to show the specificity of the interaction in the case of a cell particularly rich in microvilli. SEM-BSE images.*

The effect of different media was then tested on the cells by HR-SEM to evaluate whether HBSS influenced the CNP adhesion. In particular, the CNP interaction in HBSS was tested after 5 minutes, 6, and 24 hours of incubation and compared with DMEM (**Figure 38, A-C**). Decorated microvilli could still be detected in the presence of HBSS (without FBS), showing that protein corona was not fundamental for the adhesion of CNPs. The amount of CNPs with HBSS was even higher than with the regular culture medium (**Figure 38, B**). This could be explained by the increase in microvillus density as a consequence of starvation [Liu L., et al., 2019].

Effect of the temperature

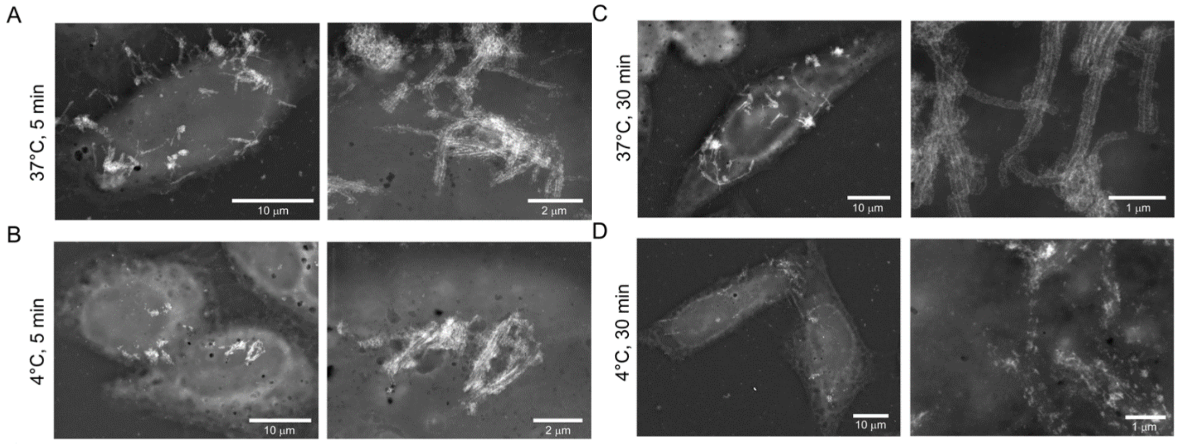

Figure 39. *(A-D) CNPs adhesion was not blocked at low temperatures. After cells were kept for 30 minutes at 4°C, CNPs were added to the medium and left for 5 (B) or 30 (D) minutes at 4°C.*

The adhesion of CNPs to microvilli was also analyzed at low temperatures (4°C) when passive diffusion could not take place and the endocytic mechanisms were inhibited. Compared to the normal incubation temperature of 37°C, CNPs added to the cells preconditioned at 4 °C for 30 minutes were still able to interact with microvilli during the subsequent 5- or 30-minutes incubation, as shown by SEM images (**Figure 39, A-D**). Although the specificity was clearly visible, a less uniform layer of NPs was observed at 4

°C than at 37°C. The patchy distribution of the CNPs could be explained considering that the lipid raft components could form larger clusters below at low temperature than at 37 °C.

3.3.5 Modification of microvilli membrane components

Given the specificity of the CNPs toward microvilli, it was considered to investigate the nature of this interaction to possibly identify the biological component mediating the NPs adhesion. For this purpose, specific inhibitors have been used to alter the microvilli structure [Poole K., et al., 2004] and then evaluate whether such modification affects the CNPs adhesion to the cell. The cells were in fact treated with substances capable of inhibiting some components of the microvilli membrane or their structure such as:

- **sphingomyelin**, typical of the microvilli membrane, especially when organized in clusters;
- **cholesterol**, a component of lipid rafts, characteristic of microvilli:
- and **F-actin**, the cytoskeletal structure of microvilli [Charras G.T., et al., 2006].

A specific agent was used for each of the above-mentioned targets:

- the synthesis of membrane lipids such as sphingomyelin was inhibited by using **myriocin**. Myriocin acts by inhibiting serine-palmitoyl transferase, an enzyme involved in the first step in the synthesis of sphingosine;
- methyl-β-cyclodextrin (**MβCD**) was used to extract cholesterol from membranes;
- the recruitment of F-actin was inhibited by using Cytochalasin-D (**Cyt-D**). Cytochalasin promotes the depolymerization of F-actin by blocking the

growing end of the actin filaments themselves, which in the case of microvilli, constitutes their internal skeleton.

The cells thus treated and subsequently incubated with FCNPs were analyzed by flow cytometry, to obtain a quantification of the pERM and FCNPs signals. Cell morphology, as well as the distribution of pERM and the degree of adhesion of CNPs, were evaluated in parallel by immunofluorescence and electron microscopy.

Effect of reduced levels of cholesterol and/or sphingolipids

Flow cytometry analysis

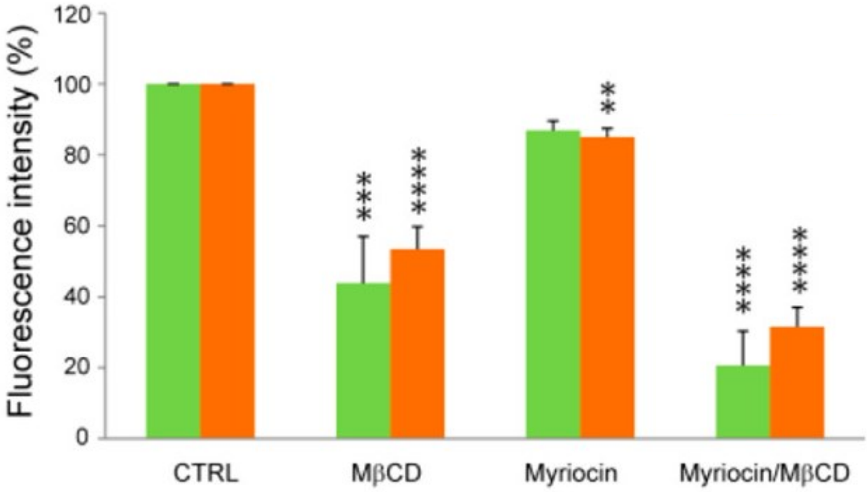

Figure 40. *Microvilli and lipid rafts are fundamental for NP−cell interaction: effect of lipid raft alteration on CNPs adhesion to microvilli. Flow cytometry measurement of cells with reduced cholesterol level (MβCD), phospholipids (Myriocin), or both (myriocin/MβCD). Data are expressed as an average from three independent experiments ± SD. **, $p < 0.01$; ***, $p < 0.001$; ****, $p < 0.0001$ versus the respective control. Green, pERM; Orange, FCNPs.*

To modify the composition of the microvilli membrane, the cells were treated with myriocin, MβCD, or a combination of the two substances. The cells were then incubated with FCNPs for 10 minutes at 37 °C. The short incubation time of 10 minutes was specifically chosen to be able to focus only on the FCNP adhesion processes, eliminating the component due to internalization, which would require longer incubation times.

Following the treatments, the signal relative to both pERM and FCNPs was analyzed by flow cytometry to verify the effectiveness of the treatments on microvilli and, as a consequence, on the CNP adhesion.

As can be seen from **Figure 40**, the signal relative to pERM is influenced differently depending on the treatment that was used. In the case of the inhibition of sphingomyelin synthesis, induced by myriocin, it was possible to observe a minimal decrease in the pERM signal compared to the untreated cells. Instead, when cholesterol was extracted from the membranes by MβCD, a drastic reduction of this signal was observed. Finally, the blocking of sphingomyelin synthesis and the simultaneous extraction of cholesterol from the cell membrane leads to an even further reduction of the pERM signal. The reduction in the pERM levels indicates that the treatment aimed at modifying the membrane components of the microvilli has actually led to an alteration of the cell protrusions.

Similarly, samples treated with myriocin and/or MβCD were then analyzed considering the FCNPs signal (**Figure 40**). As for pERM, the inhibition of the synthesis of sphingomyelin alone induced a minimal reduction in the FCNPs signal, compared to the untreated cell. Instead, when the reduction in sphingomyelin and cholesterol was simultaneous, the FCNPs signal was greatly reduced as observed for the pERM signal. By eliminating cholesterol from cell membranes with MβCD alone, there is a decrease in the pERM and FCNPs signal.

In the case of the combined treatment with MβCD and myriocin, the signal reduction already observed with MβCD alone is even more evident. A particular case occurs, however, with the reduction of sphingomyelin alone, where the pERM signal seems to be equal to or slightly higher than the control, while the FCNPs signal, although slightly decreased, is not evidently reduced. It is, therefore, possible to note that pERM and FCNP seem to be interrelated because for each treatment they behave similarly.

Confocal and electron microscopy analysis

To better understand the quantitative data obtained from the flow cytometric analysis of the samples treated with myriocin and/or MβCD, confocal and electron microscopy analyses were performed. These analyses made it possible to verify, from a morphological point of view, the effect of the alteration of the membrane components concerning the morphology of the cell surface and the level of adhesion of the CNPs.

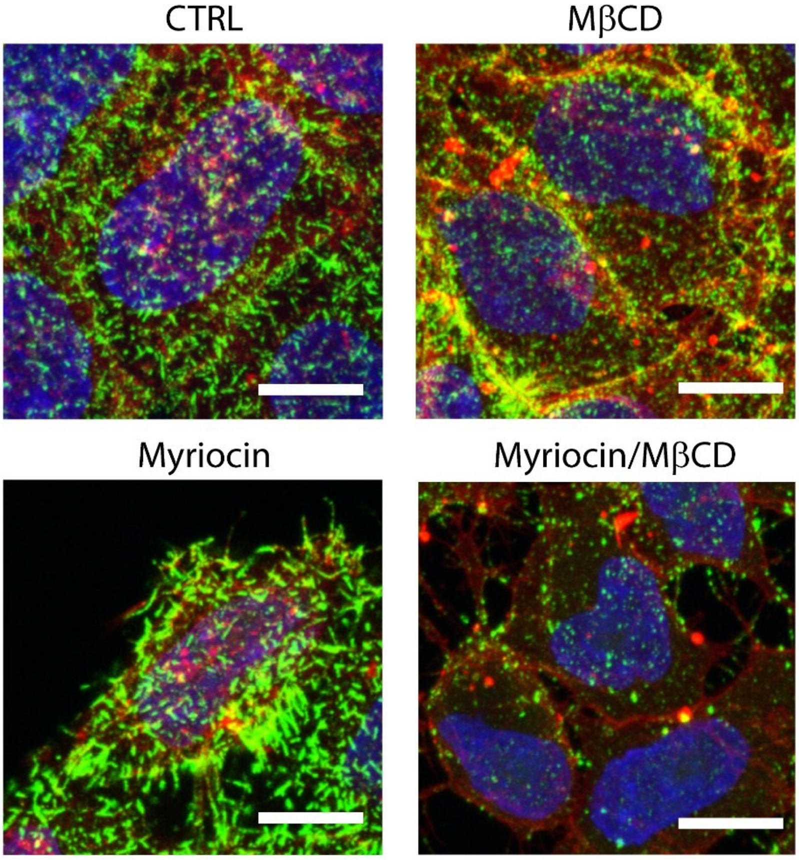

***Figure 41**. Microvilli and lipid rafts are fundamental for NP−cell interaction (A-B) Effect of lipid raft alteration on FCNPs adhesion to microvilli. (A) Confocal images of HeLa cells are treated as in **Figure 40.** Maximum projection of 15−18 0.35 μm confocal slices. Green, pERM; red, FCNP; blue, nuclei. Bar = 10 μm.*

By observing the images of the samples in which the synthesis of sphingomyelin was inhibited (**Figure 41, A**), it is possible to note that pERM, in agreement with the flow cytometry, was not reduced but remained comparable to the control sample. Upon closer inspection, the microvilli on individual cells seemed to have increased in density or increased in length and thickness.

The treatment with MβCD induced a drastic reduction of the pERM signal. This, therefore, seemed to indicate that the extraction of cholesterol caused an alteration of the structure of the microvillus such as to induce the loss of the reactive component for the anti-pERM antibody. This observation confirms the data obtained by flow cytometry in which a reduction of the pERM signal was highlighted.

On the other hand, when the cells were treated in order to inhibit the synthesis of sphingomyelin and remove cholesterol from the plasma membrane (Myriocin/MβCD), the pERM signal seemed to disappear almost completely.

By analyzing the FCNPs on cells previously treated with MβCD it was still possible to note the presence of the nanoparticles. Compared to the control conditions, however, FCNPs appeared more concentrated in a few distinct agglomerates. Treatment with myriocin did not markedly affect the ability of the nanoparticles to adhere to the microvilli of the cells. Even with the simultaneous removal of cholesterol and sphingomyelin, FCNPs were always present but, as in the previous cases, were organized in aggregates.

The effect of the alteration of the components of the microvilli was also evaluated from the morphological point of view by **SEM** (**Figure 42**). SEM allowed us to gain information about how the microvilli structure was altered and how the interaction of the CNPs with the cell surface was modified by the treatments.

By observing the images of samples where the synthesis of sphingomyelin has been blocked thanks to the action of myriocin, it is possible to note that the microvilli were still present (as observed by confocal microscopy). However, it can be noted that the specific adhesion of the CNPs towards microvilli was reduced. While in the control samples the microvilli were completely decorated by the CNPs, in this case, the nanoparticles adhered to the microvilli in patches (without forming a continuous layer).

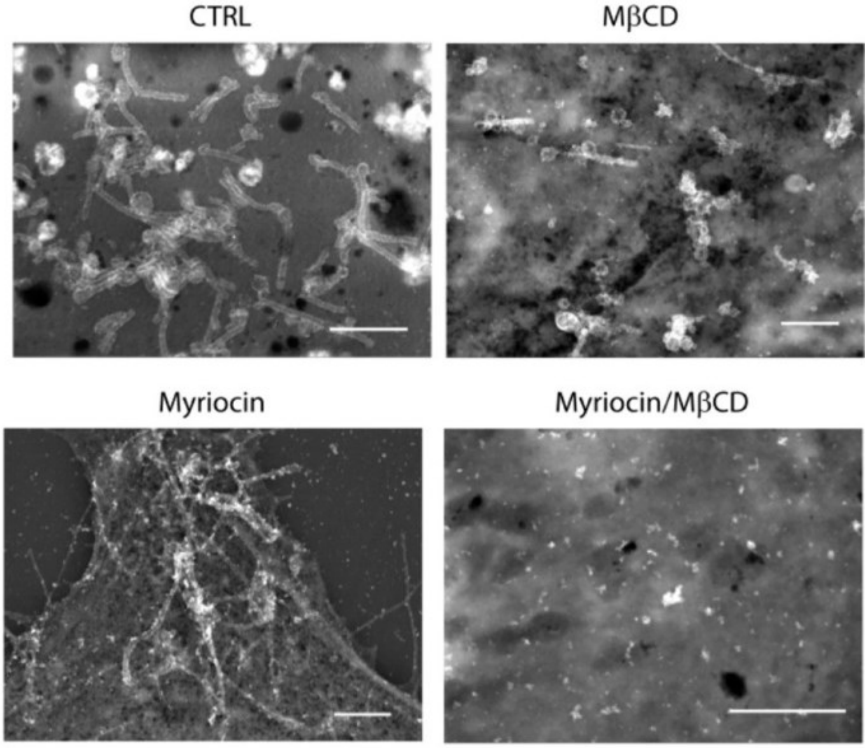

***Figure 42**. SEM BSE images of cells treated as in **Figure 41**. Bar = 2 µm.*

Treatment with MβCD induced a drastic reduction of microvilli leaving the cell surface almost completely absent of protrusions except for small spherical protrusions. Parallel to a reduction of microvilli, there was also a reduction in the number of CNPs present on the cell surface. Furthermore, those few adherent nanoparticles appeared as small agglomerates in correspondence with spherical protrusions.

The combined treatment of Myriocin and MβCD lead (as observed in confocal microscopy) to a total disappearance of microvilli (**Figure 42**). However, although the treatment was effective by inducing the loss of the microvillar structure, the CNPs surprisingly seemed to adhere to spherical membrane structures that appeared as defective microvilli, almost “curled up” on themselves.

These observations confirm that although the alteration of phospholipid alone did not reduce the formation of microvilli, it did alter CNPs adhesion, showing clearly the importance of lipid rafts for the interaction with microvilli. The reduction in CNPs adhesion was not due to a reduction in microvillus density (as for MβCD or myriocin/MβCD treatments) but to the change in their membrane composition.

Effect of inhibition of actin polymerization

HeLa cells were treated with CytD to remove actin, to alter the microvilli cytoskeleton. By inhibiting the microvilli structure, it was possible to investigate whether the interaction of CNPs with microvilli depended solely on membrane components (mostly lipid rafts) or if the microvilli structure was important in mediating the CNPs adhesion.

When cells were analyzed by SEM, it was possible to note that actin depolymerization indeed altered the microvilli structure, inducing the formation of large spherical structures (blebs) on the cell surface and the disappearance of normal microvilli (**Figure 43, A-C**). The CNPs that were present on the cells were concentrating in correspondence with those blebs which were probably defective microvilli due to the absence of actin. The fact that the CNPs were still attached to what looked like defective microvilli/remnants of microvilli supported the idea of direct interaction with a membrane component regardless of the actin presence even in the case of clearly defective microvilli. In fact, the treatment that leads to blocking the growth of the actin filaments has removed only the cytoskeleton component of the microvillus, leaving unaltered the membrane components to which the nanoparticles adhere.

When HeLa cells were analyzed by Confocal microscopy, the spherical structure/remnants of microvilli were still clearly visible **(Figure 44, A-D**). In particular, the formation of such blebs was visible in every cell (**Figure 44, A**). When observed at a higher magnification (**Figure 44, B**), these blebs were shown to be positive for pERM. Moreover, the signal derived from pERM seemed more intense when compared to control cells. This observation shows that indeed they were defective microvilli, but their collapsed membrane still maintained the original constituents. These pERM positive blebs seemed, in fact, to correspond to the actin accumulation points, since they were also stained with Phalloidin (**Figure 44, A-B**), confirming that the superficial blebs were the remnants of microvilli.

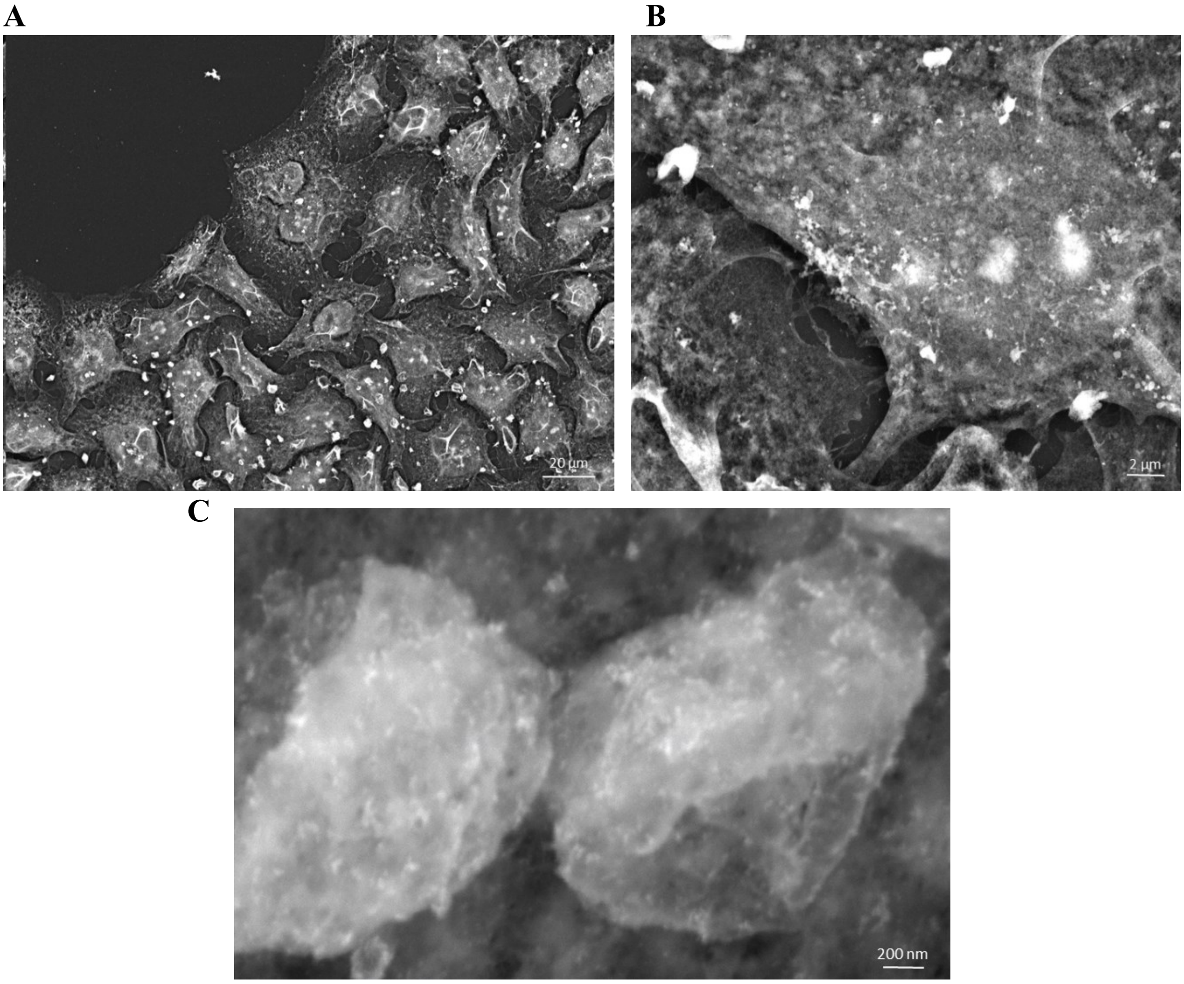

Figure 43. HR-SEM representative images of HeLa cells in which the actin polymerization was inhibited (using CytD). *(A) HeLa cells were treated with CytD 5 µM for 30 minutes and subsequent incubation of CNPs for 15 minutes. (B) enlargement of (A). CNPs (brighter spots) interact on the surface of cells by adhering to spherical structures. (C) Enlargement of the spherical swellings covered in CNPs.*

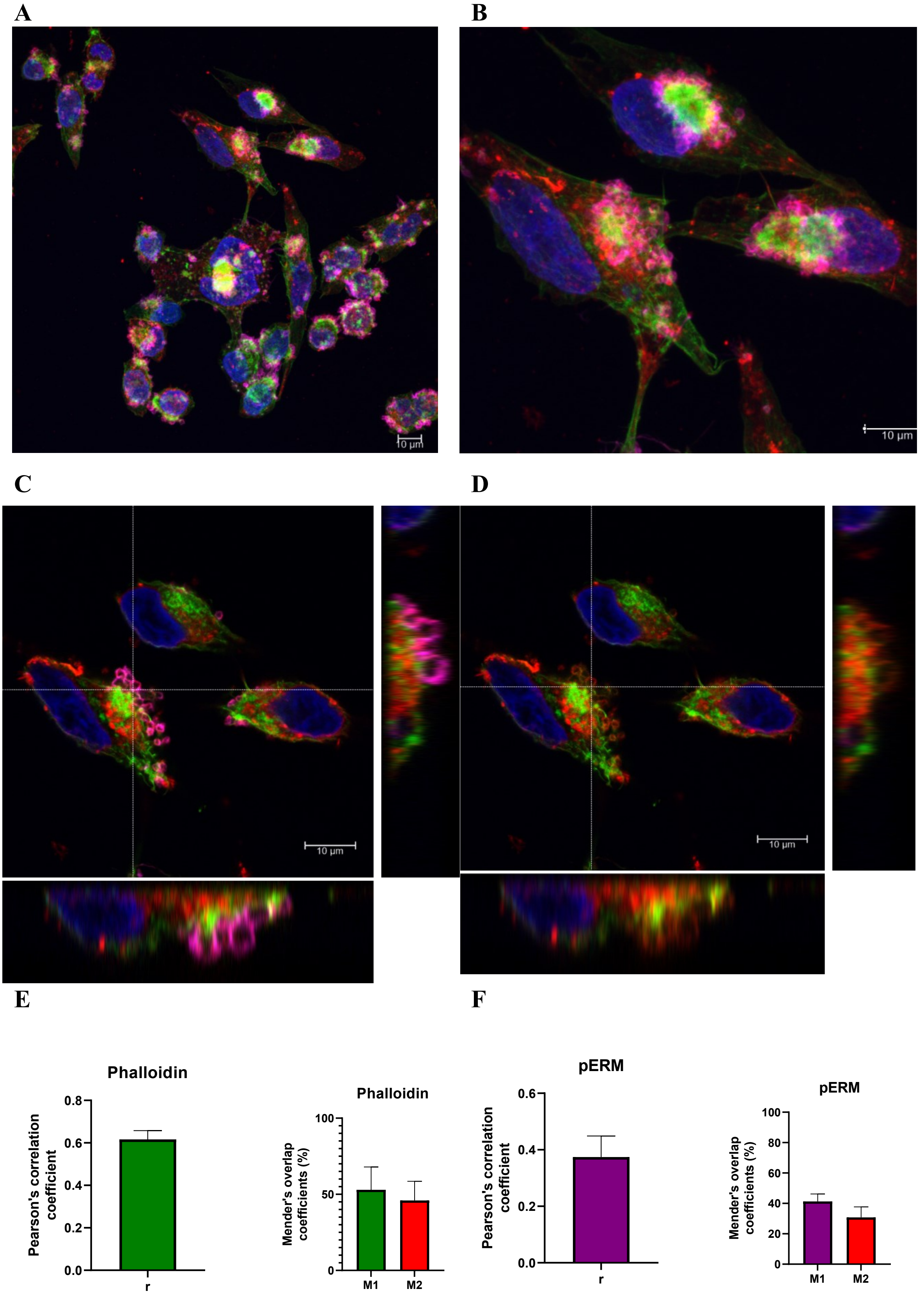
A
10 µm
B
10 µm
C
10 µm
D
10 µm
E
Phalloidin
Pearson's correlation coefficient
0.0
0.2
0.4
0.6
0.8
r
Phalloidin
Mender's overlap coefficients (%)
0
50
100
M1
M2
F
pERM
Pearson's correlation coefficient
0.0
0.2
0.4
0.6
r
pERM
Mender's overlap coefficients (%)
0
20
40
60
80
100
M1
M2

Figure 44. Representative images of HeLa cells showing the effect of the inhibition of actin polymerization observed by confocal microscopy. *(A) IF staining of actin (phalloidin), microvilli (pERM), after 30 minutes of incubation with CytD (5 µM), and 15 minutes of incubation with FCNPs. Big accumulation points of actin are visible inside cells (green saturation inside cells), after the collapsing of microvilli on blebs, surrounding the depolymerized actin. Maximum projection of 20 confocal planes, of 0,35 µm. Bar equal to 10 µm. Blue, nuclei; Green, Phalloidin; Red, FCNPs; Magenta, pERM. (B) enlargement of A. Maximum projection of 20 confocal planes of 0,35 µm. Bar equal to 10 µm. (C) single confocal plane of Figure (B) with its relative cross-sections. (D) single confocal plane of Figure (B) with its relative cross-sections. The signal of pERM is removed from the picture, but the blebs are still visible on the surface of the cell due to the signal derived from FCNPs, indicating that the NPs surrounded the collapsed microvilli, remaining attached to the lipid rafts that before constituted the external membrane of microvilli. (E) PCC between actin (phalloidin) and FCNPs, and MOC indicating how much actin colocalized with NPs (M_1) and how much of NPs colocalized with actin (M_2). (F) PCC between pERM (microvilli) and FCNPs, and MOC indicating how much of pERM colocalized with NPs (M_1) and how much of NPs colocalized with pERM (M_2). (E, F) Data were analyzed using ImageJ software. For the analysis at least 3 different images were considered. Data are expressed as average ± SD.*

As for the FCNPs, although they seemed to be more widely distributed on the cell surface, they specifically surrounded and cover the microvilli-derived blebs, confirming what was seen in SEM. The cross-sections in **Figures 44, C- D**, showed that even when the signal derived from pERM was excluded, the blebs can still be clearly visible due to the presence of the FCNPs covering entirely their surface. Overall, these observations support the idea that the CNPs adhere specifically to constituent/s of the microvilli membrane, like lipid rafts that remains unaltered when the microvilli cytoskeleton is impaired.

When the level of colocalization was calculated, a positive correlation was obtained between phalloidin signal (corresponding to actin filaments) and FCNPs, with a PCC of 0,62 ± 0,04 (**Figure 44, D**) with, 46% of FCNPs colocalized with actin, and up to 53 % of actin colocalized with FCNPs. Interesting to note, these results are similar to those observed for pERM and FCNPs in intact microvilli (**Figure 35**) confirming once more how the FCNP specificity was preserved even in structurally defective microvilli with intact membranes.

In this case, the colocalization with pERM is reduced (PCC of 0,37 ± 0,07) but still, 37% of FCNPs colocalized with the pERM proteins. This means that, after treatment with CytD, almost all the FCNPs were positioned on the collapse microvilli. These results indicate that the adhesion of FCNPs is extremely specific and happens even when microvilli are depleted of the actin cytoskeleton.

To better characterize the CNP adhesion in cells treated with CytD, pERM, and FCNPs signals were quantified by flow cytometry (**Figure 45**).

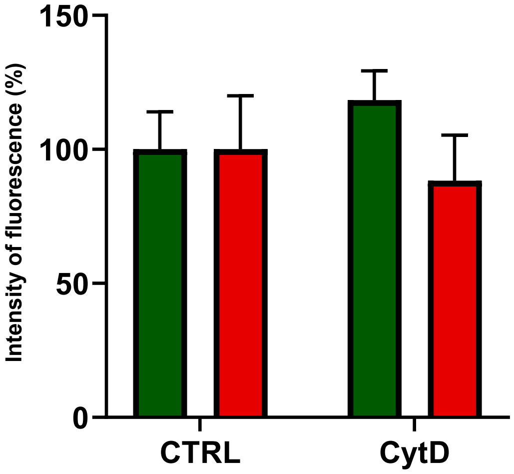

Figure 45. *Effect of actin depolymerization on HeLa cells. Flow cytometry measurement after 30' of incubation with CytD and comparison of pERM and FCNPs signal between cells not treated (CTRL) and treated with CytD (CytD). Data are expressed as an average from three independent analyses. Green, pERM; red, FCNPs.*

The analysis confirmed that the pERM signal is indeed higher when compared to control cells, as observed in confocal microcopy, probably due to accumulation (in a small area) of the proteins (already present in the membrane) before the microvillus collapsed. Interestingly, the FCNPs signals did not increase as pERM compared to controls. This could be explained because while the pERM complex was normally distributed in the microvilli membrane before the microvilli collapsed (and then became more concentrated), FCNPs were added to the cells when microvilli were already collapsed and the surface available for adhesion was reduced (due to the membrane folding).

To further investigate, cells were treated simultaneously with CytD and MβCD to alter both the microvilli cytoskeleton and their membrane component. The results were analyzed by confocal microscopy (**Figure 46, A-C**) and the intensities of fluorescence of the NPs were calculated (**Figure 46, D**). Looking at the graphic in **Figure 46, D** it is possible to see that

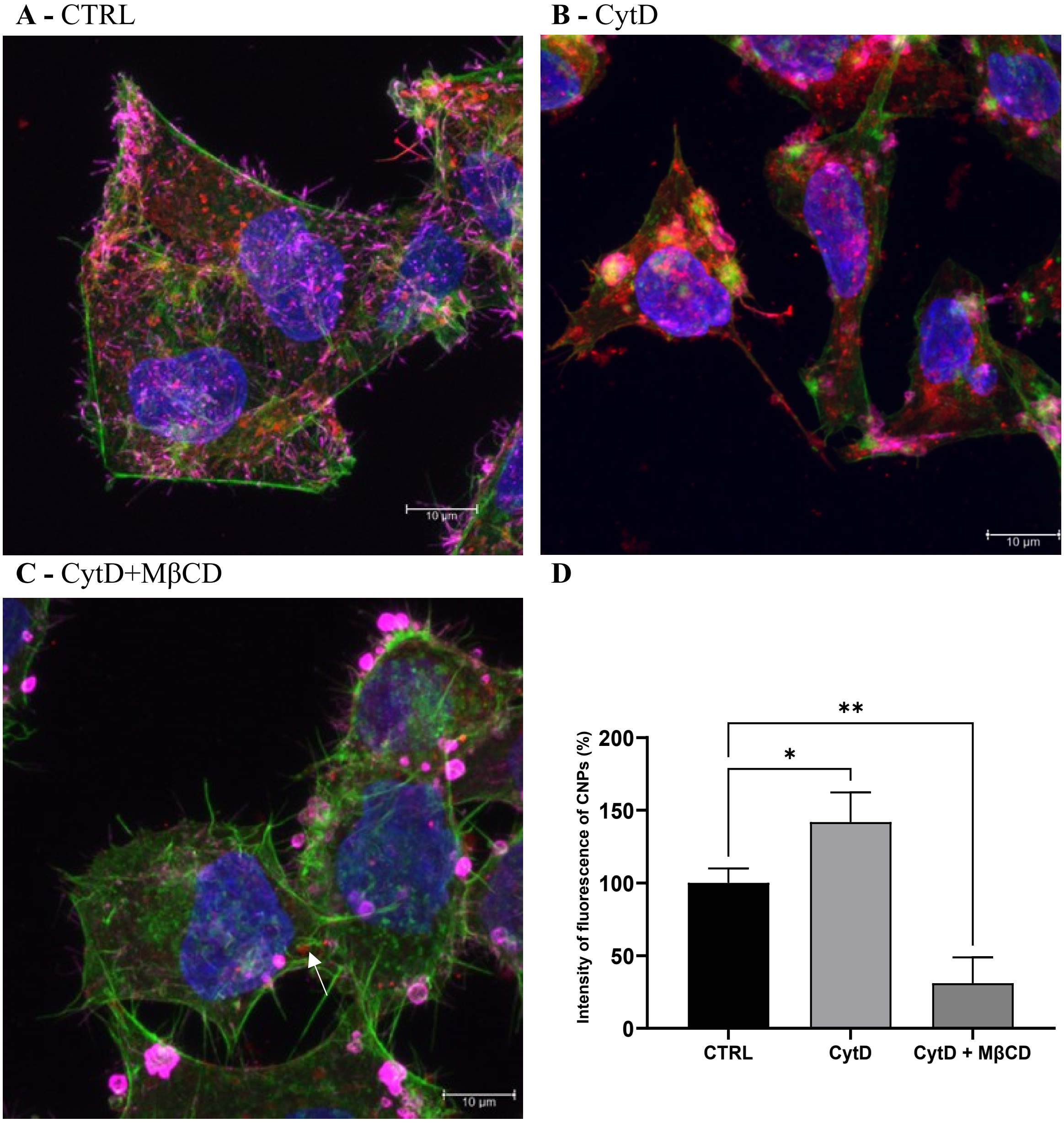

Figure 46. Effect of actin modification by CytD, and Cholesterol depletion by MβCD, on FCNPs adhesion to microvilli. *(A-C) Representative confocal images of cells treated just with FCNPs for 5 minutes (A, CTRL), with CytD for 1 hour and FCNPs for 5 minutes (B, CytD) and with CytD for 1 hour, MβCD for 30 minutes, and FCNPs 5 minutes (C, CytD + MβCD). Maximum projection of 20 confocal planes of 0.35 µm. Green, Phalloidin; red, FCNPs; Magenta, pERM; blue, nuclei. Bar = 10 µm. (D) Graphic of intensities of fluorescence of FCNPs inside cells, adjusted with the total area of cells (calculated with Phalloidin staining), calculated with ImageJ software. Average from three independent experiments, normalized versus the CTRL, ± SD. *, $p < 0.05$; **, $p < 0.01$, calculated with One way ANOVA with Tukey's multiple comparisons tests.*

the FCNPs fluorescence was higher (141%) in the case of CytD treatment than in control cells probably due to the formation of the blebs/ collapsing of microvilli. On the contrary, the presence of NPs in the sample with double treatments was lower (31% ± 17) when compared to control and CytD treated cells, indicating that FCNPs were not able to interact with the cells. As it is possible to observe in **Figure 46, C**, pERM outlines smaller blebs with a higher intensity. This is likely due to the simultaneous alteration of the microvilli cytoskeleton and the cholesterol component of the membrane, *i.e.,* lipid rafts: less cholesterol means that a portion of the membrane was depleted and consequently the blebs had a smaller dimension compared to the case when only the actin cytoskeleton was inhibited. In this case, few NPs were visible, not in correspondence of the microvilli blebs but just randomly distributed on the cells surface (**Figure 46, C**).

CNPs adhesion and the cell cycle phases

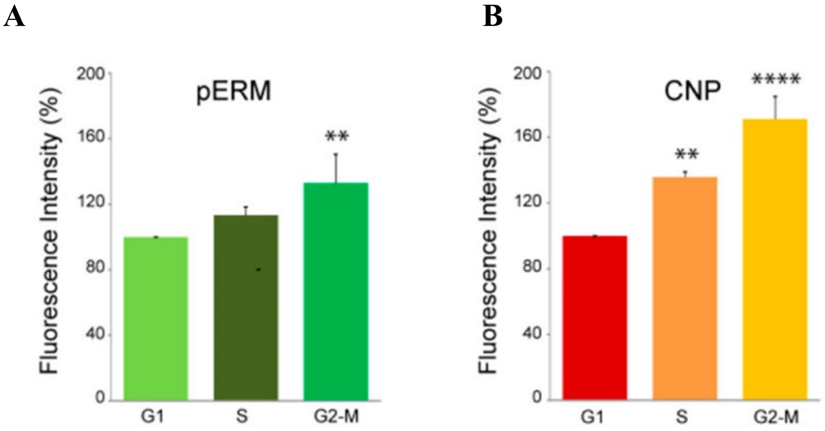

Figure 47. The amount of FCNPs adherence to the cell surface changed with the cell cycle (G2/M > S > G1) and correlated with pERM. *Flow cytometry measurement from three independent experiments. **, $p < 0.01$; ****, $p < 0.0001$ versus the respective G1 column.*

Some studies have demonstrated, by means of electron microscopy, that the density of microvilli in HeLa cells varies with the phases of the replicative cycle [Lundgren E., et al., 1976] [Fisher H.W., et al., 1967]. Given the results described so far, regarding the importance of microvilli as a way to ensure efficient adhesion and internalization of CNPs by cells, the next step of this study was to verify whether the adhesion level of CNPs was related to the stage of the cell cycle.

To verify if pERM underwent a variation in intensity in relation to the different phases of the cell cycle, the level of its signal was evaluated in relation to the DNA content. From the analysis (**Figure 47, A**), it was observed that the pERM signal was greater in the G2 / M phase than in the S and G1 phases (G2 / M> S> G1). This trend is in agreement with the literature. For example, Lundgren E. and colleagues [Lundgren E., et al., 1976], observed that the density of cell protrusions is greater in G2 / M (G2 / M> S> G1).

The same type of analysis was performed considering the FCNPs signal (**Figure 47, B**). Even in this case, it was possible to observe that the distribution of the FCNPs signal was always increased from G1 to S and G2/M phase, similarly to the trend observed for pERM. The fact that the two-signal changed accordingly, confirms how the FCNP adhesion on the cells surface depends on the presence of microvilli.

3.3.6 Cell-dependent CNPs interaction

REN- CNPs interaction

To exclude the possibility that the CNPs' specificity toward microvilli was cell-dependent, additional cell types other than HeLa were investigated. The first cell type that was analyzed was human pleural malignant mesothelioma (**REN and MSTO cell lines**).

The two cell lines were first characterized morphologically to investigate whether their protrusions resemble those observed in HeLa cells by testing pERM reactivity. To characterize the REN protrusions and see whether they resemble those observed in HeLa cells, the pERM positivity was analyzed by confocal microscopy.

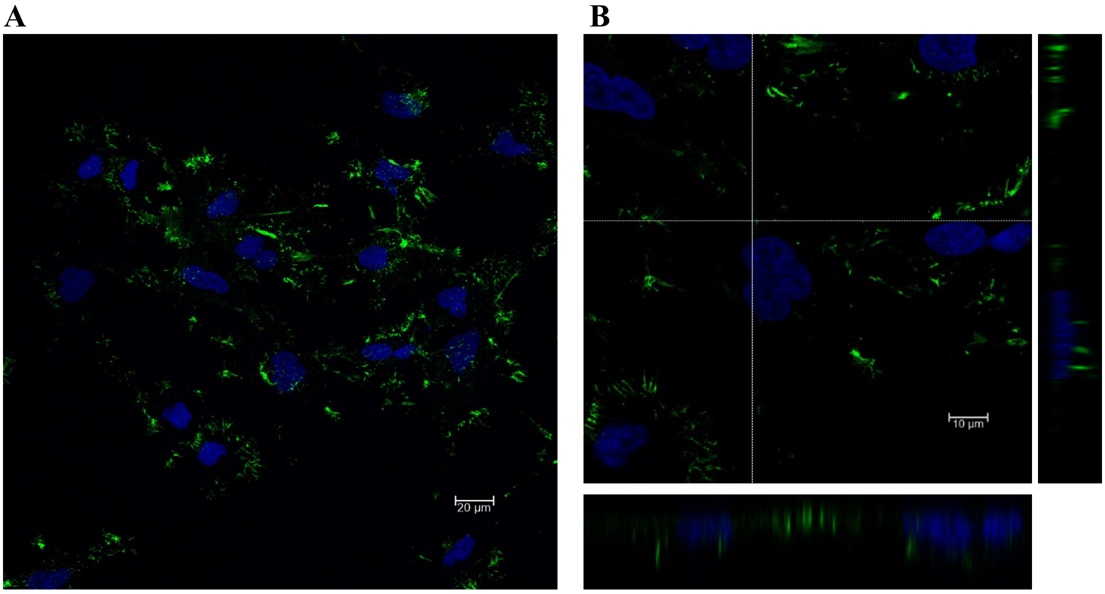

Figure 48. REN cells are positive for pERM. *(A, B) Representative confocal microscopy images of REN cells stained with pERM antibody (green) showed the presence of microvilli on the surface and around the cells. Maximum projections of 20 confocal planes. Each plane measures 0,35 µm. (B) Enlargement of a single cell and its relative cross-sections, showing the distribution of microvilli on the surface of the cell. Blue, nuclei, Green, pERM. Single confocal plane of 0,35 µm.*

In the case of REN cells, by confocal microscopy it was possible to confirm that, similarly to HeLa cells, the protrusions were **pERM positive** (**Figure 48**). Another similarity was that the distribution of microvilli was not homogeneous within a cell population, with some cells being more intensely stained than others. As for HeLa cells, also in this case this can be explained by the different stages of the cell cycle having a different number of microvilli.

When control cells were analyzed by SEM (**Figure 49**), surprisingly many different protrusions were visible, even without the contrast given by nanoparticles when attached to microvilli. In particular, each cell presented different kinds of protrusions, from very long, that connect neighbor cells (green arrow in **Figure 49, A**), to shorter microvilli on the surface of the cell (white arrow in **Figure 49, B**). Several other, medium-length protrusions were evident both on top and on the side of the cells (red arrow in **Figure 49, B**). Moreover, several extracellular structures similar to vesicles attached to the substrate were evident nearby each cell (**Figure 49, A)**.

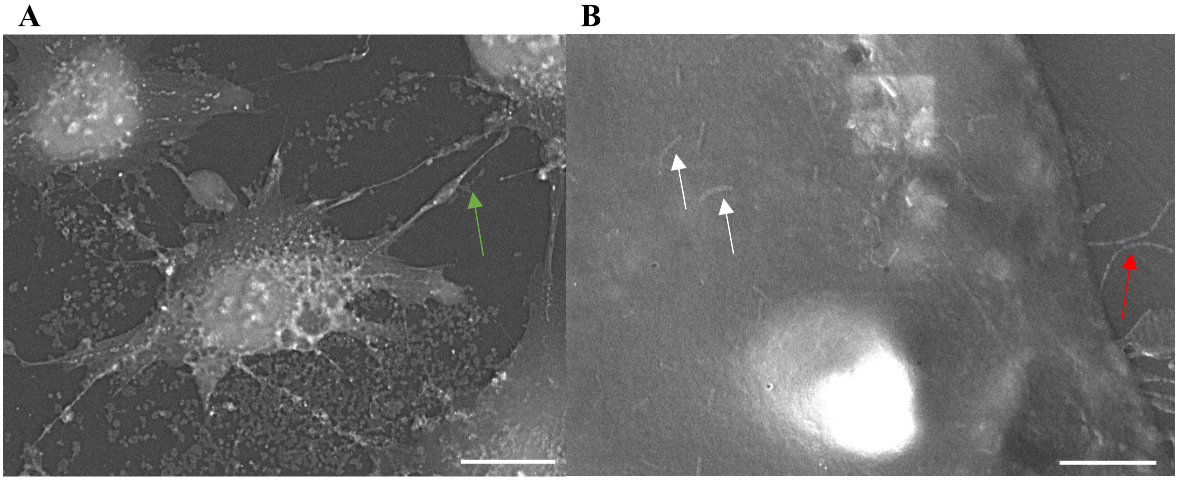

Figure 49. REN cells were observed by HR-SEM. (A) REN cells in which several cellular protrusions are evident. The bar is 20 µm (B) enlargement of a cell. Different kinds of protrusions can be seen on the surface of the cell: microvilli-like structures (white arrows) and longer protrusions (red arrow) present on the side and on top of the cells. The bar is 2 µm.

Compared to HeLa cells, some differences, however, can be found. For example, the pERM positivity in REN cells was more widely distributed on the planar region of the cells *i.e.,* more closely to the substrate, although plenty of microvilli can still be seen on the cell surface (**Figure 48, B, cross-sections**). Another difference was evidenced by SEM analysis: the protrusions had not a homogeneous length and diameter (**Figure 49, F**) compared to HeLa cells. As shown in **Figure 49, F**, even in the same cell, it was possible to find protrusions with different lengths. These cells are aggressive cancer cells and have been described as having long actin-based protrusions, commonly referred to in the literature as Tunnelling Nanotubes (TnT) that can use for various functions, from monitoring the environment to communicating to other cells [Lou E., et al., 2012] [Ady J.W., et al., 2014].

When cells were incubated with the CNPs for 5 minutes and observed by SEM, a very similar behavior was observed if compared to HeLa cells: the CNPs seemed to adhere selectively on the cellular protrusions (both present on the cell body and connecting other cells), leaving the planar membrane of the cells devoid of NPs (**Figure 50, B**).

Interestingly, they seemed to specifically adhere also to the extracellular vesicles that were clearly visible on the substrate (**Figure 50, A**) Moreover, similarly to what has been overserved for HeLa cells (**Figure 30, A**), not all the REN cells were equally "decorated" with CNPs, especially regarding the protrusions present on the cell body (**Figure 50, A**).

To better understand the dynamics of CNPs adhesion to the cellular protrusions, pulse/chase experiments were performed. For this purpose, cells were incubated with CNPs for 5 minutes, washed, and fixed after additional 15 minutes without CNPs (**Figure 50, C-E**). The SEM analysis of the CNPs distribution left on the cells revealed that the CNPs were still adherent on the extracellular vesicles, but almost no nanoparticles were visible on the protrusions present on the cell body (**Figure 50, B-C**). The length of the protrusions was then compared for experiments where the CNPs incubations were only 5 minutes or 5 minutes plus chase. Difference was evident (**Figure 50, F**): in only 5 minutes of incubation, the CNPs decorated protrusions were on average 6 ± 2 µm long, while, in the pulse/chase,

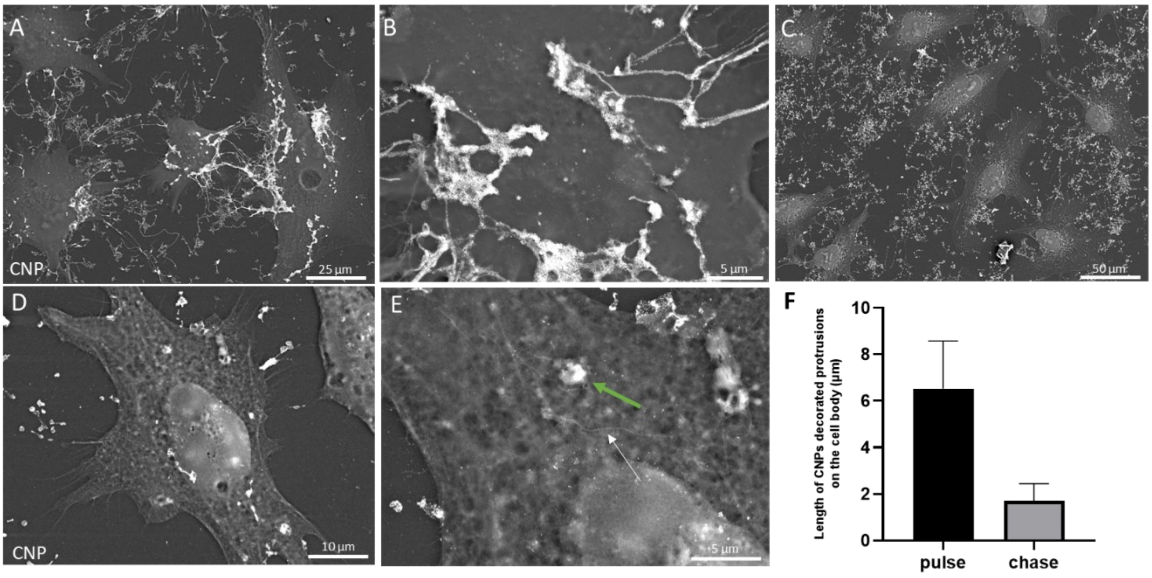

Figure 50. (A-B) REN cells were incubated with CNP for 5 minutes (pulse). (C-E) Representative SEM images of REN cells incubated with CNPs for 5+15 minutes (chase). (E) is an enlargement of (D). Is possible to observe CNPs still attached in REN's extracellular vesicles (C), but fewer of the cell body (D). In (E) in possible to observe microvilli without NPs (white arrow) and some spherical accumulation points of NPs, probably due to the microvilli internalization (green arrow). (F) Representative lengths of protrusions were CNPs adhere selectively, in the case of pulse (CNP 5 minutes) or pulse + chase (CNP 5+15 minutes).

the CNPs decorated protrusions were on average 1,7 ± 0,7 µm long. An explanation for this difference can be found when observing cells at higher magnification (**Figure 50, E**). Specifically, it was possible to observe that there were long microvilli on the cell body not decorated (white arrow), while several other structures were evident (green arrow) probably indicating where

CNPs-decorated protrusions were in the process of being internalized, thus "curving" on themselves or retiring inside the cellular membrane.

The REN-CNPs interaction was also analyzed by confocal microscopy (**Figure 51**). The analysis confirmed what was already seen by SEM: FCNPs interacted with the cellular protrusions and were mostly distributed on their entire length (**Figure 51, A**) since they were visible as long red "lines" that follow the pERM signal.

When colocalization between pERM and FCNPs was calculated, the results showed a positive correlation, but lower compared with HeLa cells (**Figure 35**), with a PCC of 0,409 ± 0,03 (**Figure 51, B**) and M_2 of 13 % ± 6 (**Figure 51, C**). It can be observed (**Figure 51, D)** that part of the FCNPs already internalized did not colocalize with pERM as such a protein complex is not present in the cell cytoplasm. As a consequence, this fraction of the overall FCNPs contributes to reducing the level of colocalization while it is clearly visible in the cell protrusions, where pERM and FCNP clearly colocalized.

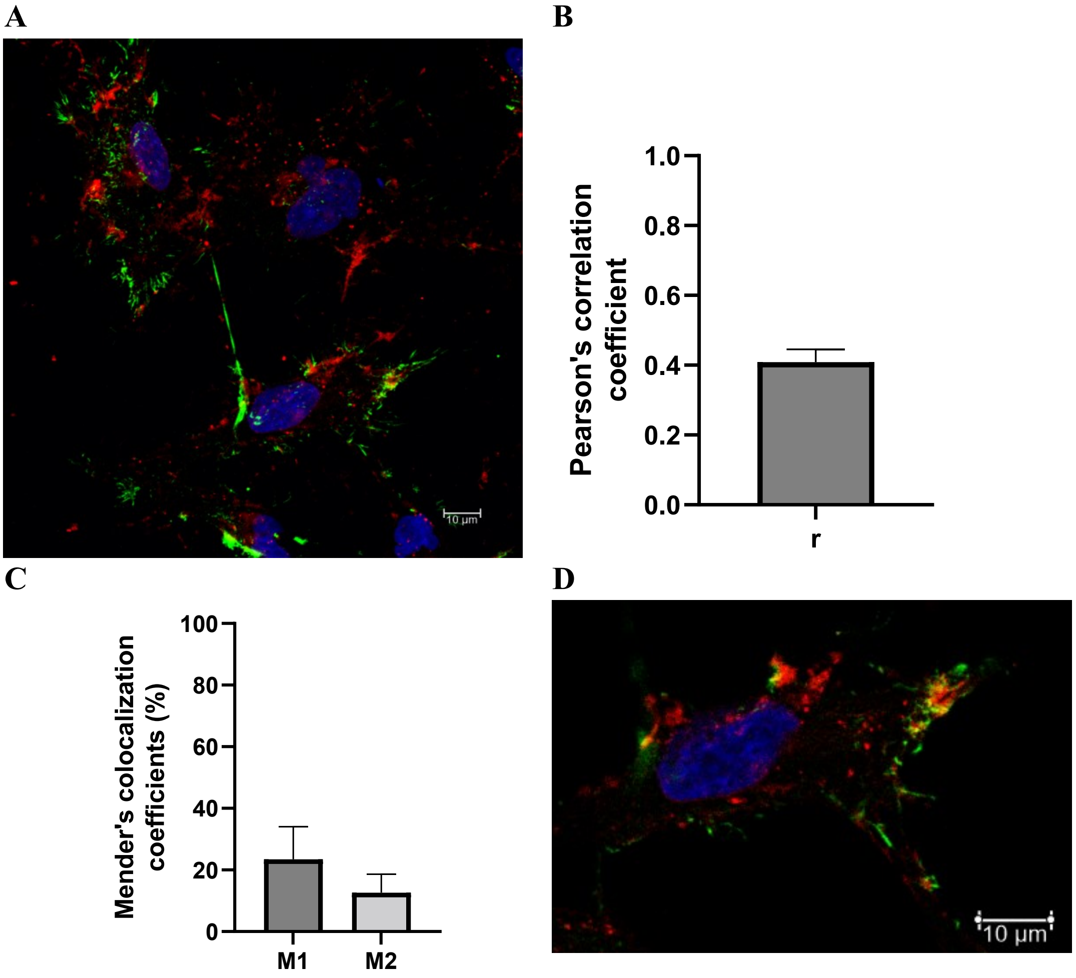

Figure 51. REN-CNPs interaction. (A) *Representative confocal image of REN cells incubated with FCNPs for 15 minutes. Maximum projection of 20 confocal planes of 0,35 µm. Green, pERM; Red, FCNPs; Blue, Nuclei. (B) PCC from pERM-FCNPs colocalization. (C) MOC. Data were analyzed using ImageJ software. For the analysis at least 3 different images were considered. Just upper stacks were analyzed. Data are expressed as average ± SD. (D) enlargement of a single REN cell incubated with FCNPs for 15 minutes. Maximum projection of 20 confocal planes of 0,35 µm.*

Analyzing the cell protrusions, it was possible to observe also some structures present on the substrate that seems to originate from the long cell processes (**Figure 52, A-B**). These vesicles were pERM negative, but the NPs were still decorating them, visible as bright red spots (**Figure 52. A**). On a closer look by SEM, these structures had a specific shape similar to pancake (**Figure 52, B-C**), and in the presence of CNPs, they resulted “decorated” similarly to the cell protrusions (**Figure 52, B**). However, the CNPs decoration was not homogeneous on all the **pancake-like structures**, but the degree of nanoparticles adhesion varied: the CNPs distribution on these structures could in fact be dense, like the protrusions, medium dense, or more sparse.

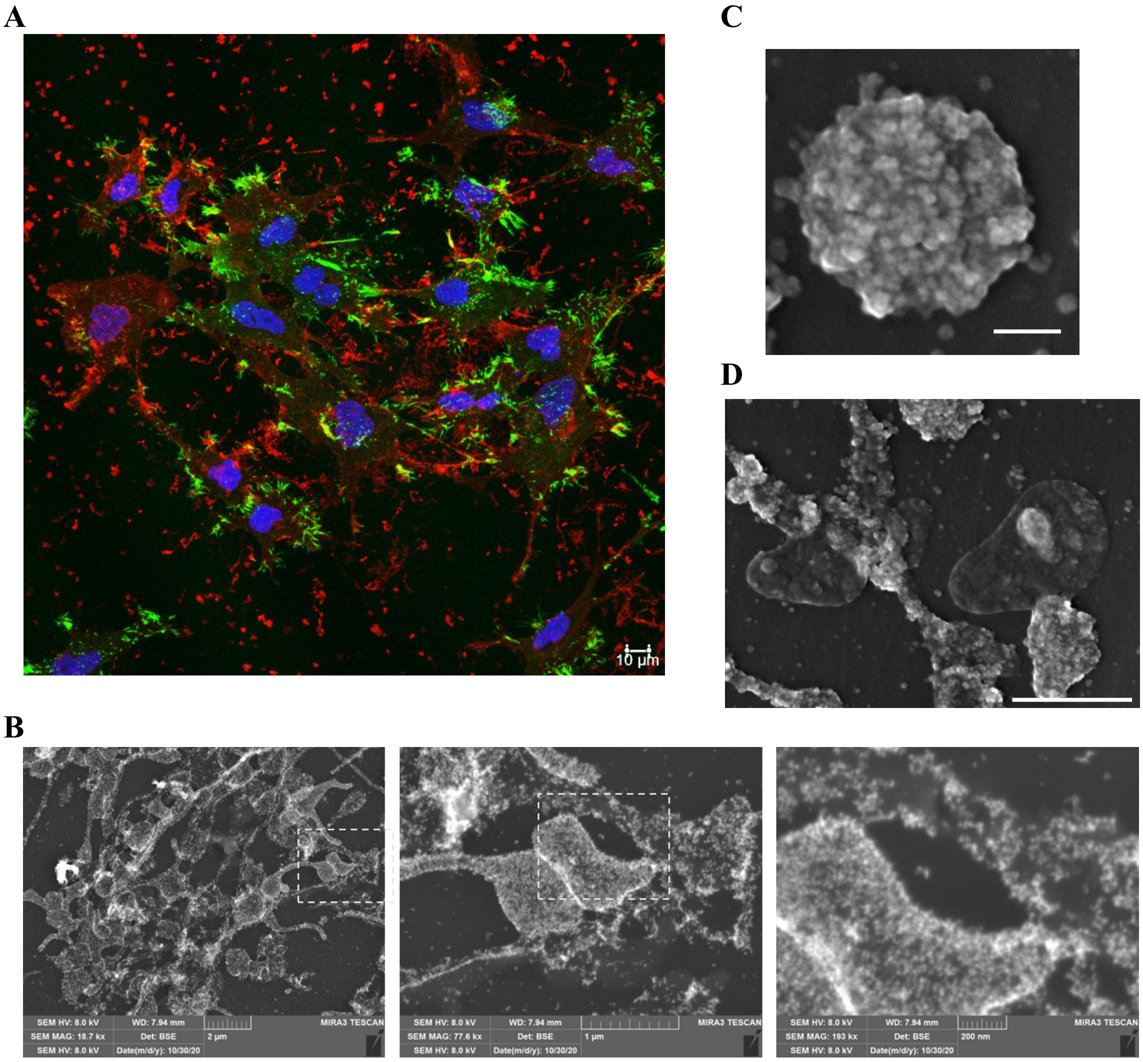

__Figure 52. CNPs interaction with extracellular vesicles.__ (A) Representative confocal image of REN cells incubated with FCNPs for 15 minutes. Is visible the specific interaction of FCNPs with extracellular vesicles, that are pERM negative. Maximum projection of 20 confocal planes of 0,35 µm. Green, pERM; Red, FCNPs; Blue, Nuclei. (B) particular of SEM of extracellular vesicles situated in proximity to the cell body. In the enlargements single CNPs are visible (white dots) covering entirely the membrane of the vesicles, while in other protrusions the distribution of CNPs is less dense (picture on the right). (C) particular of a single vesicle entirely covered of CNPs. Bar = 200 nm. (D) particular of single vesicles entirely covered of CNPs, close to others in which NPs interaction is less specific. Bar = 1 µm.

Effect of reduced levels of cholesterol on REN cells

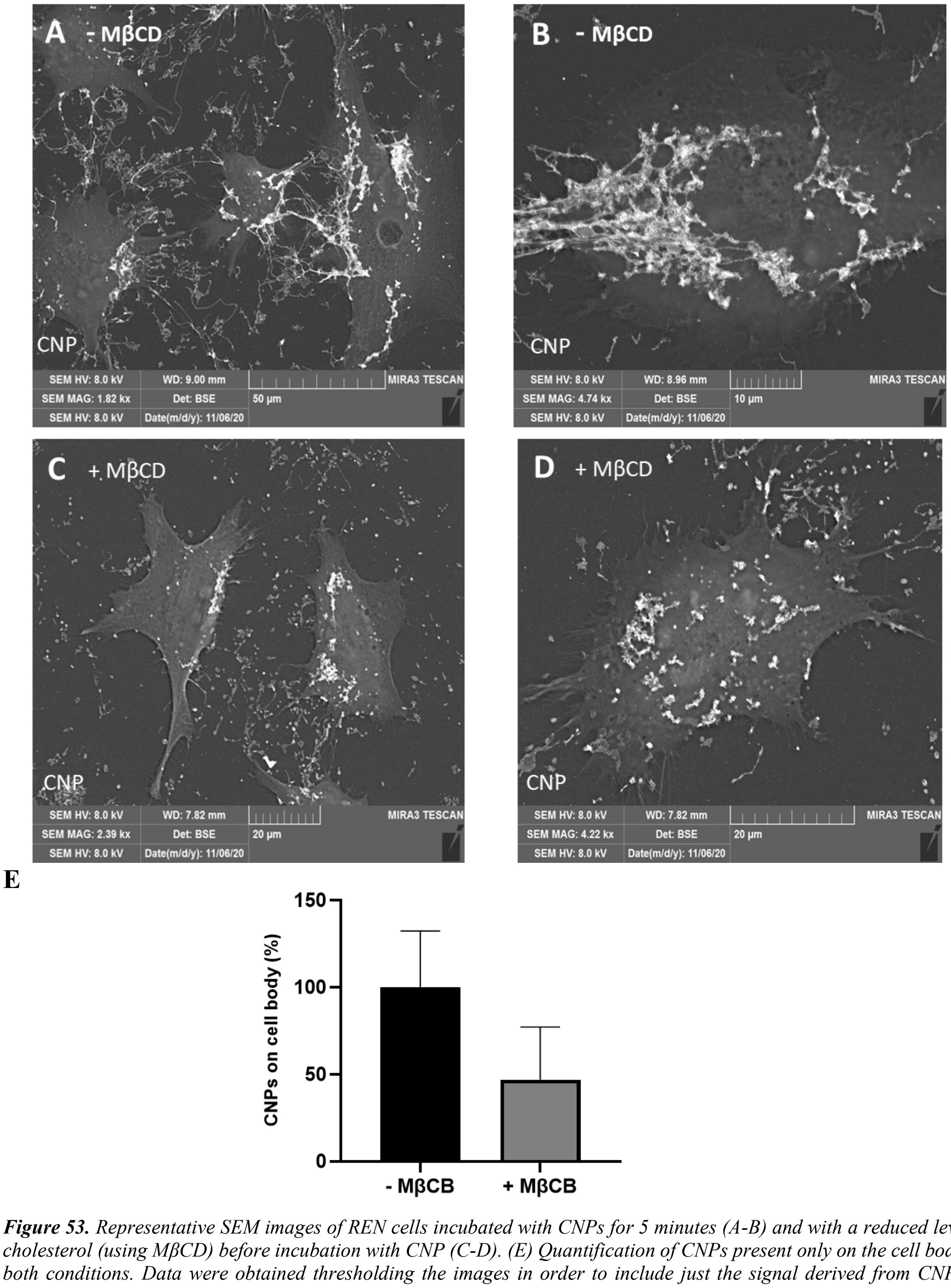

Figure 53. *Representative SEM images of REN cells incubated with CNPs for 5 minutes (A-B) and with a reduced level of cholesterol (using MβCD) before incubation with CNP (C-D). (E) Quantification of CNPs present only on the cell body for both conditions. Data were obtained thresholding the images in order to include just the signal derived from CNPs on protrusions still attached to the cells. Data are expressed as average ± SD of three different experiments, normalized with "–MβCD" as 100 %.*

As a next step, the effect of cholesterol depletion (by using MβCD) on REN-CNPs interaction was analyzed by SEM **(Figure 53**) and confocal microscopy (**Figure 54**).

When the effect of cholesterol depletion is observed by SEM (**Figure 53**), a difference in CNPs adhesion was evident. The length of the cellular protrusions connecting neighbor cells becomes shorter and less dense (**Figure 53 C-D**) when compared to control cells (**Figure 53 A-B**). Cells appeared more compact, and the NPs appeared in smaller and random distributed spots on the body of the cells. When the amount of CNPs on the body of the cells was calculated (by thresholding the images to exclude all the signals derived from the external structures), results showed that less than half of CNPs, compared to control conditions, were adherent on the cell body (47% ± 30) when the concentration of cholesterol was lower.

The effectiveness of the MβCD treatment was further confirmed by confocal microscopy (**Figure 54**).

While in SEM was possible to observe only the NPs adhering on the cell surface, confocal microscopy allowed to obtain information about both adhesion and internalization. In this case, the effect of cholesterol depletion was even more evident, since just 18% (± 25) of NPs interacted with the cells (**Figure 54, E**). No signal derived from the FCNPs adherent on the cellular protrusions was visible, and just a few NPs were evident inside the cells in a few random distributed spots (**Figure 54, D**). On the contrary, in the control sample, each cell was heavily decorated with CNPs, both on the cellular protrusions and the extracellular vesicles (**Figure 54, A-B**). In addition, differences in FCNPs uptake between cell was also observed, similar to what was observed in HeLa cells.

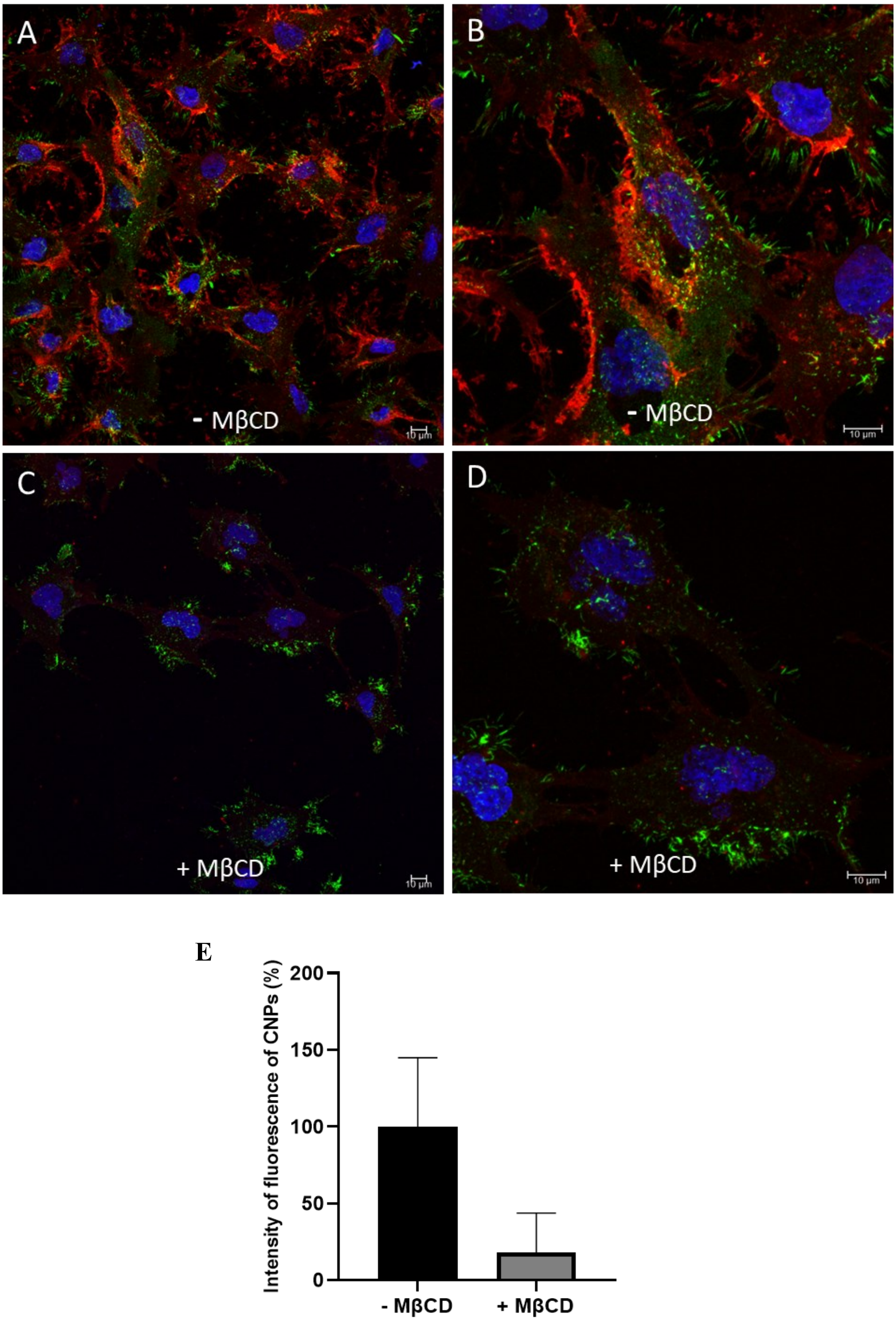

Figure 54. *Representative Confocal images of REN cells incubated with FCNPs for 5 minutes (A-B) and with a reduced level of cholesterol (using MβCD) before incubation with FCNPs (C-D). Max projections of 20 confocal planes of 0,35 µm. (E) Quantification of the intensity of fluorescence of FCNPs in the entire cell body (internalized and attached on the cell's protrusions). Data expressed are average ± SD of three different experiments, normalized with "– MβCD" as 100 %.*

A difference was observed also on the pancake-like structures when observed by SEM (**Figure 55**). After the removal of cholesterol, the number of vesicles with a very high density of CNPs adherent (**like in Figure 55, A-C**) diminished; on the contrary, smaller, more rounded-shape structures were left, where the CNPs adhesion appear still selective, but less densely packed **(Figure 55, B-D**).

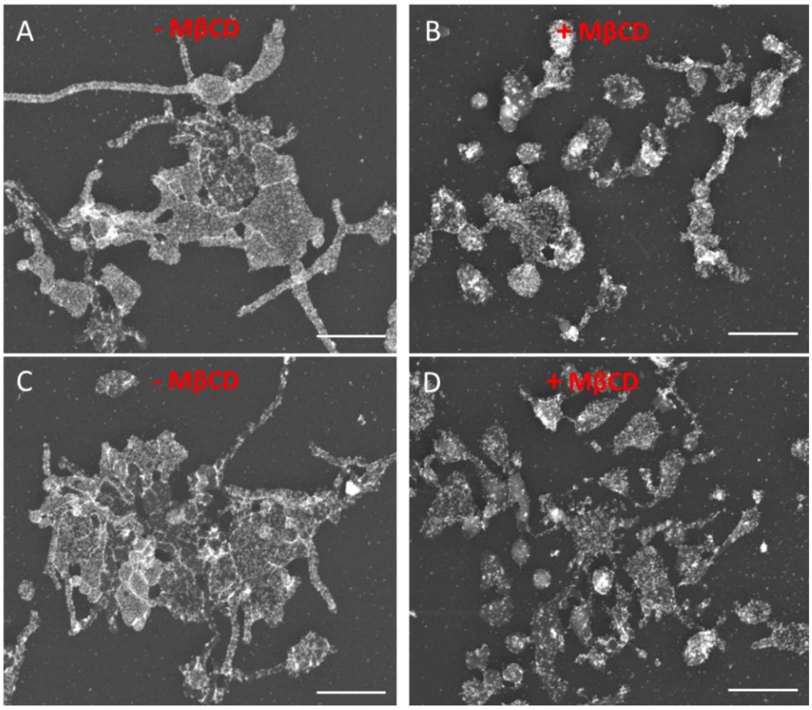

Figure 55. *Representative SEM images of pancake-like structures of REN cells incubated with CNPs for 5 minutes (A-B) and with a reduced level of cholesterol (using MβCD) before incubation with CNP (C-D).*

Characterization of the membrane composition

To understand the membrane compositions of the REN cell protrusions, specifically regarding the pancake-like structure, REN cells were further analyzed by confocal microscopy using **Flotillin** and **Cholera Toxin B**. In particular, both the membrane protrusions and the extracellular vesicles resulted positively marked by Flotillin **(Figure 56)**. Several colocalization points were visible between flotillin, a marker for lipid rafts, and the FCNPs after 10 minutes of incubation (**Figure 56, A).** Interestingly, most of the FCNPs seemed to adhere on both the long, Flotillin-positive, cellular protrusions (**Figure 56, B**, white arrow) and the extracellular vesicles (**Figure 56, B**, blue arrow), as already observed by SEM.

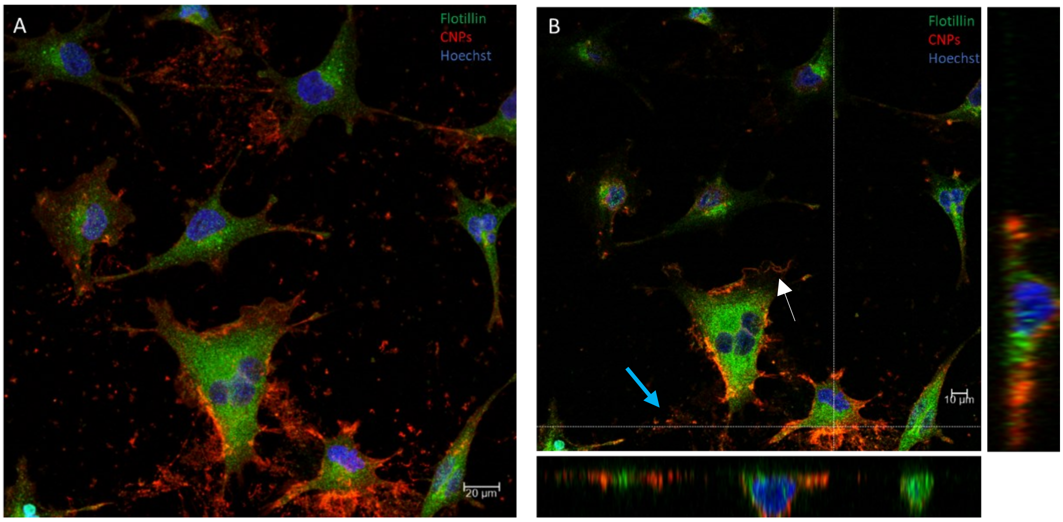

Figure 56. CNPs and flotillin reciprocal distribution is shown by IF. *(**A, B**) distribution of Flotillin (green), a component of microvilli membranes, on REN cells. FCNPs (red) were incubated for 10 minutes before fixation. Areas of colocalization FCNP-Flotillin are visible in yellow. Merge of 16 confocal planes. Each plane measures 0,35 µm. (B) same as in (A), but just a single confocal plane is visible. Tiny and very long protrusions are visible originating from the cell body, heavily decorated in FCNPs (white arrow). These protrusions are rich in lipid rafts since they are Flotillin positive. The interaction of FCNPs with pancake-like structures, Flotillin positive, is also visible (blue arrow). In the relative cross-sections, the interaction of FCNPs with cellular protrusions are evident.*

Cholera Toxin B (CTx) (**Figure 57, G-H**) is commonly used as a marker for lipid rafts and caveolae-mediated endocytosis [Sousa de Almeida M., et al., 2020] The B-chains of the toxin pentamer bind specifically to the glycosphingolipid GM1 in the outer leaflet of the plasma membrane. These regions are specialized plasma membrane invaginations rich in the protein caveolin, cholesterol, and glycolipids [Torgersen M.L., et al., 2001].

For the experiments, the incubation of CTx was maintained at 4°C, to avoid the internalization of the toxin. When cells were incubated with FCNPs *before* CTx (**Figure 57, B, E**) the signal derived from CTx was extremely lower when compared to the control (21%

± 1,8) (**Figure 57, G**); on the contrary, when FCNPs were incubated *after* the CTx (**Figure 57, C, F**), the signal derived from CTx was 69% ± 2,1 (**Figure 57, G**). When the intensity of fluorescence of FCNPs was analyzed (**Figure 57, H**), the signal was only 2% ± 2,7 if incubated *after* CTx, compared to if they were incubated *before*. CTx.

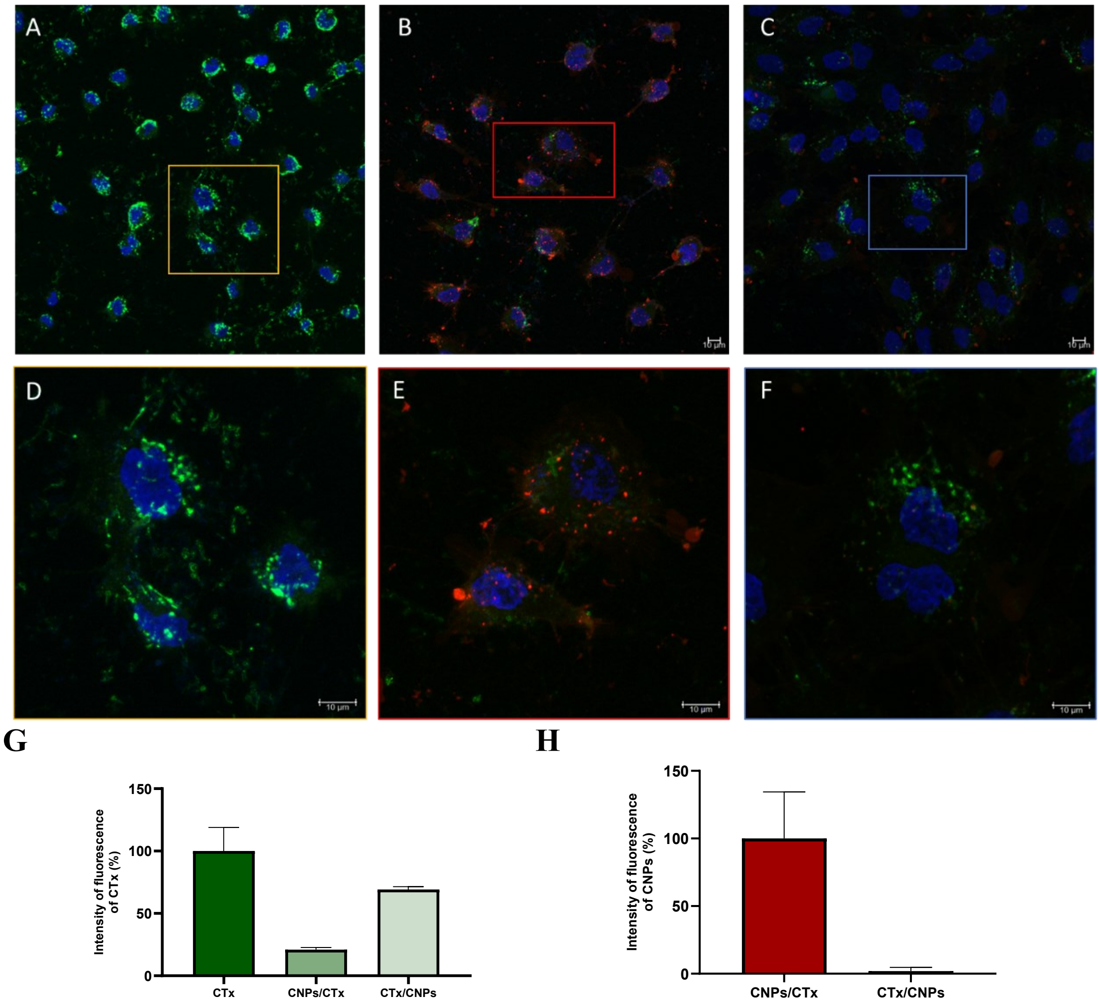

Figure 57. CTx and CNPs reciprocal distribution in REN cells. *(A)Representative images of the staining of CTx in REN control cells. (D) enlargement of (A). Microvilli are visible around and on top of the cells. (B) REN cells were incubated with FCNPs for 15 minutes before incubation of CTx. The signal derived from CTx is reduced when FCNPs are incubated before. (E) enlargement of (B). (C) REN cells were incubated with CTx for 30' before incubation of FCNPs for 15 minutes. In this case, almost no CNPs adhered on the cells. (F) enlargement of (C). All the Figures are maximum projections of 16 confocal planes. Each confocal planes measure 0,35 µm. (G) Intensity of fluorescence of CtxB (green signal) in at least 3 different pictures. The first column (CTx) referred to control cells (like in (a)); the second column (CNPs/CTx) referred to the sample in which the FCNPs were added before CTx (like in (B)); Third column (CTx/CNPs) referred to the sample in which CTx was incubated before adding the FCNPs (like in (C)). Data are expressed as an average ± SD from 3 different experiments. (H) Intensity of fluorescence of FCNPs (red signal) in at least 3 different pictures. The first column (CNPs/CTx) referred to the sample in which the FCNPs were added before CTx (like in (B)); the second column (CTx/CNPs) referred to the sample in which CTx was incubated before adding the FCNPs (like in (C)). Data are expressed as an average ± SD from 3 different experiments.*

This evidence could be an additional demonstration that the FCNPs bind a part of the microvilli membrane rich in lipid rafts as they seem to compete with the CTx.

Altogether, these results suggest that the pancake-like structures observed by SEM and confocal microscopy originates directly from the long cellular protrusions of REN cells. For this reason, they share the same membrane composition (they are both rich in lipid rafts as they are sensitive to cholesterol depletion with agents like MβCD), but not the internal structure, since the TnTs have an active cytoskeleton and are pERM positive, while the pancake-like structures appeared to positive just for Flotillin. As a consequence, the CNPs decorated the pancake-like structures in a similar way as for the protrusions. The difference in the CNPs decoration on the pancake-like structures can be probably originating from different stages of development of these structures. REM cells confirmed once more that CNPs interact with membranes rich in lipid rafts.

MSTO-CNPs interaction

The interaction of CNPs was tested also on the MSTO-211H cell line, originally obtained from the pleural effusion of a patient with biphasic mesothelioma of the lung.

When analyzed by SEM, it was possible to confirm that also in this case, as for the REN cells, the interaction of CNPs was very selective toward microvilli (**Figure 58, A**). This was particularly evident when observed at higher magnification (**Figure 58, B**), where long, densely decorated protrusions were evident, while on the planar region no nanoparticles were visible.

That observed by SEM was also confirmed also by confocal microscopy (**Figure 58, C**), where FCNPs were visible both on the cellular protrusions positive for pERM and inside the cells. Moreover, even in this case, the cells released pancake-like structures (**Figure 58, A**), as seen in REN cells **(Figure 50, D).**

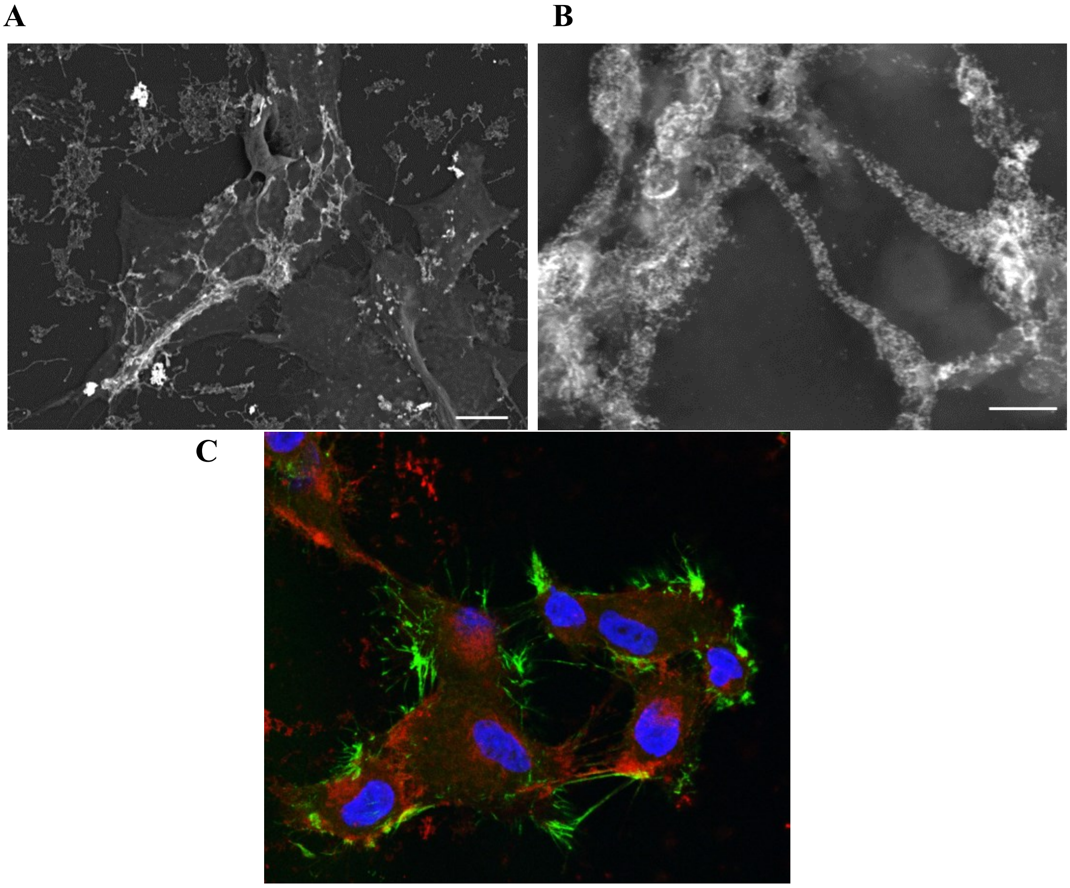

Figure 58. *(A) SEM of MSTO 211-H cell line incubated with CNPs (white spots) for 15 minutes. Bar = 10 µm. (B) Enlargement of (A). A very selective interaction with cellular protrusions is evident. The protrusions are also densely decorated with particles. Bar = 1 µm. (C) confocal microscopy of MSTO 211-H cell incubated with FCNPs for 15 minutes. Green, pERM; Red, FCNPs; Blue, Nuclei. Single confocal plane (0,35 µm). Bar = 20 µm.*

To confirm that the effect of cholesterol depletion diminishes the binding with NPs also in the MSTO 211-H cells, they were treated with MβCD before incubation with CNPs (**Figure 59**). As it's possible to observe in **Figure 59**, the control cells showed long, densely decorated microvilli (**Figure 59, A**), numerous pancake-like structures in different shapes (circled but also spaghetti-shaped) (**Figure 59, A**), and several blurred circles indicating internalization (**Figure 59, B**). In the case of MβCD treatment, however, the number of nanoparticles appeared significantly lower (**Figure 59, C)**. It should also be noted that the protrusions were different compared to the control; the cells appeared more rounded, and their protrusions, which were reduced in number, seemed short to the point of becoming round structures (**Figure 59, D**).

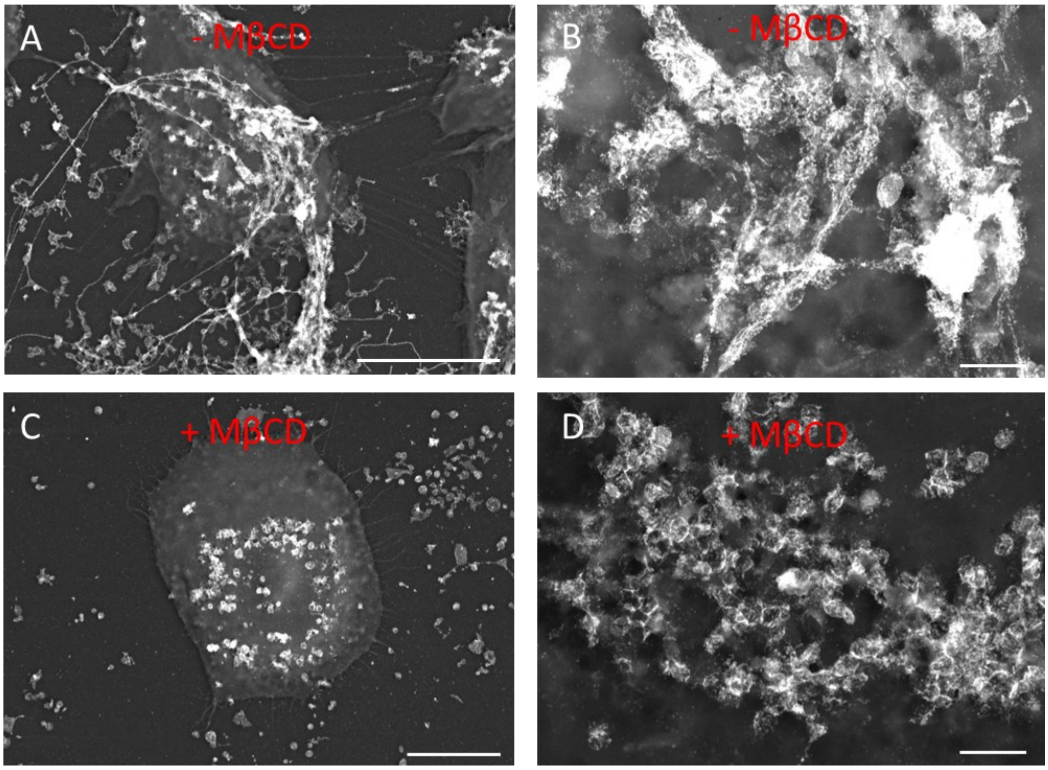

Figure 59. *Representative SEM images of* MSTO 211-H *cells incubated with CNPs for 5 minutes (A) and with a reduced level of cholesterol (using MβCD) before incubation with CNP (C). (B) Enlargement of (A). (D) Enlargement of (C). (A, C) Bar = 20 µm. (B, D) Bar = 2 µm*

A431-CNPs interaction

The interaction of CNPs was tested in the **A431** cell line. This cell line, like HeLa, REN, and MSTO cell lines, is known to possess microvilli pERM positive on the cellular surface [Yonemura S., et al., 1999].

When A431 cells were incubated with CNPs for 10 minutes and analyzed by SEM, the same specific interaction with microvilli was observed (**Figure 60, A-C**). At bigger enlargements (**Figure 60, B**), it was possible to observe long and densely decorated protrusions originating from the cellular body. They were decorated all along their length but right where they emerged from the planar region of the membrane, the nanoparticles abruptly stop adhering and a clear line of demarcation is visible (white arrow).

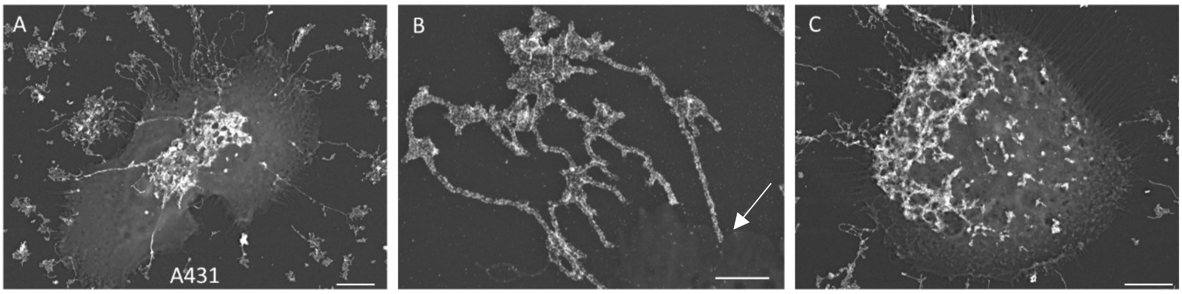

Figure 60. CNPs adhesion A431 cell line. *(A-C) CNPs showed specific adhesion to the A-431 cell line after 10 minutes of incubation, similarly for HeLa, REN, and MSTO cells. (B) Enlargement of (A). CNPs interact specifically with cellular protrusions, but abruptly stop adhering when the cellular membrane starts (white arrow). Bar = 10 µm. (C) Two types of protrusions are visible: one type, on the cellular surface, fully decorated with CNPs, the second one, adhering on the substrate, showed no specific interaction with CNPs (white circle). Bar = 2 µm.*

COS7-CNPs interaction

The interaction of CNPs was tested in the **COS 7** cell line. The reason for using other cell types was to exclude the possibility that this kind of interaction was cell-dependent. When COS7 cells were incubated with CNPs for 10 minutes and analyzed by SEM (**Figure 61, A-C**), no specific adhesion was observed. In particular, CNPs seem to be distributed on the cell membrane as small patches (**Figure 60, E**). In fact, opposed to HeLa, REN, MSTO, and A431 cell lines, COS 7 lacks microvilli on the cellular surface.

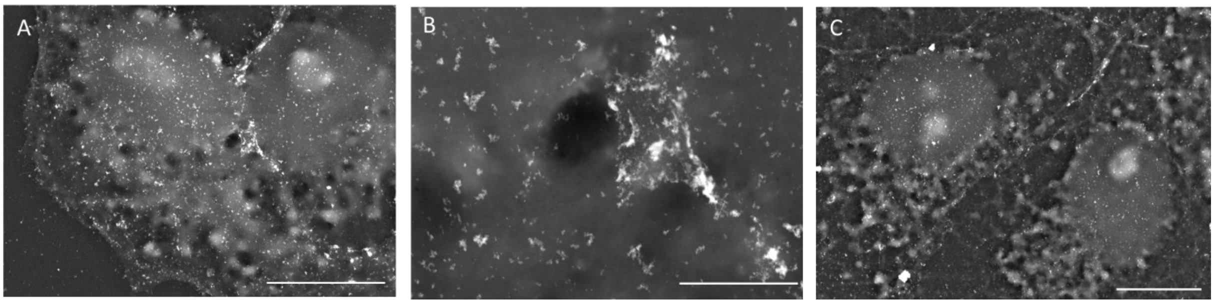

Figure 61. CNPs adhesion to COS7 cell line. *(A-C) No specific adhesion was observed in the case of the COS-7 cell line, where CNPs were distributed on the entire cell bodies without showing any specificity for structures. SEM-BSE images. (A and C) Bar = 10 µm. (B) Bar = 2 µm.*

.

3.3.7 Influence of NP core on the interaction with microvilli

To better understand the origin of the specific microvilli-CNPs interaction, a new kind of NPs with the same coating (PAA) and same dimension but different core (IONPs) was synthesized in our laboratory.

IONPs synthesis and characterization

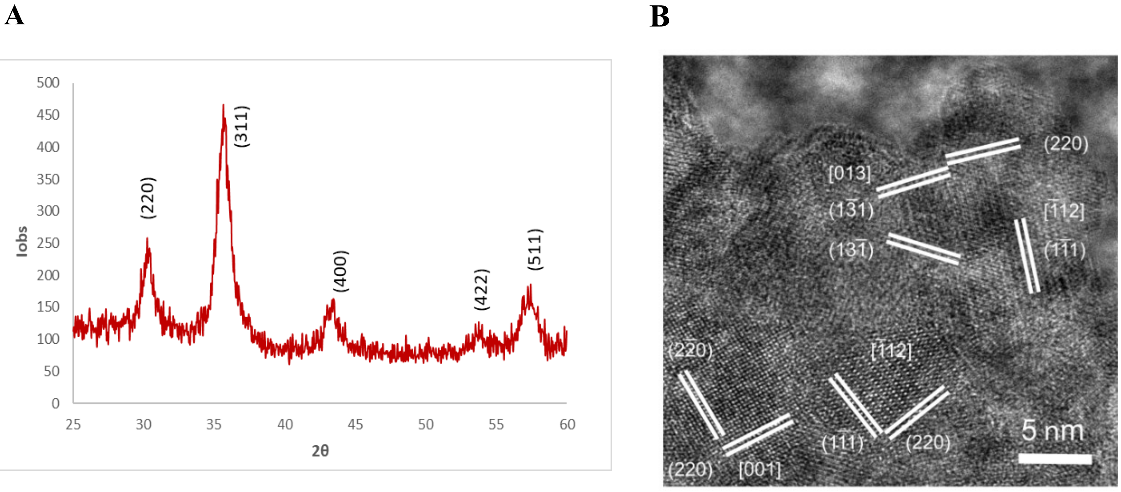

Figure 62. *(A) XRD analysis of IONPs. (B) TEM imaging of IONPs.*

PAA-coated Fe_3O_4 (**IONPs**) were synthesized as described in Materials and Methods [Santra, S. et al., 2009]. Diffraction peaks at 2 θ = 30.2 °, 35.5 °, 43.2 °, 53.5 °, and 57.1 °, which correspond respectively to the crystallographic planes (220), (311), (400), (422) and (511) of the structure of magnetite (**Figure 62, A**). The product of the synthesis can therefore be considered monophasic and free of impurities due to other iron oxides.

By applying the Scherrer equation, an average diameter of **5.2 ± 0.2 nm** is obtained, a size comparable to the CNPs size. The dimensions of the particles observed with the DLS technique showed a dimension of **42 nm ± 1 nm**. The dimensions of the particles observed with the DLS technique and with X-ray diffraction were significantly different from each other. This phenomenon is due to the fact that the DLS technique detects not only the nanoparticle core but also its hydrodynamic surroundings, which also includes the capping polymer and the solvation sphere of the particle.

TEM images (**Figure 62, B**) showed neither evidence of internal defects nor of significant agglomeration and estimated the mean particle size to be 5 ± 0.9 nm.

Viability of HeLa cells with IONPs

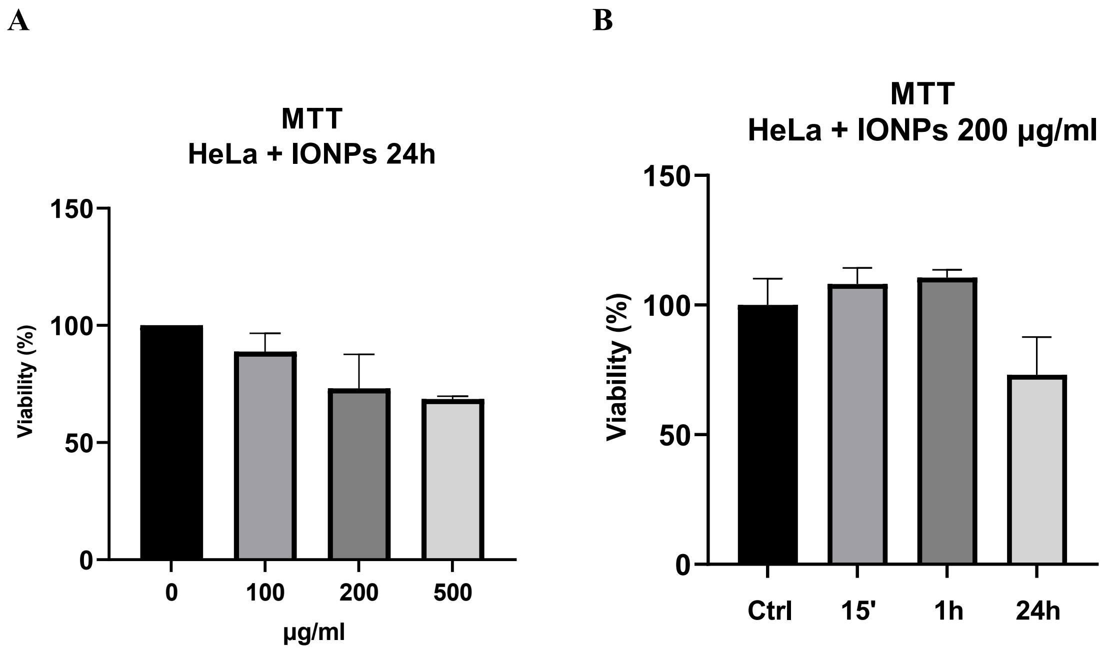

Figure 63. Effect of CNPs on the viability of HeLa cells. *Effect of different concentrations of IONPs (100, 200, or 500 µg/ml) after 24 h of incubation (A). Effect of different incubation times of IONPs 200 µg/ml on the viability of HeLa cells (B). Average from three independent experiments ± SD, versus the respective CTRL column*

The toxicity limits of IONPs concerning the HeLa cell line were determined using the MTT cytotoxicity/ cytostatic test, based on mitochondrial functionality. As it's possible to observe in **Figure 63, A**, after 24 hours of treatment there was no evident sign of toxicity for 100 and 200 µg/ml **(**89% ± 7,8 for 100 µg / mL, and 73,06% ±14 for 200 µg / mL). Only the highest concentration of IONP showed viability of 69% ± 1,2.

Based on this test, it was decided to use the intermediate concentrations of 200 µg / mL for further analysis, and viability was tested at different incubation times (**Figure 63, B**).

Even in these cases, the nanoparticles didn't show signs of toxicity, with levels of viability higher than 95% for all the incubation times tested. For this reason, the concentration of 200 µg / mL with the incubation times tested were maintained for all the following experiments.

Interaction of IONPs with HeLa cells

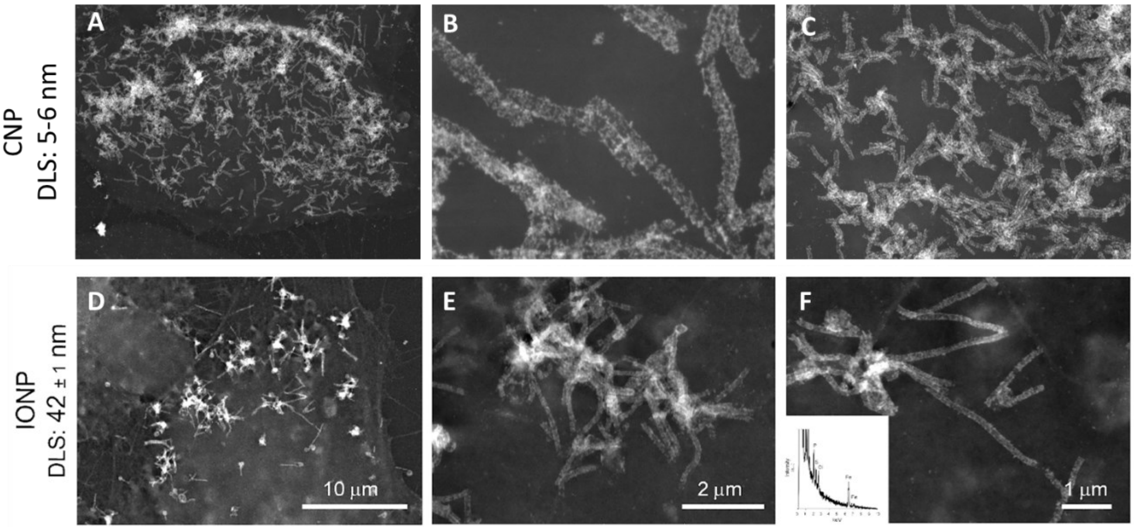

Figure 64. IONPs interact with microvilli of HeLa cells in a similar way to CNPs. *(A) Representative SEM images of HeLa cells incubated with CNPs for 15 minutes. (B-C) enlargements of (A). Numerous highly CNPs-decorated microvilli are visible. No NPs adhere to the planar region of the cellular membrane. (D) Representative SEM images of HeLa cells incubated with IONPs for 15 minutes. (E-F) enlargements of (D). Numerous highly IONPs-decorated microvilli are visible. No NPs adhere to the planar region of the cellular membrane. (F, inset) Representative SEM-EDS analysis of the IONPs present on the cells.*

HeLa cells were incubated with IONPs and CNPs for 15 minutes, and their distribution on the surfaces of the cells was analyzed and compared by SEM (**Figure 64**). IONPs showed the same specific interaction with microvilli observed for CNPs **(Figure 64, A-C)** with densely decorated protrusions (**Figure 64, D-F**). Also, the high selectivity was maintained as in fact no NPs were visible on the planar region of the cellular membrane **(Figure 64, E-F)**.

It is possible to conclude that, similarly to the CNPs, the interaction of the IONPs with microvilli was fast and highly specific. This demonstrates that the inorganic core chemical composition does not affect the NP adhesion on microvilli.

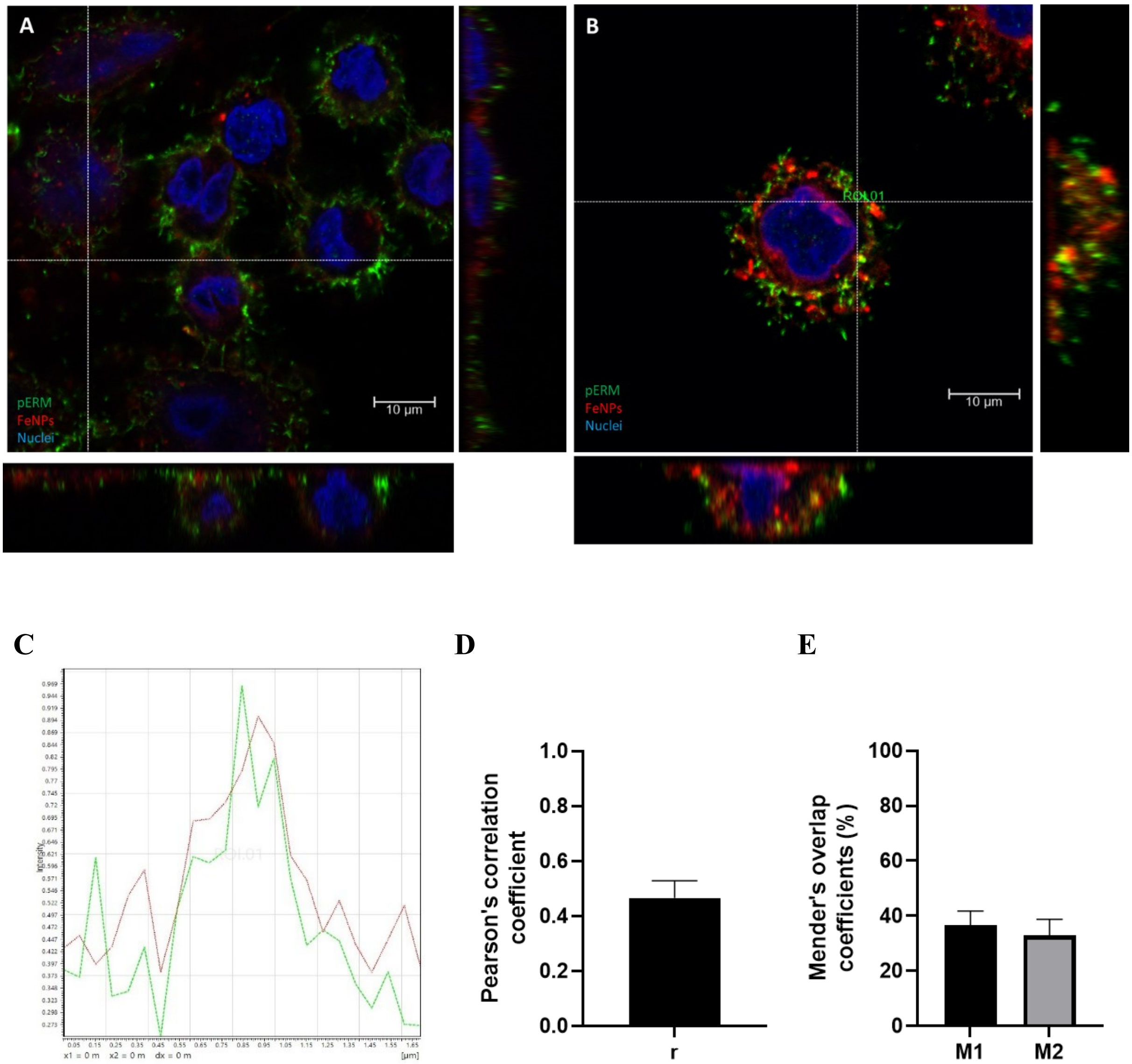

Figure 65. Co-localization analysis of IONPs and pERM. (A) *Representative confocal image of HeLa cells incubated with IONPs for 15 minutes. Maximum projection of 20 confocal planes of 0,35 µm. The relative cross-sections show the relative distribution of IONPs (red) and pERM (Green) on the surface of the cells. (B) Enlargement of a single cell. The image is a single confocal plane, specifically in the upper part of the cell body, where just microvilli and adherent IONPs were present. The relative cross-sections show the zones of co-localization between pERM and IONPs (C) Intensities of green and red fluorescence plot against distance (µm) from the picture (B) (ROI01). It is possible to appreciate a common profile of red and green fluorescence. (D) Pearson's coefficient from pERM-IONPs colocalization. (E) Mender's overlap coefficients (%). Data were analyzed using ImageJ software. Colocalization was calculated through the JACoP plugin. For the analysis at least 3 different images (zoom 1.5) were considered. Just upper stacks were analyzed. Data are expressed as average ± SD.*

The IONP-cell interaction was also confirmed by confocal microscopy (**Figure 65**). For this type of analysis, the IONPs were made fluorescents by intercalating the DiI fluorophore (ex. 540 nm; em. 585 nm) in the PAA coating, as it was done for CNPs (**Figure 35**).

After 15 minutes of incubation, the IONPs clearly decorated microvilli but they were also visibly already internalized (**Figure 65, A-B**). The cross-sections in **Figure 65, B** shows how the correlation between microvilli and IONP is evident (**Figure 65, C**), as the pERM-positive microvilli appeared also positive for the IONPs signal.

These observations were confirmed by the colocalization analysis (**Figure 65, D-E**). A positive correlation between pERM and IONPs appeared, with a PCC of 0,5 ± 0,06 (**Figure 65, D**) and 33% ± 5,9 of IONPs overlapping with the signal of pERM (**Figure 65, E**).

To confirm that also in the case of IONP as for CNPs was mediated by microvilli, **flow cytometry analysis** was performed. In particular, the adhesion of IONPs was analyzed after 15 minutes in different conditions: control cells, cells with reduced levels of sphingomyelin (using myriocin), cells with reduced levels of cholesterol (using MβCD), or a combination of both treatments (**Figure 66**). The treatments aimed at interfering with the microvillar structure, in order to observe how the interaction of the nanoparticles with the cell was affected.

As can be seen from the graph in **Figure 66**, the pERM signal was influenced differently depending on the treatment. The inhibition of sphingomyelin synthesis, by myriocin, led to no difference in the pERM signal compared to the control (100,5% of myriocin vs 100% the control). The extraction of cholesterol from the membranes, by MβCD, was instead accompanied by a drastic reduction (33,7%) of the signal. Finally, the blocking of sphingomyelin synthesis and the simultaneous extraction of cholesterol from the cell membrane leads to an even further reduction (21,6%) of the pERM signal.

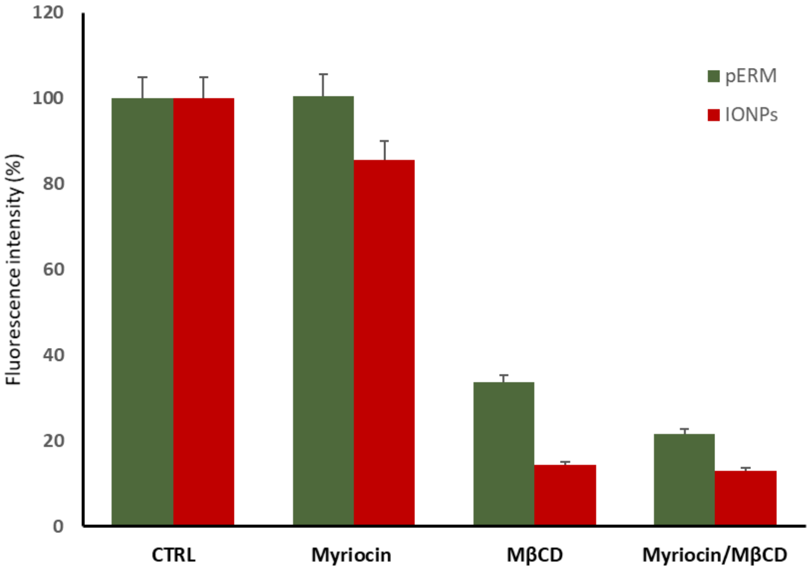

Figure 66. *Microvilli and lipid rafts are fundamental for NP−cell interaction: effect of lipid raft alteration on IONPs adhesion to microvilli. Flow cytometry measurement of cells with reduced phospholipids levels (Myriocin), cholesterol (MβCD), or both (myriocin/MβCD). Data are expressed as an average from three independent experiments ± SD.*

The reduction in the pERM levels indicates that the treatment, aiming at modifying the membrane components of the microvilli, has actually led to an alteration of the cell protrusions.

Samples treated with myriocin and/or MβCD were then analyzed considering the IONPs signal (**Figure 66**). The treatments that lead to inhibition of sphingomyelin synthesis and extraction of cholesterol from the membranes, showed a reduction in IONPs compared to the control. Specifically, the removal of cholesterol was accompanied by a reduction in IONPs signal, both when MβCD was used alone (14,2%) or when it was in combination with the inhibitor of sphingomyelin synthesis (12,9%). Differently, by only inhibiting the synthesis of sphingomyelin, there was a minimal reduction compared to the control (85.6%). These results are in accordance with those obtained for HeLa cells and the CNPs (**Figure 40**).

Interaction of IONPs with REN cells

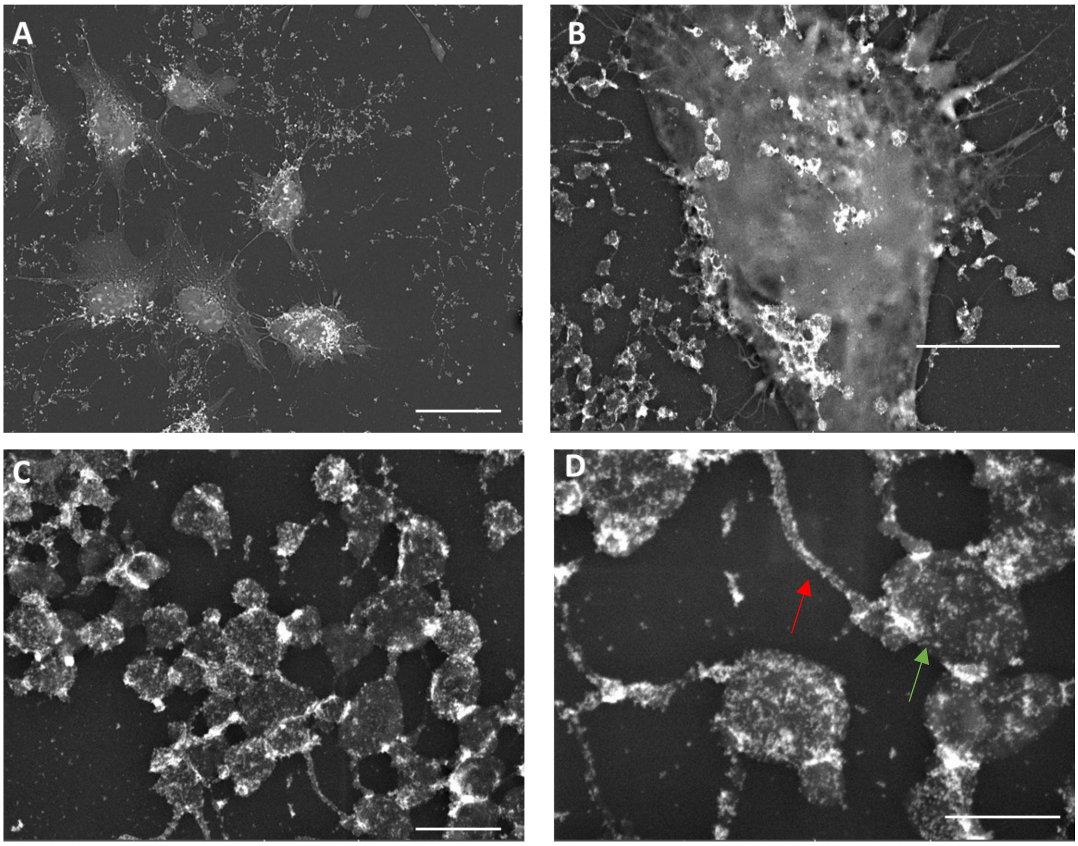

Figure 67. Representative images of the interaction of IONPs with microvilli of REN cells. *(A) All the REN cells seemed to interact in the same way with IONPs. Bar = 50 µm. (B) enlargement of a single cell. IONPs interact selectively with the cellular protrusions of REN cells. Bar = 10 µm. (C) IONPs interacted selectively also with the extracellular protrusions. Bar = 2 µm. (D) enlargement of (C). Single NPs are visibly interacting with the membrane of extracellular protrusions. Bar = 1 µm.*

IONPs proved to possess the same kind of selective interaction with microvilli also in REN cells when analyzed by SEM (**Figure 67**). When REN cells were incubated with IONPs for 15 minutes, instant binding with the cellular protrusions and the pancake-like structures was visible (**Figure 67, A**). In the enlargement (**Figure 67, B**) it is possible to appreciate the selectivity of the interaction: while the protrusions were densely decorated with IONPs, the planar part of the membrane was instead clean of NPs. IONPs interacted also with the pancake-like structures attached to the substrate (**Figure 67, C-D**). As in the case of CNPs, also for the IONPs different kinds of interaction were visible, with vesicles highly decorated close to others where the interaction appeared more sparse (**Figure 67, D**).

3.3.8 Effect of the NP size on the interaction with microvilli

Synthesis and characterization of NPs of different size

To evaluate the role of NPs dimensions on the interaction with microvilli of HeLa cells, IONPs of different sizes were obtained by centrifugation of the nanoparticles at different speeds. Moreover, to obtain even larger NPs, NPs with a boron carbide core (B) were covered with IONPs (**B-IONPs**). The multifunctional B-IONP nanomaterials were obtained by precipitating the Fe3O4 in the presence of B to obtain a stable solution of B-IONP of dimension bigger than IONPs alone.

The dimensions of the NPs (after being separated by centrifugation) were analyzed by DLS (**Table 3**).

Sample	***DLS***
B-IONPs	91 ± 15 nm
IONPs (fraction 1)	79 ± 5 nm
IONPs (fraction 2)	56 ± 4 nm
IONPs (fraction 3)	42 ± 1 nm

Table 3. DLS of the IONPs fractions obtained.

From these results is possible to conclude that 3 different fractions of IONPs were separated, from smaller aggregates (42 nm ± 1 nm) to medium (56 nm ± 4 nm) to larger aggregates (79 nm ± 5 nm). Aggregates of almost 100 nm were obtained by adding a boron carbide core.

Interaction of NPs of different sizes with HeLa cells

Once NPs of different dimensions were obtained, the specific adhesion to microvilli was tested on HeLa cells and observed by SEM (**Figure 68**). IONPs with the smallest dimension (41 nm) (**Figure 68, A-B**), adhered on the surface of the microvillus membrane creating a continuous and uniform layer (**Figure 68, B**). With bigger dimensions (**Figure 68, B-C**), IONPs still interacted specifically with microvilli, but the adhesion on their surface was less uniform. At higher magnifications (**Figure 68, C**) it was possible to observe that the nanoparticles formed aggregates adhering on the surface of the microvillus in patches, while also interacting with the planar membrane of the cell. By increasing the dimensions to 79 nm (**Figure 68, E-F**), the specificity was further reduced as only sporadic aggregates were visible on microvilli. When B-IONPs of 91 nm were used, (**Figure 68, G-H**) no specific adhesion to microvilli was visible. B-IONPs formed instead aggregates randomly distributed on the surface of the cell.

In all three cases, the NPs presented the same constitutive elements represented by small IONPs, showing a strong affinity toward microvilli; therefore, it can be concluded that the observed different behavior was due to the NPs’ dimensions.

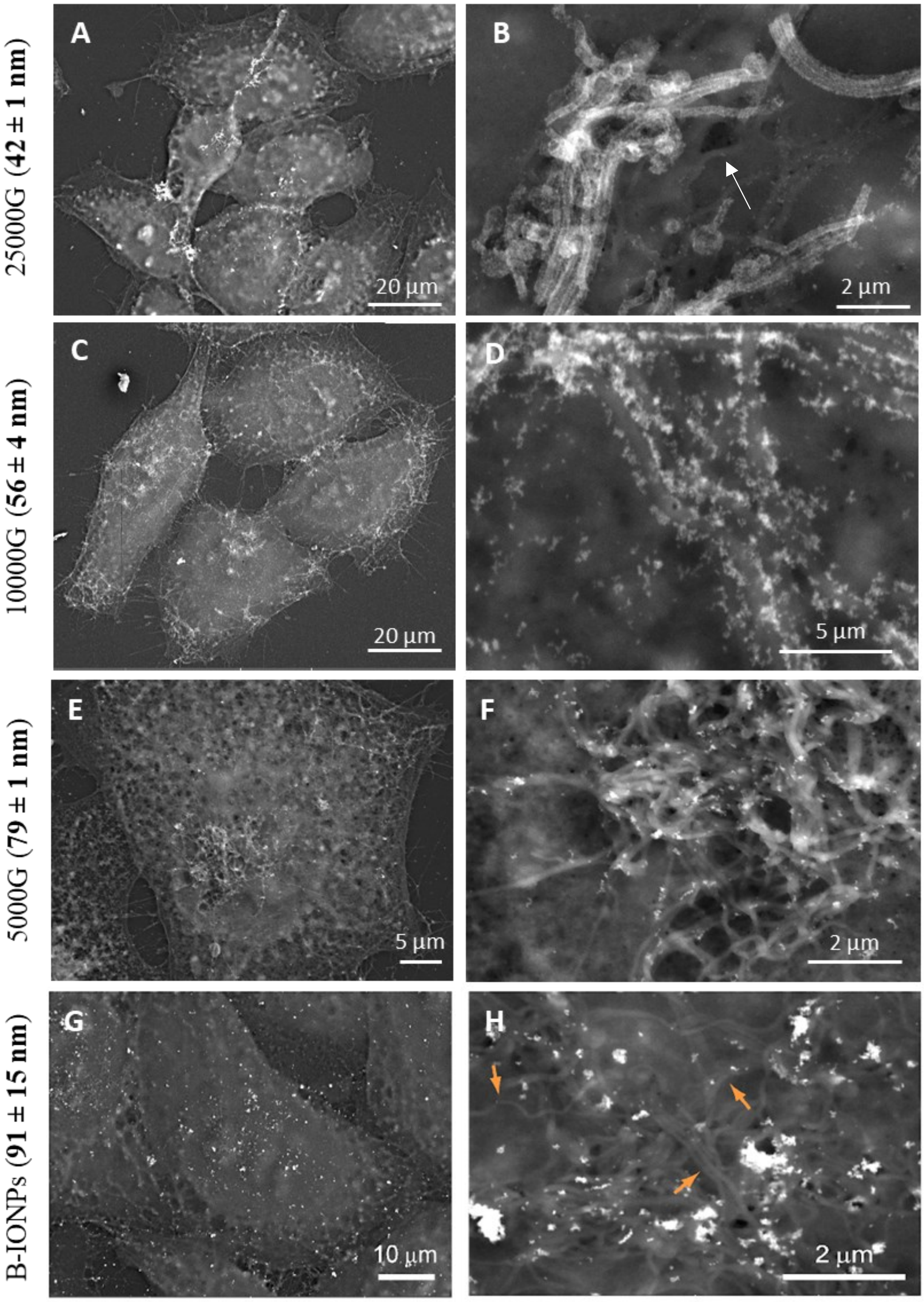

Figure 68. Influence of NPs size on microvilli interaction. *(A) IONPs of smaller size interacted with the microvillous surface in a way similar to CNPs. (B) enlargement of (A). The selective interaction of IONPs with microvilli's membrane is visible. Other microvilli with no nanoparticles on their surface are visible (white arrow). (C) The affinity toward microvilli was reduced by increasing the size of IONP aggregates (56 nm). (D) Enlargement of (C). In this case, IONPs still showed specific interaction with microvilli, but were distributed less continuously. (E) The largest aggregates (79 nm) did not show any interaction with microvilli. (F) Enlargement of (E) IONPs still were attracted to microvilli, but no specific interaction was observed. (G) B-IONPs, nanoparticles of even larger diameter (91 nm) did not interact with microvilli. (H) Enlargement of (G) No microvilli-mediated adhesion is visible, but nanoparticles are randomly distributed in big aggregates.*

3.3.9 Effect of the NP surface charge

To verify the role of the PAA coating in defining the selective interaction of CNPs with microvilli, the adhesion of CNPs with different kinds of functionalization was investigated. Specifically, three different NPs were synthesized in our laboratory:

1. substituting PAA with polyethyleneimine (PEI) (**PCNPs**).
2. substituting PAA with dextran (**DCNPs**);
3. excluding altogether PAA from CNPs synthesis (**CNP w/o PAA**);

Synthesis and characterization of PCNPs

To test the role of the CNPs surface charge on the selective nanoparticles adhesion to microvilli, CNPs with a positive charge were obtained. For this purpose, **PEI** was used, which is a cationic and water-soluble polymer that contains three types of amino groups, namely primary, secondary and tertiary, both in the main chain and in the branches. PEI-CNPs were analyzed by DLS and Z potential (**Table 4**).

Sample	DLS	Z potential
PCNPs	39 ± 2 nm	+20 (± 0.6) mV

Table 4. DLS and Z potential od PCNPs

The results showed that these nanoparticles were effectively monodisperse and with a very low hydrodynamic diameter, comparable with that of PAA-CNP (D = 14.8 (± 0.4) nm, Z Pot. -42 (± 2) mV). In terms of Z potential, the results were excellent because the CNPs assume a positive value, thanks to the presence of the protonated amino groups of the PEI on the surface.

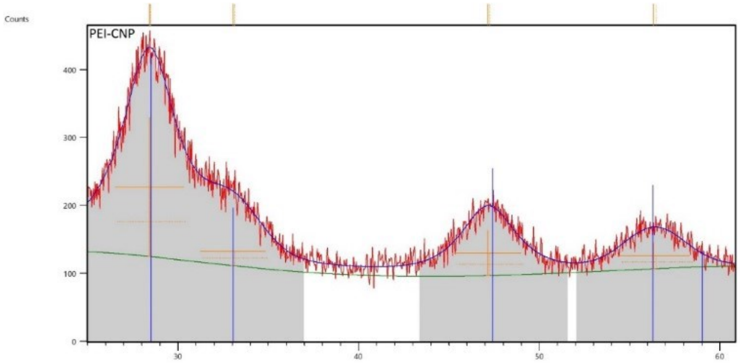

Figure 69. XRD analysis of PCNPs

The X-ray diffraction analysis provided the pattern shown in **Figure 69**. The pattern showed the presence of a single-phase attributable to ceria, but the peaks were considerably widened compared to the result obtained with the PAA-CNP (**Figure 23**), so that the first two signals, at 28.5° and 33°, were superimposed on each other. This indicates that the dimensions of the crystallites were very small; in fact, the application of the Scherrer equation resulted in an average diameter of 1.8 (± 0.5) nm, significantly lower than that of PAA-CNP (6.0 (± 0.8) nm). The comparison of this data with the DLS results, which show a size of 39 nm, suggests the presence of an extended polymeric shell or a moderate agglomeration level. This phenomenon is probably associated with the fact that the particles had a smaller diameter and, consequently, greater surface energy, which made them more likely to interact with both the polymer and other nanoparticles.

Interaction of HeLa cells with PCNPs

To test the PCNP ability to interact with the cells, PCNPs were incubated for 15 minutes with HeLa cells, as well as the CNPs, and the results were analyzed by SEM (**Figure 70**).

Figure 70, C-D, show how PCNPs were randomly distributed on the cell surface, without showing a particular specificity towards microvilli, as opposed to CNPs (**Figure 70, A-B**). The lack of adhesion of the PCNPs on the microvilli membrane is shown in detail in **Figure 70, D**. The microvilli present on the surface of the cell were clearly visible (orange arrows), but no adhesion of the NPs was observed. These images prove how PCNPs, despite having comparable dimensions with PAA-CNPs but different charge and chemical nature of functionalization, do not show any specificity toward microvilli. This result suggests that the surface charge, in addition to the size, is also a fundamental element in defining the specificity of adhesion on the microvilli membrane. Another possibility is that the same chemical nature of PAA is the factor that determines the adhesion between the CNPs and some specific component of the microvilli membrane.

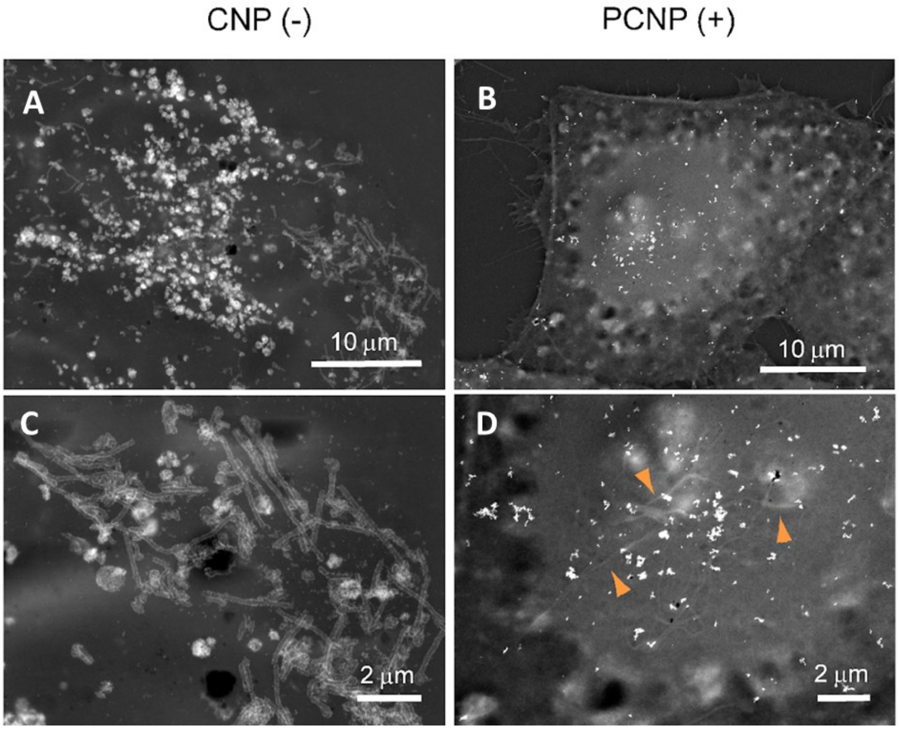

Figure 70. SEM-BSE images of cells treated with CNPs and PCNPs. *These NPs were negatively and positively charged, respectively. Different from CNPs, PCNPs did not interact with microvilli (indicated by arrowheads).*

Interaction of HeLa cells with DCNPs and CNPs w/o PAA

DCNPs were produced similarly to CNPs except for the substitution of PAA with Dextran. DLS showed a dimension of 6.5 ± 0.5 nm, and by XRD it was obtained a dimension of the crystallites of 3 nm. These DCNPs had an ionically neutral surface.

DCNPs and CNPs w/o PAA were incubated with HeLa cells for 15 minutes and the results were analyzed by SEM (**Figure 71**).

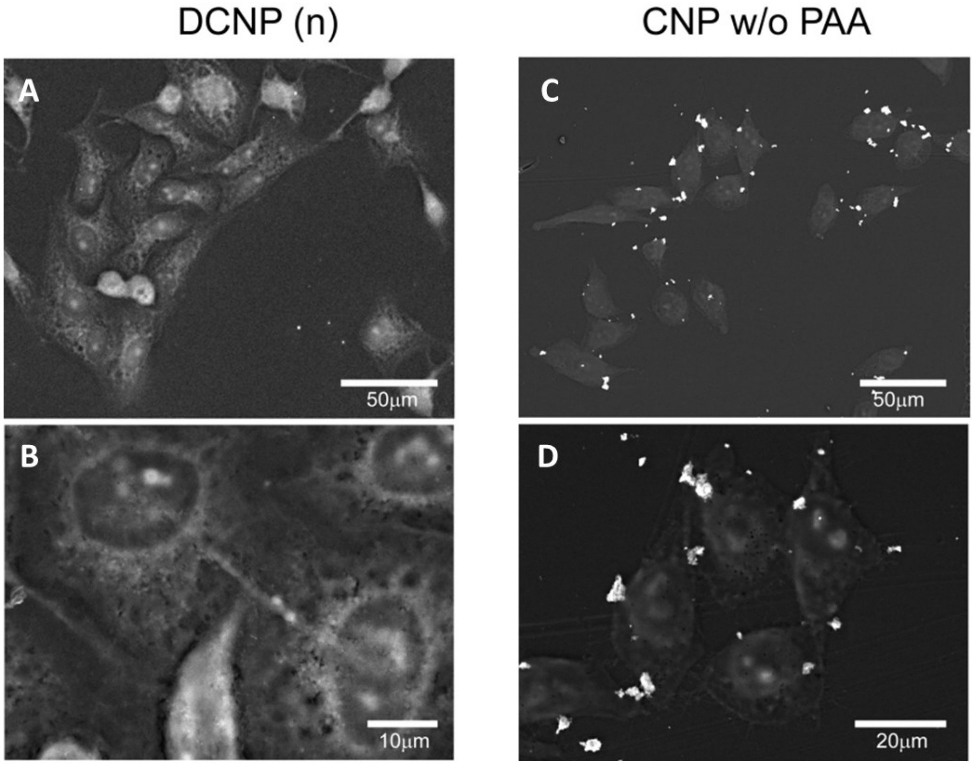

***Figure 71**. **CNP functionalization modified NP–cell interaction.** (A, B) Dextran coating reduced NP adhesion and internalization. (C, D) The absence of PAA on the NP surface eliminated specific interaction with the cell membrane, resulting in a random distribution of only a few large aggregates. SEM BSE images.*

In the case of DCNPs (**Figure 71, A-B**), no interaction with microvilli, or with the cells in general, was observed. When the PAA coating was excluded from the CNPs synthesis (**Figure 71, C-D**), the nanoparticles appeared on the cell surface distributed in random and large aggregates, but no interaction with microvilli was observed even when investigated at higher magnification (**Figure 71, D**).

This result suggests that the PAA coating and the negative surface charge of the NPs, in addition to size, are fundamental elements in defining the selective interaction with microvilli.

3.3.10 CNPs internalization in HeLa cells

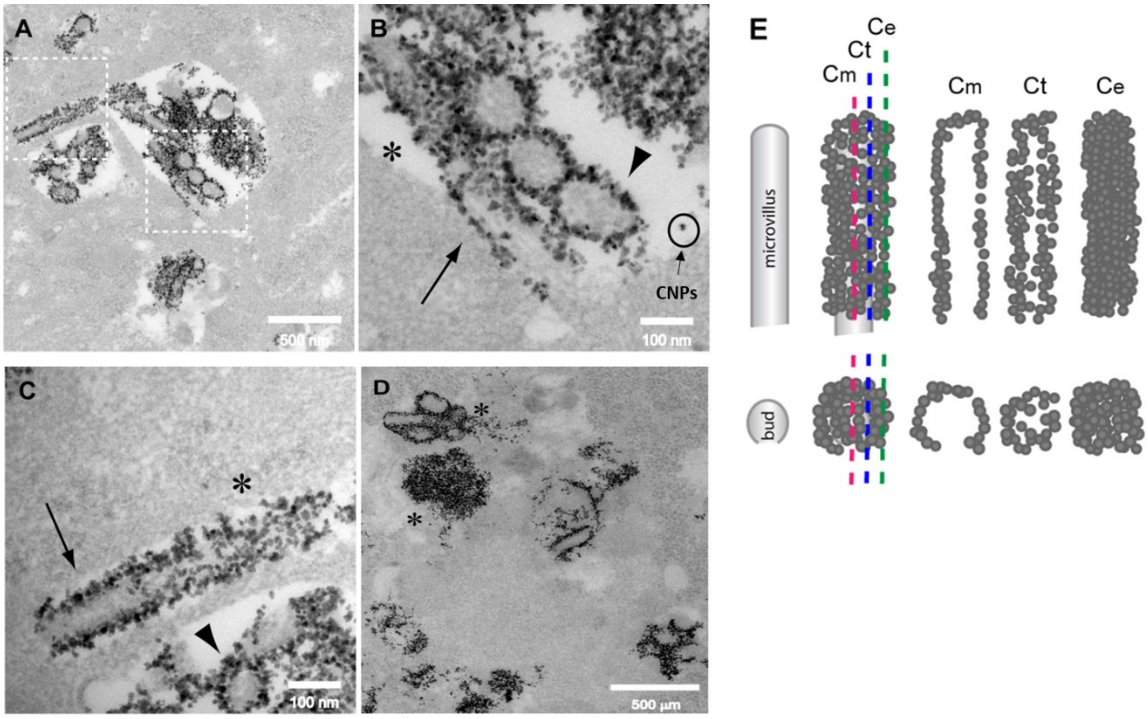

Figure 72. CNPs internalization in HeLa cells. *(A-D) Representative TEM analysis of HeLa cells incubated with CNPs (in black) after 24 hours of incubation. (A) CNPs were concentrated inside endolysosomal structures. (B, C) Enlargement of areas outlined in (A) showed only a few free CNPs inside the vesicles (circle), with most being adherent to cylindrical structures resembling microvilli (arrows) or bud-like structures (arrowhead) that mediated their extracellular adhesion. (D) Larger CNP aggregates are derived from several microvilli/buds assembled together (*). (E) CNP-covered microvilli/buds appeared different depending on the position of the sectioning plane. When sectioned in proximity to the external surface, only a uniform layer of NPs was observed (Ce and regions marked by * in B, and C). The internal structures of microvilli or buds began to appear if the cutting crosses tangentially (Ct) the microvilli surface. When the section crossed in the middle of the microvilli or buds (Cm), the CNPs appeared as a granulated uniform layer outlining their perimeter (arrow and arrowhead in B and C).*

Once the adhesion of CNP on the cell surface was characterized, the next question was how CNPs, adhering to microvilli with such a peculiar affinity, could be internalized by the cell. Further TEM analysis evidenced some unusual characteristics, as it’s possible to observe in **Figures 72**. Following adhesion to microvilli, CNPs (visible in this case as black dots) were transferred into endolysosomal structures. However, within these structures, the

CNPs appeared to be still mostly attached to portions of the microvilli or buds of growing microvilli. The diameter of the CNP-decorated structures observed in the endolysosomes was comparable to that of the microvilli/buds observed on the cell surface (75.88 ± 14.17 vs 74.60 ± 13.25 nm, respectively). The diameter of the microvilli and buds was determined only on structures similar to those shown in **Figure 72, C** (arrow, microvilli; arrowhead, buds) whose structure is schematized in **Figure 72, E** as *Cm*. Decorated structures indicated by an asterisk in **Figure 72, C** were not considered for the measurements. This observation suggests that once "decorated" by CNPs, microvilli, and buds were not disassembled but were internalized as a whole, probably being perceived as material to be eliminated.

To further determine the role of endocytic pathways and vesicle compartments in CNPs entry, Colocalization with the lysosomal-associated membrane protein **LAMP-1** was investigated after 2 hours of incubation.

When LAMP1 was tested, a positive correlation was observed in all the cells (**Figure 73, E**). In the relative cross-sections of single-cell enlargement (**Figure 73, F**), several colocalization points were visible around the nucleus of the cell (visible in yellow). When this colocalization was quantified, it was obtained a PCC of 0.64 ± 0.04 (**Figure 73, G**), while 74% ± 8 of FCNPs were found inside lysosomes (M_2) (**Figure 73, H**).

This result is in accordance with recent findings from our group [Ferraro D., et al., 2017]**.** Specifically, previous results indicated that the expression of LAMP-1 increased by 20% after 6 hours of incubation with CNPs, outlining an accumulation of the NPs inside lysosomes after the uptake.

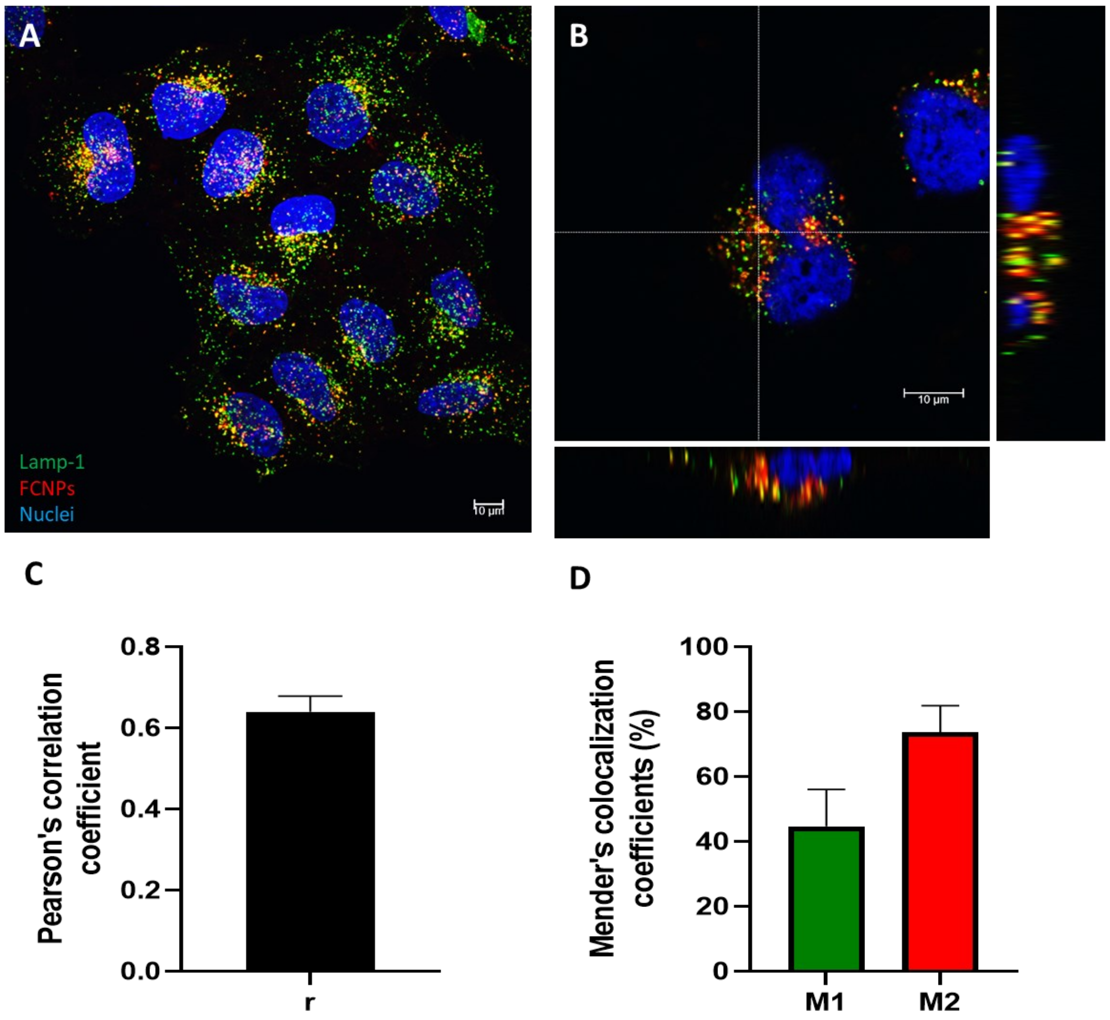

Figure 73. intracellular fate of CNPs in HeLa cells. *(A) Representative image of HeLa cells incubated with FCNPs for 2 hours. Maximum projection of 20 planes of 0,35 µm. Blue, nucleus; Green, LAMP-1; Red, FCNPs. (B) Enlargement of (A) and relative cross-sections where the LAMP-1-FCNPs colocalization spots are visible in yellow. (C) PCC from LAMP-1-CNPs colocalization. (D) MOC from LAMP-1-FCNPs colocalization (M_1) and from FCNPs-LAMP-1 colocalization (M_2). All data were analyzed using ImageJ software. Colocalization was calculated through the JACoP plugin. For the analysis, at least 3 different images were considered. In every image, every cell was analyzed separately. Just upper stacks were analyzed. Data are expressed as average ± SD.*

Inhibition of CNPs endocytosis

In order to characterize the mechanism of endocytosis by CNPs, inhibitors were used to perturb endocytosis. Results were analyzed by flow cytometry.

The process of CNPs internalization was already investigated by Singh S. and colleagues [Singh S., et al., 2010]. In particular, the authors studied the internalization of CNPs functionalized with Carboxyfluorescein in a transformed aneuploid immortal keratinocyte cell line (HaCaT cells). They obtained nanoparticles of 5-6 nm and a surface charge of -18 mV. [Singh S., et al., 2010] They concluded that uptake of the CNPs was energy-dependent and mediated via Clathrin-dependent endocytosis from lipid rafts.

To study the internalization process of our PAA-coated NPs, it was first determined if the uptake of CNPs was energy-dependent, by analyzing whether the NPs internalization changes at low temperatures in HeLa cells. As it is possible to observe in **Figure 74**, flow cytometry analysis showed that after 10 minutes of incubation at 4°C the FCNP adhesion was comparable to the adhesion obtained at 37°C, while the internalization levels evaluated after 2 hours of incubation, were blocked by low temperatures (693% vs 114%). In this case, the CNPs were incubated for 10 minutes or 2 hours after preconditioning at 4°C for 30 minutes. Low-temperature incubation of cells not only slows the metabolism of the cells but also imparts rigidification of the lipid membrane [Letoha T., et al., 2005].

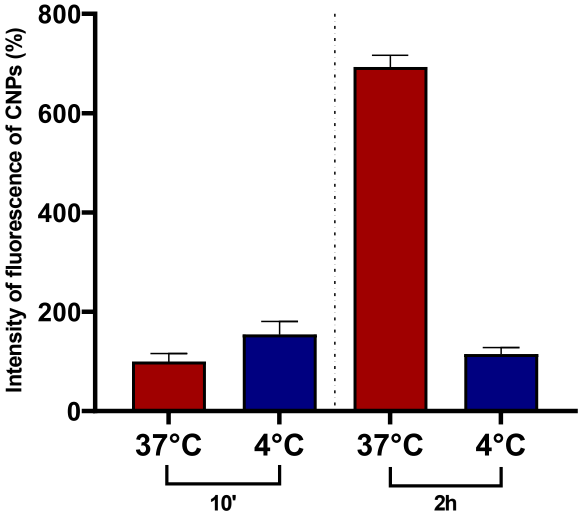

Figure 74. Low temperatures block CNPs internalization on HeLa cells, but not adhesion. *Cytofluorimeter analysis showing comparison of adhesion (10 minutes) of FCNPs on HeLa cells incubated at 37°C or 4°C. And comparison of internalization (2h) of FCNPs on HeLa cells incubated at 37°C or 4°C. Bars are normalized with 37°C -10' considered as 100%. ± SD of 3 independent experiments.*

As a second step, to determine whether CNPs entry could be inhibited, different inhibitors targeting multiple endocytic pathways were used. However, compounds that block specifically each type of endocytic mechanism are not yet available. For this reason, a combination of different inhibitors was used. For each one of them, concentration and incubation time were chosen according to the literature [Sousa de Almeida M.S., et al., 2021].

The inhibitors chosen were:

- **CytD**, known to block actin polymerization. The actin cytoskeleton is essential for many important cellular processes including muscle contraction, cell motility, cell division cytokinesis, vesicle and organelle movement, and cell shape. Generally, it is used as a marker for blocking phagocytosis and macropinocytosis. However, it can affect also other endocytic mechanisms [Kuhn D. A., et al., 2014] [Fujimoto L. M., et al., 2000]. The interference of CytD in the adhesion of CNPs on microvilli in HeLa cells was already discussed (**Figure 46**).
- **Hypertonic sucrose** used to investigate whether Clathrin was involved in the uptake of CNPs. Hypertonic sucrose can disrupt the formation of cellular Clathrin-coated pits and vesicles, thus can be related to the inhibition of Clathrin-mediated endocytosis (**CME**) [Singh S., et al., 2010].
- **Wortmannin** interferes with the actin cytoskeleton, by inhibiting the phosphatidylinositol3-kinase. Wortmannin is commonly used as an inhibitor for macropinocytosis [Nakase I., et al., 2004].
- **Amiloride**, commonly used to block macropinocytosis [Beignon A.S., et al., 2005].
- **Nystatin** and **MβCD** interfere with lipid rafts and have been proposed as indicators for caveolae-mediated endocytosis [Sousa de Almeida M.S., et al., 2021]. MβCD's role was already described in previous paragraphs, and the interference of cholesterol depletion in the adhesion of CNPs on microvilli was discussed (**Figure 40)**. Nystatin can decompose cholesterol, and thus also inhibit caveolae/lipid-mediated endocytosis [Singh S., et al., 2010].

For quantitative analysis, HeLa cells were incubated with CNPs for 15 minutes (*pulse*), washed with PBS, and incubated with NPs-free medium for 1 hour (*chase*) before fixation. For all the conditions, the inhibitors were kept in the medium prior, during and after the incubation with NPs. Results were analyzed by flow cytometry.

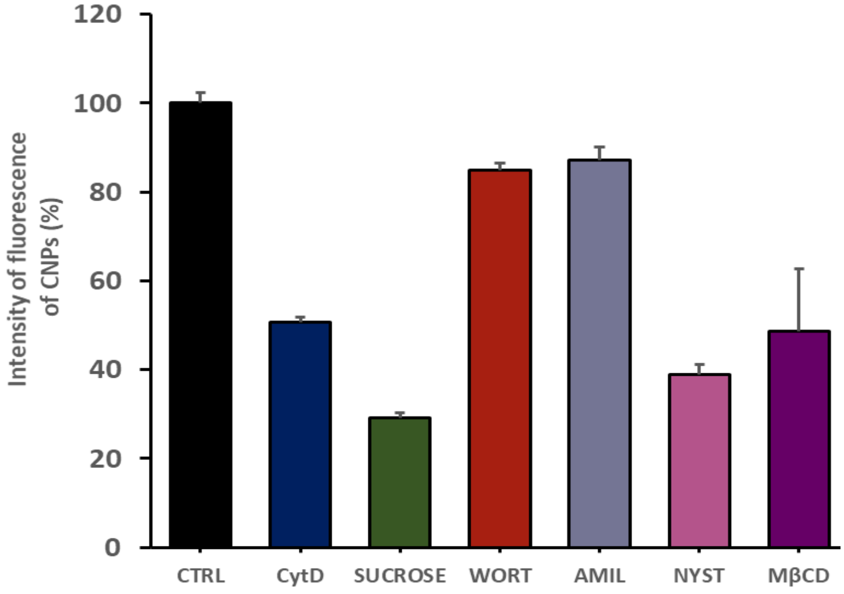

Figure 75. Relative fluorescent intensity of FCNPs with the selective inhibitors in HeLa cells. *Data are presented as mean ± SD versus the respective ctrl (cells incubated with CNPs w/o inhibitors).*

As it is possible to observe in **Figure 75**, the least effective in the inhibition of CNPs endocytosis were Amiloride and Wortmannin, respectively 87.1% (± 3) and 84.9% (± 1.64). On the contrary, hypertonic sucrose was able to reduce the uptake of CNPs to 29.1% (± 1.09). CytD, on the other hand, showed to powerfully inhibit the internalization of CNPs, which was reduced by half (50.67% ± 1.05), even if previous analyses showed no influence in the CNPs-adhesion (**Figure 45**). This difference can probably be attributed to the longer incubation times of both CytD and CNPs.

Finally, the depletion of cholesterol appeared to also be fundamental for the CNPs internalization. MβCD and Nystatin, in fact, were both effective on the inhibition of the uptake of CNPs, with values respectively to 48.7% ± 14 and 39% ± 2.26

3.4 Discussion

This thesis aimed to study the interaction of CNPs with biological model systems. Thanks to their antioxidant properties, CNPs can be considered a potential pharmacological defence in the treatment of those diseases that are characterized by a high level of free radicals, such as neurodegenerative diseases (*e.g.*, Alzheimer's) [Spuch C., et al., 2012]. Although a mechanism has been hypothesized that justifies their antioxidant activity, this mechanism has never been validated through a detailed study of their behavior in a biological environment. Understanding the intracellular behavior of CNPs, however, is a crucial information for optimizing their possible future use *in vivo*. The role that CNPs play in the cells is also closely linked to the mechanism by which they are internalized. To optimize their intracellular action, it is therefore essential to understand the previous phase of cell uptake. The purpose of this thesis was precisely to understand how and through which mechanism the CNPs interact with the cell and are internalized. For this purpose, CNPs were synthesized "in-house" using PAA functionalization. PAA is a coating agent, rarely used for the synthesis of NPs, and with its deprotonated carboxyl groups make the nanoparticle negatively charged. The synthesis allowed to obtain PAA-CNP with a core size of 6 nm and an overall hydrodynamic diameter of 14.8 nm. The use of nanoparticles in the order of a few nm allowed to highlight for the first time a process of adhesion and internalization which had never been described previously. In fact, from what is present in the literature to date, the attention has largely been directed to the study of NPs with dimensions in the range of tens of nm [Li Y., et al., 2016]. Moreover, together with size, also functionalization played a great role in discovering the CNPs adhesion process.

The HeLa cells were initially used to evaluate the cell adhesion of the NPs. **HRSEM analyses** showed that CNPs interacted selectively with cellular protrusions, giving rise to an extremely specific decoration that took place in a few minutes. By analyzing the length and diameter of the cellular protrusions decorated with CNPs, it was possible to identify them as microvilli (**Figure 31**). The adhesion to microvilli was so specific that CNPs covered the entire length of the microvilli **(Figure 30, E)** while leaving the rest of the cell membrane completely devoid of particles. A clear line of demarcation was visible at the base of the microvilli where CNPs abruptly stopped adhering (**Figure 32, B**), confirming that the CNPs did not adhere uniformly over the entire cell surface, but only in correspondence with the microvilli. It should be emphasized that this observation was possible thanks to the use of samples fixed as monolayer and not, as commonly done, as cell pellets. In the latter case, the cells are generally detached from the substrate by an enzymatic treatment, and this produces not only an alteration of the three-dimensional structure of the cell monolayer and the cells themselves, but it would alter the microvilli and other fine structures. The "in place" fixation of the entire cell monolayer made it possible to analyze the preparation under the conditions most similar to the situation *in vivo* while preserving even the most fragile cell structures.

Another characteristic to note was that, contrary to what was expected, the nanoparticles were not uniformly picked up by the cells (**Figure 30, A**). Within the same areas, it was possible to find groups of cells containing high amounts of CNPs contiguous to groups where there was no uptake and/or internalization.

The specific interaction of CNPs with microvilli was particularly evident by **HRTEM analysis** (**Figure 75**). Due to such a specific interaction with microvilli, this type of adhesion was called **Microvilli Mediated Adhesion** (**MMA**). To nature of the CNP high selectivity was investigated using different strategies. In particular, it was evaluated how incubation time, NP concentration, type of cell culture medium, and incubation temperature influenced the CNPs adhesion. HRSEM analyses showed that CNPs specificity was not influenced by different concentrations (100, 200, and 500 µg/mL) or different exposure times (5 minutes or 6 and 24 h) **(Figure 36)**. Interestingly, the adhesion was shown to be already evident after only 5 minutes of exposure, demonstrating how specific the interaction was. Even the temperature changes showed to not affect heavily the MMA. CNPs added to cells preconditioned at 4°C, were still able to interact with microvilli (**Figure 39)** although the specificity was partially lost, and a less uniform layer of NPs was visible compared to the continuous "decoration" in the case of incubations at 37°C. The patchy distribution of the CNPs could be explained by the redistribution of the lipid raft components to form larger clusters below 37°C [Gorelik, J., et al, 2003].

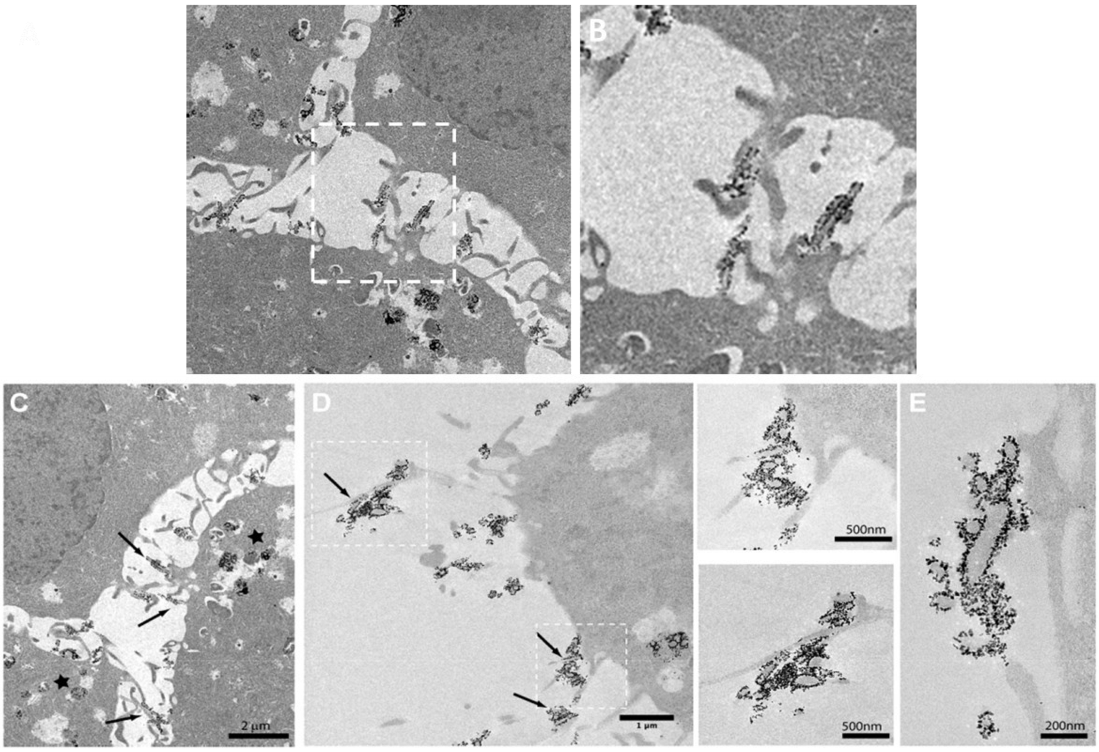

Figure 75. *(A-C), HeLa cells were incubated with CNPs for 24 h. CNPs, visible as black spots, were present on cell protrusions (arrows) and accumulated inside vesicles (stars). (B), enlargement of (A) showing the specific interaction with membrane protrusions. (D), On the cell surface, CNPs decorated only the cell protrusions (arrows) without adhering to the planar region of the membrane. (E) two enlargements of (D), showed the specific interaction between CNPs and microvilli.*

Pulse-chase experiments were also performed to follow the microvilli dynamics in the presence of CNPs. The literature reports that the lifecycle of short microvilli of 500 nm, like those in HeLa cells, is ~12 min [Gorelik, J., et al, 2003]. Based on this observation it was hypothesized that, after a chase period> 12 minutes, no decorated microvilli should have been observed on the cell surface because they should have already been internalized or dismantled. In contrast, 2 hours after the removal of CNPs, decorated microvilli were still detected, suggesting that the dynamics of the CNP-bearing microvilli could have been impaired or altered.

MMA, observed first by electron microscopy, was then confirmed by **confocal microscopy** using fluorescence CNPs. With the use of pERM, a protein complex is characteristic of the microvilli membrane, it was possible to confirm the specificity of the CNPs towards the cell protrusions. **Colocalization** between CNP and pERM (**Figure 35**) was observed, confirming that the cell protrusions decorated by the CNPs were indeed microvilli. This result demonstrated how the MMA, previously observed only by electron microscopy, could also be efficiently analyzed by flow cytometry and fluorescence microscopy. This allowed expanding the possibilities of analysis, allowing to study in a more targeted way the role of microvilli and their membrane components in the adhesion mechanism, without depending exclusively on scanning electron microscopy analyses.

The fact that the nanoparticles adhered so quickly and specifically to the microvilli and not on the planar membrane suggested that the microvilli membrane contains one or more target components that make it exclusive for the interaction with CNPs. Microvilli, in fact, have a different membrane from the rest of the planar membrane of the cell, both in composition, distribution, and density. Furthermore, some membrane proteins that are localized in the lipid rafts of the microvilli are almost exclusively present at the level of the protrusions and not in the planar membrane. The pERM protein complex, which acts as a bridge between actin and the membrane, is an example, being a primary constituent of microvilli. To evaluate how the membrane/lipid raft was fundamental in mediating the adhesion with CNPs, the cells were treated with agents that alter the **cholesterol** and **sphingomyelin** content. Through flow cytometry analysis it was possible to monitor the effect of the treatments by observing the trend of the pERM level (**Figure 40**). The reduction of sphingomyelin synthesis did not determine a decrease in microvilli, compared to the control conditions, but it induced an unexpected increase. Differently, the reduction of the cholesterol level proved to be very effective, reducing the level of pERM by about half compared to the control, an indication that the microvilli must have actually been altered. However, the maximum effect was obtained following the combined treatment in which both sphingomyelin and cholesterol were altered. Parallel analyses of the CNPs levels, concerning the alteration of microvilli, showed a trend similar to pERM (with the reduction in CNPs adhesion mimicking the pERM levels), except when only sphingomyelin was reduced.

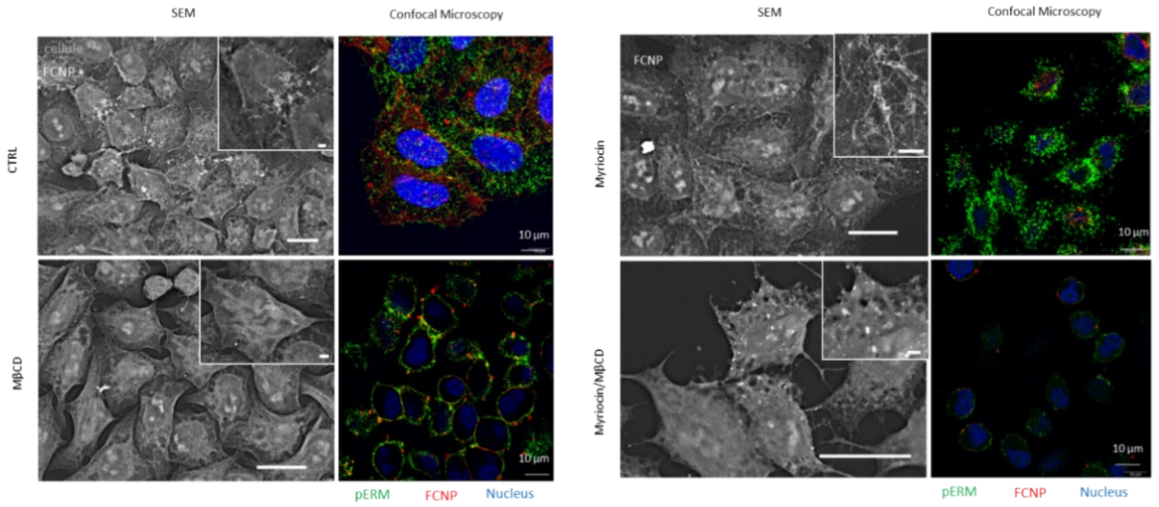

Figure 76. HRSEM and confocal microscopy analysis of the effect of the alteration of the microvilli membrane components on the levels of pERM and CNPs adhesion/internalization. *Green, pERM; Red, CNPs; Blu, nuclei. HRSEM images**:** bar equal to 20 µm; inset: bar equal to 2 µm.*

These observations confirmed that, by modifying the membrane components of the microvilli, it was possible to alter their formation and prove that this alteration led to a simultaneous modification of the adherent CNPs. This demonstrates how these protrusions are important for the interaction of ceria nanoparticles with cells. It was still difficult to identify which component was responsible for such a specific adhesion on microvilli. However, since there was a loss of specificity following the alteration of the membrane, it can be stated that cholesterol and sphingomyelin, the main elements of lipid rafts, were likely the mediators of the interaction between CNPs and the microvilli membrane.

Since the quantitative analysis obtained by flow cytometry did not allow us to understand how the microvilli had actually been altered by the removal of cholesterol and/or sphingolipids, it was decided to observe the cells by confocal microscopy and electron microscopy (**Figure 76**). By visualizing the actual alteration of the microvilli and the distribution of the residual CNPs, the IF analysis made it possible to clarify that, following the alteration of the membrane components of the microvilli, the nanoparticles aggregated in various points of the cells.

Although the analysis using confocal microscopy had helped to define a clearer picture of the CNP-cell interaction, only an ultrastructural analysis could have provided more precise information about the state of the cell protrusions/microvilli and the type of interaction of the residual CNPs with the altered microvilli. Concerning the treatment that led to the removal of the sphingomyelin, the HRSEM analysis showed the presence of very small aggregates on the planar membrane and long microvilli. However, the adhesion of the CNPs on these microvilli was not uniform, as in the control condition, but was more sparse, appearing as "pitting" along the microvilli. The fact that, despite the removal of sphingomyelin, a portion of CNPs continued to adhere to the microvilli could lead to the deduction that the anchoring areas are precisely the lipid rafts, whose integrity is lost in the absence of the sphingomyelin, which does not determine however the disappearance of the microvilli, while the cholesterol share is reorganized in a more lax way. Perhaps in this could lie the reason why, in the absence of sphingomyelin, but the presence of cholesterol, the microvilli stretch as a result of altered lipid rafts. Furthermore, the increased number of microvilli and the adhesion of CNPs to the planar membrane would explain why the reduction to sphingomyelin was not matched, in flow cytometry, to an equal reduction in

CNPs. On the contrary, where the cholesterol is removed, the architecture of the microvillus was completely modified, causing it to shorten or wrap around itself. It is precisely in these areas that the residual CNPs were concentrated which, covering a much smaller area in total due to the shortening of the microvilli, were present in lower quantities than in the control. The fact that these short protrusions were completely covered with CNPs may indicate that, since there was no total elimination of cholesterol but only a reduction, the residual share continues to produce adhesion or that the adhesion is also mediated by other membrane constituents that remained associated with what was left of cholesterol.

To understand whether the failure and/or reduced adhesion of CNPs to cells depleted of cholesterol or sphingomyelin is due to the loss of the global architecture of the microvillus and/or to the loss of an adhesion "platform" consequent to the disorganization of the proteins, cells were treated to reduce the polymerization of actin. By analyzing the effects of **CytD** on HeLa cells by confocal microscopy and HRSEM, it was possible to prove that the adhesion was not blocked in this condition, but CNPs were still able to interact with the membrane of microvilli, even if the cytoskeleton of microvilli was destroyed. Microvilli appeared like blebs on the membrane of the cells. In this case, their original shape was lost, but not the membrane constituents, which consequently were concentrated in a smaller space, probably exposing more constituents of the lipid rafts, hence favoring the nanoparticle adhesion. This observation can justify why, by quantifying the signal by confocal microscopy (**Figure 44**) – and later confirmed by flow cytometry (**Figure 45**) – the adhesion of CNPs was not reduced but increased, maintaining colocalization with Phalloidin and pERM (PCC respectively 0,62 ± 0,04 and 0,37 ± 0,07) (**Figure 44**).

To confirm this theory, cells were treated to destroy both actin and cholesterol, thus also altering the membrane composition (**Figure 46**). The analysis showed that, in the case of the combined treatment, the adhesion and internalization of CNPs were blocked. This result was of fundamental importance because, together with the analysis conducted so far, it proved that the MMA depends on the membrane composition of microvilli (specifically lipid rafts), but not on the microvillus cytoskeleton.

Since has been shown that in HeLa cells the density of microvilli varies with the phase of the **cell cycle**, peaking towards the G2 / M phase [Lundgren E., et al., 1976], it was investigated whether the microvilli density could influence the level of CNPs adherent to the cells. The results not only confirmed the actual variation in the density of microvilli (G1 <S <G2 / M), as described in the literature [Lundgren E., et al., 1976], but once again demonstrates the close correlation between CNPs-adhesion and microvilli.

To exclude the possibility that MMA was **cell-dependent**, the interaction of CNPs on other cell types was tested. Specifically, by analyzing for short incubation times by HRSEM, it was possible to confirm that the MMA was present also in MSTO, REN, and A431 cell lines. However, no specific adhesion was observed in COS-7 cells, that lacked microvilli on their surface. Here, CNPs were distributed on the cell membrane as small patches. Moreover, by analyzing the pERM signal together with the CNPs adhesion, it was possible to confirm in REN and MSTO cells that the cellular protrusions observed by electron microscopy were indeed microvilli, being pERM-positive, and showing colocalization of 0,409 ± 0,03 in REN cells (**Figure 51**).

In REN cells it was also possible to confirm the results obtained in HeLa cells, by seeing a reduction in the nanoparticle adhesion and internalization in the case of the cholesterol removal or the combined treatment. Interestingly, from the cells originated several extracellular vesicles with a pancake-like structure, that were able to interact with CNPs in the same way as with the cellular protrusions still attached to the cell body. By analyzing the membrane components of these extracellular vesicles and comparing that to the cellular protrusions, it was possible to observe that they did not contain pERM, but were Flotillin

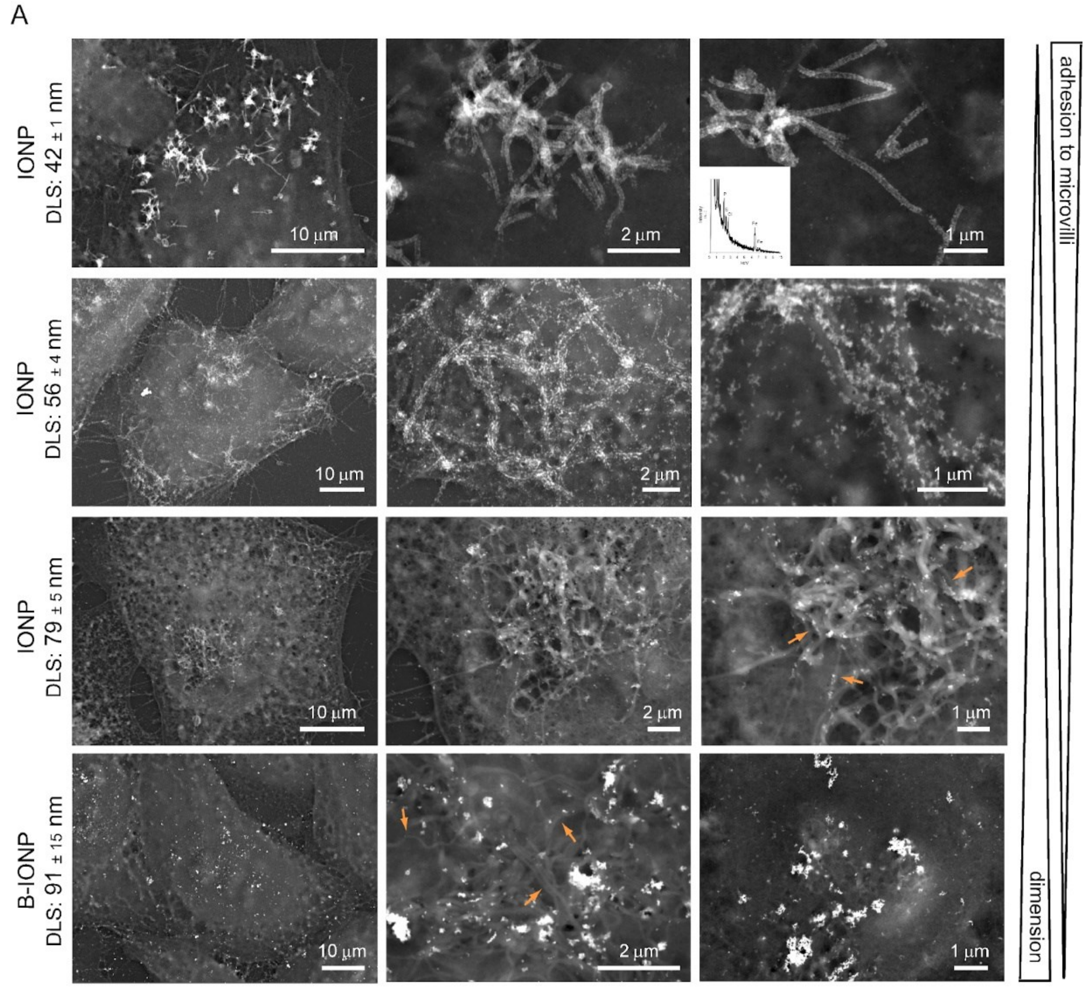

Figure 77. Influence of NPs surface charge, inorganic core chemical composition, and size on MMA. *(A) The chemical nature of the NPs' inorganic core did not affect MMA. NPs of PAA-coated* Fe_3O_4 *(IONPs) interacted with the microvillous surface in a way similar to CNPs. (inset) Representative SEM-EDS analysis of the IONPs present on the cells. MMA was instead affected by NP size. The affinity towards microvilli was reduced by increasing the size of IONP aggregates. The largest aggregates, including inert* B_4C *NPs (B-IONP, lower row), did not show any interaction with microvilli. NPs size was inversely proportional to the degree of MMA.*

positive. Moreover, they appeared to be sensitive to cholesterol removal as well, since MβCD were able not only to alter the shape of the pancake-like structures but also the NPs adhesion. These observations confirm that the main membrane constituents of the pancake-like structures were lipid rafts and that they contained the same component(s) that can attract the nanoparticles, thus mediating the microvilli adhesion and nanoparticle internalization.

To exclude the possibility that the MMA was mediated by the **inorganic core chemical composition** and the **dimensions**, different nanoparticles were tested.

Specifically, NPs of PAA-coated Fe_3O_4 (**IONPs**) tested on HeLa and REN cells showed an affinity towards microvilli similar to that presented by the CNPs, covering the surface of microvilli with a uniform layer (**Figure 63** and **Figure 66**).

Moreover, IONP showed also the same sensitivity to cholesterol and/or cholesterol/sphingolipid removal when analyzed by flow cytometry (**Figure 65**), confirming that the inorganic core chemical composition is not involved in the adhesion process. To evaluate the role of the NPs' dimensions, IONPs with different levels of aggregation and a negative surface charge were used (42, 56, 79, and 91 nm). The 56 nm IONPs still decorated the microvilli but formed a discontinuous layer (**Figure 77**), suggesting a lower ability to interact with the membranes of the microvilli. The specificity was further reduced with IONPs of 79 nm. However, when the size was increased further to 91 nm, no specific adhesion on the cell protrusions was detected (**Figure 77**). In all three cases, the IONPs

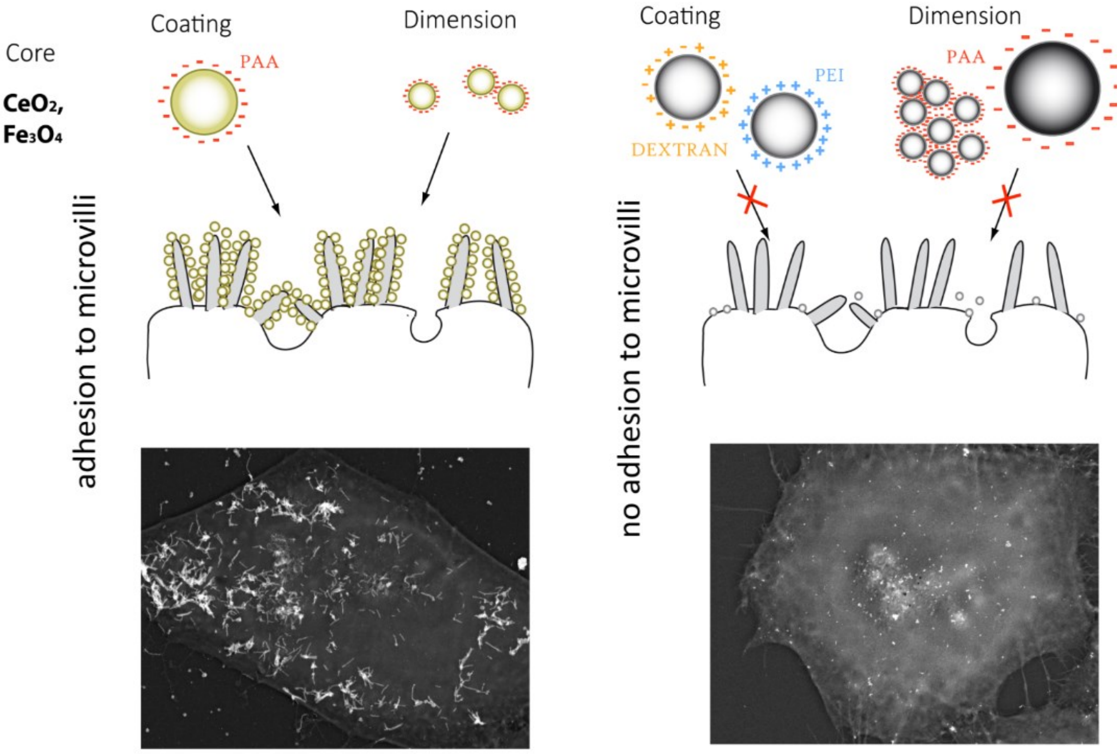

Figure 78. Scheme of the NPs characteristics fundamental for the microvilli-mediated adhesion (MMA).

presented the same constitutive elements; therefore, it can be concluded that the different behavior was due to the NPs' dimensions. The size cut-off for MMA can probably be placed between 70 and 80 nm (**Figure 77**).

The role of the chemical nature of the coating used was also analyzed. It is known that the behavior of NPs in a biological environment strongly depends on the type of functionalization. To evaluate this effect, the adhesion of **P-CNPs** (positively charged NPs) was evaluated compared to the negative charged CNPs. The results show how the variation of the surface charge totally causes the loss of selectivity towards the microvilli, with the nanoparticles being distributed in a completely random way on the cell surface (**Figure 70**). The importance of PAA in the adhesion mechanism was also confirmed using NPs with dimensions similar to the PAA- CNPs but functionalized with dextran (**DCNP**) or **without coating**. Both these NPs failed to adhere to microvilli (**Figure 71**).

Altogether these results, summarized in (**Figure 78)**, suggest that the specificity of the nanoparticles towards microvilli does not depend on the chemical nature of the NP or the cell type, but is influenced by the size and the type of functionalization, with the PAA coating essential for the membrane interaction. Moreover, the data suggest that the microvilli's membrane integrity, but not the microvillus' structure/architecture integrity is fundamental for the interaction with CNPs **(Figure 79**). Specifically, the presence of cholesterol together with sphingolipids is of fundamental importance in mediating the NPs-cell adhesion.

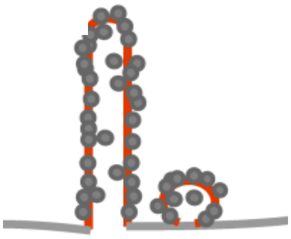

Figure 79. MMA does not require microvillus integrity, but a specific membrane composition.

Considering the peculiar mechanism of CNPs adhesion, the process of internalization was also investigated. HRTEM analysis showed endolysosomes containing CNPs-decorated structures suggesting that, after adhering on microvilli, the CNPs-decorated protrusions are internalized as a whole (**Figure 80, A-D**) carrying the CNPs still attached on their surface. When the diameter of these decorated structures was measured it was observed that they exactly corresponded to microvilli (**Figure 80, E**), This suggested that the CNPs are internalized and accumulated inside intracellular vesicles still attached on microvilli (**Figure 72**). Investigating the process of internalization, preliminary data suggested that the uptake of CNPs is **energy-dependent** since the internalization, differently from adhesion, was blocked by low temperatures (4°C), as shown by HRSEM and flow cytometry analyses (**Figure 39** and **Figure 72**). Different kind of inhibitors targeting multiple endocytic pathways were used. The results showed that the least effective in the inhibition of CNPs endocytosis were amiloride and wortmannin, excluding the possibility of macropinocytosis. On the contrary, hypertonic sucrose (that is used to disrupt the formation of cellular Clathrin-coated pits and vesicles), reduced the uptake of CNPs suggesting the involvement of CME.

CytD showed to powerfully inhibit the uptake of CNPs, which was reduced by half (50.67% ± 1.05). CytD is known to reduce the uptake through macropinocytosis and phagocytosis, even if several studies proved also the involvement of a dynamic actin cytoskeleton in CME. [Fujimoto L. M., et al, 2000] [Yarar D., et al., 2005] In particular, the involvement of the actin cytoskeleton in the internalization process seems to be discordant in literature due to the high variability of the cell type used for the studies. In this specific case, it is important to consider that the PAA-CNPs show specific adhesion to microvilli, which need actin for their cytoskeleton integrity. For this reason, by affecting the microvilli structure the inhibition of actin polymerization could interfere with the internalization of PAA-coated CNPs. Since it was already excluded the role of macropinocytosis due to the levels of inhibition of Amiloride and Wortmannin, it is possible to hypothesized that the inhibition

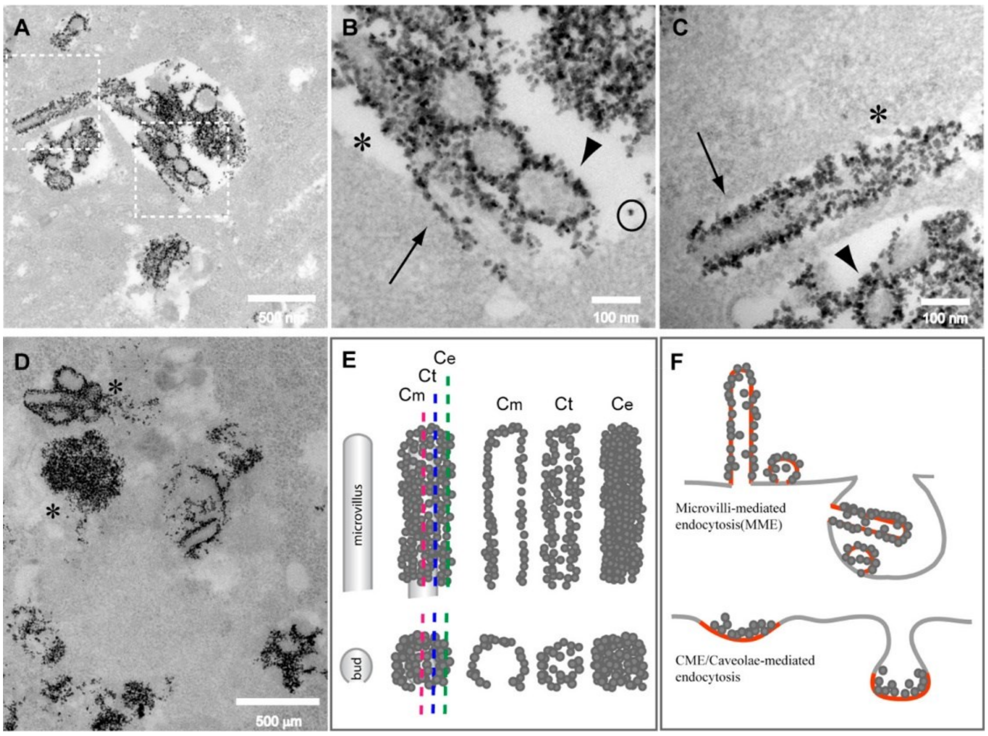

Figure 80. TEM analysis of CNP internalization. *(A) After 24 h incubation, the internalized CNPs were concentrated inside endolysosomal structures. (B, C) Enlargement of areas outlined in (A) shows only a few free CNPs inside the vesicles (circle), with most being adherent to cylindrical structures resembling microvilli (arrows) or bud-like structures (arrowhead) that mediated their extracellular adhesion (B, C). (D) Larger CNP aggregates derived from several microvilli/buds assembled (*). (E) CNP-covered microvilli/buds appeared different depending on the position of the sectioning plane. When sectioned in proximity to the external surface, only a uniform layer of NPs was observed (Ce and regions marked by * in (B) and (C)). The internal structures of microvilli or buds began to appear if the cutting crosses tangentially (Ct) the microvilli surface. When the section crossed in the middle of the microvilli or buds (Cm), the CNPs appeared as a granulated uniform layer outlining their perimeter (arrow and arrowhead in (B) and (C)). (F) Schematic representation of the difference in NP internalization between classical endocytosis and internalization following MMA. In MMA, the membrane where NPs adhered (red) did not become part of the membrane of the newly formed endocytic vesicle. In contrast, in internalization via CME/caveolae endocytosis, the membrane that promotes NP adhesion (red) participated in forming the vesicle membrane.*

of actin on the uptake of CNPs could be addressed to the involvement of **Phagocytosis** and **CME**.

These results suggest that the internalization of CNPs in HeLa cells was mediated by Phagocytosis with possible smaller involvement of CME, strongly dependent on the integrity of the lipid rafts components. Specifically, the involvement of microvilli in the adhesion and internalization process evidenced a completely new mechanism that, to the best of my knowledge, was never described in the literature before and might represent an interesting alternative approach for selective NP delivery (**Figure 80, F**).

Altogether, the results presented in this thesis suggest the involvement of microvilli in the internalization of PAA-coated CNPs.

4. Whole organism – NPs interaction (Drosophila melanogaster)

4.1 Scientific background

Free radicals, reactive oxygen species (**ROS**), and reactive nitrogen species (**RNS**) are normally produced during regular cellular functions, but when present in large quantities (oxidative stress), they can alter the normal cell physiology and be responsible for several diseases. Alzheimer's and Parkinson's disease, which are characterized by high levels of ROS, are among those pathologies that at present do not have ab effective cure. CNPs could be a good candidate as a possible therapeutic agent because their ROS scavenging property is associated with the equilibrium between the two-oxidation state of cerium (Ce^{3+} and Ce^{4+}) through a self-regenerating mechanism. [Li H., et al., 2020] Experiments performed by our team [Ferraro D., et al., 2017], carried out on cultured cells at the European Synchrotron Radiation Facility (ESRF) in Grenoble (France), showed that the oxidation state of the CNPs is somehow modified once inside cells and that the interaction of CNPs with cells involves a complex mechanism, where different areas inside the cells might play different roles.

The distribution of CNPs, their ability to reach different areas, and the Ce^{3+}/Ce^{4+} equilibrium could be more complicated in a living organism, compared to an *in vitro* model. To test whether the use of CNPs could be worth considering for new therapeutic strategies, it was fundamental to assess the CNPs absorption and distribution in a model animal. In such conditions, CNPs must cross various physiological barriers to diffuse into the different organism's areas and exert the antioxidant effect. For this reason, it was decided to use **Drosophila melanogaster** as an ***in vivo*** model, one of the most genetically and experimentally accessible model organism used in biological investigations. The fruit fly Drosophila melanogaster is, in fact, one of the most valuable organisms in biological research, particularly in genetics and developmental biology. Drosophila has been used as a model organism for research for almost a century [Vega-Alvarez S., et al., 2014]; it is a small animal easy to handle, with a short life cycle, easy to keep at large numbers, and cheap [Salah-Eddin A., et al., 2015]. Regarding the use of Drosophila in testing the effects of nanomaterials, it has already been used to answer different questions related to the potentially toxic and genotoxic properties of nanomaterials, in addition to other questions related to the internalization of nanoparticles, cellular uptake, and tissue distribution [Alaraby M., et al., 2015]. At present, there is an increasing number of studies testing the biological effects of different nanoparticles in this organism. All these studies pointed out the relevance of using Drosophila to identify the possible mechanisms of action of nanomaterials on living organisms. [Ong C., et al., 2014]

Preliminary studies were performed on the CNPs distribution in Drosophila, in preparation to prove the advantage of the use of NPs over the existing therapies. A project planning to investigate in Drosophila the CNPs distribution and the oxidation state, as well as the antioxidant effects, have been submitted to the European Synchrotron Radiation Facility (ESRF) scientific board. The project received excellent evaluations and was selected. Although the beam time had been allocated early in 2020, the experiment has been postponed due to the COVID pandemic and it will be performed in February 2022.

To study the distribution of NPs in Drosophila flies was considered a new kind of nanoparticles, **Fe_3O_4 NPs covered with a boron carbide core** (**B-IONPs**). This was part of a bigger project which consider the use of nanoparticles of boron carbide as an alternative and more efficient delivery system of ^{10}Boron (^{10}B) for **Boron neutron capture therapy** (**BNCT**). BNCT is a radiotherapy treatment based on the accumulation of a ^{10}B-containing drug in the tumor and subsequent irradiation with low energy neutrons, causing the death of the neoplastic cells [Achilli C., et al., 2014]. To date, one of the most common compounds that is clinically used is a borated amino acid, p-**Boronophenylalanine** (**BPA**). Although far from being ideal, his therapeutic efficacy has been demonstrated in patients with high-grade gliomas, and a much smaller number with cutaneous and extra-cutaneous melanomas [Barth R.F., et al., 2018] [Diegelmann S., et al., 2017]. Because of the limitations of present treatments, great effort has been expended to develop of new boron delivery agents for clinical use that had more favorable uptake and biodistribution (in tumoral vs normal cells) and higher boron content. In this context, the use of B-IONPs seems to be a promising alternative due to the higher ^{10}B content.

Our group recently obtained encouraging results on HeLa cells. For the detection of B, it was used a semi-standard neutron autoradiography technique, based on a CR-39 detector, which is a 35 passive Solid-State Nuclear Track Detector (SSNTD). At the end of the treatment, it was possible to overlap the optical images of cells and the optical image of tracks (of alpha particles and lithium ions coming from the boron neutron capture reaction), obtaining useful information on the distribution and accumulation of ^{10}B at subcellular level [Postuma I., et al., 2021].

Studies demonstrating the *in vivo* distribution or pharmacokinetics of boron-containing NPs are lacking. For this reason, it was considered to use Drosophila as an animal model to follow *in vivo* the ^{10}B uptake and distribution. Preliminary studies of the distribution of BPA and B-IONPs in Drosophila were performed, in order to prove the advantage of the use of NPs over the existing therapies. This would be the first step toward a more complex protocol, where tumor-bearing Drosophila fly would be treated with BNCT, and the post-irradiation effects followed *in vivo*.

4.2 Materials and methods

4.2.1 NPs synthesis and characterization

All the syntheses were carried out using sterilized glassware in order to avoid bacterial contamination. The CNPs were produced by direct precipitation from an aqueous solution and stabilized in presence of PAA, as described previously [Ferraro D., et al., 2017]. The precursor chosen for the synthesis is a Cerium (III) salt, Cerium nitrate hexahydrate Ce $(NO_3)_3 \cdot 6H_2O$ (Sigma Aldrich, purity ≥ 99.0%; 22350). 1,085 g of this salt were weighed and subsequently dissolved in 43.65 mL of distilled water, filtered (sterile minisart, 0.20µm). An aqueous suspension of PAA was then made by diluting 600 mg of commercial PAA suspension (*Polysciences, Inc.*, 63% w/w; 06513) with 31 mL distilled water. PAA was then transferred with multiple washes into a 50 mL tube. It was necessary to shake vigorously to develop as much foam as possible before continuing with another transfer (leaving the foam behind). Of the 31 mL of the diluted PAA solution, only 20 mL were added to the Ce $(NO_3)_3 \cdot 6H_2O$ solution, all under constant stirring and in a thermostated bath.

Concentrated NH_4OH solution (Sigma Aldrich, 28.0-30.0% di NH_3; 221228) was added dropwise to obtain pH ~12 and the solution was kept under constant stirring. Immediately after the addition of NH_4OH the solution is pale pink/red and milky. The suspension becomes a transparent brown solution after 4 hours and yellow and clear after 1 day. The solution is left under constant stirring for additional 24 hours in order to allow the complete evaporation of nitrogenous species that could affect the viability of the cells.

To remove excess PAA, the suspension was centrifuged at 13,000 *g* for 30 min and the pellet recovered in the original volume of deionized water.

The B-IONPs were obtained by modifying the procedure used for IONPs and precipitating Fe_3O_4 in the presence of B_4CNPs. Commercial B_4C nanopowder (*SkySpring Nanomaterials Inc.,* Houston, TX, USA) was subjected to a ball milling treatment using a planetary mill (Fritsch pulverisette 7 premium line) with tungsten carbide jar and balls, to reduce agglomeration. The obtained nanopowder was recovered in deionized water. This suspension of B_4C (3 mg/ml) was added to the stirring iron salts solution prepared as above, before NH_4OH and PAA incorporation. After 1 hour, the resulting suspension was centrifuged at 300 *g* for 30 minutes to remove the largest aggregates and the supernatant was centrifuged at 15 000 *g* for 30 minutes to remove unreacted reagents. The pellet was washed twice and, eventually, recovered in deionized water.

For the preparation of fluorescent CNPs or fluorescent IONPs, DiI fluorescent dye (Sigma–Aldrich, St. Louis, MO, USA) was dissolved in dimethylsulfoxide (1.2 mg/mL) and then added under stirring to the 6 mg/mL CNPs or IONPs suspension (1:20 v/v), as described previously [Asati, A. et al., 2010]. The CNPs suspension was centrifuged at 17,000 · *g* for 20 min to remove free DiI in solution, and the pellet recovered in deionized water. Thanks to this approach it was possible to introduce a fluorescent molecule inside the ceria particles coated with PAA, without compromising the solubility of the nanoparticles themselves in aqueous solution and without reducing the number of functional groups available on their surface. This allowed following the nanoparticle-cell interaction using fluorometric techniques. DiI possesses a maximum emission wavelength of 585 nm, which means that it will be visualized in confocal microscopy with the color red.

CNP, IONP, B-IONP characterization included **XRD**, **DLS, and Z potential**. The CeO_2 and Fe_3O_4 content was determined by **ICP-OES** analysis (ICP-OES Optima 3300 D; Perkin Elmer, Santa Clara, CA, USA).

X-Ray Powder Diffraction (XRD)

XRD analysis was performed on films obtained by evaporating 150 μL CNP or B-IONP suspensions on glass microscope slides. The XRD patterns were acquired using a

Bruker D8 Advance diffractometer (Bruker Corp., Billerica, MA, USA) with a Cu anticathode (λ-Cu-K_α = 1.541838 Å) operated at 40 kV and 40 mA. Diffractograms were acquired in θ–θ mode, with a step of 0.03° 2 θ and an acquisition time of 20 s per step.

Dynamic Light Scattering (DLS) and Z potential

The determination of the hydrodynamic diameter and the Z potential of the NPs was carried out starting from suspensions of the various products at a concentration of ~ 1 mg/ml, in order to obtain interference-free measurements. For the DLS characterization, each sample was allowed to equilibrate for 30 s at a temperature of 25 ° C and, subsequently, subjected to three measurements each consisting of 10 readings lasting 10 s. The determination of the Z potential was carried out on the same suspensions used for the previous analysis; for each sample, three measurements were made, each consisting of 12-14 readings. For both analyses, the instrument was programmed defining ceria as reference material (refractive index 2.100, absorption 1.000) and water as solvent (viscosity of 0.8872 cP, refractive index 1.330, and dielectric constant 78.5, at a temperature of 25 ° C).

ICP-OES analysis

The ICP-MS analysis was used to quantify the CeO_2 or Fe_3O_4 obtained in the synthesis of NPs and to determine the concentration of Ce ions released by the nanoparticles at various pHs. In order to carry out the analysis, it was necessary to carry out acid digestion in a bomb. The procedure involved placing 200 µl of suspension inside the bomb, *i.e.,* a hydrothermal reactor consisting of a Teflon container closed in a steel jacket, to which 200 µl of dH2O and 400 µl of ultrapure nitric acid were added. (Sigma Aldrich, very pure pa, concentration ≥ 65%, 30709-M). The digestion process was carried out in an oven at a temperature of 150 °C for 3 hours. In the end, the bomb was opened under the hood as the reaction leads to the formation of NOx species, which are notoriously harmful. The solution remaining inside the Teflon container was perfectly clear, indicating that digestion was successful.

In the case of PAA-CNP solubility studies, the supernatant obtained by ultracentrifugation did not need to be subjected to further treatments and could be analyzed as it is. For all the samples analyzed, 5.00 ml of the solution were transferred into a test tube and 100 µl ultrapure 65% HNO_3 were added in order to prevent the material from anchoring to the walls of the container.

As determined by **ICP-OES** analysis, the final CNPs suspension had a CeO_2 content of 6 mg/mL, whereas the final B-IONPs suspension had a Fe_3O_4 content of 3.50 mg/mL.

4.2.2 Drosophila Melanogaster

Flies' husbandry

Two strains of Drosophila Melanogaster were used: Wild Type (W118) flies and flies expressing GFP-Beta tubulin.

The flies and larvae were harvested at 24 °C ± 1 °C on standard Drosophila food Nutry-Fly Bloomington Formulation (by Genesee Scientific), containing maize flour, yeast, sugar, agar-agar, and propionic acid.

Every 15 days flies were transferred to new tubes. For the experiments, 2-3 days-old flies were transferred in fly-cages with only agarose-based media supplemented with yeast as food.

Feeding flies with NPs

Figure 81. NPs administration in Drosophila *through microcapillaries of 5 µL, as used for the experiments described in this section.*

For the experiments, two- or three-days old flies were transferred to a cylindrical container. Food was administered through microcapillaries of 5 µL of volume (**Figure 81**), containing a solution of NPs diluted in water. **Brilliant Blue** (**BB**), a dye that once ingested stains the fly's body, was used to identify those flies that ingested a consistent amount of food/NPs. For the experiments, 5 µL of volume with a solution of CNPs (6 mg/ml, or otherwise indicated), BPA (5 mg/kg) or B-IONPs (3.55 mg/ml), BB 0,5%, and sucrose 20% was administrated. Only adult female flies were used for all the experiments.

Survival essay

For testing the toxicity of NPs, a survival assay was used. Two-three days old W118 flies were used. Briefly, two different concentrations of NPs were used (6 mg/ml and 3 mg/ml); water supplemented with sucrose 20% was used as a control sample. Flies were divided into different vials, each one containing 15 flies for every condition, maintaining the same proportion of female and male flies (2:1). The number of dead flies was recorded every 2 hours. The observation continued till all flies were dead.

Three sets of independent experiments were carried out for each assay. 15 flies were transferred in each food vial with at least 4 repetitions for each condition. A total of 180 files for each condition were considered.

Dissection of Drosophila organs

For experiments with NPs, flies were transferred in fly-cages in small groups (max 20 flies for each vial) maintaining the same proportion of female and male flies (2:1). For measuring the food intake, in each vial, only 2 microcapillaries of 5 µL volume were inserted, containing water supplemented with sucrose 20% or NPs diluted in water (or otherwise indicated). NPs supplemented food was stored in appropriate conditions to avoid exposure to light.

For dissection of the organs, flies were kept for 2-3 minutes in ice and then transferred under the microscope in a petri dish placed on ice. Flies were dissected in Hank's Balanced Salt Solution (HBBS) using 105 mm tweezers. The isolated organs were then washed with PBS and centrifuged at 15 rpm for 5 minutes. Only adult female flies were used.

Isolation of hemolymph from 3rd instar larvae

Larvae were fed with standard medium, or medium supplemented with NPs, for 24h (or otherwise indicated). At least 10 different 3rd instar larvae of the strain W118 were used for each condition. Larvae were collected and washed with PBS three times. Briefly, Larvae were placed on a small square of parafilm, in 50 µl of Schneider's medium (Invitrogen), with the dorsal side facing up. Hemolymph cells were then collected by rupturing the larval cuticle with a pair of fine forceps, without using anesthesia (**Figure 82**). 10 to 20 µl or hemolymph was extracted each time. Cells were collected in 1 ml of Schneider's medium at room temperature, containing 1 complete mini protease inhibitor mixture (Roche Applied Science) to prevent melanization, clump formation, and autolysis. Cells were left on a petri dish with 18 · 18 mm glass coverslips at the bottom, supplemented with a layer of Poly-Lysine, to allow hemocytes to adhere for 2 hours at 37°C. Cells were then washed with PBS and fixed in 4% formaldehyde for 15 min. After that, cells were processed for immunofluorescence staining as previously described.

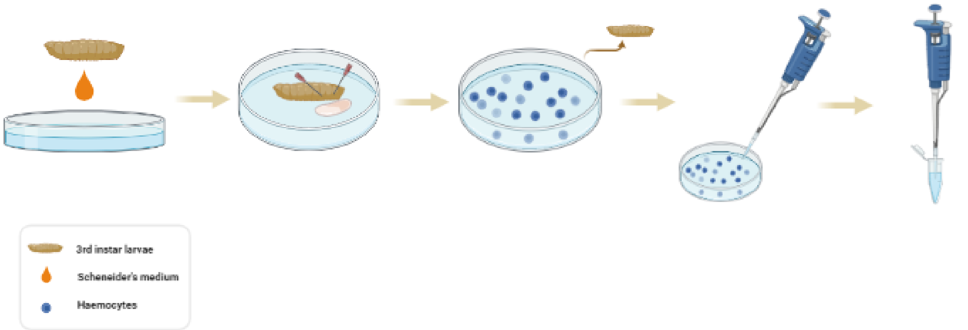

Figure 82. Protocol for Hemocytes extraction from Drosophila's 3rd instar larvae

Bromophenol blue (BPB) staining

To understand the variation of pH in the Drosophila's gut, **Bromophenol blue (BPB)** was used (Sigma Aldrich, 115-39-9) as previously described [Shanbahg S., et al., 2009]. BPB is a very sensitive pH indicator, showing a darker blue/brownish color for lower pH (**Figure 83**). Briefly, BPB was mixed with H2O (0,15%), then mixed with the yeast, forming a paste that was added to the agarose-based media. Flies were left eating this mix for 24h at room temperature. Guts were dissected as previously described and analyzed with a Phase-Contrast microscope, by Leica.

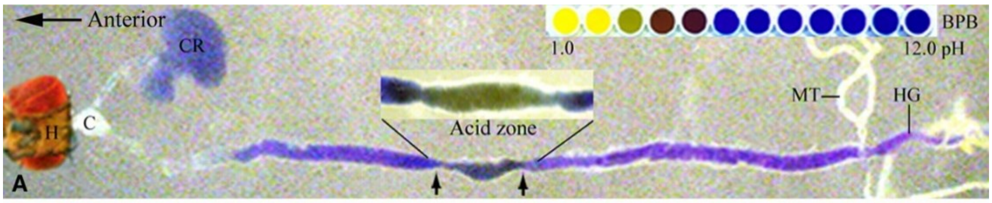

***Figure 83**. **Acidification in Drosophila Melanogaster detected in the adult middle midgut** (arrows, acid zone) where the color of Bromophenol Blue (BPB) dye changed from blue to greenish-brown (acid zone, pH<4.0); C, cardia; CR, crop; H, head; HG, hindgut; MT, Malpighian tubules. Reproduced from Shanbahg S., et al., 2009.*

Cryosections

Two-three days old flies W118 were systematically and consistently prepared. To the best of my knowledge, there is no recommended protocol for the preparation of Drosophila Melanogaster organs and whole-body sections. Reproducible sample preparation of this tiny fly is especially complicated due to its external and internal anatomy and the hydrophobic external cuticle.

As a first step, under a stereomicroscope, wings, and legs were removed from each fly. The guts were dissected and treated with 4% PFA at room temperature for 30 minutes, then infiltrated overnight with 20% sucrose at 4°C. As for the whole body, the flies were soaked in Petri dishes filled with ethanol (40, 70, and 100 %, for 5 minutes each). Ethanol facilitates dehydration of the insects and helps to keep the integrity of the whole insect morphology. Then the flies were inserted in 1,5 ml Eppendorf, embedded with Tissue-Tek cryo embedding compound (compound 4583) (OCT) medium diluted 1:1 with water, at room temperature, for 1 h. This step helps prevent the formation of bubbles around the body of the insects, which can complicate maintaining the integrity of the body while cutting the slices. Samples were included in OCT medium and stored at -80°C for one day. The next day 10 µm sections were cut by a Leica CM 1850 cryostat at – 20°C. The sections were stored at -20°C for no more than 3 months. Just female flies were used for all the experiments.

Immunofluorescence and confocal microscopy

Three different markers were used for marker microvilli in the enterocytes of Drosophila’s gut: antibodies anti-pERM (1:200; Cell Signalling Technology, Leiden, The Netherlands), Prominin CD-133 (a protein of microvilli) (1:250), and Phalloidin (Sigma P5282) (1:400).

Intact adult guts were dissected and fixed in 10% formalin in PBS without Ca and Mg for 1 hour. After washing for 10 minutes with PBS containing 0,2% Saponin (PBSS), samples were incubated overnight with primary antibodies in PBS at 4°C.

The intestines were washed in PBSS for 15 minutes and incubated with secondary antibody anti-rabbit 488 (1:400; Jackson Immunoresearch, West Grove, PA, USA) overnight at 4°C. Following incubation, the samples were washed and nuclei counterstained with Hoechst 33258 (Sigma–Aldrich) for 10 minutes, then mounted with Mowiol. After one night, samples were analyzed with a TCS SP8 confocal laser scanning microscope equipped with an HC PL APO CS2 40·/1.30 oil-immersion objective (Leica Microsystems, Heidelberg, Germany). Images were processed using ImageJ software and related plugins (National Institutes of Health, Bethesda, MD, USA).

For the staining of the Cryosections, two different markers were used: antibodies anti-pERM (1:200) and Phalloidin (1:400). Briefly, sections were fixed in 10% formalin in PBS without Ca and Mg for 20 minutes. After washing for 10 minutes with PBS containing 0,2% Saponin (PBSS), samples were incubated for 1h with primary antibodies in PBS at room temperature. The sections were washed in PBSS for 15 minutes and incubated with a secondary antibody (anti-rabbit 488, 1:400) for 1h at room temperature. Following incubation, the samples were washed 3 times with PBS and nuclei counterstained with Hoechst 33258 for 10 minutes, then mounted with Mowiol. After one night, samples were analyzed with a TCS SP8 confocal laser scanning microscope equipped with an HC PL APO CS2 40·/1.30 oil-immersion objective (Leica Microsystems, Heidelberg, Germany). Images were processed using ImageJ software and related plugins (National Institutes of Health, Bethesda, MD, USA).

SEM analysis

Two-three days old W118 flies were used. Briefly, NPs were used for 24 or 48h; water supplemented with sucrose 20% was used as a control sample. Food was administered through capillaries, as explained previously. Flies were divided into different vials, each one containing 15 flies for every condition, maintaining the same proportion of female and male flies (2:1). BB at 0.5%, a dye that once ingested stains the fly's body, was used to identify those flies that ingested a consistent amount of food/NPs. NPs supplemented food was stored in appropriate conditions to avoid exposure to light.

For dissection of the organs, flies were kept for 2-3 minutes in ice and then transferred under the microscope in a petri dish placed on ice. Flies were dissected in HBBS using 105 mm tweezers. The isolated organs (heads, guts, and ovaries) were divided into different Eppendorf containing 200 µl of PBS. Organs were washed three times with PBS and centrifuged at 15 rpm for 5 minutes. Only adult female flies were used.

For fixation, the organs were extensively washed with PBS and then with 0.05 M cacodylate buffer, pH 7.3. Fixation was performed in 2.5% glutaraldehyde (Sigma G5882) in the cacodylate buffer at room temperature overnight. Organs were dehydrated by increasing the concentration of ethanol (from 70 to 100%) for 15 min each. Samples were spotted in black tape for SEM analysis and left to dry completely.

All samples were carbon-coated and observed with a field-emission gun, high-resolution scanning electron microscope (Mira3 XMU; Tescan, Kohoutovice, Czech Republic) equipped with an EDAX EDS microprobe and SE and BSE detectors.

ROS quantification

Two-three days old W118 female flies were used. Food was administered through capillaries, as explained previously. Flies were divided into different vials, each one containing at least 20 flies for every condition. Each vial was stored in appropriate conditions to avoid exposure to light.

Three different conditions were tested: (**Figure 26,** *a)* water supplemented with sucrose 20% for 6h (base level of ROS production); (**Figure 26,** *b)* water supplemented with sucrose 20% for 3h and water supplemented with sucrose 20% and with H_2O_2 10 mM for 3h (for induction of ROS); (**Figure 26,** *c)* CNPs (6 mg/ml) for 3h first, and water supplemented with sucrose 20% and with H_2O_2 10 mM for the last 3h.

For dissection of the guts, flies were kept for 2-3 minutes in ice and then transferred under the microscope in a petri dish. Flies were dissected in HBBS using 105 mm tweezers. Exactly 10 guts for each condition were isolated. The isolated guts were then washed with PBS and centrifuged at 15 rpm for 5 minutes. Guts were resuspended in 50 µl of PBS and transferred in micro-homogenizers with glass pestle, size 20 (Exacta+Optech, 9.651 637). Cells were homogenized by twisting the pestle 30 times on the mortar. Cells were then resuspended in 200 µl of PBS.

	Blank	**(a) Control**	**(b) ROS**	**(c) CNPs + ROS**
1 - 3 h	CNPs	H_2O	H_2O	CNPs
4 - 6 h	H_2O_2	H_2O	H_2O_2	H_2O_2

Figure 84. Scheme of the samples for quantification of ROS in Drosophila melanogaster's guts.

For staining of ROS, 2’,7’ –dichlorofluorescin diacetate (DCFDA) (Sigma, D399) 30 μM was used. DCFDA is a fluorogenic dye that measures hydroxyl, peroxyl and other ROS activity within the cell. Samples were transferred in a 96-well plate and were read with a microplate reader (Bio-Rad Model 680 microplate reader) after 30 minutes of incubation of DCFDA at room temperature. Approximate Fluorescence Excitation and Emission, in nm: 492–495/517–527 was used. Organs alone (with CNP and H_2O_2, but without DCFDA) were used as blank (**Figure 84**). Each sample was analyzed in triplicate and the mean value was then obtained from the measurements. The results expressed are the mean ± SEM for at least three independent experiments. ROS production was calculated by subtracting the mean value of the blank for all the samples and expressed as a percentage of the group treated with H_2O_2 alone (that was set to 100%).

Drosophila treated with BPA and B-IONPs

Two- or three-days old flies were transferred to a cylindrical container with microcapillaries of 5 μL of volume with a solution of BPA (5 mg/kg) or B-IONPs (3.5 mg/ml), BB 0,5%, and sucrose 20%. For dissection, flies were kept for 10 minutes on ice then dissected in Hank’s Balance Salt Solution (HBBS) using 105 mm tweezers. The isolated organs were then washed with PBS. Only adult female flies were used.

Neutron autoradiography

The neutron autoradiography technique is based on the irradiation of samples enriched with ^{10}B in direct contact with a passive detector that is only sensitive to high Linear Energy Transfer charged particles (*i.e.,* low energy He and Li nuclei). The charged particles coming from neutron capture in ^{10}B, create latent tracks in the detector which can be made visible by chemical etching. Depending on the calibration of the technique (neutron fluence, etching parameters), it can be employed to obtain quantitative information on boron concentration or qualitative imaging of boron spatial distribution [Postuma I., et al., 2016].

Quantification of ^{10}B in the different organs of Drosophila

For the quantification of ^{10}B in the different organs of Drosophila, at least 20 flies were transferred to a cylindrical container with microcapillaries of 5 µL of volume with a solution of BPA (5 mg/kg) and let to feed for 2 hours. After this time, the microcapillaries were substituted with others containing just water supplemented with sucrose 20% for a different amount of time (see results). 10 female flies were then sacrificed, their organs isolated in separate vials (1 vial with 10 heads, 1 with 10 guts, and 1 with 10 ovaries). The organs were washed once with PBS and then lysed mechanically with multiple passages (15–20) into a micro-pestle (volume 100 µl). After that, the organs were resuspended with 100 µl of PBS and left to dry on a CR39.

For boron measurement by neutron autoradiography, we used the set-up by Postuma et al. [Postuma I., et al., 2016]. For this technique, the biological samples are deposited on a passive nuclear track detector, which is subsequently irradiated with neutrons at the Thermal Column of LENA’s TRIGA MarkII reactor of the University of Pavia. After the irradiation, the tracks are counted and with appropriate calibration, it is possible to measure the boron concentration in the deposited biological sample. A parameter that must be taken into account is the amount of water loss occurring after the preparation of the tissue samples. This is necessary since distinct tissues may lose water in different percentages; therefore, the dry to fresh mass ratio is needed to renormalize the result concerning the calibration curve. To do so, the total mass of every class of organs was measured when diluted in 100 µl of PBS, then let to dry completely, therefore measured again.

Once the dry to fresh mass ratio is obtained, it was possible to measure boron concentration in the Drosophila samples. Instead of randomly taking a picture through the sample area, a uniform scan in a predetermined area (≈1 cm^2) was implemented. This picture sampling was possible because Image Pro Plus can manage the movable table that is installed in the Leica microscope. The software outputs files recording the track morphological characteristics. These files were analyzed with homemade Python software. Accordingly, threshold values were imposed, then for each picture, the track density was calculated. Thus, by comparison with the tissue calibration curve, for each picture the boron concentration was evaluated by considering water evaporation. Finally, these values were plotted in an image where each color represents a ^{10}B concentration value, resulting in a map of boron concentration.

4.2.3 Statistical analysis

Confocal and SEM images were processed and analyzed with LAS X and ImageJ/Fiji software. Colocalization analyses were performed using JaCoP, a plugin of ImageJ/Fiji software. Each cell was analyzed separately, for a better approximation of the colocalization. The pERM-CNPs colocalization is expressed using two different coefficients, widely used in the literature: **Pearson's correlation coefficient** (PCC) and **Mander's overlap coefficients** (MOC) [Adler J., et al., 2010]. The PCC is a well-known correlation measure that dates back to the late 1800s. It ranges from +1 (perfect correlation) to 1 (perfect but negative correlation), with 0 representing the lack of a link. It is only recently that it has been used for the detection of fluorophores' colocalization. The MOC can be defined as values ranging from 0 to 1, expressing the fraction of intensity in a channel that is located in pixels where there is above zero (or threshold) intensity in the other color channel [ImageJ]. The

MOC is considered to be easier to interpret than the PCC since it only reports positive values. The two coefficients are almost identical and differ only in the use of the absolute intensity, by the MOC, or the deviation from the mean, by the PCC, a small but significant change [Adler J., et al., 2010]. For this reason, for a different and most complete interpretation of the colocalization, it was chosen to use both parameters.

Statistical analysis was carried out with GraphPad Prism 7.

4.3 Results

4.3.1 Drosophila – CNPs interaction

Flies viability

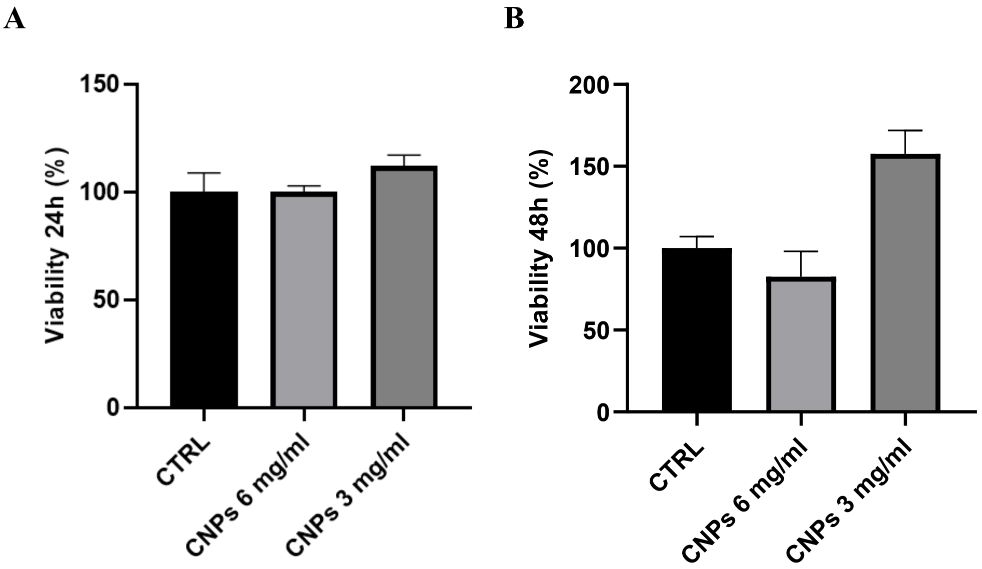

Figure 85. *(A) Viability of flies when breaded with two different concentrations of CNPs (6 mg/ml and 3 mg/ml) for 24 hours. (B) Viability of flies when breaded with two different concentrations of CNPs (6 mg/ml and 3 mg/ml) for 48 hours. All data are expressed as an average ± SD of four independent experiments, expressed as a percentage considering the control sample (water supplemented with sucrose 20%) as 100%. 60 flies/condition were used for each experiment (= 240) flies tested for each condition.*

The first step of this work was to define the concentration of CNPs to feed the flies and the duration of the exposure, in order to evaluate the higher dose with no toxic effect.

To investigate the possible effects of CNPs *in vivo*, lifespan studies were performed. Data are expressed as the viability of flies compared to the control, considered as 100%.

As it’s possible to observe in **Figure 85, A**, 24 hours after the treatment there was no evident sign of toxicity, with the highest concentration of CNPs that didn’t show any difference to the control (100% ± 2.9). In particular, for the lower concentration (3 mg/ml), the viability on the flies increased (112.1% ± 5). This result can be explained by the fact that CNPs can alter cellular metabolism by reducing ROS levels, thus creating better conditions for the flies to survive.

Similar results were obtained by counting the number of dead flies after 48 hours of incubation (**Figure 85, B**). In particular, the higher concentration (6 mg/ml) showed partial toxicity (82.5% ± 15.5), while 3 mg/ml was revealed to maintain higher the general lifespan of the flies (157.5% ± 14.4). These results are in accordance with literature data [Alaraby M., et al., 2015].

Since the highest concentration (6 mg/ml) didn't show signs of toxicity for the flies, it was decided to keep it as the higher concentration limit for further analysis.

CNPs intake and distribution in the intestinal tract

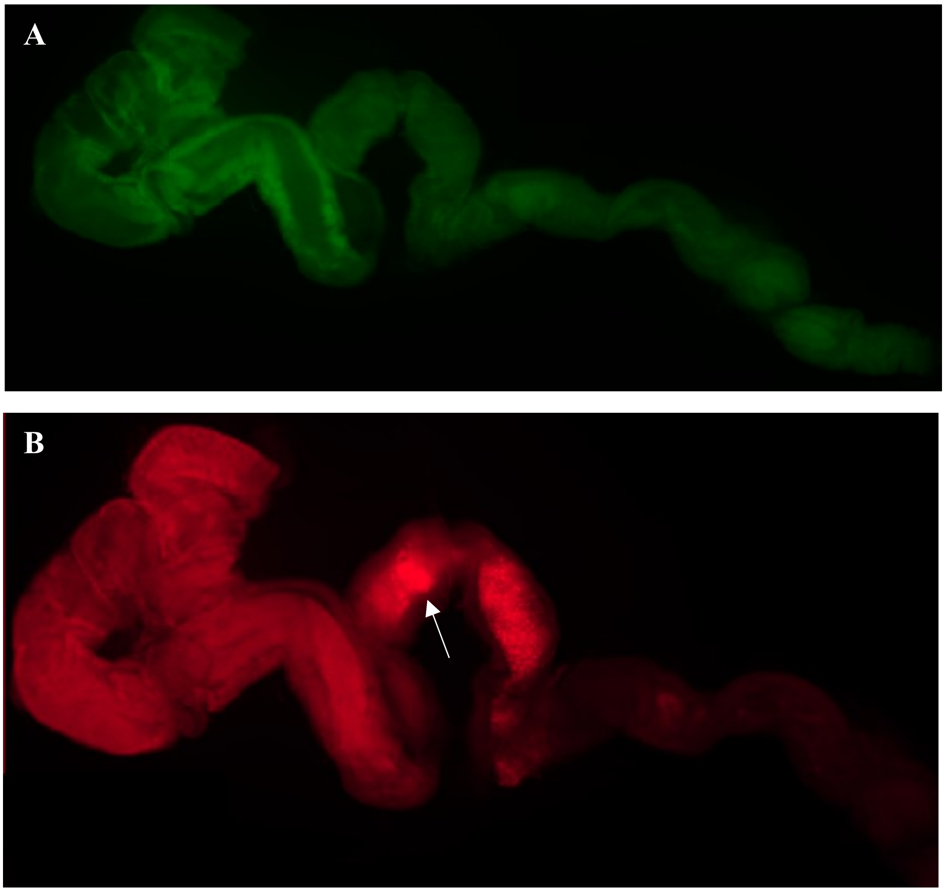

Figure 86. *Representative image of the isolated intestine of Drosophila expressing beta-Tubulin GFP (A) fed with FCNPs for 24h (B). Fluorescence microscopy. Each image is a composition of multiple images.*

First, it was studied the best way to isolate the intestine from the flies that had been fed with NPs for 24 hours. Results were analyzed by fluorescence microscopy. For this purpose, fluorescent CNPs had been prepared by intercalating the DiI fluorophore on the external PAA coating (FCNPs). FCNPs had been used to follow their distribution once ingested by the flies. As it is possible to appreciate from **Figure 86,** the FCNPs were clearly visible in the isolated intestine even at a low dose of 2,5 mg/ml. This showed that indeed the FCNPs had been ingested and moved along the intestine preserving their fluorescent signal. As shown in this image, the fluorescence was not homogeneously distributed along the entire intestine, but the FCNPs seemed to be more concentrated in a specific portion of the intestine (**Figure 86, B**, white arrow).

Due to the apparent non-homogeneous distribution of the FCNPs along the intestine, it was important to identify where the adhesion of the FCNPs was more evident. This would help identify the specific portion of the intestine to focus on for the analyses. The adult midgut is segmented into anterior, middle, and posterior regions. Each one of them is characterized by different pH [Lemaitre B., et al., 2013]. For this reason, a sensitive pH indicator, Bromophenol blue (BPB), was used on a control fly. Its changing in color from blue to darker

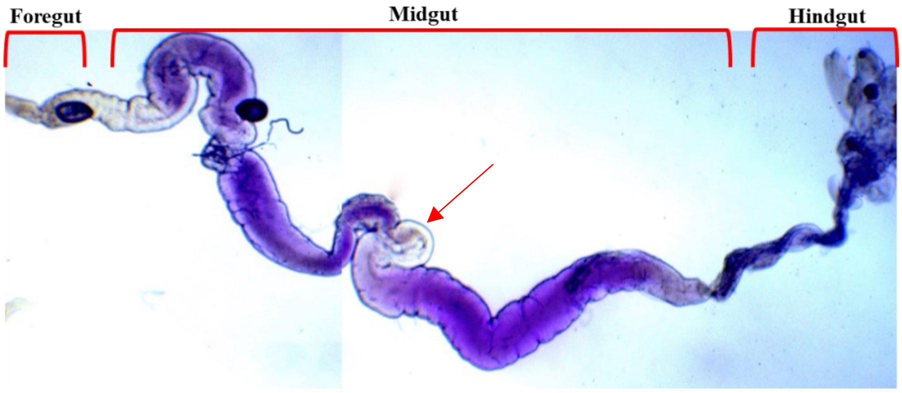

Figure 87*. Isolated gut of a fly fed with BPB for 24h. The most acidic zone in the midgut has a yellow/brownish color (indicated by the red arrow). Phase-contrast microscope (4x). The image is a composition of multiple images.*

blue/brownish indicated which part of the intestine was more acidic compared to other portions [Shanbahg S., et al., 2009].

As it is possible to observe in **Figure 87**, the intensity of blue is different in the different portions of the gut, underlying the variations of pH. A very acid portion in the middle midgut (red arrow) (the blue became brownish) corresponding to pH 4-5, was visible.

The analysis was then performed in flies fed with FCNPs and BPB so that the change in pH was combined with the FCNPs fluorescence intensity along the intestine (**Figure 88**). This analysis confirmed that, when flies were fed with FCNPs for 24 hours, the nanoparticles were more concentrated in that portion of the intestine which corresponded to the middle midgut and was more acid.

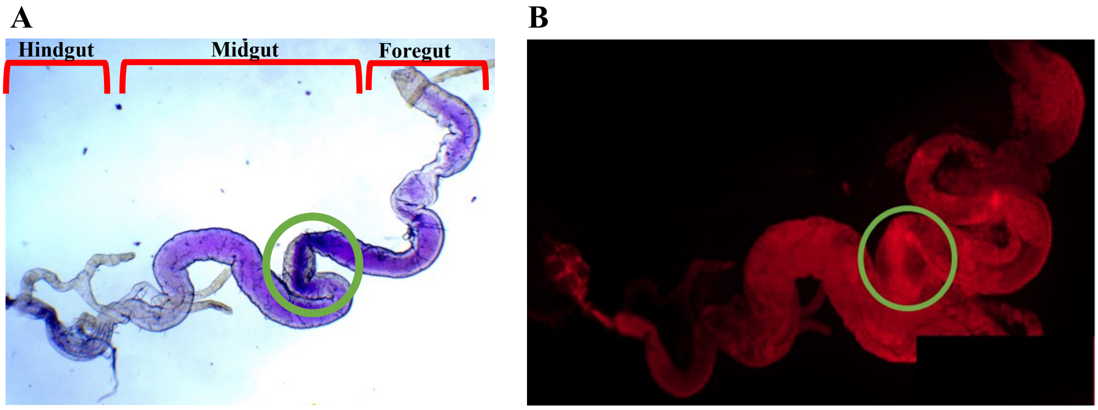

Figure 88. *(A) Isolated gut of a fly fed with FCNPs and BPB for 24h. Phase-contrast microscope (4x). The image is a composition of multiple images. (B) Fluorescence microscopy image of picture (A). Each image is a composition of multiple images. FCNPs seem to accumulate mainly in those regions where the pH is acidic (green circle).*

The objective of this study was to investigate whether the CNPs were able to interact with the intestinal brush border and, after that, be effectively internalized. For this reason, different markers for the intestinal brush border/epithelial cells villi were tested: CTx, Prominin CD133, Phalloidin, and pERM.

- CTx is commonly used as a marker for lipid rafts. The B-chains of the toxin pentamer bind specifically to the glycosphingolipid GM1 in the outer leaflet of the plasma membrane. GM1 accumulates in specific invaginations of the plasma membrane, specifically rich in the protein caveolin, cholesterol, and glycolipids [Torgersen M.L., et al., 2001], present in high concentrations in the microvilli of the brush border.

- Prominin CD133 is a cell surface marker that recognizes endogenous levels of total CD133, a protein specific for microvilli. The antibody that had been chosen was specific for human cells, but not generally tested in Drosophila. However, a comparison between the conserved amino acids of the epitope, showed it was well conserved in Drosophila since it differs for just three amino acids.
- Finally, considering the results on HeLa and REN cells showing a strict relationship between CNPs and microvilli (see chapters 3.3.4 and 3.3.6), it was chosen to test also Phalloidin and pERM on the Drosophila's gut. Phalloidin is a highly selective bicyclic peptide used for staining actin, which is the main constituent of the actin cytoskeleton of microvilli.
- pERM is a group of proteins that support the structure of the microvillus by connecting the actin filaments to the plasma membrane, thus are extensively present specifically in the intestinal brush border.

Because the whole isolated Drosophila's intestine is long and convoluted, different conditions were tested in order to make sure the antibody could reach the lumen of the gut and bind to the luminal membrane of the epithelial cells. In order to find the best protocol, different permeabilization protocols (Triton X-100 or Saponin) were tested, and, for each antibody, different concentrations, as well as incubation times, were used.

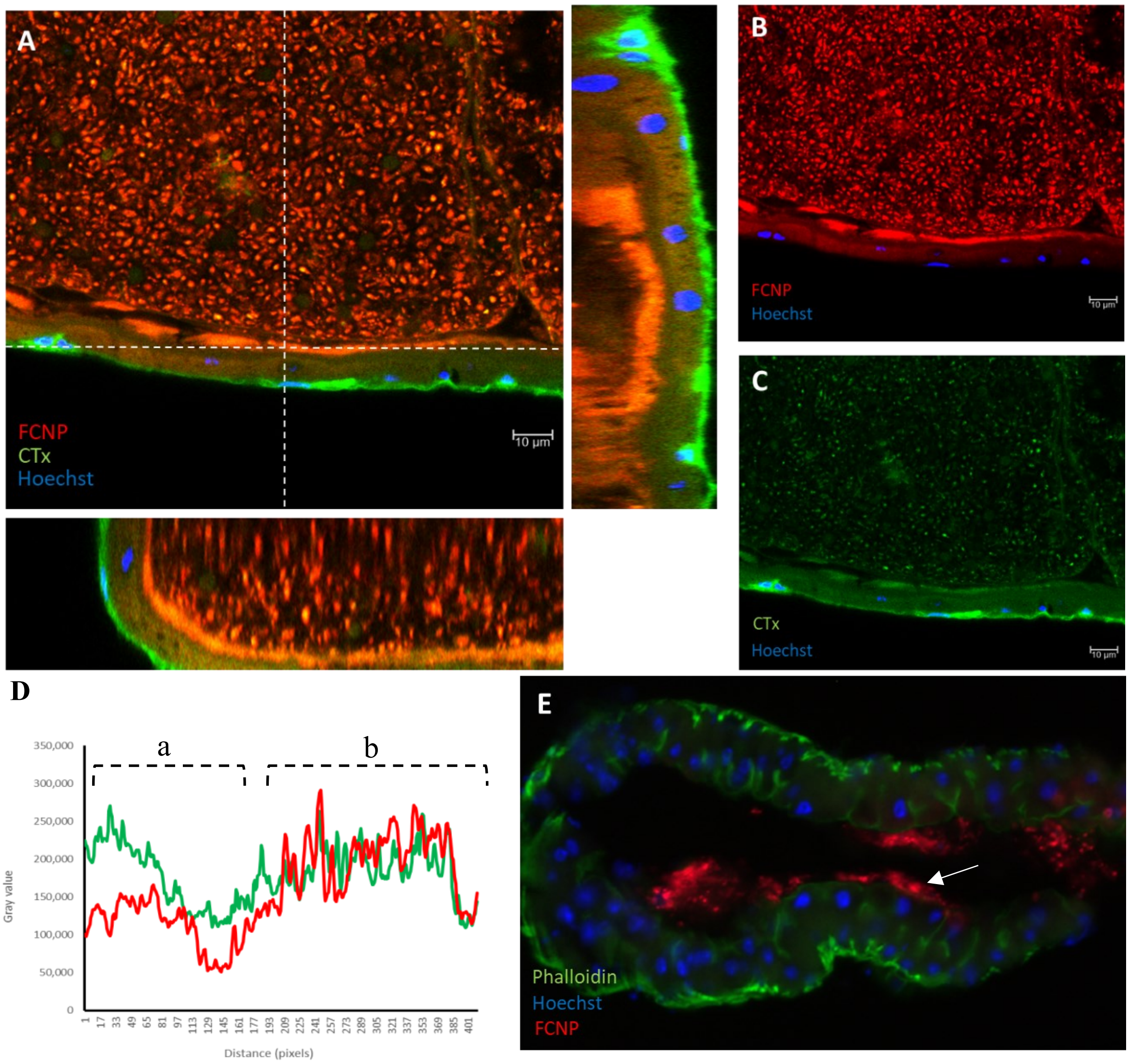

__Figure 89. CNPs interact with the enterocyte brush border.__ (A) Middle midgut of WT fly fed with FCNPs for 24h. Staining with CTx (green) and Hoechst (blu). The relative cross-sections show the point of colocalization between CTx and FCNPs (in yellow). (B, C) Same picture in (A) but separated channels, FCNPs (red) and Hoechst (blu) in (B) and CTx (green) and Hoechst (blu) in (C). (D) The fluorescence intensities of green (CTx) and red (FCNPs) were plotted against distance (pixels) taken in the areas in (A) (dotted lines). It was possible to appreciate a common profile of red and green fluorescence (specifically in the segment (b)). (E) Cryosection of the midgut of WT Drosophila, stained with Phalloidin (green). It is possible to appreciate the interaction between the FCNPs and the brush border/villi (white arrow). All the pictures are from confocal microscopy, a single confocal plane of 0.5µm.

In **Figure 89, A** it is possible to see a representative image of an isolated entire intestine of Drosophila fed for 24 hours with a suspension of FCNPs. Because the lumen appears full of nanoparticles it was challenging to quantify whether there were areas of possible colocalization present at the brush border. In this portion of the intestine, the FCNPs appeared to extensively interact with the brush border of enterocytes (in this case stained with CTx), as the first step before internalization. Here the red fluorescence was more intense and yellow (indicating colocalization) in the portion corresponding to the luminal portion of the cell membrane. This interaction was even more clear in the relative cross-sections (**Figure 89, A**), where the fluorescence intensities of CTx and FCNPs, taken across the brush border and plotted against distance (**Figure 89, D**), indicated that at least a partial colocalization exists.

The interaction between the CNP and the intestinal cells was investigated further with the 10 µm-cryostat sections (**Figure 89, E)**. Specifically, the isolated intestine was included in OCT and processed for generating thin cross-sections, while preserving the biology of the sample thanks to the cold temperatures. The advantage of this technique, as opposed to the previous type (in which the entire intestine was isolated a processed for confocal microscopy), is that it was possible to eliminate the non-adherent FCNPs from the gut lumen so that the only visible FCNPs were either the adherent FCNPs or the ones internalized. When actin was stained using phalloidin, some nanoparticles appeared to be in close proximity to the villi (white arrow).

The interaction with microvilli was confirmed also with Prominin CD133 (**Figure 90**). In this case, a whole intestine was isolated and processed for confocal microscopy. Once

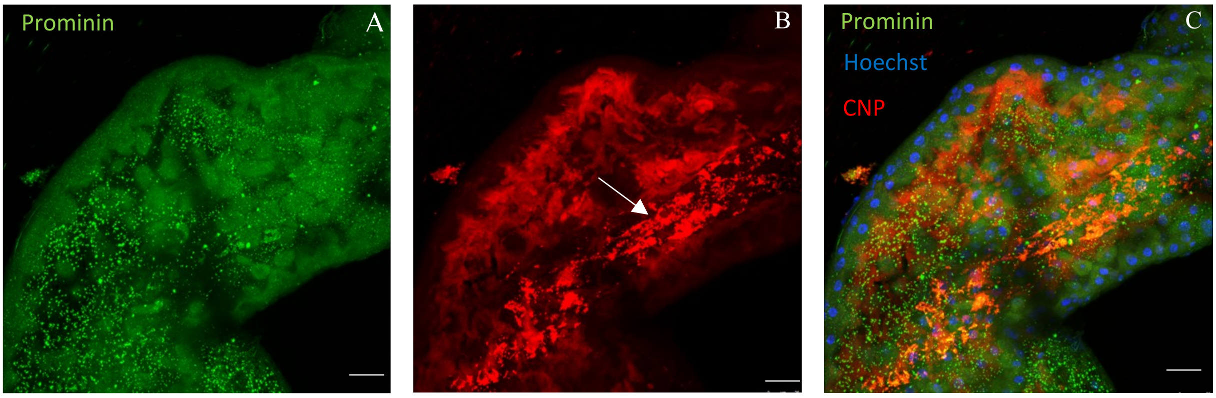

Figure 90. *Representative image of Drosophila (WT) fed with FCNPs for 24h. Red, FCNPs; Blue, Hoechst; Gren, Prom CD133. White arrow points to the FCNPs present in the lumen and not adherent to the epithelial cells. Images (C) is an overlap of (A) and (B). Single confocal plane. Bar is 25 µm.*

excluded the signal derived from the nanoparticles present in the lumen (**Figure 90, B**, white arrow), Pearson's correlation coefficient (**PCC**) between CD-133 and CNPs was **0,682 ± 0.05**, proving that the FCNPs indeed interact with the microvilli of the enterocytes.

4.3.2 Internalization of CNPs in the enterocytes of the midgut

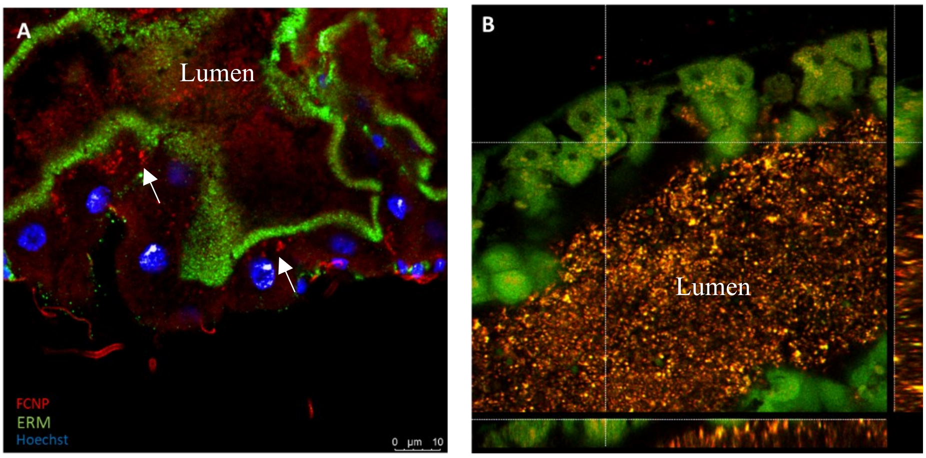

Figure 91. Internalization of CNPs inside enterocytes of Drosophila. *(A) Representative confocal microscopy image of Drosophila middle midgut stained with pERM and fed with FCNPs for 24 hours. Z-stack of 10 planes (out of 190). Accumulation of NPs inside vesicles was visible just under the brush border (white arrows). (B) Drosophila expressing B-Tub GFP, fed with FCNPs for 24 hours. Z-stack of 10 planes (out of 190). Accumulation of NPs inside the cells was visible in the relative cross-sections (yellow dots inside the cells).*

The first method to study the internalization through the flies' gut was confocal microscopy of the intestinal lumen. As it's possible to observe in **Figure 91**, when the guts were isolated and processed entirely for confocal microscopy, in some cases it was already possible to observe the internalization. For example, in **Figure 91, A** FCNPs were visible inside the enterocytes, where they form small aggregates due to their accumulation in endocytic vesicles. In the relative cross-sections of **Figure 91, B** is possible to appreciate the internalization of the FCNPs, that extensively interacted with most of the enterocytes. However, the fluorescent signal of the nanoparticles from the lumen made it challenging to observe the internalization. This problem was solved by 10 µm cryostat cross-sections. In this case, it was also possible to appreciate the internalization of the FCNPs by the

Drosophila enterocytes in the midgut, but without the problem derived from non-specific fluorescence from the intestinal lumen. Specifically, in **Figure 92** (and in the relative enlargement) is possible to observe several intense FCNPs aggregates that were visible inside the enterocytes (white arrows), just under the intestinal brush border.

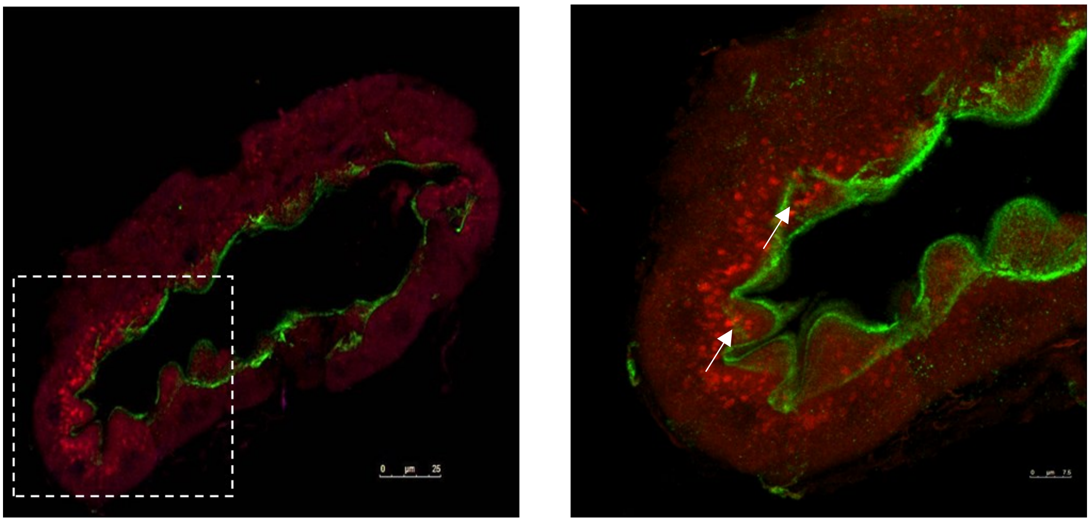

Figure 92. *Representative cryosections of the midgut of Drosophila were stained with pERM (green) and fed with FCNPs for 24h (red). Z-stack of 3-4 sections of 0.5 µm. The white arrows indicate the FCNPs internalization right under the brush border/villi.*

To confirm the qualitative data regarding the CNP internalization by the enterocytes, the **CNPs antioxidant activity** was tested in Drosophila's gut. Especially, the ability of the CNPs to reduce the stress levels in the enterocytes was analyzed after feeding the flies with CNPs for 3 hours, upon inducting stress with H_2O_2 administration in the diet. Quantitative analysis was performed through the use of a spectrofluorometer, by using a specific indicator of the ROS levels (CM-H_2DCFDA).

The results are shown in **Figure 93**. From this analysis, it was evident that CNPs could reduce the level of ROS to the basal level (H_2O) upon stress induction with H_2O_2 (CNP+ H_2O_2). The fact that free radicals, present in the enterocytes, could be counteracted by the presence of the CNPs, being reduced by more than 80% (14.17% ± 0.45), confirmed and supported the qualitative observation that CNPs could be internalized by the fly enterocytes.

These results are in accordance with previous results from our team in HeLa cells. [Ferraro D., et al., 2017]. In particular, it was discovered that the antioxidant action of CNPs in a cellular model appeared particularly high in the presence of an exogenous oxidative stress inducer (in that study *tert*-Butyl hydroperoxide (*t*-BHP) was used).

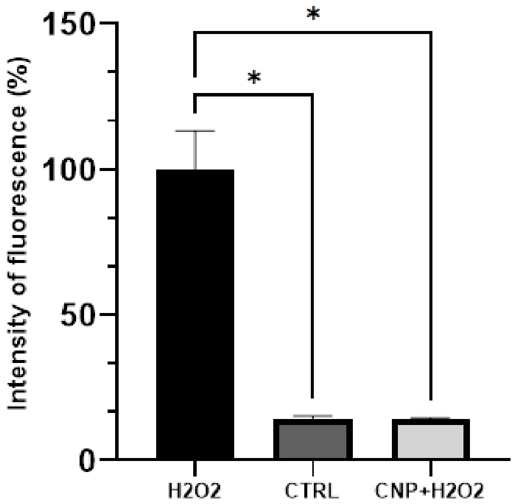

Figure 93. CNPs protect against oxidative stress in enterocytes of Drosophila's gut. *Mean values of fluorescence intensities (± SEM) of Drosophila's guts treated with* H_2O_2 *for 3h (*H_2O_2*), not treated (CTRL), or treated with CNPs 6 ml/ml for 3 hours prior* H_2O_2 *treatment (CNP-*H_2O_2*). Mean of 4 different experiments. For every sample a total of 10 guts was mixed. *,* $p < 0.05$*; ****,* $p < 0.0001$*, calculated with One way ANOVA with Tukey's multiple comparisons test.*

4.3.3 Evaluation of CNPs ability to cross the intestinal barrier

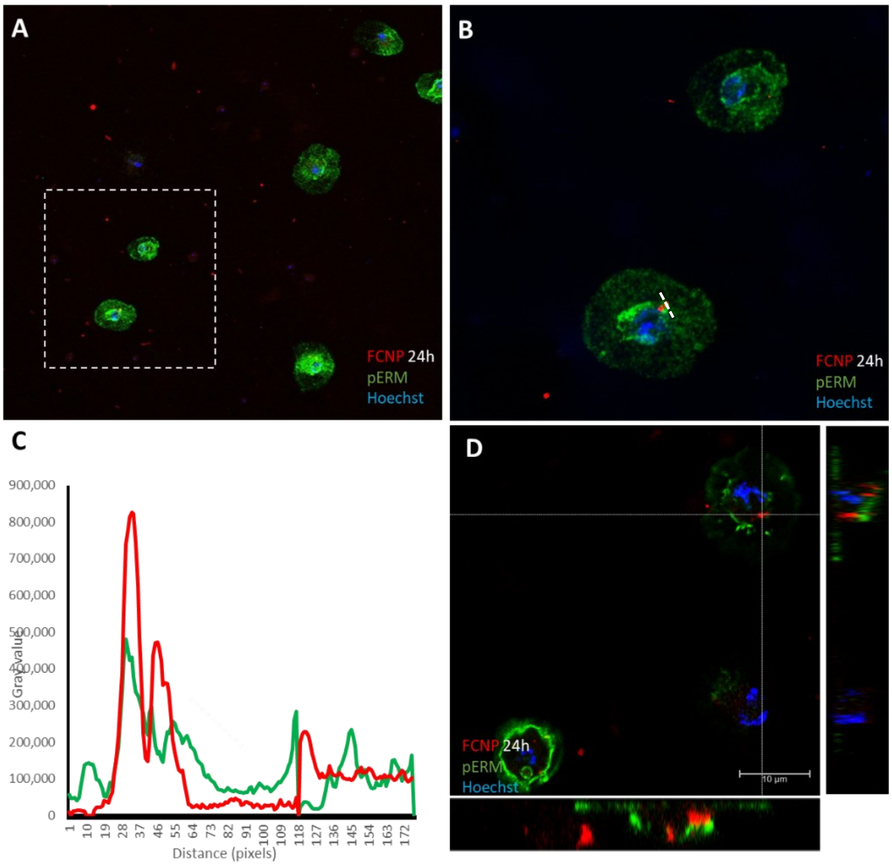

Figure 94. CNPs cross the intestinal barrier and are captured by hemocytes. *(A) Representative images of hemocytes isolated from larvae fed with FCNPs for 24h. Confocal microscope. Blu, nuclei; Green, pERM; Red, FCNPs. Enlarged in (B). The presence of FCNPs inside the hemocytes indicates that they were able to interact with the intestinal epithelium, cross the intestinal barrier, and be released into the hemolymph. (C) Intensities of green (pERM) and red (FCNPs) plot with distance (pixels), from hemocytes in (B) from the white dotted line. (D) Internalization is visible in the relative cross-sections inside the cell. Blue, Nuclei; Green, pERM; Red, FCNPs.*

To better test whether the CNPs could cross the intestine barrier, different approaches were taken. First, the **hemocytes** from the 3rd instar larvae were isolated. The hemolymph is interconnected with the fly’s gut and the isolation of the hemocytes can be used as a good indicator for the ability of the nanoparticles to cross the midgut epithelial layer. For these analyses instead of adult flies, 3rd instar larvae had been used due to the impossibility of collecting the high number of cells necessary for the analysis from the adult fly body. The collection of hemocytes from 3rd instar larvae is, on the opposite, a well-established method, used by most researchers to conduct both qualitative and quantitative analyses [Hiroyasu A., et al., 2018]. Larvae had been fed with FCNPs for 7 hours. The isolated hemocytes were put in a petri dish and expanded for 2 hours before fixation and then were processed for confocal microscopy. pERM antibody was used to outline the cell surface but primarily to visualize a possible interaction between the CNPs and the cell microvilli. Results are shown in **Figure 94,** where it is possible to spot nanoparticles inside the hemocytes. This could be considered the proof that CNPs were able, in 7 hours, to cross the intestine of the larvae and be captured by the hemolymph. The interaction of FCNPs with microvilli was even more clear in **Figure 94, D** cross-sections, where FCNPs accumulated in spots that correlated with pERM.

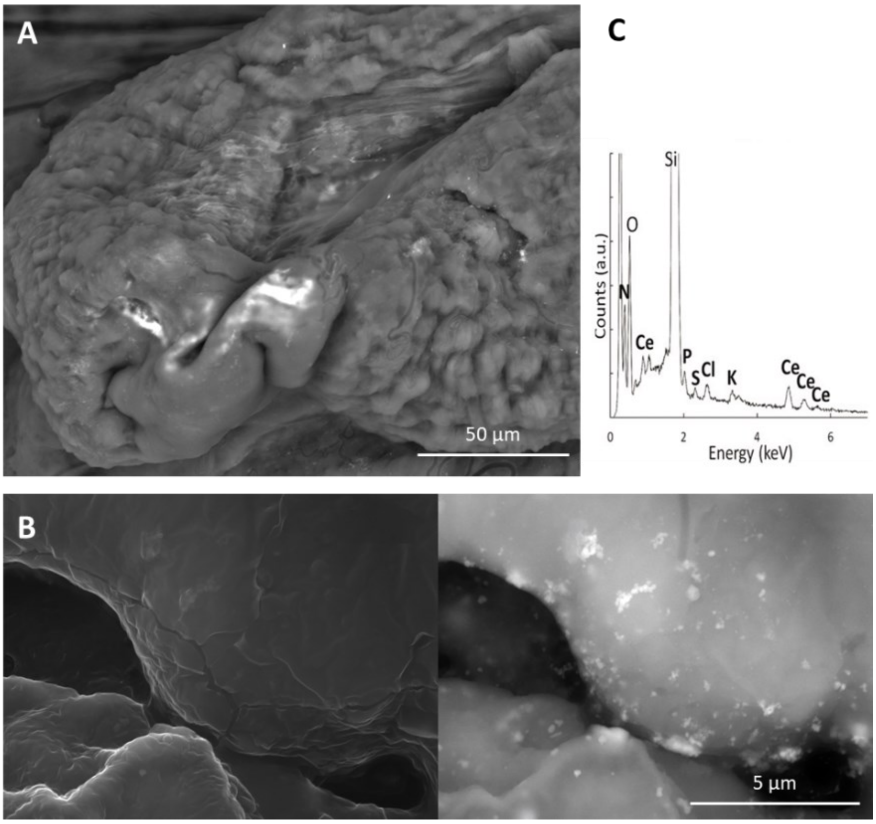

Figure 95. CNPs can cross the intestinal barrier after feeding the flies for 24 hours. *(A) Representative SEM image of the Drosophila's gut. White stains indicate the presence of CNPs. (B) Magnification of (A). The interaction of CNPs with the cells of the gut is visible in the BSE image. CNPs are visible as white spots adhering to the membrane of the gut. (C) The presence of CNPs was confirmed by SEM-EDS analysis. Signals other than Ce are due to the cell components and are fixative.*

Although these results were encouraging, it was not possible to apply the same study to the adult fly. It was then considered a different approach to study the CNPs ability to cross the intestine barrier and diffuse to other parts of the fly body. For this reason, SEM analyses were considered for the analysis of isolated portions of the fly body, like the intestine and ovaries. The results from guts isolated from adult flies fed with CNPs 3 mg/ml for 24 or 48 hours, collected and processed for SEM, are shown in **Figure 95**. The analysis, done on the isolated intestine, showed that CNPs were present on the basement membrane that surrounds the gut, confirming that CNPs moved out of the intestine, as observed by confocal microscopy. The SEM analysis allows to visualize only the topography of the external surface of the sample making it almost impossible (with this type of thick samples), to observe the presence of CNPs below the surface of the sample. As a result, it was not possible, in general, to investigate CNPs internalization and diffusion *inside* the organ analyzed with SEM. In the enlargement, is possible to visualize the accumulation of CNPs in several points of the basement membrane (**Figure 95, B**). This suggests that the visible CNPs were still somehow adherent, probably because in the process of being released.

Another interesting result is shown in **Figure 96**, where ovaries isolated from flies fed with CNPs for 48 hours, were observed. This representative image shows that the CNPs were able to reach and interact with the ovaries, distributing on the cuticles of single embryos (**Figure 96, B**). The CNPs were able to adhere to embryos of different stages of development, from the smaller ones (stage 10-11) to the bigger ones (stage 13-14) (**Figure 96, A**) [Avilés-Pagán E.E., et al., 2018]. They seemed, however, to distribute randomly on the embryos but further investigations were needed to identify the specific components because, in some areas, a pattern seemed to be visible (**Figure 96, D**).

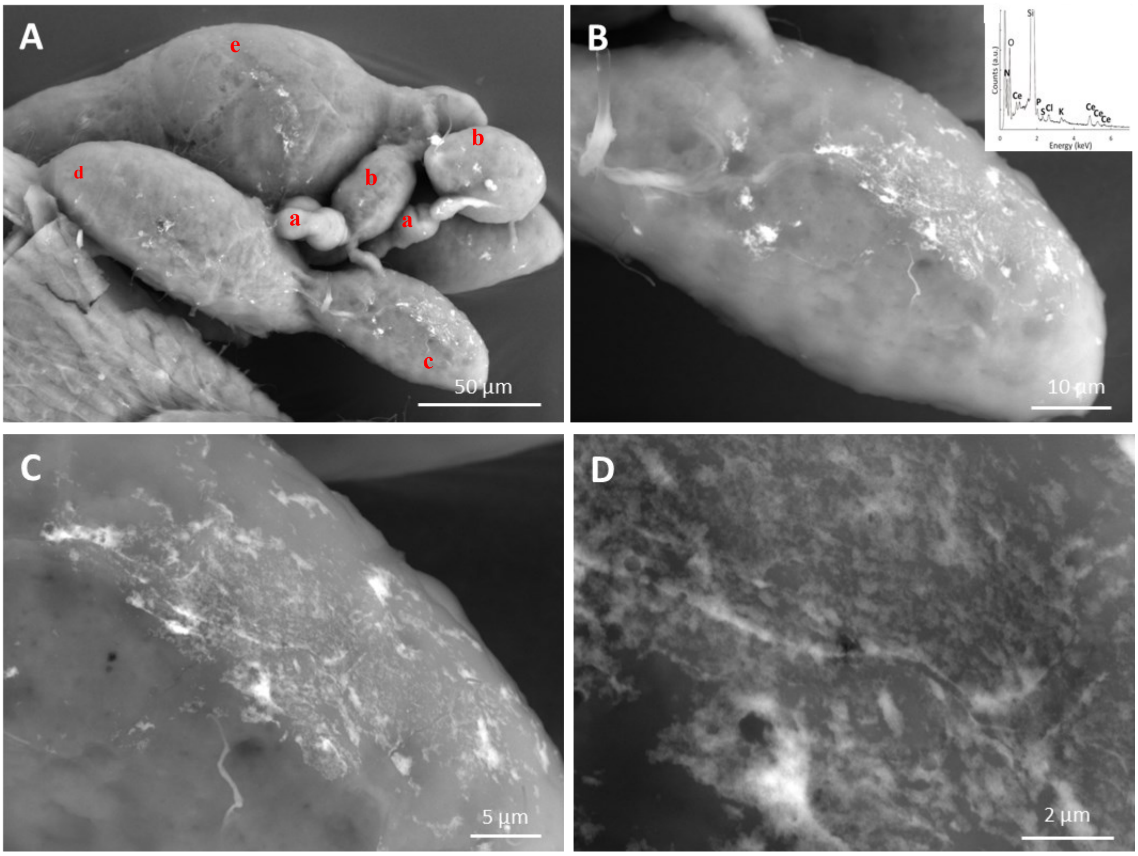

Figure 96. ***After feeding the flies for 48 hours, CNPs reach the ovaries and interact with the embryos.*** *(A) Red letters correspond to different stages of embryos development. (a) Stage 10; (b) stage 11; (c) stage 12; (d) stage 13; (e) stage 14. (B) Enlargement of (A). Inset, SEM-EDS analysis confirmed the presence of CNPs on the membrane of the embryos. (C) Enlargement of (B). (D) enlargement of (C).*

The distribution of CNPs in Drosophila's body was finally analyzed in cross-sections of the entire body. In **Figure 97, A** is possible to observe an example of a control fly stained with Phalloidin. In these 20 µm thick slices it was possible to observe a portion of a cross-section of the entire body of the fly, from the head and the thorax (with muscles) to the abdomen, with different portions of the gut and ovaries (arrows). This kind of analysis allowed a more precise visualization of the distribution of FCNPs in the entire flies' bodies. In **Figure 97, B-C** is possible to observe the distribution of the FCNPs after feeding the flies for 24 hours. As it is possible to observe, most of the nanoparticles were still accumulated in the lumen of the intestine, or just around it (white arrows), indicating internalization from the intestine. No signal was detected in the ovaries (green arrows) due probably to the shorter feeding period compared to 48 hours. However, it was possible to observe a distribution in other parts of the body, like the head (**Figure 97, B**, red arrow) or the abdomen (**Figure 97, C**, red arrow). In the abdomen, as shown in the enlargements (**Figure 97, D-E**), it was possible to visualize not only the FCNPs internalized by the enterocytes (**Figure 97, D**) but also their distribution in the haemolymphs all around the intestine (**Figure 97, E**), visible as small cells with a blue nucleus (white arrow).

The development of this technique was of fundamental importance for future analysis of the oxidation state of Cerium in Drosophila by X-ray absorption near-edge spectroscopy (XANES).

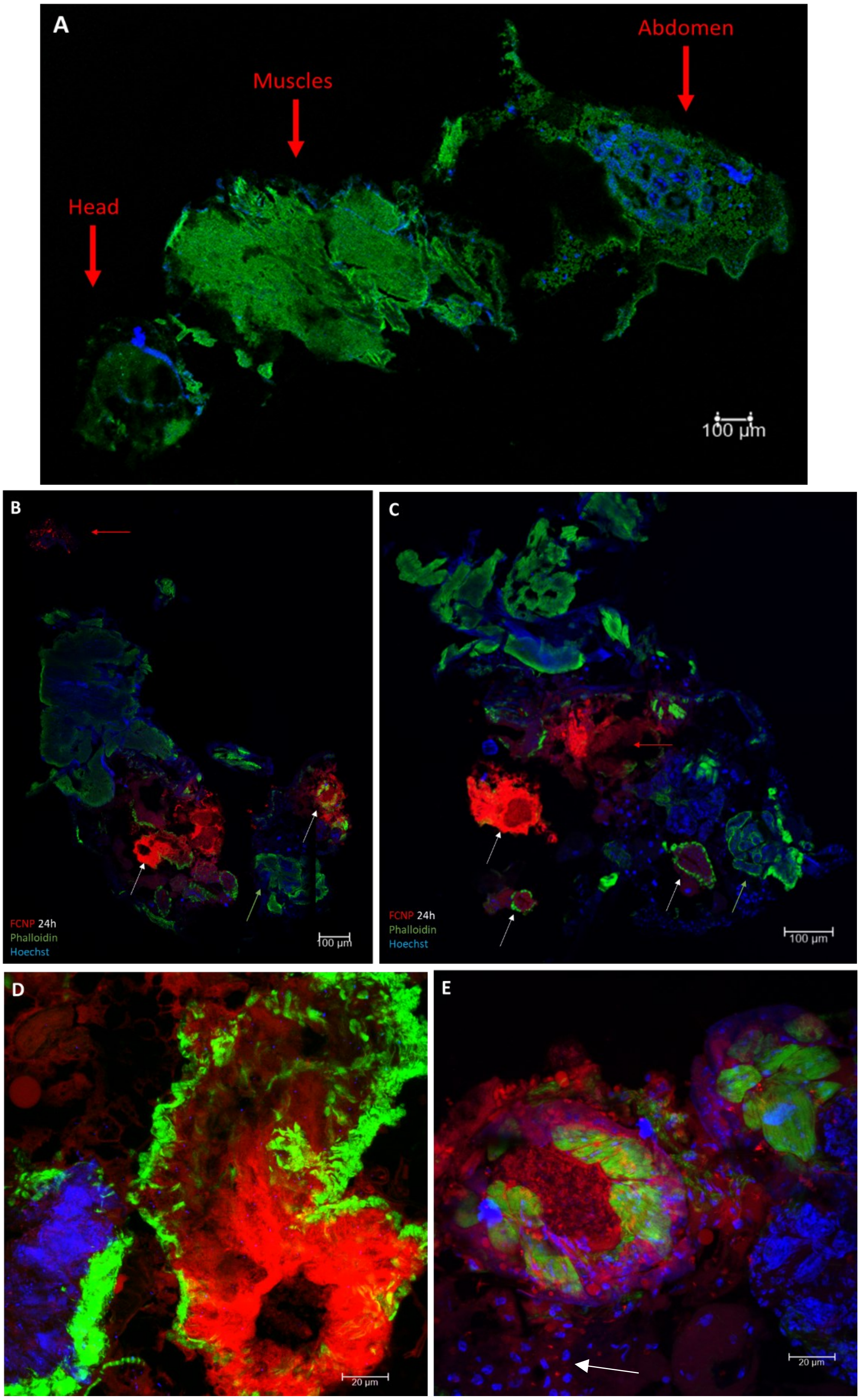

Figure 97. Representative confocal microscopy images of cross-sections of the entire body of Drosophila. *(A) Control flies, stained with Phalloidin (green) and Hoechst for nuclei (Blue). Different portions of the body are pointed by arrows. (B-C) Flies fed with FCNPs for 24 hours (Red) and stained with Phalloidin (green) and for nuclei (Blue). White arrows, intestine; Green arrow, ovaries; Red arrows, different points of accumulation of the nanoparticles, like the head in Figure (B). (D) Enlargement of (C). (E) Enlargement of (B) The internalization of FCNPs in hemocytes is visible (white arrow). Maximum projections of 15 confocal planes of 0.5 µm.*

4.3.4 Boron Neutron Capture Therapy (BNCT)

Synthesis and characterization of B-IONPs

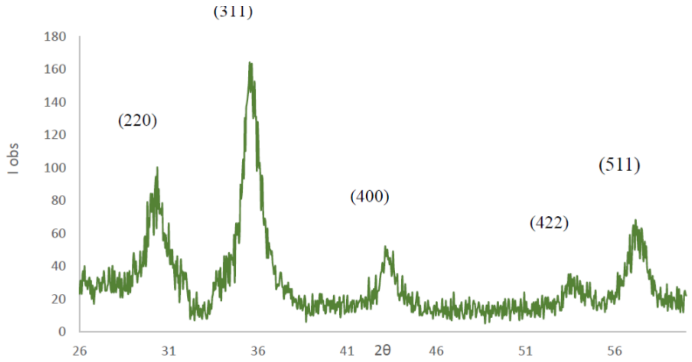

Figure 98. XRD analysis of B-IONPs

B-IONPs nanomaterials were characterized by X-ray diffraction in order to determine the size of the crystallites. The diffractograms were acquired using a step of 0.04 ° and an acquisition time per step of 8s.

The X-ray diffraction pattern in **Figure 98** showed six diffraction peaks at 2 θ = 30.2 °, 35.5°, 43.2°, 53.5°, and 57.1°, which corresponded respectively to the crystallographic planes (220), (311), (400), (422) and (511) of the magnetite structure. The product of the synthesis can therefore be considered monophasic and free of impurities due to other iron oxides. By applying the Scherrer equation, an average diameter of **5.3 ± 0.4 nm** is obtained, a size comparable to the IONPs and CNPs (see paragraph 3.3.1 and 3.3.7) The dimensions of the particles observed with the DLS technique showed a dimension of **70 nm ± 10 nm,** greater than the value obtained by XRD because it includes the capping polymer and the solvation sphere of the particle.

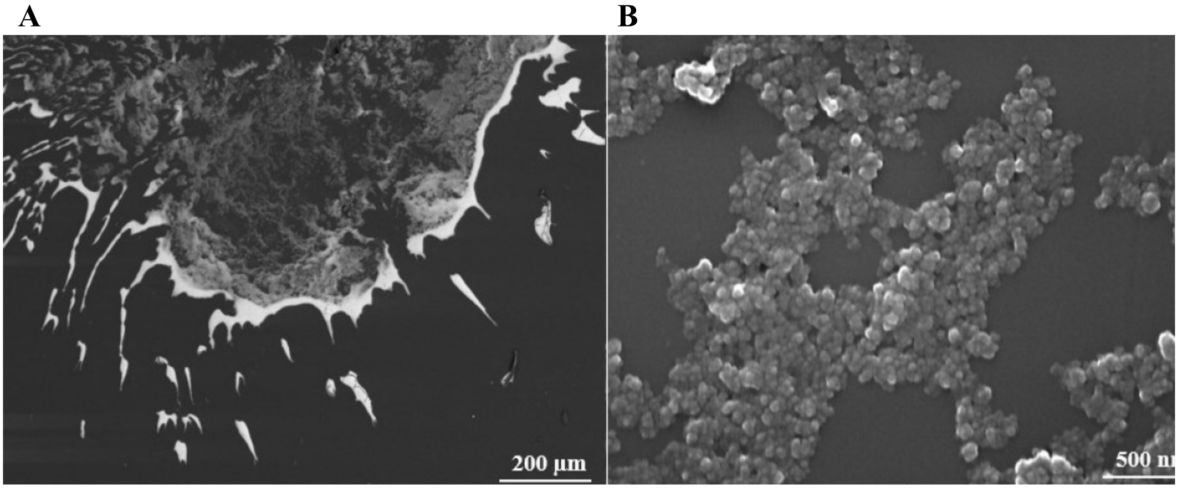

***Figure 99**. (A) Low magnification SEM image obtained in BSE. (B) Suspension of B-IONPs in the region inside the drop.*

The morphology of the nanoparticles was analyzed by SEM. The analysis was conducted on drops of the suspensions that were dried on the aluminum stubs. It was possible to distinguish two populations of nanomaterials of different sizes and morphology. The smaller fraction was located at the edge of the drop in **Figure 99**. The image was acquired using a BSE detector, so the contrast was of a compositional nature. In the most central region of the drop, it was possible to observe nanoparticles of more homogeneous dimensions in shape and size, with values compatible with those of the hydrodynamic radius obtained by DLS. This observation suggests that two fractions of nanoparticles were present in the suspension, one of the unbound magnetite nanoparticles and a fraction of IONPs-B_4C. It can therefore be reasonably confirmed that the fraction characterized by smaller dimensions consists only of IONPs, while the agglomerates of higher dimensions also contain B_4C, composed of lighter elements and consequently with a poor capacity to produce BSE signals.

In order to evaluate the effective response of B-IONPs to neutron irradiation, neutron autoradiography experiments were carried out. At this, a few drops of the suspensions were deposited on the CR39 detector, which was then irradiated and analyzed. Results showed that the B-IONPs had a concentration of ^{10}B equal to 0.7 µg/ml, obtained from the analysis of autoradiography. It is important to remember that this technique only reveals the presence of the ^{10}B isotope, which corresponds to about 20% of total boron.

Flies Viability

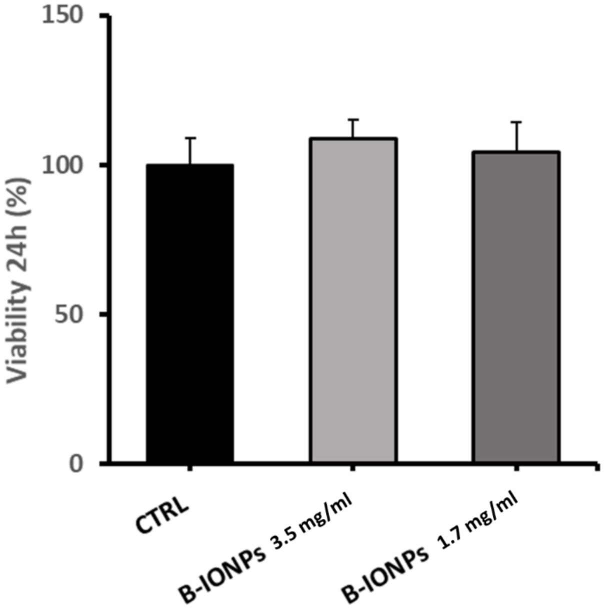

Figure 100*. (A) Viability of flies when breaded with two different concentrations of B-IONPs (3.5 mg/ml and 1.7 mg/ml of Fe3O4) for 24 hours. Data are expressed as an average ± SD of four independent experiments, expressed as a percentage considering the control sample (water supplemented with sucrose 20%) as 100%. 60 flies/condition were used for each experiment (= 240) flies tested for each condition.*

The first step was to define the concentration of B-IONPs to feed the flies and the duration of the exposure, in order to evaluate the higher dose with no toxic effect.

To investigate the possible effects of B-IONPs *in vivo*, the viability of flies fed with NPs was evaluated compared to the control fly, set at 100%. As it is possible to observe in **Figure 100,** 24 hours after the treatment there was no sign of toxicity for both the concentrations tested (3.5 mg/ml and 1.7 mg/ml of Fe_3O_4). Since the nanoparticles didn't show signs of toxicity for the flies, it was decided to keep them as the higher concentration limit for further analysis.

Evaluation of B-IONPs ability to cross the intestinal barrier

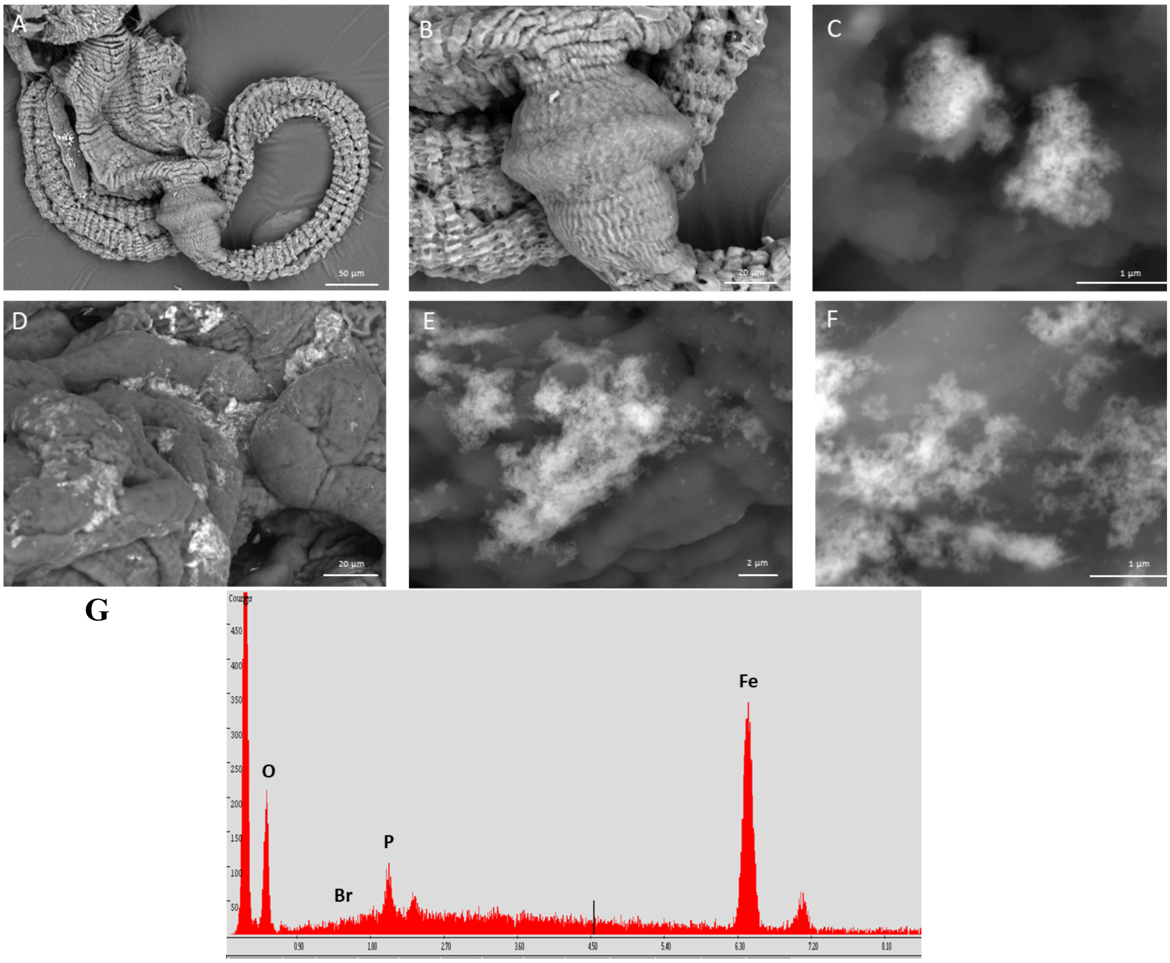

Figure 101. B-IONPs can cross the intestinal barrier after feeding the flies for 24 hours. *(A) Representative SEM image of the Drosophila's gut, after feeding the flies with B-IONPs for 24 hours. White stains indicate the presence of the B-IONPs. (B) Magnification of (A). (C) Magnification of (B). Aggregates of ≈ 70 nm of B-IONPs are visible. (D) Representative SEM image of the Drosophila's gut after feeding the flies with B-IONPs for 48 hours. (E) Magnification of (D). (F) Magnification of (E). (G) The presence of Iron in the B-IONPs was confirmed by SEM-EDS analysis.*

To evaluate the ability of B-IONPs to cross the intestine barrier, therefore be able to reach the other organs, specific portions of the fly body, like the intestine and ovaries, were isolated and processed for SEM, after feeding the flies with a suspension of B-IONPs (6 mg/ml) for 24 or 48 hours. Results are shown in **Figure 101** and in **Figure 102.**

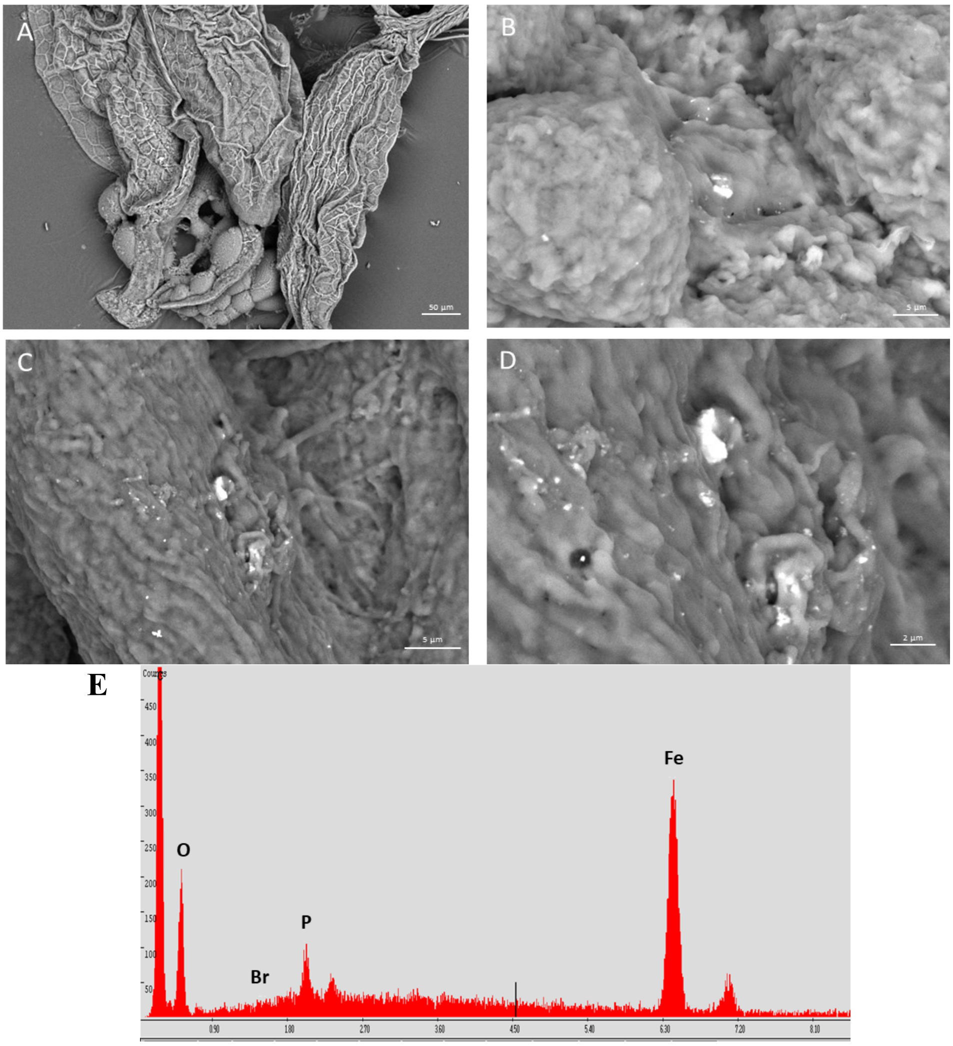

Figure 102. B-IONPs can interact with Drosophila ovaries after feeding the flies for 24 hours. *(A) Representative SEM image of the Drosophila's ovaries, after feeding the flies with B-IONPs for 24 hours. White stains indicate the presence of B-IONPs. (B) Magnification of (A). Aggregates of ≈ 70 nm of B-IONPs are visible. (C) Representative SEM image of the Drosophila's ovaries after feeding the flies with B-IONPs for 48 hours. (D) Magnification of (C). (E) The presence of Iron in the B-IONPs was confirmed by SEM-EDS analysis.*

The analysis, done on the isolated intestines, showed that B-IONPs were present on the basement membrane that surrounds the gut, confirming that the NPs moved out of the intestine, both in the case of 24 hours (**Figure 101, A-C**) or 48 hours (**Figure 101, D-E**). In both cases, in fact, several aggregates of nanoparticles are visible around the intestine, suggesting a high level of internalization. The SEM analysis allowed us to visualize only the topography of the external surface of the sample making it almost impossible, with this type of thick sample, to observe the presence of B-IONPs below the surface of the sample. As a result, it was not possible, in general, to investigate B-IONPs internalization and diffusion *inside* the organ analyzed with SEM. However, it was possible to visualize the accumulation of B-IONPs in several points of the basement membrane (**Figure 101, C, and F**). This suggests that the visible B-IONPs were still somehow adherent, probably because in the process of being released. When the diameter of the aggregates was calculated, it was in accordance with the value DLS analysis is obtained (≈ 70 nm). Moreover, to confirm that the spots visible were NPs, EDS analysis was carried out (**Figure 101, G**), as it's possible to observe in the picture, in which the signals of Fe derived from the nanoparticles is evident.

Another interesting result is shown in **Figure 102**, where ovaries isolated from flies fed with B-IONPs for 24 or 48 hours, were observed. This representative image shows that the B-IONPs were able to reach and interact with the ovaries, distributing on the cuticles of single embryos (**Figure 102, B**). They seemed, moreover, to distribute on the embryos following a specific pattern; however, further investigations were needed to identify the specific components.

Also in this case, it was possible to confirm the identity of B-IONPs by EDS analysis, where the peak relative to Iron (Fe) is evident (**Figure 102, E**).

^{10}B distribution in Drosophila

Drosophila flies, fed with B-IONPs were irradiated in order to observe (qualitatively) the distribution of ^{10}B in the different parts of the body. In **Figure 103** is possible to observe representative results of Drosophila fed with B-IONPs **(A, B)** and with BPA **(C).** As it is possible to appreciate from the pictures, after 4 hours of ingestion, ^{10}B is efficiently absorbed through the intestinal barrier and is equally distributed in the whole body, particularly in the head and in the abdomen of the flies (white arrows). The intense signal visible on the legs of the flies can be accounted for residuals of NPs in the vials where the flies were eating.

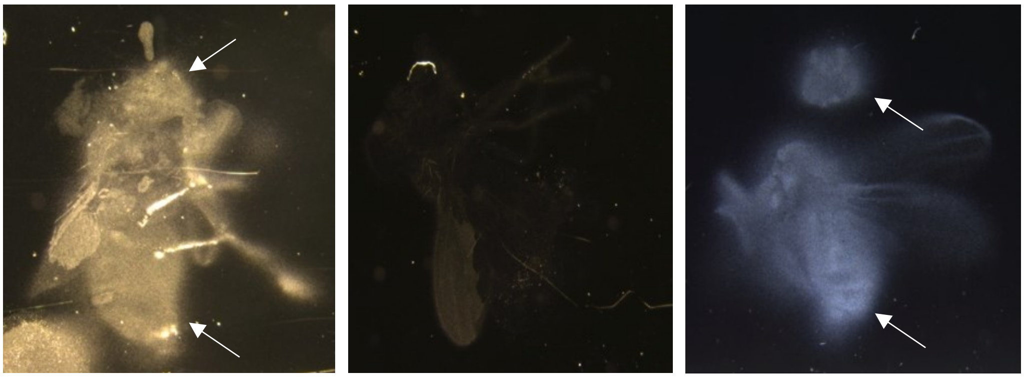

Figure 103. Representative optical images (10X) of Boron tracks left on the CR-39 by alpha and lithium ions coming from the neutron capture reaction on ^{10}B. *(A) Drosophila fed with B-IONPs for 4 hours and left for 2 hours with food without B-IONPs; (B) Drosophila fed with B-IONPs for 4 hours and left for 24 hours with food without B-IONPs; (C) Drosophila fed with BPA (5 mg/ml) for 4 hours and left for 2 hours with food without BPA.*

Additionally, the signal of ^{10}B is significantly lower, although visible, when flies were left for additional 24 hours with food without B-IONPs (**Figure 103, B**) This indicated that the elimination of the B-IONPs from the fly body required less than 24 hours, a time frame to be taken into consideration when treating tumor-bearing fly. For comparison, the fly had been fed with BPA (5 mg/kg) for the same time frame, and the distribution of ^{10}B was evaluated. As for the case of B-IONPs, the ^{10}B resulted equally distributed along the body of the flies after 24 hours, with prevalence to the head and low abdomen (**Figure 103, C,** arrows). However, it is interesting to notice that the signal derived from B-IONPs is more brilliant compared to the BPA one, suggesting a more efficient absorption and distribution of the NPs in respect to the BPA treatment. This result suggests an advantage of the administration of ^{10}B from the NPs over the existing therapy (like BPA). Moreover, proved the ability of B-IONPs and BPA to pass through the intestine barrier and reached other organs.

To confirm these qualitative data, quantitative analysis was carried out on Drosophila organs. Specifically, after preliminary analysis, it was chosen to feed the flies for two hours (*pulse*) and evaluate the distribution of ^{10}B after a period of: 0, 2, 4, 24, 48 hours, and 5 days (*chase*). After this time, organs from 10 different female flies for each condition were collected and irradiated, in order to evaluate the concentration of ^{10}B (**Figure 104**).

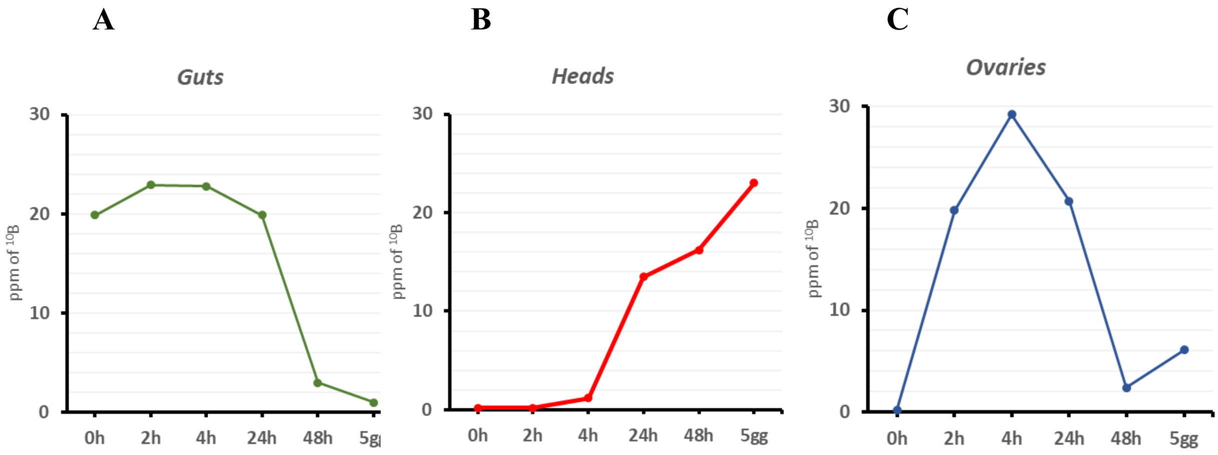

Figure 104. Concentration of ^{10}B in guts, heads, and ovaries of flies fed with BPA for 2 hours (pulse) and sacrificed at a different time (chase). *(A) Concentration of ^{10}B in the intestines. (B) Concentration of ^{10}B in the heads. (C) Concentration of ^{10}B in the ovaries. For the analysis, 10 different female flies were dissected, and their organs mixed.*

As it’s possible to observe from **Figure 104, A**, after just 2 hours (2 hours *pulse* + 0 hours *chase*) the concentration of ^{10}B in the intestine resulted to be 19.9 ± 0.7 ppm, with the maximum concentration that reached the intestine after 2 hours (2 hours *pulse* + 2 hours *chase*) (22.9 ± 0.8 ppm). This difference can be explained by the time necessary for the BPA to move from the stomach to the lower part of the intestine. The BPA remained in the intestine for the next 24 hours (*chase*), suggesting that this is the time necessary for the flies to digest and absorb the drug. After 48 hours (*chase*), the concentration of ^{10}B is drastically lower (3 ± 0.3 ppm), until reaching levels close to zero after 5 days (1 ± 0.2 ppm).

From the intestine, the ^{10}B slowly reached the head and the ovaries. Specifically, after 24 hours (*chase*), when the concentration in the intestine started to diminish, the ^{10}B reached the head (13.5 ± 0.6 ppm). The concentration of ^{10}B in the head continued to increase over time, reaching 23.5 ± 0.8 ppm after 5 days. This result suggests that, after 5 days, almost all the ^{10}B ingested is accumulated in the head and not yet entirely eliminated from the body.

As for the ovaries (**Figure 104, C**), the concentration ^{10}B start to increase even faster than in the head. In fact, after 2 hours, the concentration resulted to be already higher, passing from 0.2 ± 0.1 to 19.8 ± 0.2 in just two hours. The concentration remained high for 24 hours (20.7 ± 0.7), then abruptly diminished. In fact, after 48 hours the value came back to 2.4 ± 0.2, when, at the same time, the concentration in the head increased.

4.4 Discussion

The scope of this study was to assess whether the CNPs, ingested by the Drosophila fly, were distributed in different tissues/organs, and test in a model organism how the Ce oxidation state change based on this distribution.

Despite the physiological divergences between vertebrates and insects, the modeling of human diseases is possible in Drosophila because of the high degree of conservation of the genome between Drosophila and mammals (up to 75%) [Pappus S.A., et al., 2018]. Moreover, Drosophila has been widely used for medical research for over 100 years, and now is used as a model organism for various human diseases, from neurodegenerative disorders to cancer [Yamaguchi M., et al, 2018], and might represent an optimal candidate for testing the toxicological and biological effects of nanoparticles [Pappus S.A., et al., 2018]. The experimental advantages of using Drosophila are many: a substantial level of homology to the human genome and a wealth of techniques that facilitate highly sophisticated experiments, inexpensive husbandry procedures, a short generation time (~ 12 days), and a highly prolific nature.

Compared to an *in vitro* system, animal models offer a great advantage for studying the biological interaction NPs due to their complexity and in respect to the simpler systems of cultured cells. However, compared to cultured cells, the experimental setup in the case of model animals required that many additional aspects had to be considered. Feeding NPs to the flies (NPs concentration, duration, etc.), determining their toxicity while ensuring that among the population considered all the flies received an equal amount of NPs, or obtaining representative samples out of a possible heterogeneous population, are some of the challenges that had to be addressed.

The goal of this part of the study was to find the right conditions to investigate whether CNPs could diffuse to different fly organs once ingested. This was in preparation for the experiment planned to be performed at the ESRF with the purpose of studying the Ce oxidation state. Differently from a similar study previously performed in cultured cells [Ferraro D., et al., 2017], this *in vivo* approach using Drosophila as an animal model offered a higher level of complexity which could mimic, although with many limitations, the diffusion of NPs in the human body.

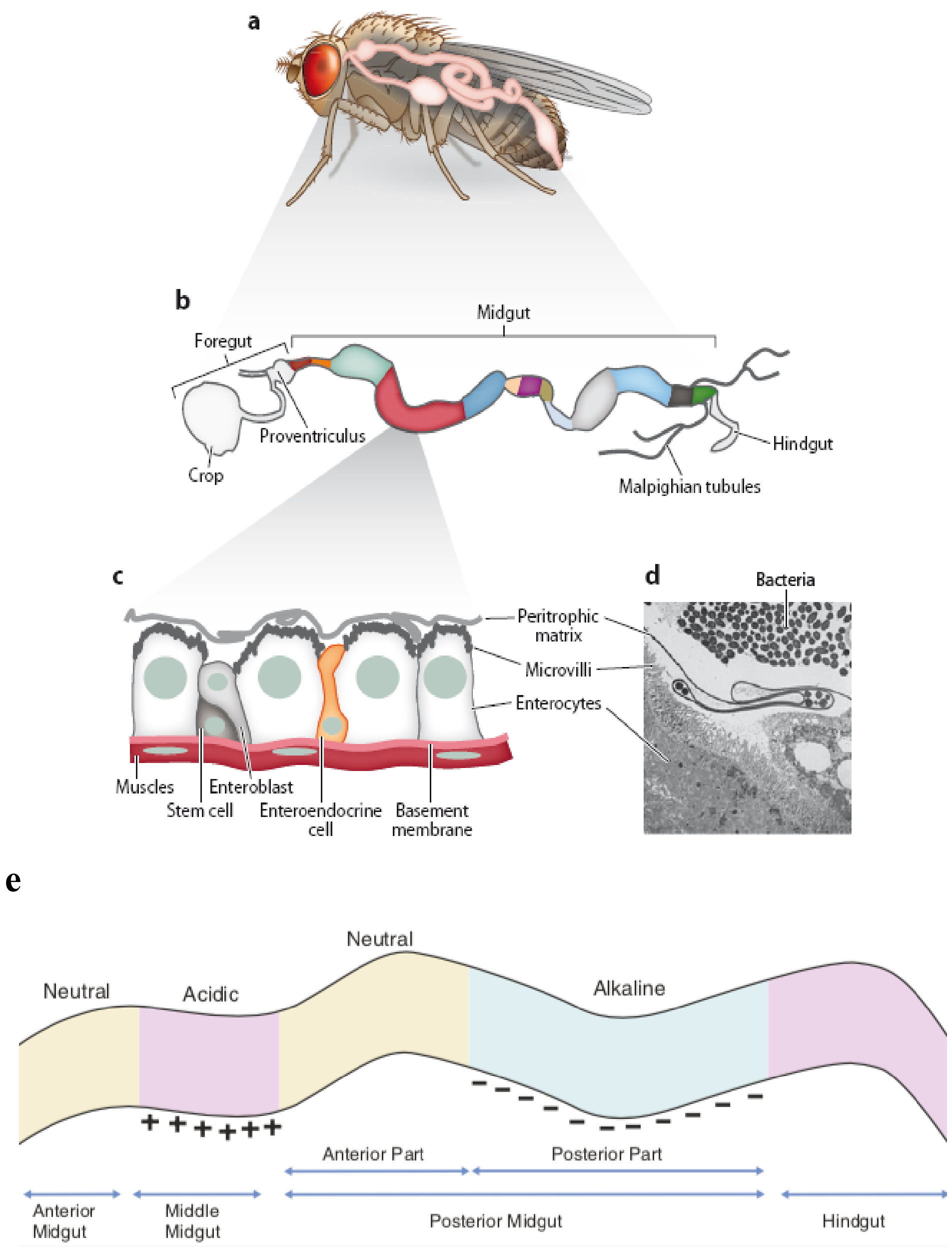

Figure 105. *(a-d) scheme of the digestive tract of Drosophila Melanogaster. Reproduced from Lemaitre B., et al., 2013. (e) Variation of pH in the gut of Drosophila Melanogaster. Reproduced from Pappus S.A., et al., 2018.*

The results obtained showed that Drosophila indeed could be a good candidate for the study related to the CNPs uptake and cell interaction. Flies could be fed with CNPs without showing signs of toxicity for concentration equal to or below 6 mg/ml. By confocal microscopy, it was possible to prove that ingested NPs were able to move along the entire intestine without losing their fluorescence while showing a different degree of adhesion on the epithelial cells. In the specific, the intestine of adult Drosophila flies is divided into three different regions: foregut, midgut, and hindgut (**Figure 105, b**). The foregut and hindgut epithelium are of ectodermal origin and are lined on the apical side by an impermeable cuticle. In contrast, the midgut epithelium is of endodermal origin and is protected on the luminal side by the peritrophic matrix (PM) (**Figure 105, d)**. The adult midgut is further subdivided into four major anatomical regions with distinct metabolic and digestive functions, each one of them characterized by a different pH (**Figure 105, e**). This consideration is of great importance when approaching the study of nanoparticles adhesion and internalization in Drosophila. It was possible to correlate the distribution of the CNPs along the intestine with the pH, confirming that longer retention of CNPs in the acidic portion of the middle midgut of Drosophila corresponded to the point of most internalization. Specifically, this can be explained by the fact that negatively charged NPs can pass the neutral pH of the midgut easily and reach the acidic middle midgut. CNPs could persist in that area for a longer time due to the electrostatic interaction [Pappus S.A., et al., 2018].

The sample preparation was also challenging because, especially for the adhesion and absorption analyses, it was important to eliminate the CNPs that did not interact with the enterocytes. This aspect was something that had to be addressed to be able to perform reliable analyses. Different media were considered in feeding the flies with CNPs (yeast versus 20% sucrose) as well as time intervals and even starvation after CNPs feeding. However, regardless of the feeding technique, the type of sample preparation resulted to be important in obtaining good results. Going from a whole intestine to 10 μm-slices analyses, allowed us to perform a more detailed investigation of the NPs interaction while eliminating the limiting factor of having free NPs present in the intestinal lumen.

As a result, it was possible to ascertain that CNPs could be ingested without causing any damage to the Drosophila fly. This confirmed that like the *in vitro* experiments with cultured cells, CNPs were not toxic. Most importantly, it was demonstrated that also *in vivo* CNPs were able to interact with the brush border of the intestinal epithelial cells, confirming what had been observed *in vitro* with HeLa cells (see paragraph 3.3.3). Colocalization between CNPs with pERM and Prominin CD133 suggested that also *in vivo*, as well as *in vitro*, the CNP-cell interaction might rely on the presence of lipid rafts on the epithelial cell membrane.

Overall, these results demonstrated that Drosophila is a good model animal for the study of NPs-cell interaction and that the CNPs not only could interact with the intestinal epithelium, but they could also diffuse and reach other organ/tissues in the Drosophila body.

This study was a preliminary condition to the success of the experiment designed to be performed at the ESRF. These results were, in fact, of vital importance in the view of understanding the distribution of Ce as well as Ce^{3+}/Ce^{4+} equilibrium inside different flies' tissues/organs and how it will be affected by oxidative stress. This analysis represents a further step toward the experimental assessment of the chemical mechanisms responsible for the CeO_2 activity in several degenerative diseases in which oxidative stress and free radical production play a crucial role.

Another focus of our research was to explore the possible use of B-IONPs for the Boron neutron capture therapy (BNCT). As concluded in several reviews [Coderre J.A., et al., 1999], [Barth R.F, et al., 1999], [Hawthorne M.F., et al., 2003], the therapeutic efficacy of BNCT requires: (1) increasing the boron concentration in the tumor, (2) improving the clearance of boron from normal tissue/blood and (3) long retention time of boron in the tumor.

The main idea of the study is that B-IONPs, compared to boronated amino acids, can offer more efficient delivery of ^{10}Boron (^{10}B) thanks to the properties of the NPs, which contain a large number of ^{10}B atoms (compared to BPA), have low toxicity and could be functionalized to increase their specificity toward the tumor, allowing to increase the concentration ratio between normal versus tumoral cell. Only very few studies are proving the efficacy of Boron Carbide *in vitro*, but *in vivo* investigations are lacking.

Here, we propose an alternative *in vivo* model using Drosophila. Preliminary results showed that flies could be fed with B-IONPs without showing signs of toxicity, supporting the idea that Drosophila could be a good *in vivo* model for this type of analysis. Moreover, the possibility to visualize ^{10}B by detecting the tracks visible on the CR-39, while comparing their position in respect to the Drosophila tissues/cells, provided valuable information about NPs reabsorption in the fly intestine and their overall distribution in the fly body. It was also possible to analyze quantitively the concentration and distribution of ^{10}B in the different organs of the flies (specifically intestine, head, and ovaries). The analysis showed that the ^{10}B from BPA remained in the intestine for 24 hours, while the ^{10}B delivered via B-IONP remained in the fly body for more than five days. This type of analysis, to the best of my knowledge, was never conducted on Drosophila.

About the effectiveness of B-IONPs in BNCT, preliminary results by SEM showed that the NPs were able to pass through the gut barrier and reach other organs. These results were also confirmed by qualitative analysis of the tracks of ^{10}B on CR-39. However, further studies are needed in order to quantify the concentration of ^{10}B in different organs and model a human tumor in Drosophila, with the aim of proving the efficacy of the new therapy with a low-cost *in vivo* model.

5. Conclusions

This project aimed to understand how super-small nanoparticles, specifically CNPs, interacted with biological systems.

In particular, the first part of the project was focused on the studying of the CNPs adhesion and internalization, and on the characterization of the specific interaction with microvilli as the first step for cellular internalization (MMA).

Given the results obtained, MMA can be considered an alternative pathway for NPs internalization that does not depend on the chemical nature of the NPs or the cell types but is influenced by the size and surface functionalization of the NPs. Especially the negative charge given by PAA seemed fundamental for the adhesion with a specific component of microvilli membrane, possibly involving lipid rafts (present in high concentration in the microvilli's membrane, but not on the planar regions). MMA might represent an interesting alternative route for drug delivery in the case of epithelial cells that abound in microvilli, such as gastric and intestinal epithelia. In cells such as HeLa, in which the density and distribution of microvilli correlate with the cell cycle, this specific adhesion could be exploited to obtain delivery controlled by the status of the cell.

The second part of the project aimed to understand the interaction, toxicity, and biodistributions of the nanoparticles in a whole organism. Specifically, Drosophila melanogaster was chosen, due to the long-existing experience of its use.

Results showed that CNPs can interact with the brush border of enterocytes, being internalized, and distribute along the entire body while exerting their antioxidant activity. By studying how the oxidation state of Cerium changes based on its distribution, it will be possible to take a further step toward understanding the chemical mechanisms responsible for CeO_2 activity in several degenerative diseases, in which oxidative stress and free radicals play a crucial role.

Moreover, by studying the distribution and concentration of ^{10}B from BPA and B-IONPs it was possible to prove the possibility of the use of Drosophila as a promising *in vivo* model for the Boron Neutron Capture Therapy (BNCT). Specifically, the goal of this part of the research was to explore the possible advantage of the use of B-IONPs for the BNCT over the existing therapies. This would be the first step toward a more complex protocol, where tumor-bearing Drosophila fly would be treated with BNCT, and the post-irradiation effects followed *in vivo*.

6. References

Achilli C., Grandi S., Ciana A., Guidetti G.F., Malara A., Abbonante V., Minetti G., Biocompatibility of functionalized boron phosphate (BPO4) nanoparticles for boron neutron capture therapy (BNCT) application, *Nanomedicine: Nanotechnology, Biology and Medicine* **(2014),** 10 (3), 589–597

Adler J., Parmryd I., Quantifying colocalization by correlation: The Pearson correlation coefficient is superior to the Mander's overlap coefficient, *Cytometry A.* (**2010**), 77(8), 733-42

Ady J.W., Desir S., Thayanithy V., Vogel R.L., Moreira A.L., Downey R.J., Fong Y., Manova-Todorova K., Moore M.A.S., Lou E., Intercellular communication in malignant pleural mesothelioma: properties of tunneling nanotubes, *Frontiers in Physiology* (**2014**), 5, 1664-042

Alaraby M., Hernández A., Annangi B., Demir E., Bach J., Rubio L., Creus A., Marcos R., Antioxidant and antigenotoxic properties of CeO2 NPs and cerium sulphate: Studies with Drosophila melanogaster as a promising in vivo model, *Nanotoxicology* (**2015**), 9(6), 749-59

Anding A.L., Baehrecke E.H., Cleaning house: selective autophagy of organelles, *Dev Cel,* (**2017**), 41(1), 10–22

Asati A., Santra S., Kaittanis C., Nath S., Perez J.M., Oxidase-like activity of polymer-coated cerium oxide nanoparticles, *Angew. Chem. Int.* (**2009**), 48, 2308–2312

Asati A., Santra S., Kaittanis C., Perez J. M., Surface-Charge-Dependent Cell Localization and Cytotoxicity of Cerium Oxide Nanoparticles, *ACS Nano* (**2010**), *4* (9), 5321–5331

Avilés-Pagán E.E., Orr-Weaver T.L., Activating embryonic development in Drosophila, *Seminars in Cell & Developmental Biology* (**2018**), 84, 100-110

Bar-Ilan O., Albrecht R.M., Fako V.E., Furgeson D.Y., Toxicity assessments of multisized gold and silver nanoparticles in zebrafish embryos, *Small*. (**2009**), 5(16), 1897-910

Barth R.F., Mi P., Yang W., Boron delivery agents for neutron capture therapy of cancer, *Cancer Commun* (**2018**), 38**,** 35

Barth R.F., Soloway A.H., Goodman J.H., Gahbauer R.A., Gupta N., Blue T.E., Yang W., TjarksBoron W., Neutron capture therapy of brain tumors: an emerging therapeutic modality, *Neurosurgery* (**1999**), 44, 433-451

Beignon A.S., McKenna K., Skoberne M., Manches O., DaSilva I., Kavanagh D.G., Larsson M., Gorelick R.J., Lifson J.D., Bhardwaj N., Endocytosis of HIV-1 activates plasmacytoid dendritic cells via Toll-like receptor-viral RNA interactions*, J Clin Invest*. (**2005**), 115(11), 3265–3275

Bohmer N., Jordan A., Beilstein J., *Nanotechnol.* (**2015)**, 6, 167–176

Bruna R., Rademakersh F. ROOT, An Object-Oriented Data Analysis Framework. 6.

Canton I., Battaglia G., Endocytosis at the nanoscale, *Chem. Soc. Rev*. (**2012**), 41, 2718-2739

Carnovale C., Bryant G., Shukla R., Bansal V., *ACS Omega* (**2019),** *4,* 242–256

Charras G.T., Hu C.K., Coughlin M., Mitchison T.J., Reassembly of contractile actin cortex in cell blebs, *The Journal of Cell Biology* (**2006**), 175 (3), 477-490

Cheng J.P.X., Nichols B.J., *Trends Cell Biol.* (**2016**), 26, 177–189

Chou L.Y.T., Ming K., Chan W.C.W., Strategies for the intracellular delivery of nanoparticles, *Chemical Society Reviews* (**2011**), 40 (1), 233-245

Christian, P., Von der Kammer, F., Baalousha, M. et al., Nanoparticles: structure, properties, preparation and behaviour in environmental media, *Ecotoxicology* (**2008**),17, 326–343

Christiansen K., Carlsen J., Microvillus membrane vesicles from pig small intestine. Purity and lipid composition, *Biochim. Biophys. Acta* (**1981**), 647, 188-195

Coderre J.A., Morris G.M., The radiation biology of boron neutron capture therapy, *Radiat. Res.* (**1999**), 151, 1-18

Crawley S.W., Mooseker M.S., Tyska M.J., Shaping the intestinal brush border, *J Cell Biol (***2014**) 207, 441-451

Das S., Chigurupati S., Dowding J., Munusamy P., Baer D.R., McGinnis J.F., Therapeutic potential of nanoceria in regenerative medicine. *MRS Bull.* (**2014**), 39(11), 976–83

Deshpande S.; Patil S.; Kuchibhatla S.V.N.T.; Seal S., Size dependency variation in lattice parameter and valency states in nanocrystalline cerium oxide, *Appl. Phys. Lett*. (**2005**), 87

Diegelmann S., Jansen A., Jois S., Kastenholz K., Escarcena L.V., Strudthoff N., Scholz H., The CApillary FEeder Assay Measures Food Intake in *Drosophila melanogaster, J Vis Exp*. (**2017**), 121, 55024

Ding L., Zhu X., Wang Y., Shi B., Ling X., Chen H., Nan W., Barrett A., Guo Z., Tao W., Wu J. and Shi X., *Nano Lett*. (**2017)**, 17, 6790–6801

Donahue N.D., Acar H., Wilhelm S., Concepts of nanoparticle cellular uptake, intracellular trafficking, and kinetics in nanomedicine, Advanced Drug Delivery Reviews (**2019**), 143, 68-96

Ferraro D., Tredici I. G., Ghigna P., Castillio-Michel H., Falqui A., Di Benedetto C., Alberti G., Ricci V., Anselmi-Tamburini U., Sommi P., Dependence of the Ce (Iii)/Ce (Iv) Ratio on Intracellular Localization in Ceria Nanoparticles Internalized by Human Cells, Nanoscale (**2017**), 9 (4), 1527–1538

Fisher H. W., Cooper T. W., Lund Electron Microscope Studies of the Microvilli of HeLa Cells, *J. Cell Biol.* **(1967)**, 34 (2), 569−576

Francia V., Montizaan D., Salvati A., Beilstein J., *Nanotechnol*. (**2020)**, 11, 338–353

Fujimoto L. M., Roth R., Heuser J. E. and. Schmid S. L, *Traffic* (**2000**), 1, 161–171

Gadan M., Bortolussi S., Postuma I., Ballarini F., Bruschi P., Protti N., Santoro D., Stella S., Cansolino L., Clerici A., Ferrari C., Zonta A., Zonta C., Altieri S., Set-up and calibration of a method to measure ¹⁰B concentration in biological samples by neutron autoradiography, *Nuclear Instruments and Methods in Physics Research* **(2018)**

Gliga A.R., Edoff K., Caputo F., K¨allman T., Blom H., Karlsson H.L., Cerium oxide nanoparticles inhibit differentiation of neural stem cells, *Sci. Rep.* (**2017**), 7, 1–20

Gorelik J., Shevchuk A.I., Frolenkov G.I.; Diakonov I.A., Lab M.J., Kros C.J., Richardson G.P., Vodyanoy I., Edwards C.R.W., Klenerman D., Korchev Y.E., Dynamic Assembly of Surface Structures in Living Cells, *Proc. Natl. Acad. Sci. U. S. A.* **(2003)**, 100 (10), 5819−5822

Gratton S.E.A., Ropp P.A., Pohlhaus P.D., Luft J.C., Madden V.J., Napier M.E., DeSimone J.M., *Proc. Natl. Acad. Sci. U. S. A.* (**2008)**, 105, 11613–11618

Guo L., Bussche A.V., Buechner M., Yan A., Kane A. B., Hurt R. H., Adsorption of essential micronutrients by carbon nanotubes and the implications for nanotoxicity testing, *Small* (**2008**), 4(6), 721–727

Hadjidemetriou M., Al-Ahmady Z., Kostarelos K., Time-evolution of in vivo protein corona onto blood-circulating PEGylated liposomal doxorubicin (DOXIL) nanoparticles, *Nanoscale* (**2016**), 8:12

Hanono A., Garbett D., Reckzek D., Chambers D. N., Bretscher A., EPI64 regulates microvillar subdomains and structure, *The Journal of Cell Biology* (**2006**), 175 (5), 803-813

Hawthorne M.F., LeeA M.W., Critical assessment of boron target compounds for boron neutron capture therapy, *J. Neuro-Oncol.* (**2003**), 62, 33-45

Herd H., Daum N., Jones A.T., Huwer H., Ghandehari H., Lehr C.M., *ACS Nano* (**2013)**, 7, 1961–1973

Hijaz M., Das S., Mert I., Gupta A., Al-Wahab Z., Tebbe C., et al., Folic acid tagged nanoceria as a novel therapeutic agent in ovarian cancer*, BMC Cancer* (**2016**), 16, 220

Hiroyasu A., DeWitt D.C., Goodman A.G., Extraction of Hemocytes from *Drosophila melanogaster* Larvae for Microbial Infection and Analysis, *J. Vis. Exp.* (**2018**), 135, e57077

Hirst S.M., Karakoti A., Singh S., Self W., Tyler R., Seal S., et al., Bio-distribution and in vivo antioxidant effects of cerium oxide nanoparticles in mice, *Environ Toxicol*. (**2013**), 28, 107–118

Hoshino A., Fujioka K., Oku T., Suga M., Sasaki Y. F., Ohta T., Yasuhara M., Suzuki K., Yamamoto K., Physicochemical properties and cellular toxicity of nanocrystal quantum dots depend on their surface modification, *Nano Lett* (**2004**), 4(11), 2163–2169

Hosseini A., Baeeri M., Rahimifard M., Navaei-Nigjeh M., Mohammadirad A., Pourkhalili N., Hassani S., Kamali M., Abdollahi M., *Hum. Exp. Toxicol.* **(2013)**, *32* (5), 544–553

Hussain S., Al-Nsour F., Rice A.B., Marshburn J., Yingling B., Ji Z., et al., Cerium dioxide nanoparticles induce apoptosis and autophagy in human peripheral blood monocytes, *ACS Nano* (**2012**), 6, 5820–5829

Hye-Ran K., Chang-Duk J., Microvilli, sensors or senders?, *Frontiers in Immunology* (**2019**), 10, 1753

Ja W.W., Carvalho G.B., Mak E.M., de la Rosa N.N., Fang A.Y., Liong J.C., Brummel T., Benzer S., Prandiology of Drosophila and the CAFE assay, *Proc. Natl. Acad. Sci. USA* (**2007**), 104, 8253–8256

Jaumouillé V., Waterman C.M., Physical Constraints and Forces Involved in Phagocytosis, *Front. Immunol*. (**2020**)

Karakoti A., Singh S., Dowding J.M., Seal S., Self W.T., Redox-active radical scavenging nanomaterials, *Chem. Soc. Rev.* (**2010),** 39, 4422–4432

Ke P.C., Lin S., Parak E.J., Davis T.P., Caruso F., A Decade of the Protein Corona, *ACS Nano* (**2017**), 11(12), 4

Kiio T.M., Park S., Physical properties of nanoparticles do matter, *J. Pharm. Investig.* (**2021**), 51, 35–5

Kirchner C., Liedl T., Kudera S., Pellegrino T., Muñoz Javier A., Gaub H.E., Stölzle S., Fertig N., Parak W.J., Cytotoxicity of colloidal CdSe and CdSe/ZnS nanoparticles, *Nano Lett* (**2005**), 5(2), 331–338

Kiss A. L., Botos E., *J. Cell. Mol. Med.* (**2009**), 13, 1228–1237

Korsvik, C., Patil, S., Seal, S., Self, W.T., Superoxide dismutase mimetic properties exhibited by vacancy engineered ceria nanoparticles, *Chem. Commun.* (**2007**), 1056–1058

Kou L., Sun J., Zhai Y., He Z., The endocytosis and intracellular fate of nanomedicines: Implication for rational design, *Asian Journal of Pharmaceutical Sciences* (**2013**), 8 (1), 1-10

Kuchma M.H., Komanski C.B., Colon J., Teblum A., Masunov A.E., Alvarado B., et al., Phosphate ester hydrolysis of biologically relevant molecules by cerium oxide nanoparticles, *Nanomedicine* (**2010**), 6, 738–744

Kuhn D. A., Vanhecke D., Michen B., Blank F., Gehr P., Petri-Fink A., Rothen-Rutishauser B., *Beilstein J. Nanotechnol*. (**2014**), 5, 1625–1636

Lai D.Y., Toward toxicity testing of nanomaterials in the 21st century: a paradigm for moving forward, *Wiley Interdiscip Rev Nanomed Nanobiotechnol* (**2012**), 4(1), 1-15

Lemaitre B., Miguel-Aliaga I., The Digestive Tract of *Drosophila melanogaster*, *Annual Review of Genetics* (**2013**), 47(1), 377-404

Letoha T., Gaál S., Somlai C., Venkei Z., Glavinas H., Kusz E., Duda E., Czajlik A., Peták F., Penke B. J., *Pept. Sci,* (**2005**), 11,805–811

Li H., Xia P., Pan S., Qi Z., Fu C., Yu Z., Kong W., Chang Y., Wang K., Wu D., Yang X., The Advances of Ceria Nanoparticles for Biomedical Applications in Orthopaedics, *Int J Nanomedicine*. (**2020**), 15, 7199-7214

Li Y., Yu Y., Duan J., Li Z., Geng W., Jiang L., Wang J., Jin M., Liu X., Sun Z., The Internalization, Distribution, and Ultrastructure Damage of Silica Nanoparticles in Human Hepatic L-02 Cells. *Part. Part. Syst. Charact. (***2016),** 33, 664–674

Lichen Y., Zhiyuan Z., 1.3.8B - Nanoparticles, Biomaterials Science (Fourth Edition), *Academic Press* (**2020**), 453-483

Lim J.P., Gleeson P.A., Macropinocytosis: an endocytic pathway for internalising large gulps, *Immunol Cell Biol* (**2011**), 89, 836-843

Liu L., Wang K., Liu J., Wei Y., Liu W., Zhang P., Hu J., Li B., Starvation Effect on the Morphology of Microvilli in HeLa Cells, B*iochem. Biophys. Res. Commun.* (**2019**), 514 (4), 1238−1243

Lord M.S., Tsoi B., Gunawan C., Teoh W.Y., Amal R., Whitelock J.M., Anti-angiogenic activity of heparin functionalised cerium oxide nanoparticles, *Biomaterials* (**2013**), 34, 8808–8818

Lou E., Fujisawa S., Morozov A., Barlas A., Romin Y., Tunneling Nanotubes Provide a Unique Conduit for Intercellular Transfer of Cellular Contents in Human Malignant Pleural Mesothelioma, *PLOS ONE* (**2012**), 7(3): e33093

Lundgren E., Roos G., Cell surface changes in HeLa cells as an indication of cell cycle events, *Cancer Research* (**1976**), 36, 4044-4051

Luo X., Killard A.J., Morrin A., Smyth M.R., Electrochemical preparation of distinct polyaniline nanostructrues by surface charge control of polystyrene nanoparticle templates, *Chem Commun* (**2007**), 3207–3209

Ma J.Y., Mercer R.R., Barger M., Schwegler-Berry D., Scabilloni J., Ma J.K., Induction of pulmonary fibrosis by cerium oxide nanoparticles, *Toxicol. Appl. Pharmacol*. (**2012**), 262, 255–264

Martens T.F., Remaut K., Demeester J., De Smedt S.C., Braeckmans K., Intracellular delivery of nanomaterials: how to catch endosomal escape in the act, *Nano Today* (**2014**), 9(3), 344–364

Mccord J.M., Fridovic I., Superoxide dismutase an enzymic function for erythrocuprein (hemocuprein), *J. Biol. Chem* (**1969**), 244, 6049–6055

Mercer J. and Helenius A., *Nat. Cell Biol.* (**2009**), 11, 510–520

Miyake Y., Kozutsumi Y., Nakamura S., Fujita T., Kawasaki T., Serine palmitoyltransferase is the primary target of a sphingosine-like immunosuppressant, ISP-1/myriocin, *Biochem. Biophys. Res. Commun*. (**1995**), 211, 396–403

Murthy S.K., Nanoparticles in modern medicine: state of the art and future challenges, *Int. J. Nanomed.* (**2007**), 2, 129–141

Nakase I.., Takeuchi T., Sonomura K., Kawabata N., Koike Y., Takehashi M., Tanaka S., Ueda K., Simpson J.C., Jones A.T., Sugiura Y., Futaki S., Cellular uptake of arginine-rich peptides: roles for macropinocytosis and actin rearrangement, *Mol Ther.* (**2004**)

Ong C., Yung L.Y., Cai Y., Bay B.H., Baeg G.H., Drosophila melanogaster as a model organism to study nanotoxicity. *Nanotoxicology* (**2014**), 25051331

Pappus S.A., Mishra M., A Drosophila Model to Decipher the Toxicity of Nanoparticles Taken Through Oral Routes, *Adv Exp Med Biol*. (**2018**), 1048, 311-322

Parkin E.T., Turner A.J., Hooper Differential N.M., Effects of glycosphingolipids on the detergent-insolubility of the glycosylphosphatidylinositol-anchored membrane dipeptidase, *Biochem. J.* (**2001**)*,* 358, 209-216

Parsons G.K.S., Wu S., Lipid Raft, *Schwab M. (eds) Encyclopaedia of Cancer. Springer* (**2012**)

Pelkmans L., Helenius A., *Traffic* (**2002**), 3, 311–320

Pezzini I., Marino A., Del Turco S., Nesti C., Doccini S., Cappello V., et al., Cerium oxide nanoparticles: the regenerative redox machine in bioenergetic imbalance, *Nanomedicine* (**2017**), 12, 403–416

Pinals R.L., Yang D., Rosenberg D.J., Chaudhary T., Crothers A.R., Iavarone A.T., Hammel M., Landry M.P., Protein corona composition and dynamics on carbon nanotubes in blood plasma and cerebrospinal fluid, *bioRxiv* (**2020**), 01(13), 905356

Poole K., Meder D., Simons K., Müller D., The Effect of Raft Lipid Depletion on Microvilli Formation in MDCK Cells, Visualized by Atomic Force Microscopy, *FEBS Lett.* (**2004**), *565* (1–3), 53–58

Postuma I., Bortolussi S., Protti N., Ballarini F., Bruschi P., Ciani L., Ristori S., Panza L., Ferrari C., Cansolino L., Altieri S., An improved neutron autoradiography set up for 10B concentration measurements in biological samples, *Reports of Practical Oncology & Radiotherapy* (**2016**), 21 (2), 123-128

Postuma I., Sommi P., Vitali A., Shu D., Martino G.D., Cansolino L., Ferrari C., Ricci V., Magni C., Protti N., Fatemi S., Tamburini U.A., Bortolussi S., Altieri S., Colocalization of tracks from boron neutron capture reactions and images of isolated cells, *Appl Radiat Isot*. (**2021**), 167:109353

Qiu S., Dong J., Chen G., Preparation of Cu nanoparticles from water-in-oil microemulsions. *J Coll Interf Sci* (**1999**), 216, 230–234

Reed K., Cormack A., Kulkarni, A., Mayton M., Sayle, D., Klaessig, F., Stadler B., Exploring the properties and applications of nanoceria: Is there still plenty of room at the bottom?, *Environ. Sci. Nano* (**2014**), 1, 390–405

Rempel J.Y., Trout B.T., Bawendi M.G., Jensen K.F., Density functional theory study of ligand binding on CdSe (0001), (0001), and (1120) single crystal relaxed and reconstructed surfaces: implications for nanocrystalline growth, *J Phys Chem B* (**2006**), 110, 18007–18016

Ribeiro F. M., de Oliveira M.M., Singh S., Sakthivel T.S., Neal C.J., Seal S., Ueda-Nakamura T., Lautenschlager S.O.S., Nakamura C.V., *Front. Bioeng. Biotechnol.* ***(*2020)**, *8*, 1–13

Riss T. L., Cell Viability Assays, *Assay Guidance Manual* (**2016**)

Rzigalinski B.A., Carfagna C.S., Ehrich M., Cerium oxide nanoparticles in neuroprotection and considerations for efficacy and safety, *Wiley Interdiscip Rev Nanomed Nanobiotechnol*. (**2017**), 9(4), 10.1002/wnan.1444

Saifi M.A., Seal S., Godugu S., Nanoceria, the versatile nanoparticles: Promising biomedical applications, *Journal of Controlled Release* (**2021**), 338, 164-189

Sajid M., Płotka-Wasylka J., Nanoparticles: Synthesis, characteristics, and applications in analytical and other sciences, *Microchemical Journal* (**2020**), 154, 104623

Salah-Eddin A., Salem N.M., Ghabeish I.H., Awwad A.M., Toxicity of Nanoparticles against Drosophila melanogaster, *Journal of Nanomaterials* **(2015)***,* 758132

Sanchez F., Sobolev K., Nanotechnology in concrete – A review, *Construction and Building Materials* (**2010**), 24, Issue 11, 2060-2071

Santra S., Kaittanis C., Grimm J., Perez J. M., Drug/Dye-Loaded, Multifunctional Iron Oxide Nanoparticles for Combined Targeted Cancer Therapy and Dual Optical/Magnetic Resonance Imaging, *Small* (**2009**), *5* (16), 1862–1868

Sau T.K., Rogach A. L., Nonspherical noble metal nanoparticles: colloid-chemical synthesis and morphology control, *Advanced materials* (**2010**), 22 (16), 1781-804

Shanbahg S., Tripathi S., Epithelial ultrastructure and cellular mechanisms of acid and base transport in the Drosophila midgut, *Journal of Experimental Biology* (**2009**), 212, 1731-1744

Shaw D.J., Colloid and surface science, 4th edn. *Butterworth-Heinemann Ltd* (**1992**)

Shen Z., Ye H., Yi X., Li Y., *ACS Nano* **(2019)**, 13, 215–228

Singh S., Kumar A., Karakoti A., Seal S., Self W.T., Unveiling the mechanism of uptake and sub-cellular distribution of cerium oxide nanoparticles, *Mol Biosyst*. (**2010**), 6(10), 1813-1820

Sousa de Almeida M., Susnik E., Drasler B., Taladriz-blanco P., Petri-Fink A., Rothen-Rutishauser B., Understanding nanoparticle endocytosis to improve targeting strategies in nanomedicine, *Chem. Soc. Rev.* (**2021**), 50, 5397-5434

Spuch C., Saida O., Navarro C., Advances in the Treatment of Neurodegenerative Disorders Employing Nanoparticles, *Recent Patents on Drug Delivery & Formulation* (**2012**), 6, 2-18

Sun Y., Li X., Zhang W., Wang P., A method for the preparation of stable dispersions of zero-valent iron nanoparticles, *Coll Surf A: Physicochem Eng Aspects* (**2007**), 31, 60–66

Swanson J. A., Yoshida S., *Philos. Trans. R. Soc.* B (**2019**), 374, 20180157

Thakur N., Manna P. & Das J., Synthesis and biomedical applications of nanoceria, a redox active nanoparticle, *J Nanobiotechnol* (**2019**), 17, 84

Tian Z., Li J., Zhang Z., Gao W., Zhou X., Qu Y., Highly sensitive and robust peroxidase-like activity of porous nanorods of ceria and their application for breast cancer detection, *Biomaterials* 59 (**2015**), 116–124

Torgersen M.L., Skretting G., van Deurs B., Sandvig K., Internalization of cholera toxin by different endocytic mechanisms, *J Cell Sci.* (**2001**), 114(20), 3737-47

Traub L.M., *Nat. Rev. Mol. Cell Biol.* (**2009**),10, 583–596

Treuel L., Docter D., Maskos M., Stauber R.H., Protein corona – from molecular adsorption to physiological complexity, *Beilstein J. Nanotechnol.* (**2015**), 6, 857–873

Tseng M.T., Lu X., Duan X., Hardas S.S., Sultana R., Wu P., et al., Alteration of hepatic structure and oxidative stress induced by intravenous nanoceria, *Toxicol. Appl. Pharmacol.* (**2012**), 260, 173–182

Tyska M.J., Mooseker M.S., MYO1A (brush border myosin I) dynamics in the brush border of LLC-PK1-CL4 cells, *Biophys J* (**2002**), 82, 1869–83

Vega-Alvarez S., Herrera A., Rinaldi C., Carrero-Mart´ınez F.A., Tissue-specific direct microtransfer of nanomaterials into *Drosophila* embryos as a versatile in vivo test bed for nanomaterial toxicity assessment, *International Journal of Nanomedicine* **(2014),** 9(1), 2031–2041

Venkatachalam K., Wong C-O., Zhu M.X., The role of TRPMLs in endolysosomal trafficking and function, *Cell Calcium* (**2015**), 58(1), 48–56

Wang Z., Tiruppathi C., Minshall R. D. and Malik A. B., *ACS Nano* (**2009**), 3, 4110–4116

Wise J.P. Sr, Goodale B.C., Wise S.S., Craig G.A., Pongan A.F., Walter R.B., Thompson W.D., Ng A.K., Aboueissa A.M., Mitani H., Spalding M.J., Mason M.D., Silver nanospheres are cytotoxic and genotoxic to Wsh cells, *AquatToxicol* (**2009**), 97 (1), 34–41

Wolfram J., Yang Y., Shen J., Moten A., Chen C., Shen H., Ferrari M., Zhao Y., The nano-plasma interface: Implications of the protein corona, *Colloids and Surfaces B: Biointerfaces* **(2014)**, 124, 17-24

Wuister S.F., Donega C.M., Meijerink A., Influence of thiol capping on the exciton luminescence and decay kinetics of CdTe and CdSe quantum dots, *J Phys Chem B* (**2004**), 108, 17393–17397

Xiao Y.F., Li J.M., Wang S.-M., Yong X., Tang B., Jie M.M., et al., Cerium oxide nanoparticles inhibit the migration and proliferation of gastric cancer by increasing DHX15 expression, *Int. J. Nanomedicine* (**2016**), 11, 3023

Xue, Y., Zhai, Y., Zhou, K., Wang, L., Tan, H., Luan, Q., Yao, X., The vital role of buffer anions in the antioxidant activity of CeO2 nanoparticles, *Chemistry* (**2012**), 18, 11115–11122

Yamaguchi M., Yoshida H., *Drosophila* as a Model Organism. In: Yamaguchi M. (eds) Drosophila Models for Human Diseases. Advances in Experimental Medicine and Biology, (**2018**), 1076, Springer

Yarar D., Waterman-Storer C.M., Schmid S.L., A dynamic actin cytoskeleton functions at multiple stages of clathrin-mediated endocytosis, *Mol Biol Cell.* (**2005**), 6(2), 964-75

Yonemura S., Tsukita S., Tsukita S., Direct Involvement of Ezrin/Radixin/Moesin (ERM)-binding Membrane Proteins in the Organization of Microvilli in Collaboration with Activated ERM Proteins, *J Cell Biol* (**1999**), 145 (7), 1497–1509

Zanganeh S., et al., Protein Corona. Opportunities and Challenges. *International Journal of Biochemistry and Cell Biology* (**2016**), 75(5)

Zholobak N.M., Ivanov V.K., Shcherbakov A.B., Shaporev A.S., Polezhaeva O.S., Baranchikov A.Y., Spivak N.Y., Tretyakov Y.D.J., *Photochem. Photobiol. B Biol.* **(2011)**, *102* (1), 32–38

7. Scientific production arisen from this thesis

Peer-reviewed publications (2021)

- Patrizia Sommi, Agostina Vitali, **Stefania Coniglio**, Daniele Callegari, Sofia Barbieri, Alberto Casu, Andrea Falqui, Lorenzo Vigano', Barbara Vigani, Franca Ferrari, and Umberto Anselmi-Tamburini**,** Microvilli Adhesion: An Alternative Route for Nanoparticle Cell Internalization**,** *ACS Nano* 2021 *15* (10), 15803-15814 (DOI: 10.1021/acsnano.1c03151)

Abstract at international meetings

- Participation in the "School of Nanomedicine" (11-13 December 2019, Trieste):

Interaction between CeO_2 Nanoparticles and Cells: use of Drosophila Melanogaster as in vivo experimental model, **Coniglio, Stefania;** Sommi, Patrizia; Ricci, Vittorio. (**Poster presentation**)

- Participation in the Workshop "Ricerca e Nanomedicina" (15 June 2021):

Microvilli adhesion: an alternative route for nanoparticle cell interaction, Sommi, Patrizia; Vitali, Agostina; **Coniglio, Stefania**; Callegari, Daniele ; Barbieri, Sofia; Casu, Alberto; Falqui, Andrea; Viganò, Lorenzo; Vigani, Barbara; Ferrari, Franca; Anselmi-Tamburini, Umberto (**Oral presentation**)

8. Acknowledgements

I thank all the Professors and Researchers for their helpfulness and courtesy; in particular:

- Professor U. Laforenza, who kindly accepted to be my Ph.D. supervisor, after the premature death of Prof. V. Ricci, my former Ph.D. supervisor;
- Professor U. Anselmi Tamburini, for welcoming me to the LAMSC laboratory;
- Dott. A. Vitali, for helping me with precious suggestions in the moments of most need;
- Dott. P. Vaghi and Dott. A. Oldani, from "Centro Grandi Strumenti" (CGS) of the University of Pavia, for the use of confocal microscopy;
- Dott. A. Azzalin, Department of Molecular Medicine, University of Pavia for the use of the FACS cytofluorimeter;
- Professor P. Pallavicini, Department of Chemistry, University of Pavia for the use of DLS;
- "Centro Interdipartimentale di Studi e Ricerca per la Conservazione del Patrimonio Culturale" (CISRiC) of the University of Pavia for providing access to SEM;
- Dott. C. Di Benedetto of the King Abdullah University of Science and Technology (KAUST) for TEM sample preparation and image acquisition;
- Prof. S. Bortolussi and Dott. I. Postuma, from the department of physics of the University of Pavia, for nuclear analysis.

Most of all, I am grateful to Dott. P. Sommi, who led me to complete my training and guided me during the last three years.

Finally, my most heartfelt thanks go to my colleagues from the Human Physiology department, and my family.